HOKKAIDO UNIVERSITY

Title	Structure Engineering of Carbon-based Materials for Efficient Photocatalysis
Author(s)	李, 云祥
Degree Grantor	北海道大学
Degree Name	博士(理学)
Dissertation Number	甲第14013号
Issue Date	2020-03-25
DOI	https://doi.org/10.14943/doctoral.k14013
Doc URL	https://hdl.handle.net/2115/80638
Type	doctoral thesis
File Information	LI_Yunxiang.pdf

Hokkaido University Collection of Scholarly and Academic Papers : HUSCAP

Structure Engineering of Carbon-based Materials for Efficient Photocatalysis

（高効率光触媒の構築に向けた炭素系材料の構造制御に関する研究）

Yunxiang LI

Graduate School of Chemical Sciences and Engineering

Hokkaido University



2020

Contents

Contents I

Abstract 1

Chapter 1 Introduction 3

1.1 Basics of photocatalysis 3

1.2 Potential applications of photocatalysis 4

1.2.1 Photocatalytic water splitting 4

1.2.2 Photocatalytic CO_2 reduction 6

1.2.3 Photocatalytic degradation of organics 7

1.2.4 Photocatalytic H_2O_2 generation 8

1.2.5 Other applications 8

1.3 Current status of research and development of efficient photocatalytic systems 9

1.3.1 Photocatalytic materials 9

1.3.2 Co-catalysts 11

1.3.3 Interfaces between photocatalysts and co-catalysts 16

1.4 Carbon-based photocatalytic systems 21

1.4.1 Modulation of polymeric carbon nitride 21

1.4.2 Modulation of carbon-based co-catalysts 31

1.4.3 Interfacial engineering of carbon-based photocatalytic systems 36

1.5 Thesis motivations and organization 38

References 41

Chapter 2 Atomic carbon chains-mediated carriers transfer over polymeric carbon nitride for efficient photocatalysis 49

2.1 Introduction 49

2.2 Experimental section 50

2.2.1 Materials preparation 50

2.2.2 Material characterization 51

Contents

2.2.3 Photoelectrochemical measurement 52

2.2.4 Photocatalytic activity measurement 52

2.3 Results and discussion 53

2.3.1 Atomic carbon chains linked polymeric CN 53

2.3.2 Carbon chains-mediated photocarriers separation and transport 61

2.3.3 Superior light-driven H_2 evolution and CO_2 reduction 66

2.4 Conclusions 70

References 70

Chapter 3 Targeted exfoliation and reassembly of polymeric carbon nitride for efficient photocatalysis 74

3.1 Introduction 74

3.2 Experimental section 75

3.2.1 Material preparation 75

3.2.2 Material characterization 77

3.2.3 Photocatalytic activity measurement 78

3.3 Results and discussion 79

3.3.1 Formation of shallow surface-alkalized polymeric CN 80

3.3.2 Reversible exfoliation-reassembly of CNK-OH and related mechanism 82

3.3.3 Exfoliated-reassembled samples deliver high photoactivity 97

3.4 Conclusions 105

References 105

Chapter 4 Single-Co on N-rich carbon as co-catalyst for efficient photocatalytic H_2 production: the key roles of cleared interfaces and isolated metal sites 109

4.1 Introduction 109

4.2 Experimental section 111

4.2.1 Materials preparation 111

4.2.2 Material characterization 112

4.2.3 Photoelectrochemical measurement 113

4.2.4 Computational details 113

Contents

4.2.5 Photocatalytic activity measurement 114

4.3 Results and discussion 115

4.3.1 Synthesis and characterization of co-catalyst Co-NC 115

4.3.2 Photocatalytic H_2 evolution activity 120

4.3.3 The roles of cleared interfaces and robust Co-N_4 moieties in high performance 127

4.4 Conclusions 139

References 140

Chapter 5 Conclusions and future prospects 144

5.1 General conclusions 144

5.2 Future prospects 145

Acknowledgement 147

Abstract

Metal free carbon-based materials, featuring low cost, editable structure and unique physicochemical property, are promising candidates for photocatalytic systems. Among them, polymeric carbon nitride (CN) has attracted extensive attention as photocatalyst in recent years due to its low cost, ease of synthesis, and appropriate band structure. However, efficient solar-to-energy conversion over CN still encounters great challenges because of its inherent drawbacks, such as the fast recombination of photocarriers, poor electronic conductivity. Furthermore, the lack of robust active sites on carbon co-catalysts and interfacial contamination with adventitious carbon severely limit the overall photocatalytic efficiency of carbon-based photocatalytic systems. In this work, the object is to design and develop carbon-based materials via modulating the intrinsic properties of photocatalyst CN, creating novel carbon-based co-catalyst and removing the relevant interfacial adventitious carbon for efficient photochemical processes and thus to further understandings of carbon-based materials as well as the corresponding mechanism of photocatalysis.

In chapter 1, an overview of photocatalysis was introduced first. Then, a review of photocatalytic system, including the photocatalysts, co-catalysts, interfaces and relevant modulation strategies, was given. In the end, the recent development of carbon-based photocatalytic system was summarized.

In chapter 2, to improve the poor electronic conductivity of CN and thus to promote the charge carrier transfer and separation behavior, a conceptual and facile strategy was developed to construct carbon chains incorporated CN. Various kinds of carbon chains can connect the in-plane defects of CN via strong covalent C-N bonds. Those embedded atomic carbon chains could efficiently mediate the electron transfer in the basal plane of CN. As a result, the optimal carbon chains-planted CN delivers a remarkably enhanced photocatalytic performance, achieving a 13.2 and 29.2-fold improvement in H_2 evolution and CO_2 reduction, respectively. This study provides an in-depth insight into the modulation of in-plane electrical conductivity at molecular scale over CN and offers new opportunities for reinforcing the reaction kinetics of organic-based photocatalysts.

In chapter 3, a facile, green, and reversible exfoliation-reassembly strategy was developed to switch the features of polymeric CN for different photoredox reactions. The

OH groups are implanted between the layers of CN in advance, then the introduced small-sized protons enter into the layer spacing and neutralize the OH to produce H_2O. The giant expansion effect of in situ-generated H_2O molecules confined to the interlayer results in the mass production of ultrathin polymeric CN nanosheets, giving a high yield, i.e., up to 48%, of ultrathin nanosheets in a mild solution (pH ~1.3). Interestingly, the exfoliation-reassembly process, as well as the properties of CN are largely reversible via alternating the interlayer groups. Moreover, the exfoliated and reassembled CN achieve a superior photocatalytic activity for *iso*-propanol (IPA) degradation (acetone: 345 μmol/h; CO_2: 23 μmol/h) and H_2 evolution (1370 μmol/h), resulting in a high apparent quantum yield (AQY) of 27% and 46%, respectively, at ~420 nm. This new proof-of-concept strategy will open up further opportunities for more effective delamination of extensive layered 2D materials towards advanced applications.

In chapter 4, a robust single cobalt co-catalyst Co-NC (with isolated Co-N_4 moieties on N-rich carbon sheets) was fabricated and anchored on photoharverster CdS. Subsequently, the interfacial adventitious carbon between CdS and Co-NC was targetedly removed by a facile annealing process, resulting in a cleared interface with small resistance. It's found that surface-trapped electrons can readily migrate to the firmly attached Co-NC across the cleared interface between CdS and Co-NC. The small-resistance interfacial carrier path and the robust single-cobalt sites work in a cooperative way and hence achieve a superior visible-light-driven H_2 generation activity with a rate of 4.34 mmol/h, an apparent quantum yield (AQY) of 63.9 % at 400 nm and a ultrahigh turnover frequency (TOF) of up to 16714.7 h^{-1}. This finding will motivate future work in creating clean interfaces and unique single active sites for high-performance photocatalysis.

In chapter 5, an overall summary of this dissertation work was presented. This thesis carried out a systematic study on the construction of efficient carbon-based materials for visible-light-driven photocatalytic reactions, including H_2 evolution, CO_2 reduction, and isopropanol (IPA) degradation. This thesis reveals that the structure engineering carbon-based materials and relevant interfaces are of significance to improve photocatalytic activity. Furthermore, the findings in this study also deepen the understanding of carbon-based photocatalytic systems, shed light on the mechanism of photocatalysis, and importantly, highlight some universal design strategies for efficient photochemistry processes.

Chapter 1 Introduction

1.1 Basics of photocatalysis

Clean and renewable energy has become a top priority for the sustainable development of human society because of the energy crisis and environment problem. Harvesting solar energy and its subsequent conversion via photocatalysis technology provide a promising solution for realizing environment remediation and counteracting energy storage. The core mission of photocatalysis research is to develop low-cost, highly efficient, stable photocatalytic systems for practical application. Towards this goal, photocatalysis has been explored extensively over the past decades and substantial progress has been achieved in various applications mainly including the following aspects: (1) photolysis of water to generate H_2 and/or O_2;[1] (2) mimicking natural photosynthetic processes to synthesize hydrocarbons;[2] (3) photooxidation of hazardous pollutants in air/water;[3, 4] (4) photosynthesis of green oxidant H_2O_2;[5] (5) photo-driven synthesis/transformation of organics;[6] (6) photoelectrochemical conversion,[7, 8] etc.

From the perspective of semiconductor photochemistry, photocatalytic materials mainly play a role in triggering and accelerating redox reactions under light irradiation. Generally, a typical process of photocatalytic reactions is mainly divided into several steps[2, 9] as shown in Figure 1.1: (1) the light with energy matching or exceeding the bandgap of photocatalysts triggers the electrons transition from the valence band (VB) to the conduction band (CB) and results in free charge carriers, i.e., an electron and a hole; (2) the photogenerated electrons and holes undergo several de-excitation pathways including recombination in the bulk or on the surface of semiconductors and migration to their surface for the desired redox reactions. The prerequisite for a photocatalytic reaction to occur is governed by the band levels of semiconductors and the redox potentials of reactions. In detail, the CB level of semiconductor is required to be negative than the reduction potential of reactions; the VB level of semiconductor needs to be positive than the corresponding oxidation potential of reactions.

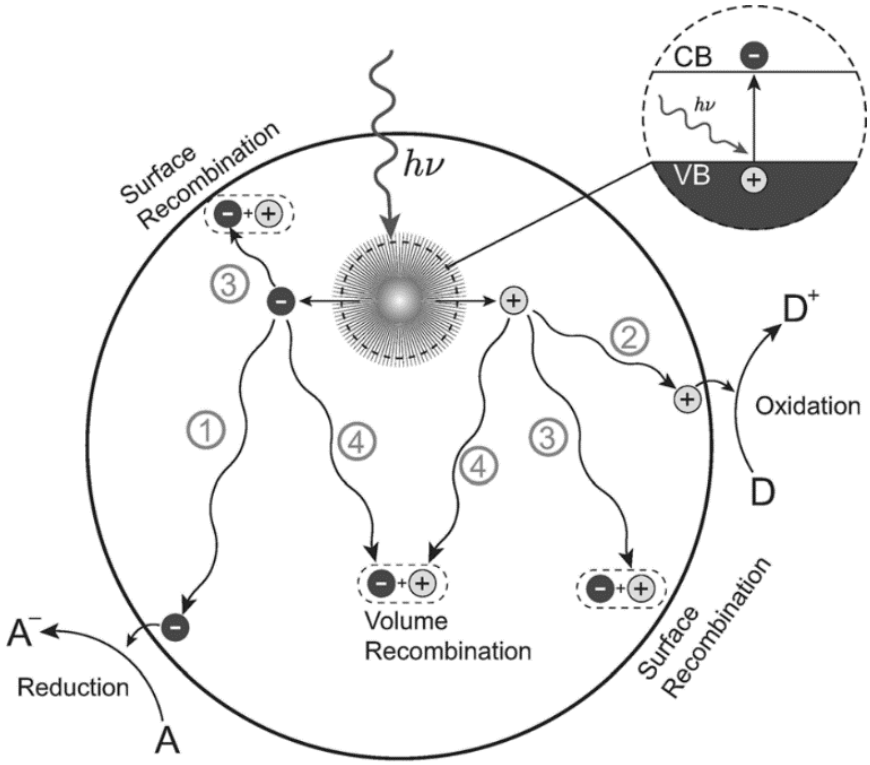


Figure 1.1 Schematic illustration of the basic mechanism of a semiconductor photocatalytic process. A = electron acceptor, D = electron donor. Pathways 1 and 2: donation of the carrier to the acceptor reactants on the surface, which results in the desired redox reactions. Pathway 3: carriers recombination occurs on the surface of a semiconductor. Pathway 4: carriers recombination occurs in the bulk of the semiconductor.[2]

1.2 Potential applications of photocatalysis

1.2.1 Photocatalytic water splitting

Photocatalytic water splitting has been widely regarded as an attractive approach to produce clean H_2. Such a promising reaction involves the reduction of H^+ by photoexcited electrons in CB and the oxidation of H_2O by holes in VB. The overall water splitting reaction is a thermodynamically uphill and unfavorable reaction (ΔG^o = 237 kJ/mol) involving multiple electron transfer processes. A suitable photocatalyst candidate for one-step excitation overall water splitting should meet several basic requirements as below: (1) the bandgap should be larger than 1.23 eV; (2) the bottom of CB should locate at a more negative potential than the redox potential of H^+/H_2 (0 V vs. NHE); (3) the VB maximum should be more positive than the redox potential of O_2/H_2O (1.23 V vs. NHE).

Although the ideal potential required for overall water splitting is as low as 1.23 V, the practical energy for driving the photocatalytic water splitting should be much larger because of thermodynamic and kinetic limitations.

1.2.1.1 Overall water splitting

Since the pioneering research on photoelectrochemical water splitting in a Pt/TiO_2 cell by Fujishima and Honda,[7] photocatalytic overall water splitting has been extensively studied. There are various materials, such as TiO_2, $SrTiO_3$,[10, 11] which can be used to split water into H_2 and O_2 under ultraviolet (UV) irradiation when modified with appropriate co-catalysts. However, those photocatalysts can only split water under UV light irradiation, which accounts for only 4% of solar energy and thus renders those single materials impractical. For this reason, tremendous efforts have been devoted to developing photocatalysts capable of splitting water using abundant visible light. Typically, Zou et al. developed the first visible-light-responsive photocatalyst nickel doped indium-tantalum-oxide ($In_{1-x}Ni_xTaO_4$ (x = 0-0.2)) for overall water splitting into stoichiometric amount of H_2 and O_2.[12] After that, Domen and co-workers reported a solid solution material $(Ga_{1-x}Zn_x)(N_{1-x}O_x)$ with an absorption edge at ~510 nm for efficient overall water splitting under visible light irradiation.[13]

1.2.1.2 Z-scheme overall water splitting

Construction of Z-scheme photocatalytic systems, mimicking the natural photosynthesis system, is an alternative and flexible pathway to achieve visible-light-driven pure water splitting. Z-scheme contains two kinds of semiconductors: one for H_2 generation and the other for O_2 evolution. Compared with the system composed of single semiconductor, it's more flexible and optional to select semiconductor photocatalysts for the Z-scheme systems, because the candidate photocatalysts in Z-scheme are only required to be active for half-reactions of water splitting. Up to now, Various semiconductors can be used for H_2 evolution in a Z-scheme system, such as TiO_2, Rh doped $SrTiO_3$, TaON, and g-C_3N_4.[1, 14, 15] The commonly used O_2-evolution semiconductor include WO_3, $BiVO_4$, etc.[14] Apart from the suitable semiconductors for H_2 and O_2 evolution, an electron mediator is usually required to mediate the electron transfer between two adjacent semiconductors in a Z-scheme system. The electron mediators could be in the form of soluble ions pairs (e.g., Fe^{3+}/Fe^{2+}, IO_3^-/I^-) or solid state (e.g., graphene oxide nanosheets, gold nanoparticles).[14, 16]

1.2.1.3 H_2 evolution with sacrificial reagents

Although the direct photocatalytic overall water splitting to generate H_2 and O_2 is highly promising for solar energy conversion, the photocatalytic efficiency of the water splitting systems explored so far is still low, far from meeting the industrial requirement. To screen out the excellent photocatalyst for the assembly of an efficient photocatalytic overall water splitting system, it is often necessary to investigate H_2 evolution and O_2 evolution half-reactions in the presence of sacrificial electron donors and acceptors, respectively.[17] The study of half-reactions in the presence of sacrificial agents also enables us to deepen the understandings of the photocatalytic mechanism.

Inspired by the oxidation process of organic sacrificial agents during the photocatalytic H_2 generation, researchers have designed some dual-functional photocatalytic systems, where the organic substrates not only serve as the electron donor to efficiently consume the hole but also can be converted into value-added compounds. For example, very recently, Uekert et al. reported a heterogeneous photocatalyst carbon nitride/nickel phosphide ($CN_x|Ni_2P$), which could transform plastic waste (e.g., abundant and freely available poly(ethylene terephthalate) and poly(lactic acid)) into clean hydrogen and corresponding valuable organic chemicals (e.g., acetate and formate) under visible light irradiation.[18] Such an oxidation half-reaction greatly improves overall process value and the sustainability of the system. Abundant biomass can also act as hole sacrificial agent to coproduce solar fuels and value-added chemicals as reported by Luo et al.[19] Those advanced examples highlight that suitable half oxidation reactions are significant for constructing a valuable photocatalytic H_2 evolution system.

1.2.2 Photocatalytic CO_2 reduction

The photochemical conversion of carbon dioxide into hydrocarbon fuels is regarded as one of the most promising strategies currently to simultaneously realize solar energy storage and reduce the greenhouse effect. Diverse products, such as HCOOH, CO, CH_4, can be generated via photocatalytic CO_2 reduction. The standard potentials of CO_2 reduction reactions are summarized as below (vs. normal hydrogen electrode (NHE), pH = 0):[20]

$$CO_2 + 2H^+ + 2e^- \rightarrow HCOOH\ (E^0 = -0.2V) \quad (1)$$

$$CO_2 + 2H^+ + 2e^- \rightarrow CO + H_2O\ (E^0 = -0.12V) \quad (2)$$

$$CO_2 + 4H^+ + 4e^- \rightarrow HCHO + H_2O\ (E^0 = 0.07\ V) \quad (3)$$

$CO_2 + 6H^+ + 6e^- \rightarrow CH_3OH + H_2O$ ($E^0 = 0.03$ V) (4)

$CO_2 + 8H^+ + 8e^- \rightarrow CH_4 + 2H_2O$ ($E^0 = 0.17$ V) (5)

Activation of the CO_2 molecule is the first step in the CO_2 reduction process. It is often claimed that activation and reduction of CO_2 are rather difficult because CO_2 is a very stable molecule or the first electron transfer to form the $CO_2^{\bullet-}$ radical intermediate requires a much negative redox potential (-1.9 V vs. NHE). Appropriate catalysts are quite important to lower the activation energy of CO_2 molecules by forming a chemical bond between CO_2 and catalyst, such that $CO_2^{\bullet-}$ radical or reaction intermediate can be formed at a less negative redox potential.[21] Although tremendous progress has been achieved in the photocatalytic CO_2 field, significant challenges regarding energy conversion efficiency, selectivity, stability, and cost of the photocatalytic system need to be tackled if photochemical carbon dioxide reduction is to become a viable option for storing solar energy.

1.2.3 Photocatalytic degradation of organics

The environmental contamination caused by organic pollutants in air/water/soil is an overwhelming problem all over the world. Photocatalytic degradation of organic pollutants is one of attractive routes to remove those pollutants. Photocatalytic degradation generally involves the degradation of pollutants by oxygenated free radicals and holes with strong oxidative properties.

The photocatalytic activation mechanism of organic compounds and O_2 molecules has been widely studied in the photodegradation of organic pollutants. Upon excitation by the photon with energy larger than the band-gap, the reductive conduction band electrons and oxidative valence band holes will undergo the following possible pathways to oxide the organic molecules.[3] The holes in VB can directly oxidize the organic molecules into their radicals or activate the adsorbed H_2O to generate •OH radicals. In the aerated systems, the energetic electrons in CB usually react with O_2 molecules and generate superoxide radical anions, such that both the O_2 molecules and organic substrates are activated. The subsequent radical reactions usually exhibit low- or non-barriers, leading to the facile oxidation of organic substrates.

1.2.4 Photocatalytic H_2O_2 generation

Hydrogen peroxide (H_2O_2), a mild and environment-friendly oxidant for organic synthesis and environmental remediation, has attracted increasing attention. It possesses the highest content of active oxygen and generates clean byproducts H_2O and O_2.[5] Photocatalytic synthesis of H_2O_2 is a green and sustainable process because it uses proton and oxygen as the source materials and solar light as the energy. There are two pathways for the generation of protons: either oxidizing organic compounds or oxidizing water by holes in VB. In the latter case, the sluggish kinetics of water oxidation reaction still severely restricts the efficiency of direct H_2O_2 synthesis from pure H_2O and O_2.

In general, there are two routes for the generation of H_2O_2: either a sequential two-step single-electron indirect reduction ($O_2 \rightarrow O_2^{\bullet-} \rightarrow H_2O_2$) or a one-step two-electron direct reduction ($O_2 \rightarrow H_2O_2$) route.[5] The generation of H_2O_2 via the sequential two-step single-electron indirect reduction pathway is shown as below: the O_2 is first reduced by one electron in CB to generate superoxide radicals ($O_2^{\bullet-}$), which further couple with H^+ to produce $HO_2^{\bullet-}$ radicals. Then, the $HO_2^{\bullet-}$ radicals can facilely be reduced by one-electron to produce HO_2^- anions. Finally, the HO_2^- would react with H^+ and generate H_2O_2. As for the H_2O_2 production via a one-step two-electron direct reduction of oxygen, the O_2 would be directly reduced by two-electron followed by the coupling with H^+ to form H_2O_2 product.

1.2.5 Other applications

Besides the aforementioned photocatalytic reactions, there are still many other photocatalysis applications, such as organic synthesis and N_2 fixation. Organic transformation triggered by light irradiation is an attractive approach towards the synthesis of many important compounds under mild conditions. Very recently, Ghosh et al. adopted mesoporous graphitic carbon nitride (mpg-CN) as a visible-light photoredox catalyst to orchestrate oxidative and reductive interfacial electron transfers to two different substrates for direct twofold C–H functionalization of arenes and heteroarenes.[22] Photocatalytic reduction of nitrogen to ammonia is highly attractive and holds great potential with regard to sustainable energy solutions compared with the industrial Haber–Bosch process operated under harsh conditions. Advanced photocatalysts can efficiently activate and cleave the highly stable N≡N triple bond (bond

energy: 940.95 kJ mol^{-1}), relying on light-excited electrons from semiconductors and designed active sites.[23]

1.3 Current status of research and development of efficient photocatalytic systems

1.3.1 Photocatalytic materials

Since the landmark event of photoelectrochemical water splitting in a Pt/TiO_2 cell by Fujishima and Honda in 1972,[7] extensive efforts have been devoted to the development of TiO_2-based photocatalysts. These studies mainly focus on unraveling the related mechanism, extending application scope, and boosting the photocatalytic efficiency in various reactions. However, because of its wide bandgap (3-3.2 eV), the pristine TiO_2 can only work under ultraviolet (UV) irradiation. The UV light only accounts for no more than 5% of the solar energy that reaches the earth's surface. It severely impedes the effective utilization of solar energy to drive the reactions when the pristine TiO_2 is adopted as the photocatalyst. Doping of TiO_2 with metallic and nonmetallic elements creates impurity states in the bandgap and thus extends its optical absorption to the visible region. However, doping states, especially those caused by metal dopants, usually accelerate charge recombination.[24] Meanwhile, various other inorganic semiconductors have been exploited (e.g., semiconductors comprising metal-based oxides, sulfides and nitrides, as well as their mixed solid solutions[25-30]) as inorganic solar energy transducers to generate energetic electrons and holes for targeted chemical reactions. The application of these photocatalysts is still hindered due to the moderate photocatalytic efficiency. Numerous strategies have been explored to modify their properties and enhance their performance, including band structuring engineering, nanostructure engineering, heterostructure construction[9] and reaction environment modulation.[31]

Sustainable utilization of solar energy requires the development of more abundant and stable catalysts working under visible light irradiation. Recent studies on novel photocatalysts have delivered some attractive substitutes, including metal organic frameworks (MOFs),[32] conjugated polymers (CPs),[33] and polymeric carbon nitride (CN)[34]. Among those novel materials, polymeric carbon nitride (Figure 1.2a, 1.2b, and 1.2c), mainly composed of carbon and nitrogen, has attracted extensive attention in recent years due to its low cost, ease of synthesis, and appropriate band structure. Additionally, polymeric CN exhibits typical layered structure, analogous to the widely studied graphene. Polymeric carbon nitride possesses a bandgap of ~2.7 eV (corresponding to an

absorption edge at ~460 nm, Figure 1.2d), with the conductive band (CB), and valence band (VB) positions locating at ca. -1.4 eV and ca. +1.3 eV vs. normal hydrogen electrode (NHE) (Figure 1.2e), respectively.[35] Notably, the CB level of CN is more negative than the redox potential of H^+/H_2 (0 V vs. NHE) and the VB level is more positive than the redox potential of O_2/H_2O (1.23 V vs. NHE) (Figure 1.2e and 1.2f). Such a band structure not only guarantees it to be visible-light-active materials but also endows it with the possibility for overall water splitting. The theoretical calculation revealed that the valence and conduction bands are mainly composed of the nitrogen p_z orbitals and carbon p_z orbitals, respectively (Figure 1.2g and 1.2h).[36] Such an calculation result suggests that the carbon atoms would be the reduction sites for H^+ to H_2, whereas the nitrogen atoms act as the preferred oxidation sites for H_2O to form O_2. Polymeric CN was first identified as a promising and metal-free photocatalyst for the generation of hydrogen under visible light in 2009.[36] Since then, extensive efforts have been made to improve the efficiency of CN-based photocatalytic systems. Owing to the layered feature and unique chemical composition, polymeric CN possesses high adjustability and thus provides huge potential to tailor its structure and properties towards diverse applications. At present, the application of CN-based materials has been extended to all kinds of solar to chemical energy conversion processes, including H_2/O_2 evolution from water splitting, CO_2 reduction, H_2O_2 production, N_2 fixation, and organic transformation. The detailed modulation strategies over polymeric CN will be presented in Section 1.4.1.

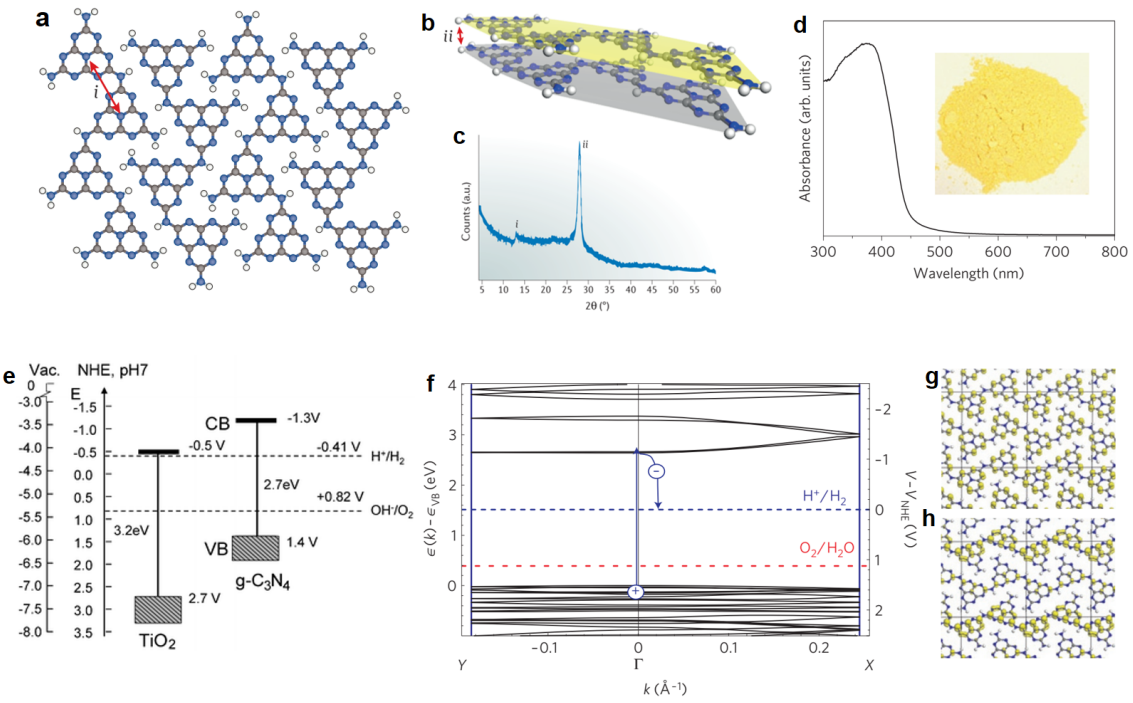


Figure 1.2 (a, b) The structural illustration of the polymeric carbon nitride (CN, melon), features characteristic in-plane repeats between heptazine (C_6N_7) units and a stacking motif of the very same heptazines on top of each other. Note: gray, blue, and white balls refer to C, N, and H atoms, respectively. (c) The powder X-ray diffraction pattern of polymeric CN.[14] (d) Ultraviolet–visible diffuse reflectance spectrum of the polymeric CN. Inset: photograph of the polymeric CN powder.[36] (e) Band structure of polymeric CN and TiO_2.[35] (f) Density-functional-theory band structure for polymeric melon. (g) The Kohn–Sham orbitals for the valence band of polymeric melon. (h) The corresponding conduction band.[36]

1.3.2 Co-catalysts

In addition to the excellent light-harvesters for massive generation of energetic carriers, robust active sites decorated on the surface of semiconductors are quite crucial for achieving efficient photocatalytic processes. However, most photocatalysts lack proper active sites catalyzing targeted reactions on their surfaces, leading to a poor/moderate performance.[37] Two reasons account for this point: (1) the fast recombination of excited carriers before migrating to the surface; (2) the targeted reactions occurred on the semiconductor surface are too slow to consume the charges efficiently.[17] Therefore, loading co-catalysts with targeted active sites on the semiconductors is a necessary and useful way to boost the efficiency of photocatalytic systems.

In a hybrid photocatalytic system composed of photocatalyst and co-catalyst, the photogenerated electrons in the conduction band (CB) and holes in the valence band (VB) of the semiconductor are transferred to the corresponding co-catalysts for a reduction and oxidation reaction, respectively. Generally, co-catalysts mainly play two pivotal roles during the photochemistry processes for various kinds of photocatalytic processes: (1) improving the catalytic kinetics by decreasing the activation energy or the overpotential of targeted reactions; (2) accelerating the photogenerated electron-hole separation and transfer inside the photoexcited semiconductors and across the semiconductor/co-catalyst junctions. Also, the suitable co-catalysts for water oxidation can efficiently suppress the photocorrosion of semiconductors during the water oxidation process.[38]

1.3.2.1 General guidelines for co-catalysts

In general, to develop the efficient co-catalyst for improved photocatalytic performance, several important requirements should be taken into consideration simultaneously: (1) specially designed active centers capable of activating and converting targeted reactants. The adsorption strength of pivotal intermediates should be moderate, neither too strong nor too weak, for an ideal catalyst with robust activity; (2) higher Fermi level than the flat band potential of semiconductors, which ensures the rapid electron flow from semiconductors to co-catalysts; (3) high electronic conductivity to guarantee the fast electron shuttling within the co-catalysts, realizing fast injection of electrons into the active sites for driving the reactions; (4) abundant surface functionalities to establish high-quality interface connection with light absorber, for fast interfacial charge transport; (5) robust structural stability, which could enable the long-term operation.

When searching the efficient co-catalysts towards different photocatalytic reactions, the most important point should be considered is the specifically designed active center able to convert the targeted molecules. The other points mentioned above, including the electronic conductivity, surface functionalities, Fermi level of co-catalysts, could accelerate the reaction rate by fast injection of photogenerated electrons into the co-catalysts. The rational design of active sites on co-catalysts strongly depends on the specific photocatalytic reactions. Brief introduction about co-catalysts for different reactions, including H_2 evolution, O_2 evolution, and CO_2 reduction, are separately discussed as below.

1.3.2.2 Co-catalysts for photocatalytic H_2 generation

For the photocatalytic H_2 generation, the traditional noble metals, such as the Pt, Pd, have been widely adopted as efficient co-catalysts. That is because those noble metals not only exhibit excellent intrinsic H_2 generation activity but also possess low Fermi level. The latter factor endows them with a better ability to capture the photogenerated electrons from semiconductors. However, their high-cost and extreme scarcity strongly restrain the potential commercialization of the current photocatalytic system. During the past decades, great achievement has been made in exploring noble-metal-free co-catalysts to replace precious metals for constructing a cost-effective photocatalytic system. The noble-metal-free co-catalysts mainly include transition metal (e.g., Cu, Ni, Co) and their oxides, hydroxides, sulfides, and carbides.[38] By optimizing their morphology, component,

exposed facet, surface defect, the co-catalytic H_2 evolution activity can be improved.[39] Among those noble-metal-free co-catalysts, MXene, a new family of two-dimensional metal carbides, nitrides or carbonitrides, have exhibited great potential as co-catalysts for photocatalytic H_2 generation. Typically, Ran et al. fabricated Ti_3C_2 nanoparticles and anchored them with robust photocatalyst cadmium sulfide (CdS).[40] In this hybrid, the Ti_3C_2 serves as the co-catalyst for H_2 generation, whereas CdS acts as the photocatalyst. The obtained composite Ti_3C_2/CdS delivered remarkable H_2 production under visible light irradiation. Such a high performance mainly originates from the favorable Fermi level position, electrical conductivity, and hydrogen evolution ability of co-catalyst Ti_3C_2.

However, several issues related to the intrinsic properties of current co-catalysts still exist for H_2 generation. First, those transition metal-based co-catalysts still require considerable usage of metal element and exhibit unsatisfactory atom utilization efficiency, because they usually exist as aggregation state.[38] To reduce the usage of metal in the co-catalysts and maximize their atom utilization, downsizing the co-catalysts to the atomic scale is one effective way. Second, the intrinsic activity towards H_2 generation is still needed to be improved. Hence, it is highly imperative to design and construct favorable active sites with merits of cost-effective and high utilization efficiency for realizing efficient solar energy conversion. Several pioneering approaches have been sought from the perspective of this sight. Typically, Fang et al. confined single Pt atoms into a metal–organic framework (MOF),[41] where photogenerated electrons transfer from the MOF photosensitizer to the isolated Pt sites for H_2 production under visible light irradiation. Notably, the system maximizes the utilization efficiency of Pt atoms with a turnover frequency of 35 h^{-1}, which is ~30 times that of Pt nanoparticles stabilized by the same MOF. Employing single transition metal co-catalysts to replace the single noble metal Pt can further reduce the cost of a photocatalytic system. Liu et al. loaded single Co site on phosphorus-doped CN and constructed Co-P_4 sites on P doped CN nanosheets.[42] The unique atomically dispersed Co-P_4 active sites greatly promote charge separation and transfer and thus boost the efficiency of overall water splitting. In these two aforementioned cases, the active sites are directly anchored on the photocatalysts; therefore the atomic coordination of single metal and its catalytic activity strongly depend on the surface structure/property of photocatalysts, and sometimes it could restrict the design of more favorable single site for efficient photochemistry process. In this regard, the implantation of single atom on suitable non-photocatalytic substrates provides a great

opportunity for creating more robust sites for co-catalytic H_2 evolution. Vert recently, Zhang et al. reported the synthesis of double transition metal MXene nanosheets ($Mo_2TiC_2T_x$) with Mo vacancies in the exposed outer layers.[43] The abundant Mo vacancies could be used to stabilize single Pt atoms, which significantly enhances the electrochemical H_2 evolution activity of $Mo_2TiC_2T_x$. The optimized catalyst exhibited an excellent catalytic H_2 evolution ability with low overpotentials of 30 and 77 mV at 10 and 100 mA cm^{-2}, respectively, which even exceeds that of advanced commercial Pt/C catalysts. Such an advanced catalyst in electrocatalysis field can inspire rational design and synthesis of single-atom cocatalytic sites on non-photocatalytic supports for efficient light-driven H_2 production.

Carbon-based materials, as promising alternative to those transition metal-based co-catalysts, are attractive for different photocatalytic reactions. A detailed discussion will be given in Section 1.4.2.

1.3.2.3 Co-catalysts for photocatalytic O_2 evolution

The O_2 evolution half-reaction in photocatalytic overall water splitting is a more difficult step compared with H_2 generation half-reaction, that is because it involves a four-electron transfer process coupled to the removal of four protons from H_2O molecules to form an oxygen molecule.[38] As a result, semiconductor photocatalysts usually suffer from the low activity for O_2 evolution due to the uphill multi-proton coupled electron transfer process and rapid charge recombination. In this context, co-catalysts towards efficient oxygen evolution are essential for boosting the efficiency of photocatalytic water splitting systems. So far, noble metal oxides, such as RuO_2 and IrO_2,[44, 45] are efficient water oxidation co-catalysts for improving the photocatalytic O_2 generation performance because of their excellent intrinsic water oxidation ability.

Nevertheless, cost-effective oxygen evolution co-catalysts are quite desirable to replace the noble metal-based ones. In recent years, many kinds of cost-effective co-catalysts, such as CoO_x, Co-Pi, MnO_x, for the photocatalytic O_2 production have been exploited.[38] Similar to the common co-catalysts for H_2 evolution, those oxygen evolution co-catalysts usually exist as aggregation state; thus only the surface region contacting the reactants could involve in the catalytic reactions, which significantly decrease the atom utilization efficiency and apparent performance. Atomization of these metal-based co-catalysts via rational coordination design is an effective strategy to maximize the atom

utilization efficiency and boost the performance. Recently, Fei et al. prepared a series of monodispersed atomic transition metals (Fe, Co, Ni) embedded nitrogen-doped graphene with a common and unambiguous MN_4C_4 (M refers to Fe, Co, Ni) moiety.[46] Both the density functional theoretical and electrochemical measurements confirmed that those anchored MN_4C_4 sites on carbon substrate could efficiently catalyze oxygen evolution with activities following the trend Ni > Co > Fe. Specifically, the Ni–NC catalyst showed an onset potential of 1.43 V (defined as the potential at 0.5 mA cm^{-2}) and its overpotential at 10 mA cm^{-2} is 331 mV, much smaller than those of Co–NC (402 mV) and Fe–NC (488 mV). This advanced example could motive rational design and synthesis of single atom co-catalysts for improving photocatalytic oxygen evolution performance.

1.3.2.4 Co-catalysts for photocatalytic CO_2 reduction

Loading suitable co-catalysts onto semiconductors is an effective strategy to boost the activity and selectivity of photocatalytic CO_2 reduction.[47] The key functions of co-catalysts towards CO_2 reduction are summarized as below: (1) boosting the selectivity towards targeted hydrocarbon products, meanwhile suppressing the undesired H_2 evolution; (2) reducing the overpotential of CO_2 photoreduction via favorable activation of CO_2 molecules; (3) promoting the separation and transfer of photogenerated carriers. Noble metals, such as Pt, Pd, and Au co-catalysts on suitable semiconductors, can selectively reduce CO_2 under light irradiation.[48-51] Typically, co-catalyst Pt nanocrystals on carbon-coated In_2O_3 can serve as the main active sites catalyzing the CO_2 conversion under visible light irradiation.[50] The drawbacks of those noble metal-based co-catalysts, such as the high cost and the moderate intrinsic activity, hinder their large-scale application. Some efficient earth-abundant metal-based co-catalysts have been developed and exhibit considerable activity and selectivity towards photoreduction of CO_2. For instance, Gao et al. synthesized well-defined Co_3O_4 hexagonal platelets with varied exposed crystal facets. When adopting $[Ru(bpy)_3]Cl_2$ as a photosensitizer, Co_3O_4 hexagonal platelets with specific exposed facets exhibited highly efficient visible-light-driven CO_2 conversion.[52]

However, the utilization efficiency of the atom in such co-catalysts is still low because of their aggregated status. The intensive homogeneous molecular co-catalysts could achieve considerable turnover frequency because active sites of them usually exist in the form of isolated atom coordinated with some anions. Advanced examples include noble metal-based molecular (e.g., Ru, Re complexes) co-catalysts and the ones based on cheap

transition metal, e.g., Fe, Co.[53-58] Those molecular co-catalysts can be used in both homogeneous and heterogeneous photocatalytic systems. For instance, Rao and co-workers reported a co-catalyst—iron tetraphenylporphyrin complex functionalized with trimethylammonio groups.[59] Such a co-catalyst can efficiently convert CO_2 into CO and CH_4 when operated in an acetonitrile solution containing a photosensitizer—$Ir(ppy)_3$ (ppy refers to phenylpyridine) and a sacrificial electron donor.

However, several key drawbacks, such as the inconvenient separation of metal complexes, the moderate apparent turnover frequency of metal sites, the complicated molecular complexes as well as the costly and time-consuming synthesis, significantly restrict their practical application. The rational design of more active molecular complexes and integrating them with suitable heterogeneous semiconductors could largely overcome the disadvantages of homogeneous complexes mentioned above. Kuriki et al. constructed a robust heterogeneous photocatalyst system comprising a co-catalyst (mononuclear ruthenium complex) and light-harvester (carbon nitride).[53] The optimized system can efficiently convert CO_2 into formic acid under visible light irradiation with a turnover number of greater than 1000 and an apparent quantum yield of 5.7% at 400 nm. The directly anchored single atom on heterogeneous semiconductors can also serve as an efficient co-catalyst for light-driven CO_2 reduction. For example, Di and co-workers incorporated isolated single cobalt into Bi_3O_4Br layers.[60] Those single cobalt atoms, serving as the active sites for CO_2 reduction to CO, not only promote the charge transition and carrier separation but also favor CO_2 adsorption and activation. Notably, isolated Co could lower the CO_2 activation energy barrier through stabilizing the COOH* intermediates and alter the rate-limiting step from the formation of adsorbed intermediate COOH* to CO* desorption. Benefitting from those merits, the single Co modified Bi_3O_4Br layers delivered an around four times improvement in CO evolution than that of bare Bi_3O_4Br layers. This study highlights the great potential of single atom-based co-catalysts for robust solar-powered CO_2 conversion.

1.3.3 Interfaces between photocatalysts and co-catalysts

Heterostructures, integrating with multi-component and various merits, represent the most promising and efficient photocatalytic system. Upon the formation of heterostructured photocatalytic systems comprising different components, such as photocatalysts/co-catalysts, the interfaces between those distinct components emerge. Generally, the heterostructured interfaces, where electrons shuttle and separate, are

extremely crucial for the separation and migration of photogenerated charge carriers between two components. The charge transfer efficiency at the junctions between different components determines the overall efficiency of photocatalytic system.[47] Although significant achievements have been made in optimizing the structure and property of photocatalysts and co-catalysts, fewer efforts have been put into creating high-quality interfaces for the smooth transfer of photogenerated carriers between adjacent components.

There are two kinds of methods for fabricating heterostructural photocatalytic systems: in situ approaches (e.g., photodeposition, hydrothermal or solvothermal treatment) and ex situ approaches (e.g., mechanical grinding, electrostatic self-assembly).[47] The in situ synthesis processes usually result in relatively tight interfacial contact between different components, which enables the considerable charge separation and transfer across the junctions; while the ex situ synthesis procedures often lead to weak interaction between different components, although the ex situ approaches could provide more opportunities to control the structure and property of each component. The weak coupling of composites fabricated by the ex situ synthesis methods should be strengthened to improve photocatalytic activity through the post-treatment.

The rational modulation of interfacial parameters aiming at creating unobstructed charge channels between photocatalysts and co-catalysts is one of the crucial pathways to construct an efficient photocatalytic system. In principle, the efficiency of charge transfer across the junctions is mainly determined by the interfacial coupling strength, which can be modulated from several aspects, including the interfacial composition, interfacial mediator, contact area of two adjacent components, interfacial facets, interfacial bonding strength, etc. The following discussion will focus on the engineering of interfaces between photocatalysts and co-catalysts towards boosting the efficiency of photocatalytic systems from those aspects mentioned above.

The composition of the interface, where the photocatalyst contacts with the adjacent co-catalyst, is a key parameter affecting the efficiency of charge transfer across the interfaces.[39] The similar composition of two adjacent components would favor their intimate contact and strong bonding for highly efficient charge transfer. Typically, transition metal sulfides (e.g., MoS_2,[61] WS_2[61] and CoS_2[62]) were often used as H_2 evolution co-catalysts for CdS-based photocatalysts because their analogous composition (S^{2-} anions) assist in forming a covalent junction at the interface to facilitate interfacial

charge transfer. Recently, the interfacial Co–$S_{5.8}$ transition layer at the junction between CdS to CoS_2 was unraveled and it was found that such a layer could introduce interfacial states and provide a charge-migration pathway for electrons transfer from CdS to CoS_2.[62] Thus, more photoinduced electrons and holes can participate in the surface photocatalytic reaction, which leads to a higher photocatalytic H_2 evolution activity than bare CdS and CoS_2. Similarly, at the junction of black phosphorous/Co_2P, new Co–P bond forms and acts as an atomic level charge transfer channel to mediate the electrons' delivery to the co-catalysts Co_2P.[63] In virtue of this novel charge channel and the robust feature of co-catalyst Co_2P, the photocatalytic H_2 generation rate of the Co_2P/BP nanosheets photocatalyst is 39.7 times greater than that of bare BP nanosheets.

When the compositions/properties of two adjacent components are incompatible, introducing an exterior additive or binder could assist in creating a relatively intimate junction with considerable carriers transferability. For example, the interfaces component between a Ta_3N_5 semiconductor and a CoO_x oxidation co-catalyst has been tailored by introducing a magnesia nanolayer on Ta_3N_5 toward improved water oxidation performance.[64] Intimate contact could hardly be realized between the hydrophobic Ta_3N_5 and hydrophilic CoO_x because of the distinct surface properties. To solve this issue, Chen et al. coated a hydrophilic magnesia nanolayer on the hydrophobic Ta_3N_5 to switch its surface properties and then anchored co-catalyst CoO_x, whereby the interfacial contact between the hydrophilic CoO_x co-catalyst and the modified Ta_3N_5 semiconductor was greatly improved. As a result, the photocatalytic oxygen evolution rate of the resultant CoO_x/MgO(in)–Ta_3N_5 composites is much higher than that of the pristine Ta_3N_5 sample under visible light irradiation.

Introducing interfacial mediators as conductive bridges between photocatalysts and co-catalysts is also an effective strategy to enhance the interfacial charge transfer.[47] Those mediators locating at interfaces could mainly play two roles for the whole photochemistry process: (1) reduce the interfacial defects density; (2) enhance the transport of electrons from semiconductors to co-catalysts through strengthening the interfacial communication between them. Previously, various interfacial mediators, such as metal ions,[65] molecular ligands,[66] metallic nanocrystals,[67, 68] and nanocarbons,[69, 70] have been successfully employed to enhance the photocatalytic activity of semiconductor/co-catalyst heterojunction. For instance, a small number of metal ions (Ca^{2+}, Cr^{3+}, Mn^{2+}, Fe^{2+}, Cu^{2+}, etc.) at the interfaces between CdS and graphene can efficiently mediate the carriers

transfer across the interfaces and thus lead to a significant improvement in photoredox reactions.[65] Cui et al. employed molecular ligands to bridge the photocatalysts gold nanoclusters (Au NCs) and the active metal ions (Fe^{2+}, Co^{2+}, Ni^{2+} and Cu^{2+}).[66] As such, the molecule chain can mediate the photoelectron transfer from Au NCs to co-catalytic metal ions for efficient CO_2 reduction.

Other strategies, such as enhancing the interfacial contact area and thus increasing interfacial bonds, have attracted significant attention in recent years. The interfacial contact area between the semiconductor and co-catalyst could be enlarged via their 2D−2D coupling. Taking the Janus bilayer photocatalyst as an example, Zhang et al. reported the fabrication of Janus (Cl_2)-($Bi_{12}O_{17}$)-(MoS_2) bilayer junctions with large contact area by assembling MoS_2 monolayers on ($Bi_{12}O_{17}$) end-faces of $Bi_{12}O_{17}Cl_2$ monolayers (Figure 1.3).[71] In this hybrid, electrons originating from photo-excited $Bi_{12}O_{17}C_{l2}$ were first driven by the internal electric field between (Cl_2) and ($Bi_{12}O_{17}$) end-faces to ($Bi_{12}O_{17}$) end-faces and further transferred via the Bi–S bonds formed across the interfaces between $Bi_{12}O_{17}Cl_2$ and MoS_2 monolayers to MoS_2 monolayers for H_2 evolution. In this case, particularly, the large contact area between 2D adjacent layers provides numerous carriers transport channels and thus are essential for the electron delivery to the co-catalyst, such that realizing a superior visible-light-driven H_2 evolution activity with a rate of 33 mmol h^{-1} g^{-1} and a quantum efficiency of 36% at 420 nm.

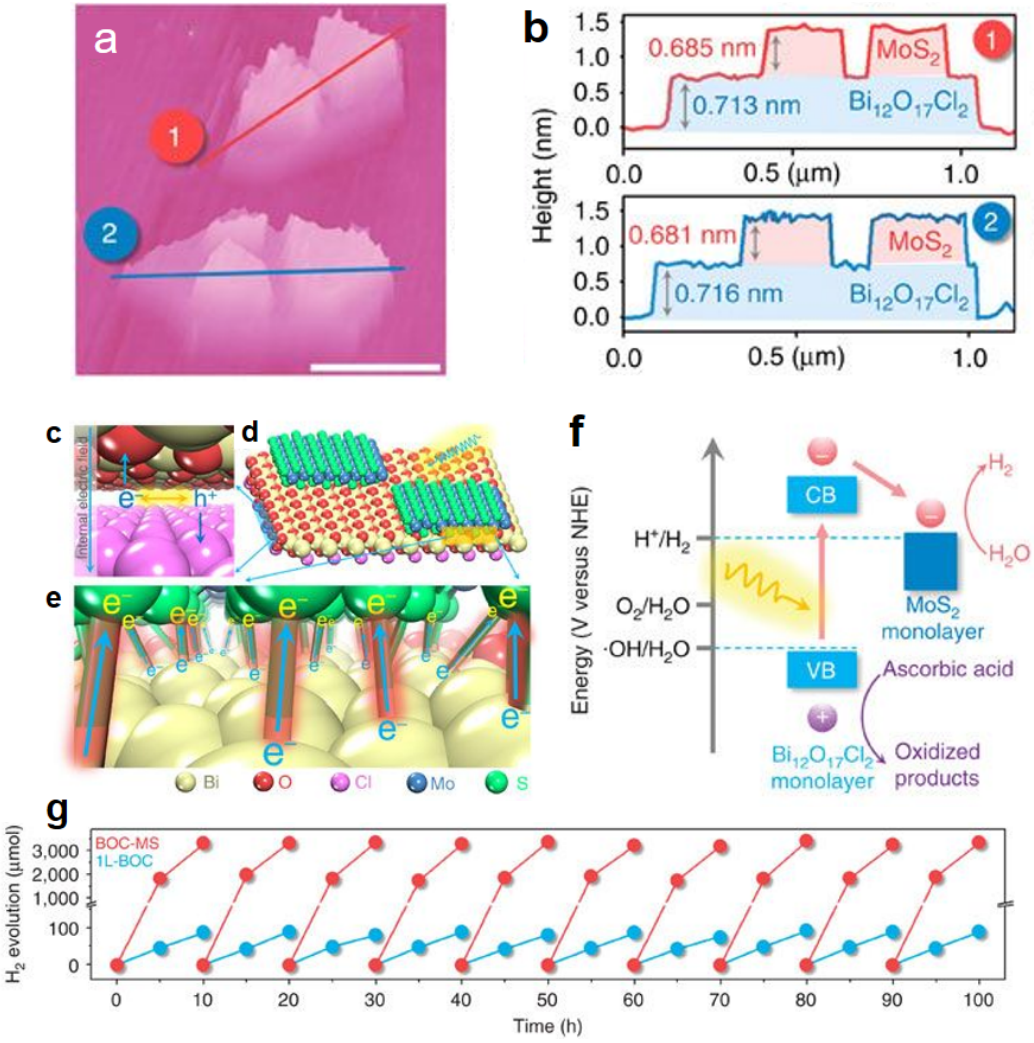


Figure 1.3 (a) AFM images of (Cl_2)-$(Bi_{12}O_{17})$-(MoS_2) (BOC-MS) bilayer junctions. Scale bar, 500 nm. (b) Height profiles along the lines in (a). (c, d, e) Schematic illustration of the crystal structure of BOC-MS (d) and the charge flow processes within BOC-MS, including the electron–hole separation within 1L-BOC (c) and the interfacial electron transfer from 1L-BOC to 1L-MS along the Bi–S bonds (e). (f) Band alignments in 1L-BOC and 1L-MS. (g) Cycling tests of photocatalytic hydrogen evolution over BOC-MS and 1L-BOC.[71]

As revealed by the excellent examples mentioned above, besides the structure/property of semiconductors and co-catalysts, the fabrication of a high-quality heterostructured interface is significant for the fast charge transfer across junctions and thus for achieving a remarkable photocatalytic activity.

1.4 Carbon-based photocatalytic systems

Although tremendous progress has been achieved in developing metal-based photocatalytic systems, those system exhibits moderate photocatalytic activity and requires considerable usage of metal. Carbon-based materials with distinctive advantages, such as metal free, low-cost, unique physicochemical property and high structural adjustability, are promising and attractive alternative to metal-based ones. Polymeric carbon nitride (CN) and carbon are typical carbon-based light absorber and co-catalysts, respectively. However, the unmodified carbon-based materials usually exhibit unsatisfactory performance. In this regard, various strategies towards the optimization of photocatalyst CN, carbon-based co-catalysts and relevant interfaces have been proposed to enhance the photocatalytic efficiency. The detailed discussions are presented as below.

1.4.1 Modulation of polymeric carbon nitride

Efficient solar-to-energy conversion over polymeric CN still encounters great challenges due to many drawbacks of pristine CN, such as the long carriers transportation distance, abundant defects in layers, low electronic conductivity, rapid recombination of charge carriers and limited light absorption range. To improve the photocatalytic efficiency of CN, researchers have explored a number of strategies to overcome its drawbacks aforementioned.[34] In this section, we will discuss various modulation strategies over CN for improving its photocatalytic activity, including nanostructure design, atomic structure modulation and heterostructure design.

1.4.1.1 Nanostructure engineering

The rational design of CN nanoarchitectures is a useful strategy to make the best use of the material and structure functions. Nanostructure design can assist in overcoming the intrinsic drawbacks of CN, in particular, the fast charge recombination and poor mass diffusion.

1) Two-dimensional nanosheets

Polymeric carbon nitride is a graphite-like layered material, where weak van der Waals force exists between layers. Bulk CN with many disadvantages, such as long carriers transport distance, rich defects inside the bulk, usually exhibits poor photocatalytic performance. The delamination of bulk CN into two dimensional (2D) nanosheets could induce unique physicochemical properties, including increased surface area/active sites,

short bulk diffusion length for reducing the recombination probability of carriers and enlarged bandgap (increased reduction ability and/or oxidation ability) due to the quantum confinement effect. Previous exfoliation strategies for fabricating ultrathin CN nanosheets are generally classified into two categories: 1) the universal methods available for various layered materials such as the liquid exfoliation in solvents;[72] 2) the exfoliation approaches intentionally established based on its unique chemical composition and structure.[73, 74] Liquid exfoliation of CN was first reported by Yang and co-workers (Figure 1.4a).[72] This simple liquid exfoliation method involved bulk CN powder as the starting material and various organic solvents as the dispersion mediums. Remarkably, the exfoliated CN nanosheets in isopropanol (IPA) delivered a thin morphology with a thickness of ~2 nm. Another widely adopted exfoliation method for CN is thermal oxidation etching (Figure 1.4b).[75] The hydrogen-bond cohered strands of polymeric melon units in the layers, which are not stable enough against the oxidation process in air, will be gradually oxidized away from the bulk material so that the thickness of bulk CN will decrease to the desired nanoscale. The obtained nanosheets in those two cases feature large surface area, abundant active sites, and improved electron transportability along the in-plane direction. These characteristics endow the nanosheets with a much higher photocatalytic performance for H_2 evolution than that of bulk CN under visible light irradiation.

In addition to those two exfoliation methods for CN, several other strategies, such as solid template-directed method,[76] gas template-assisted exfoliation (Figure 1.4c),[77] chemical exfoliation (Figure 1.4d),[78] are also developed to fabricate CN nanosheets. By using the solid silica as a template, Wang and co-workers built CN nanospheres assembled from 2D CN nanosheets with sharp exposed edges.[76] In this case, besides the 2D feature, the sharp edges tips of assembled nanosheets can induce a similar promotion like ‘lightning rod effect’ to achieve fast charge collection and separation at the tips. As such, the assembled nanosheets with exposed sharp edge tips exhibited higher activity than that of free-standing nanosheets under the same conditions.

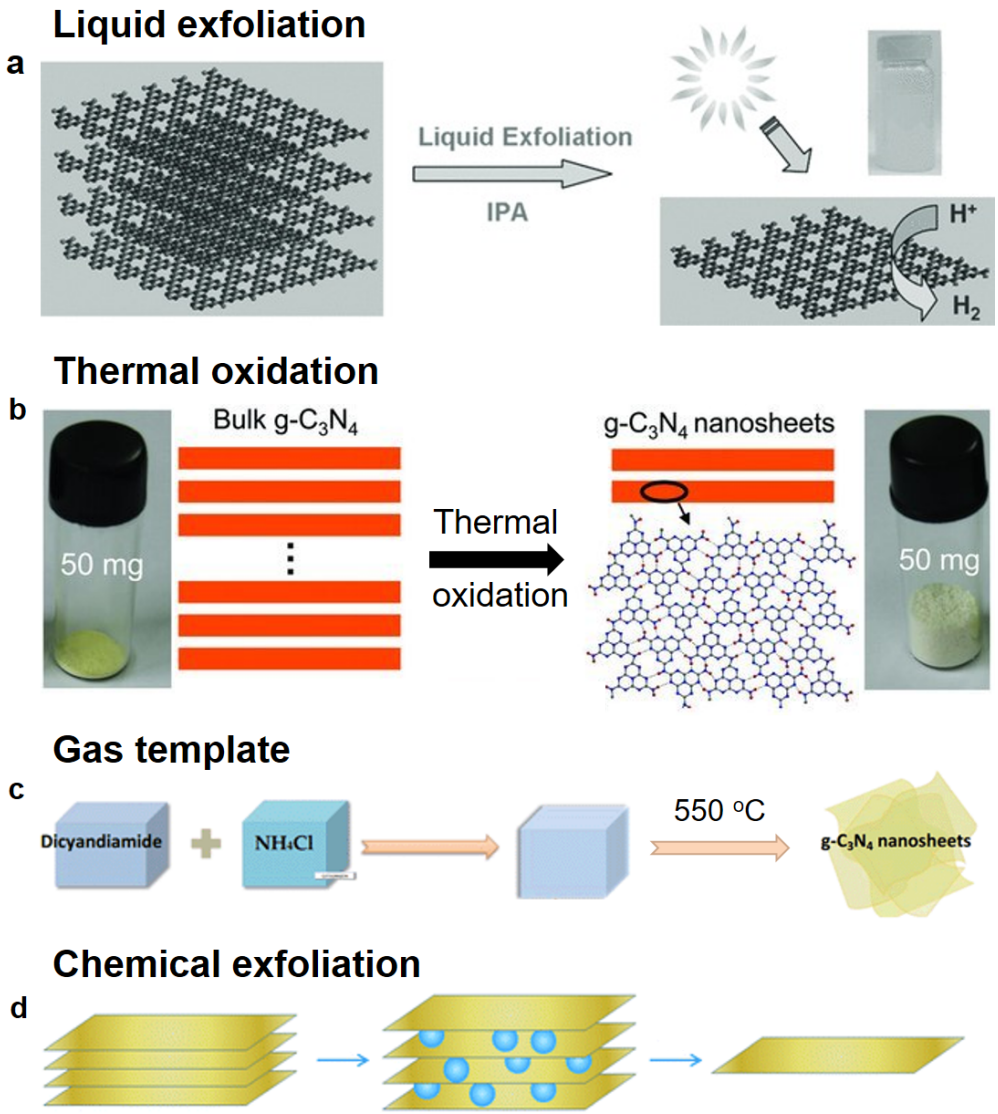


Figure 1.4 Schematic illustration of the synthesis process of CN nanosheets by various methods. (a) Liquid-exfoliation method from bulk CN powders.[72] (b) Thermal oxidation method from bulk CN powders.[75] (c) Gas template method from precursor dicyandiamide.[77] (d) Chemical exfoliation method from bulk CN powders, the blue sphere refers to intercalated H_2SO_4 in the space of adjacent layers.[78]

It worth noting that the delamination of CN into 2D nanosheets will inevitably decrease their light absorption due to the broadened bandgap, although it can shorten the carrier migration distance and promote the mass transfer. The decreased light absorption reversely restricts the photocatalytic performance. To overcome this drawback, Rahman et al. annealed the precursor melem at 620 °C and obtained ultrathin CN nanosheets with narrow band gap.[79] The ultrathin feature and the narrow bandgap ensure favorable

carrier kinetics and increased light absorption, respectively, both of which contribute to the outstanding photocatalytic H_2 evolution activity.

Although previous exfoliation strategies for CN have achieved substantial progress, several drawbacks still exist, such as high energy consumption, moderate exfoliation yield, moderate photocatalytic performance, and uncontrollability of thickness. It's still desirable to exploit green, robust and controllable exfoliation method for large-scale production of CN nanosheets with efficient photocatalytic performance.

2) Porous structure

Porous materials are highly promising and attractive as catalysts due to their accessible porous nature with large surface area and fully exposed active sites. For CN, the formation of a porous structure, has been proved as an effective route to enhance the photocatalytic performance mainly via promoting light absorption, charge carriers transfer and separation, active site exposure, and mass diffusion during the photocatalytic process. At present, porous CN with a large surface area is often fabricated using a soft/hard template or self-sacrificial template as the scaffold. Typically, Wang and co-workers fabricated mesoporous CN from precursor cyanamide using silica nanoparticles as the solid template.[80] It was found that the introduction of mesoporosity into polymeric CN can realize a ~10 times enhancement in photocatalytic H_2 generation. A seaweed-like mesoporous CN via direct calcination of the pre-modified dicyandiamide was reported by Han et al.[81] Such a unique architecture favors light-harvesting, charge separation, utilization of active sites and thus achieves efficient photocatalytic behavior for water splitting.

Implanting abundant pores on ultrathin CN nanosheets can further improve carriers kinetics and accelerate mass transfer of CN nanosheets, resulting in excellent photocatalytic activity. Han et al. prepared mesoporous nanomesh of polymeric CN.[82] With the unique structural advantages for electron transfer, light-harvesting, aligned energy levels, and available reaction sites, the atomically thin mesoporous CN nanomesh exhibited a superior photocatalytic H_2 evolution activity with a rate of 8510 μmol h^{-1} g^{-1} under visible light irradiation.

3) Other nanostructures

In addition to 2D and porous geometric morphology, the design and exploration of other distinct morphologies, such as hollow structures and helical structure, are also attractive and promising for boosting the photocatalytic activity of CN. Typically, Guo and co-workers prepared phosphorus-doped hexagonal tubular carbon nitride with the layered stacking structure.[83] The tubular structure favors light scattering and increases the active sites, which can enhance the photocatalytic H_2 evolution activity. Another typical example is helical CN nanorods fabricated using chiral mesoporous SiO_2 templates.[84] The helical architecture could favor charge separation and mass transfer of CN, which enables it to be more efficient for H_2 evolution and CO_2 reduction than the unmodified CN. The hollow structure can be used to separate the reduction sites and oxidation sites for overall water splitting. Zheng et al. fabricated Pt and Co_3O_4 nanoparticles onto the interior and exterior surface of hollow carbon nitride spheres, respectively.[85] Such a spatial separation of reduction and oxidation sites significantly prevents the undesired reverse reaction of water splitting, decreases charge recombination, and finally enhances the overall water splitting performance.

1.4.1.2 Atomic structure modulation

1) Doping

Doping is an effective strategy to modulate the electronic structures of semiconductors as well as their bulk/surface properties. Various kinds of heteroatom dopants, including non-metallic elements and metallic elements, can be separately or simultaneously incorporated into/onto the framework of polymeric CN for targeted solar energy conversion reactions.[34] Many anions, such as B, C, O, P, S and I, have been successfully incorporated into CN. For instance, Ran et al. fabricated porous P-doped CN nanosheets via combining P doping and thermal exfoliation strategies.[86] The optimized P-doped CN nanosheets delivered a high visible-light photocatalytic H_2 evolution rate (1596 μmol h^{-1} g^{-1}) and apparent quantum efficiency (3.56%) at 420 nm. This outstanding performance was attributed to the P-doped conjugated system and the porous nanosheets morphology, which extended the light absorption range and boosted the mass-transfer process, respectively. In particular, the improved visible-light absorption could be ascribed to the mid-gap states (-0.16 V vs. standard hydrogen electrode) induced by P doping. Ou et al. incorporated Se element and C≡N motifs into the matrix of CN simultaneously, which

results in the electron donor domain and electron acceptor domain in the layer of CN and lead to a p-n type homojunction.[87] This p-n homojunction can accelerate the separation and transfer of charge carriers inside the bulk CN and enhance the photocatalytic activity.

Besides non-metallic elements, metal ions, such as Fe, Pt, Pd, can also be easily used to modify the properties of pristine CN for targeted reactions.[88-90] Those doped metal usually exists in a single-atom state, which not only modulates the electronic structure of CN but also serves as the active sites for specific reactions. For example, the incorporation of Pt ions into the framework of CN via one-pot polymerization can dramatically broaden its light absorption via metal-to-ligand charge transfer (MLCT) mechanism, enabling vis–NIR photocatalytic H_2 production.[89] The MLCT can locally work in the N conjugated aromatic units, which is different from the conventional HOMO-LUMO transition and avoids long-distance charge transport. Furthermore, the incorporated Pt ion can also assist in reducing the protons into H_2 when it captures the electrons. As a result, the Pt modified CN exhibited further enhanced photocatalytic performance under broad-spectrum irradiation. Such a function mechanism had also been proven valid to the transition metal Cu^+ coordinated CN.

In some cases, the incorporated metal sites mainly serve as active sites towards targeted reactions. For example, Li and co-workers anchored a new form of co-catalyst isolated Pt atoms on CN nanosheets at a relatively low temperature (Figure 1.5).[91] Such a system realizes maximized atom efficiency of the noble metal and highly efficient photocatalytic H_2 evolution. Besides the excellent H_2 evolution activity of isolated Pt, the anchored single Pt can induce a surface trap state below the CB and prolong the lifetime of photogenerated electrons for efficient performance. The low-cost transition metal can also be embedded in the framework of CN as co-catalysts for H_2 evolution under visible light irradiation. Typically, Cao et al. induced cobalt salts on the surface of CN and identified that atomically dispersed Co atoms are successfully grafted by covalently forming a Co_1-N_4 moiety on CN nanosheets.[92] Theoretical calculation revealed that the coordinated N sites could increase the electron density and lower the formation barrier of key Co hydride intermediate, thereby promoting H–H coupling to enhance H_2 generation.

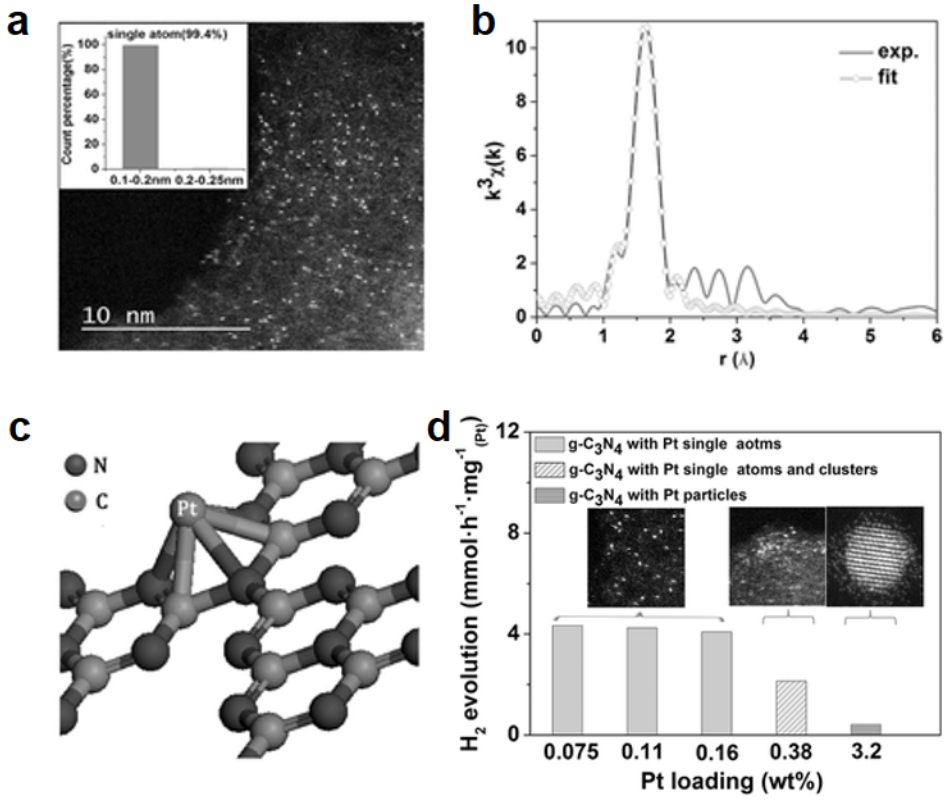


Figure 1.5 (a) HAADF-STEM image of Pt-CN. Inset is the size distribution of the bright spots. (b) Comparison of Fourier transformed Extended X-ray absorption fine structure (FT-EXAFS) curves between the experimental data and the fit of the Pt-CN. (c) Schematic models of Pt-CN. (d) Photocatalytic activity comparison of CN with various Pt contents normalized to per Pt atom.[91]

In addition to element doping aforementioned, small-sized carbon-based motifs can also be doped into the framework of CN to tailor the physicochemical property and facilitate the charge carrier kinetics. Che et al. incorporated graphitic carbon ring (C_{ring}) into the layers of CN and created a novel in-plane heterostructural C_{ring}-CN (Figure 1.6).[93] Such a molecular level plane heterostructure can separate the photoexcited electron−hole pair efficiently and facilitate the transportation photocarrier for direct photocatalytic water splitting. The diffusion length and lifetime of photocarrier are significantly increased by a factor of 10 compared with those of pristine CN, and thus the C_{ring}−CN can effectively split pure water under light irradiation with outstanding H_2 production rate up to 371 μmol g^{-1} h^{-1}. By modifying the fabrication procedures, similar graphited carbon rings can be doped into the superficial layers of CN with gradient content; such a structure feature endows this modified CN with suitable energy band layouts and built-in electric fields.[94] It drastically accelerated carrier separation by

impelling photogenerated electrons and holes into diverse directions and hence elevated the photocatalytic hydrogen evolution rate by a factor of 21. Similarly, carbon quantum dots, with relatively larger size compared to atomic carbon ring, were also implanted in the 2D plane of CN seamlessly to facilitate the photoelectron transport.

Those incorporated small-sized carbon-based species mainly improve the kinetics of photogenerated carriers and slightly affect the light absorption of CN. Extending the light absorption of CN to cover the whole range of solar light is important for boosting the photocatalytic performance. Zhang and co-workers demonstrated that the optical absorption of CN semiconductor is extendable into the visible region up to ~750 nm by simple copolymerization with organic monomers like barbituric acid.[95] Those studies demonstrate the great promotion effect of embedded carbon-based species on photocatalytic performance of CN.

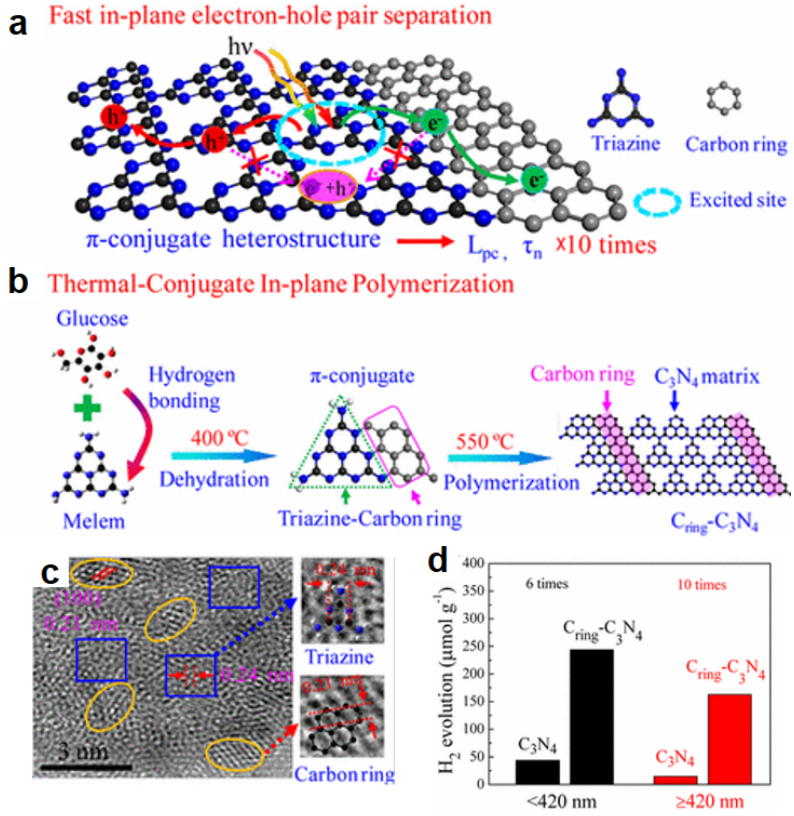


Figure 1.6 (a) Schematic for photocarrier transfer in (Cring)–CN, where L_{pc} and τ_n represent the photocarrier diffusion length and lifetime, respectively. (b) Synthetic route for the in-plane heterostructure of (Cring)–CN. (c) High-resolution TEM image for the sample. (d) H_2 evolution under UV (< 420 nm) and visible light (≥ 420 nm) per hour.[93]

2) Vacancies

In contrast to the doping of exterior elements or molecules into the plane of CN, selectively removal of inherent motifs has also been proved to be an effective strategy to modulate the properties of CN by introducing additional energy levels and/or acting as reactive sites. At present, both carbon and nitrogen vacancies can be created in CN, which dramatically affects its band structure, light absorption, charge carriers kinetics, and finally, enhances targeted photocatalytic reactions. Typically, Niu et al. induced rich nitrogen vacancies inside bulk CN via a thermal reduction process with H_2, which greatly narrows the bandgap of sample from original 2.78 to 2.03 eV and accordingly extends the light absorption range to 556 nm.[96] The resultant samples exhibited extremely low radiative recombination of photo-excited charge carriers and showed dramatically enhanced photocatalytic activity. In some cases, those vacancies can be used to targetedly activate the reactant molecules and lower the activation energy of photocatalytic reactions. Recently, Yang et al. implanted carbon vacancies in a melon polymeric matrix.[97] It was found that those vacancies can function as the sites for CO_2 activation while stabilizing COOH* intermediates, thereby boosting the reaction kinetics and thus significantly improving the CO generation.

Therefore, incorporation of exterior motifs or creation of interior vacancies can be a multifunctional strategy to boost the photocatalytic performance of CN via extending light absorption, promoting carriers separation and transfer or providing favorable active sites.

1.4.1.3 Heterostructure construction

Construction of heterostructures, integrating with multi-component and various merits, has been widely applied to the design of efficient photocatalytic system with accelerated electron–hole separation and transfer, extended light absorption, improved stability.[98] Such a strategy has also been well explored to construct efficient polymeric CN-based heterojunctions.

Polymeric CN can form many heterostructures with various kinds of materials, such as inorganic semiconductors, organic semiconductors, and carbon.[34] Usually, CN-based heterojunctions can provide a series of improvements in following aspects: (1) accelerate charge migration and separation by hybridizing with suitable semiconductors or co-catalysts; (2) reduce the activation energy by loading favorable co-catalysts; (3) enhance

light absorption by coupling with suitable narrow bandgap semiconductors. Zhang and co-workers reported the isotype heterojunction, i.e., CN and sulfur-mediated CN, with greatly improved carriers kinetics.[99] The band alignment between the two adjacent materials results in the formation of type II heterojunction. The CB offset between CN and CNS can drive the migration of photogenerated electrons from CN to CNS, while the photoinduced holes are transferred from CNS to CN by the VB offset. Such a band alignment greatly reduces the carriers recombination and thus improving the photocatalytic activity.

In many cases, to efficiently consume the photogenerated carriers of CN and accelerate their separation, the other component with desired active sites is often loaded onto CN for constructing efficient photocatalytic systems. For example, MoS_2/WS_2, typical layered materials with favorable H_2 evolution ability, were directly grown on mesoporous CN for efficient photocatalytic H_2 production.[100] This nanolayered hybrid possesses several advantages: (1) large contact area facilitate the fast electron transfer across the interface; (2) matched band structure enables the directional electrons transport from CN to MoS_2; (3) the anchored MoS_2 can the efficiently reduce the protons upon collecting the energetic electrons from CN. Those features of this junction promote photocatalytic H_2 evolution activity under visible light irradiation, which was comparable to that of CN loaded with Pt under the same conditions.

1.4.1.4 Reaction environment modulation

The reaction environment also has great influences on the photochemical processes, as demonstrated by many studies. Surface alkalization has been proved to be a useful strategy to modify the surface properties and thus improve the photocatalytic performance of oxide semiconductors, such as $SrTiO_3$,[101, 102] TiO_2[103] and WO_3[104]. Reaction environment modulation with other inorganic salts has been reported by Liu et al. for promoting the photochemical process of CN. They explored an environmental "phosphorylation" strategy that could mimic phosphate-involving natural photosynthesis to improve the photocatalytic H_2 production of g-C_3N_4 nanosheets.[31] Notably, the optimized addition of a phosphate (K_2HPO_4) to the reaction system boosted the H_2 generation rate to 947 $\mu mol\ h^{-1}$ under visible light, and an extremely high apparent quantum yield of 26.1 % was observed at a wavelength of 420 ± 14.5 nm. Those studies highlight the significant effect of reaction environment on promoting the photocatalytic process.

Although tremendous progress has been achieved in developing CN-based photocatalyst, the activity of CN remains moderate. Therefore, further exploration is highly desirable to advance this field and to gain a deep insight into the mechanism of photocatalysis.

1.4.2 Modulation of carbon-based co-catalysts

Ideally, the co-catalysts should be low cost, abundant, and efficient. In this regard, carbon-based materials provide a great opportunity for constructing cost-effective co-catalysts. Metal-free carbon-based materials, a promising alternative to those transition metal-based materials mentioned in Section 1.3, feature high electrical conductivity, large surface area, excellent stability, and diverse morphologies. Particularly, it's feasible to optimize the property/activity of the carbon materials due to their editable structure.

1.4.2.1 Carbon-based co-catalysts for photocatalytic H_2 evolution

Up to now, extensive studies have shown that carbon nanomaterials could be used as cost-effective co-catalysts for photocatalytic H_2 production.[38] Generally, the carbon-based co-catalysts used in photocatalysis can be roughly divided into several types, including graphene,[105] (reduced) graphene oxide,[106, 107] doped carbon,[108] graphdiyne,[109] their derivatives,[110] etc. (structure illustration of graphene and graphdiyne is presented in Figure 1.7a and 1.7b) For instance, Han et al. coupled nitrogen-rich carbon with mesoporous polymeric CN nanofibers via one-pot polymerization of modified dicyandiamide and pyrrole, where the N-rich carbon (NC) could serve as co-catalysts for H_2 generation.[111] The favorable structure and composition of the nanofibers as well as strong coupling between the adjacent components endow them with improved light-harvesting properties, promoted charge carriers separation and a smooth electron transport path across the entire architectures. Those favorable factors cooperatively enhance photocatalytic H_2 production performance. Similarly, nitrogen rich carbon derived from ZIF-8 (zeolitic imidazolate framework) can also acts as efficient co-catalyst over polymeric carbon nitride (CN) for H_2 generation.[108] Those studies not only highlight the excellent catalytic performance of N-rich carbon as co-catalyst for H_2 evolution, but also demonstrate the great contribution of tight interfaces between semiconductors and co-catalysts to the whole performance of photocatalytic system.

It worth stressing that the CN/NC photocatalytic system mentioned above were prepared via one-pot polymerization, that is, the precursors of photocatalyst CN and co-

catalysts NC were mixed first and then were annealed at high temperature. Such a method could ensure the tight interfacial contact of CN (photocatalyst)/NC (co-catalyst), while the organic molecules or inorganic ions in the precursors of NC are easy to be doped into the CN matrix and usually brings significant improvement in performance (as mentioned in Section 1.4.1), thus the researchers should pay attention to the considerable contribution of doping effect to the final activity.

Although those carbon serving as co-catalyst over CN can exhibit good H_2 evolution regardless of possible doping contribution. Rational functionalization and synthesis of those carbon-based co-catalysts provide a great opportunity for further enhancing their intrinsic activity towards H_2 production. Recently, single-atom catalysts, with isolated metal sites supported on solid substrates, are emerging as a highly attractive class of catalysts because they integrate the merits of homogeneous and heterogeneous catalysis, such as high activity, selectivity, stability, easy separation from reactants/products and maximization of atom utilization efficiency. Notably, the atomization of metal sites on substrates usually possesses unsaturated coordination environment and large surface free energy compared with the subnano, nano, bulk ones. As such, those isolated sites is much active for chemical reactants (Figure 1.7c).[112]

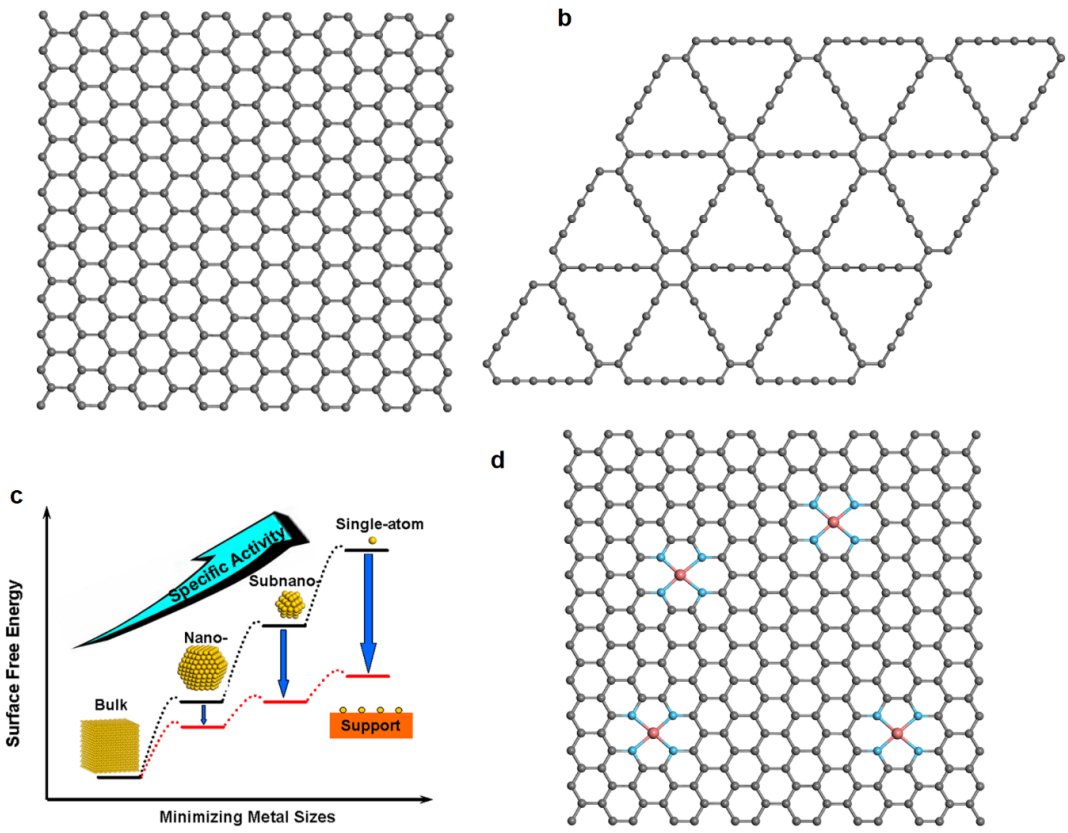


Figure 1.7 Schematic molecular configurations of (a) graphene, (b) graphdiyne, (d) single atom incorporated graphene. Grey, blue, and red balls refer to carbon, nitrogen, and metal atom, respectively. (c) Schematic illustration of the changes of surface free energy and specific activity per metal atom with metal particle size and the support effects on stabilizing single atoms.[112]

Among various single-atom catalysts, single-atom incorporated N-rich carbon (M-NC, M typically refers to cost-effective transition metals, such as Fe, Co, Ni; the typical structure illustration is presented in Figure 1.7d) is particularly of interest. It has attracted extensive attention in various fields, especially in electrocatalysis field, due to its low cost, editable metal center and coordination, unique electronic properties and unexpected performance. Compared with the NC without metal, the M-NC usually exhibits higher activity in the electrocatalysis field. For example, atomic cobalt decorated N-rich graphene (Co-NG) exhibited an excellent electrochemical H_2 evolution activity with an overpotential of 147 mV at 10 mA cm^{-2} in 0.5 H_2SO_4 aqueous solution, while the bare NG show poor performance (with an overpotential more than 400 mV under the same conditions) (Figure 1.8).[113] Similarly, Fan et al. reported a single Ni grafted N-rich carbon (NC) electrocatalyst, which even exhibited higher H_2 evolution activity compared with Co-NG mentioned above.[114] However, in those two cases, although the metal sites are isolated from each other, the exact atomic structure is not revealed. Determination of atomistic structure and its catalytic properties is crucial for the rational design and synthesis of single atom doped NC catalysts with high catalytic activities. Chen et al. incorporated single Mo atom on NC support and revealed the atomic structure of Mo center, i.e., $Mo_1N_1C_2$ (coordinated with one nitrogen atom and two carbon atoms).[115] Such a single-Mo catalyst possesses excellent electrochemical H_2 evolution activity as well as good stability. After that, they fabricated single-W-atom embedded N-rich carbon and revealed that the $W_1N_1C_3$ may be the favored local structure and accounting for the superior electrochemical H_2 evolution activity (almost equal to that of commercial Pt/C).[116] Such a superior electrochemical H_2 evolution activity related to the isolated metal sites highlights the great potential of M-NC employed as co-catalysts towards photocatalytic H_2 generation. However, such kind of material have rarely been used as co-catalysts in the photocatalytic system, especially for achieving outstanding performance in photocatalysis. It's highly desirable to develop robust single atom

incorporated NC with well-defined atomic coordination as efficient co-catalysts for the cost-effective photocatalytic system.

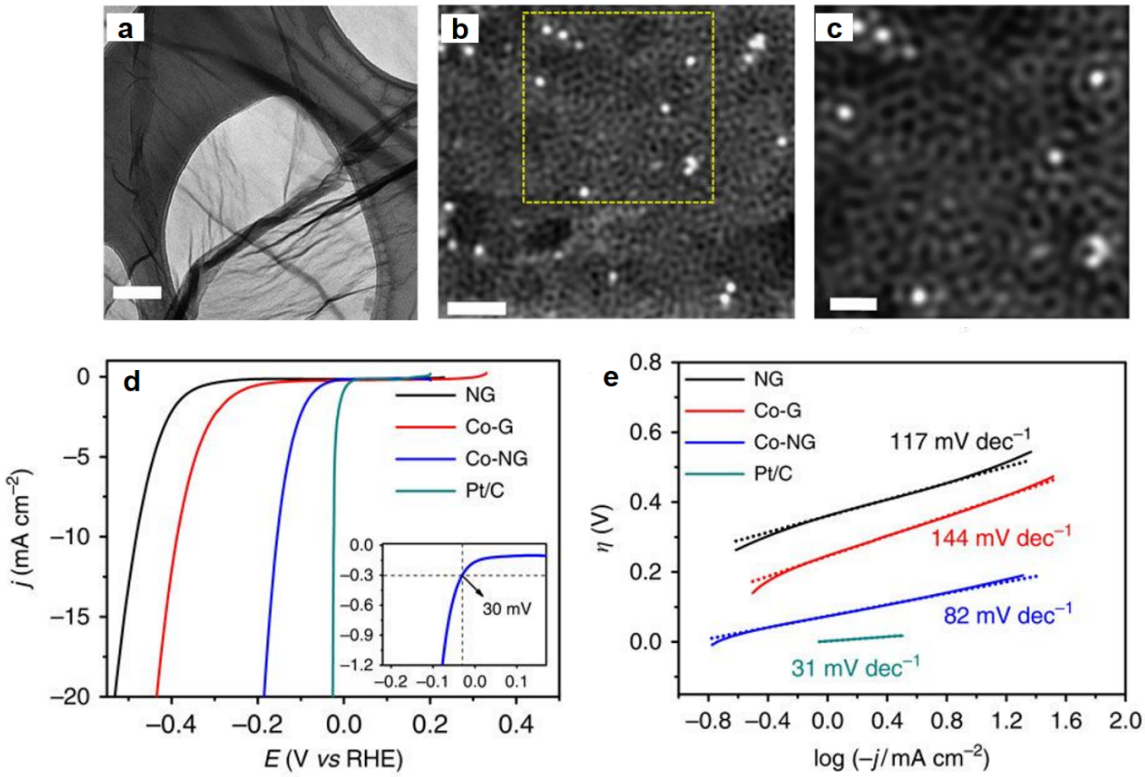


Figure 1.8 (a) TEM image of the Co-NG nanosheets atop a lacey carbon TEM grid. Scale bar, 50 nm. (b) High-angle annular dark-field scanning transmission electron microscopy image of the Co-NG, showing many Co atoms well-dispersed in the carbon matrix. Scale bar, 1 nm. (c) The enlarged view of the selected area in b. Scale bar, 0.5 nm. (d) Linear sweep voltammetry (LSV) of NG, Co-G, Co-NG, and Pt/C in 0.5 M H_2SO_4 at a scan rate of 2 mV s^{-1}. The inset shows the enlarged view of the LSV for the Co-NG near the onset region. (e) Tafel plots of the polarization curves in (d).[113]

Apart from those carbon materials and their derivatives, a new carbon allotrope, graphdiyne (GDY, Figure 1.7b), has attracted great attention in various fields recently. This material consists of aromatic rings made by *sp*- and sp^2-carbon and carbon–carbon triple bonds linked by an acetylenic linkage. Such a unique structure endows GDY with excellent stability, highly π-conjugated structure and superior electronic conductivity. Considering the unique structure and feature of GDY, Xu and co-workers synthesized the polymeric carbon nitride (CN)/GDY hybrid via a facile calcination approach, followed by photodeposition of Pt on the composite.[109] The system with GDY showed a great enhancement in photocatalytic H_2 evolution compared with that of CN under the identical

conditions. Such an enhancement can be ascribed to the new C-N bonds at the interfaces, which can serve as a charge carrier channel that facilitates the migration of photogenerated electrons from CN to GDY. However, this system still requires the use of high-cost Pt as co-catalyst towards H_2 generation. Exploring cost-effective, highly efficient, and durable GDY-based co-catalysts towards H_2 evolution is important to reduce/avoid the use of noble metal.

Very recently, various kinds of single atom (e.g., Mo, Fe, Ni) have been successfully anchored on GDY, those embedded single-metal sites could exhibit outstanding performance in the electrochemical field. Typically, Xue et al. reported the facile anchoring of the zero valence single-atom Ni and Fe on GDY via an electrochemical reduction method.[117] These GDY-supported single-atom catalyst exhibited extremely high electrocatalytic activity and long-term stability towards H_2 evolution. Taking the single Fe/GDY as an example, it showed an onset potential of 9 mV and overpotential of 66 mV (10 mA cm^{-2}). The outstanding H_2 evolution performances can be ascribed to strong chemical interaction and electronic coupling between the single-atom Fe and GDY support, which leads to high degrees of charge transport between the active catalytic sites and the supports. The superior performance of such single metal decorated GDY renders them to be excellent candidates of co-catalysts for photocatalytic H_2 generation and also can inspire the design and synthesis of more advanced single atom-based co-catalysts with superb catalytic activity.

1.4.2.2 Carbon-based co-catalysts for photocatalytic CO_2 reduction

Carbon-based materials can also be applied as co-catalysts for photocatalytic CO_2 reduction. Typically, Yu et al. prepared reduced graphene oxide (RGO)/CdS composite, wherein the RGO sheets not only promote the separation and transfer of charge carriers but also act as co-catalyst for adsorption and activation of CO_2 molecules.[118] As a result, the composites exhibited an efficient conversion of CO_2 to CH_4. Very recently, the same group fabricated monolayer nitrogen-graphene coated CdS hollow spheres via an in situ chemical vapor deposition method. This system exhibited efficient photocatalytic CO_2 reduction.[119] The monolayer nitrogen-doped graphene in this hybrid acts as the co-catalyst for adsorbing, activating and converting CO_2 molecules into CO and CH_4. Due to high-temperature annealing treatment required for the growth of graphene layer, a compact adhesion between the CdS and N-rich graphene was achieved at the same time, which significantly facilitates the separation and transfer of carriers. The similar

photocatalytic system mainly composed of Pt nanoparticles and carbon layer coated In_2O_3 has also been constructed for photocatalytic CO_2 reduction.[50] The carbon coating can promote the absorption of visible light, improve the separation of photoinduced electron−hole pairs and increase the chemisorption of CO_2. To further increase the intrinsic CO_2 reduction activity of carbon-based materials, Gao and co-workers anchored Co sites coordinated on the partially oxidized graphene nanosheets, which can serve as a highly active and durable heterogeneous catalyst for CO_2 conversion.[120] In this system, the isolated Co sites serve as the active centers for CO_2 conversion and the graphene bridges homogeneous light absorbers with single-atom catalytic sites for the efficient transfer of photoexcited electrons. As a result, the turnover number for CO production reaches a high value of 678 (after 3 h visible light irradiation) with a high turn-over frequency of 3.77 min^{-1}. There exists a vast development space to design robust single active sites for photocatalytic CO_2 reduction, considering the rapid progress of single atom embedded N-rich carbon in the electrochemical CO_2 reduction field. For example, many moieties, such as Ni-N_4,[121] Bi-N_4,[122] Co-N_5,[123] on N-rich carbon support, have been successfully fabricated and exhibit outstanding electrochemical CO_2 reduction activity, which could greatly inspire the design of active sites towards photocatalytic CO_2 reduction.

Recently, GDY has also been successfully employed as the co-catalysts for CO_2 reduction. Xu and co-workers coupled co-catalyst GDY with TiO_2 nanofibers for photocatalytic CO_2 reduction.[124] It was found that GDY mainly plays two roles in the photochemical process. First, the delocalized electrons in GDY can hybrid with the empty orbitals in TiO_2 and form an internal electric field at the interfaces, promoting the interfacial charge transfer; second, the GDY efficiently adsorbs and activates CO_2 molecules, promoting the subsequent photoreduction of CO_2.

1.4.3 Interfacial engineering of carbon-based photocatalytic systems

As mentioned in Section 1.3.3, strengthening the interface coupling is crucial to boost the charge carriers transfer across the junctions towards improving the photocatalytic efficiency. For the carbon-based photocatalytic system, the interfacial coupling can be constructed or reinforced by various strategies, including direct mixing, electrostatic self-assembly, annealing treatment, etc.

Ran et al. reported a metal-free 2D/2D phosphorene/g-C_3N_4 (CN) Van der Waals heterojunction obtained by mechanically mixing and used it as a metal-free photocatalyst.[125] They found that an electronic interaction exists between 2D phosphorene and 2D g-C_3N_4, whereby the electrons readily migrate from CN sheets to phosphorene sheet and realizing an efficient H_2 evolution activity under visible light irradiation. A very similar system was also constructed via a simple mixing process by Zhu and co-workers.[126] The main difference between those two cases lies in the clarification of the P-N bond at the interface and its effect on the photocatalytic process in the latter study. They pointed out that the P-N bonds at the interfaces in black phosphorus (BP)/CN is essential for improving photocatalytic performance. Under visible light irradiation, the CN acted as the main photocatalyst and generated energetic electrons, whereas BP collected the excited electrons from CN for H_2 evolution. When the composite was irradiated using near-infrared light, only BP was excited, the generated electrons in BP were trapped in the P−N coordinate bonds at the interfaces to generate H_2. Those P−N trapping sites can greatly prolong the lifetime of excited BP. However, it worth stressing that those carbon-based hybrids are obtained via simple mixing procedures at room temperature without special treatment. In such composites, the interfacial coupling is usually weak, although electron transport phenomenon can be observed. Suitable treatment before or after the formation of heterostructure is necessary and holds great potential to strengthen the interfacial coupling for fast charge carriers transfer across the junctions. For instance, to improve the interaction between rGO and g-C_3N_4 for efficient interfacial charge transport, Ong et al. fabricated the rGO (negatively charged) /protonated g-C_3N_4 (pCN, positively charged) heterojunction photocatalyst by an electrostatic self-assembly strategy.[127] It was revealed that the electrostatic self-assembly strategy could result in an intimate 2D−2D interfacial coupling between rGO and pCN. Such an intimate junction is favorable for charge transfer across the rGO/pCN heterojunction and suppresses electron−hole recombination, thus leads to a considerable photocatalytic CO_2 reduction performance. In addition to the interfacial electrostatic self-assembly strategy, the intimate heterojunctions with strongly coupled interfaces can also be fabricated through suitable heat treatment. In this regard, Yu et al. coupled g-C_3N_4 with WO_3 seamlessly via a heat treatment process and obtained a direct Z-scheme g-C_3N_4/WO_3 photocatalyst.[128] Due to the high-temperature annealing treatment, a well-defined interface formed. The interfacial covalent W-O-N-$(C)_2$ interaction and internal

field at the junction could mediate the electron transfer from WO_3 to g-C_3N_4 and greatly boost the photocatalytic H_2 evolution activity.

Besides those strategies, very recently, the vacancies can also mediate the interfacial charge transfer in carbon-based photocatalysis system. Typically, Xue et al. introduced nitrogen vacancies in the framework of CN and coupled it with co-catalyst MoS_2.[129] They found that the nitrogen vacancies in CN play a critical role in the interfacial electrons transfer across the junctions between N vacancies-rich CN and MoS_2. In detail, the N vacancies in CN could introduce shallow trap states (STSs) below the conduction band for photogenerated electrons and thereby facilitate the interfacial electron transfer process due to large energy differences between STSs and charge separation states. In addition, the transferred photoinduced electrons in MoS_2 could be trapped by the shallow Mo^{4+} states, where the transferred photo-generated electrons could be further trapped to drive H_2 evolution efficiently. This work demonstrates an attractive strategy to modulate interfacial electron transfer of heterojunction photocatalysts for achieving highly efficient photocatalytic reactions.

1.5 Thesis motivations and organization

On the basis of the above-mentioned overview about the photocatalysis, components of photocatalytic system, and the related strategies for optimizing each component, we can conclude: (1) each component of photocatalytic system, including the photocatalysts, co-catalysts, and interfaces between them, is crucial for the apparent photocatalytic efficiency; (2) polymeric carbon nitride (CN) and carbon are promising candidates of photocatalyst and co-catalyst, respectively. As mentioned in Section 1.4.1, layered polymeric carbon nitride, a metal-free and chemically stable material, has attracted intense interest in all kinds of solar to chemical energy conversion processes. However, polymeric CN still suffers from rapid recombination of charge carriers mainly due to long transportation distance, poor electronic conductivity, and rich defects in the layers, which severely restricts its photocatalytic efficiency. Besides, conventional carbon-based co-catalyst usually lacks robust active centers on its exposed surfaces, which restricts their co-catalytic performance. In addition to excellent photocatalysts and co-catalysts, clean and strongly coupled interfaces are crucial for the interfacial charge transfer and for the overall photocatalytic efficiency.

In this dissertation, we focus on the modulation of carbon-based materials, including CN photocatalyst, carbon co-catalyst, and relevant interfaces to enhance photocatalytic efficiency and to understand the related mechanism. First, two strategies, i.e., reversible exfoliation-reassembly and atomic carbon chain incorporation, are proposed to optimize the structure and property of photocatalyst CN and thus to enhance its photocatalytic activity. Then, single-Co implanted ultrathin N-rich carbon (Co-NC) wad fabricated as efficient H_2 evolution co-catalyst and the interfaces between commercial CdS and Co-NC were cleared for boosting the photocatalytic activity.

This dissertation is divided into five chapters. A summary of the remaining four chapters is described as below:

Chapter 2 Atomic carbon chains-mediated carriers transfer over polymeric carbon nitride for efficient photocatalysis

Efficient solar-to-energy conversion over polymeric CN still encounters great challenges of sluggish radiative carriers transfer within layers due to the long transportation distance and rich defects in layers. In this chapter, we aim to improve the electronic conductivity of CN layers by incorporating atomic carbon chains into the basal plane of CN while remaining the pristine tri-s-triazine structure. Usually, carbon materials, such as carbon nanotube, graphene, and even the doped carbon matrix in the basal plane of CN, own excellent electrical conductivity. Thus, we believe that the carbon chains interconnected with the intrinsic structure of CN covalently could enable the electron with faster mobility throughout the layers compared with the original layers. Therefore, these mediated carbon chains are expected to reinforce the separation and transfer of photogenerated carriers in the basal plane of CN, leading to enhanced photocatalytic performance, including H_2 generation and CO_2 reduction.

Chapter 3 Targeted exfoliation and reassembly of polymeric carbon nitride for efficient photocatalysis

Polymeric carbon nitride can only exhibit considerable performance in a single photocatalytic reaction at present; it is still a great challenge to fulfill its full potentials in diverse photoredox reactions for remarkable performance. Generally, the optimal efficiency of different photocatalytic reactions requires a distinct balance among diverse parameters, such as light absorption, exposed active sites and kinetics of photocarriers. Targeted and reversible regulation of these parameters to achieve outstanding activity in different photocatalytic reactions will promote solar energy conversion and storage. For

CN with typical layered structure, reversible, efficient and controllable exfoliation-reassembly may enable the targeted switch of these properties over CN, and thus make full use of these features in different photoredox reactions. In this chapter, we aim to construct a reversible exfoliation-reassembly functionalized CN by switching its interlayer structure. Hydroxyl (OH) groups were implanted into the interspaces of CN first. The induced protons are expected to neutralize the OH groups and generate H_2O within the confined layers to expand CN into nanosheets. These exfoliated nanosheets may reassemble by rebuilding surface OH besause the re-grafted OH on the exfoliated sheets possibly will form hydrogen bond interaction. Importantly, the exfoliation-reassembly effect of CN is expected to cause the switchable properties, which may be favorable for different photocatalytic reactions and exhibit considerable performance.

Chapter 4 Single-Co on N-rich carbon as co-catalyst for efficient photocatalytic H_2 production: the key roles of cleared interfaces and isolated metal sites

Creation of robust single active sites and clean interfaces without contamination of adventitious carbon is highly desirable for the delivery and utilization of electrons in sunlight-driven hydrogen production. Implanting suitable single metal sites on carbon substrate might give rise to significant enhancement towards cocatalytic H_2 generation. Upon loading such kind of co-catalysts on photoharvester, it also inevitably brings a contaminated interface between photoharvester and co-catalyst caused by the adventitious carbon at the junction. A contaminated interface will severely block the electron transfer to the co-catalytic single-site. Those considerations motivate us to create a clean heterostructured interface aiming at speeding up the carriers flow to the designed single-site co-catalysts for constructing a photocatalytic system with record activity and metal utilization efficiency. In this chapter, atomically dispersed metal embedded ultrathin nitrogen-rich carbon (Co-NC) was fabricated and subsequently anchored on excellent photoharvester CdS. Inspired by the potential decomposition of adventitious carbon under heat treatment, we annealed the hybrid CdS/Co-NC to realize an expected interface with less contamination. It can be expected that a less contaminated interface can enable fast carriers transfer from CdS to Co-NC co-catalyst. By combining the cleared interface between CdS and Co-NC and robust single Co sites for HER, the designed heterostructure system may exhibit highly efficient photocatalytic H_2 generation.

Chapter 5 General conclusions and future prospects

Chapter 1

This chapter presents an overall summary and conclusion of this dissertation and gives the prospects based on our research.

References

[1] A. Kudo, Y. Miseki, *Chem. Soc. Rev.,* 2009, **38**, 253-278.

[2] S. N. Habisreutinger, L. Schmidt-Mende, J. K. Stolarczyk, *Angew. Chem., Int. Ed. Engl.,* 2013, **52**, 7372-7408.

[3] C. Chen, W. Ma, J. Zhao, *Chem. Soc. Rev.,* 2010, **39**, 4206-4219.

[4] J. Tang, Z. Zou, J. Ye, *Angew. Chem., Int. Ed. Engl.,* 2004, **43**, 4463-4466.

[5] H. Hou, X. Zeng, X. Zhang, *Angew. Chem., Int. Ed. Engl.,* 2019, DOI: 10.1002/anie.201911609.

[6] A. Savateev, M. Antonietti, *ACS Catal.,* 2018, **8**, 9790-9808.

[7] A. Fujishima, K. Honda, *Nature,* 1972, **238**, 37-38.

[8] T. Hisatomi, J. Kubota, K. Domen, *Chem. Soc. Rev.,* 2014, **43**, 7520-7535.

[9] H. Tong, S. Ouyang, Y. Bi, N. Umezawa, M. Oshikiri, J. Ye, *Adv. Mater.,* 2012, **24**, 229-251.

[10] R. Li, Y. Weng, X. Zhou, X. Wang, Y. Mi, R. Chong, H. Han, C. Li, *Energy Environ. Sci.,* 2015, **8**, 2377-2382.

[11] K. Domen, S. Naito, M. Soma, T. Onishi, K. Tamaru, *J. Chem. Soc., Chem. Commun.,* 1980, 543-544.

[12] Z. Zou, J. Ye, K. Sayama, H. Arakawa, *Nature,* 2001, **414**, 625-627.

[13] K. Maeda, K. Teramura, D. Lu, T. Takata, N. Saito, Y. Inoue, K. Domen, *Nature,* 2006, **440**, 295.

[14] S. Chen, T. Takata, K. Domen, *Nat. Rev. Mater.,* 2017, **2**, 17050.

[15] Z. Pan, G. Zhang, X. Wang, *Angew. Chem., Int. Ed. Engl.,* 2019, **58**, 7102-7106.

[16] K. Iwashina, A. Iwase, Y. H. Ng, R. Amal, A. Kudo, *J. Am. Chem. Soc.,* 2015, **137**, 604-607.

[17] J. Yang, D. Wang, H. Han, C. Li, *Acc. Chem. Res.,* 2013, **46**, 1900-1909.

[18] T. Uekert, H. Kasap, E. Reisner, *J. Am. Chem. Soc.,* 2019, **141**, 15201-15210.

[19] N. Luo, T. Montini, J. Zhang, P. Fornasiero, E. Fonda, T. Hou, W. Nie, J. Lu, J. Liu, M. Heggen, L. Lin, C. Ma, M. Wang, F. Fan, S. Jin, F. Wang, *Nat. Energy,* 2019, **4**, 575-584.

[20] E. Fujita, *Coord. Chem. Rev.,* 1999, **185-186**, 373-384.

[21] Y. Y. Birdja, E. Pérez-Gallent, M. C. Figueiredo, A. J. Göttle, F. Calle-Vallejo, M. T. M. Koper, *Nat. Energy,* 2019, **4**, 732-745.

[22] I. Ghosh, J. Khamrai, A. Savateev, N. Shlapakov, M. Antonietti, B. Konig, *Science,* 2019, **365**, 360-366.

[23] S. Wang, F. Ichihara, H. Pang, H. Chen, J. Ye, *Adv. Funct. Mater.,* 2018, **28**, 1803309-1803335.

[24] M. Ni, M. K. H. Leung, D. Y. C. Leung, K. Sumathy, *Renewable Sustainable Energy Rev.,* 2007, **11**, 401-425.

[25] S. Liang, L. Wen, S. Lin, J. Bi, P. Feng, X. Fu, L. Wu, *Angew. Chem., Int. Ed. Engl.,* 2014, **53**, 2951-2955.

[26] K. Maeda, T. Takata, M. Hara, N. Saito, Y. Inoue, H. Kobayashi, K. Domen, *J. Am. Chem. Soc.,* 2005, **127**, 8286-8287.

[27] Q. Wang, M. Nakabayashi, T. Hisatomi, S. Sun, S. Akiyama, Z. Wang, Z. Pan, X. Xiao, T. Watanabe, T. Yamada, N. Shibata, T. Takata, K. Domen, *Nat. Mater.,* 2019, **18**, 827-832.

[28] M. Higashi, K. Domen, R. Abe, *J. Am. Chem. Soc.,* 2012, **134**, 6968-6971.

[29] S. S. Ma, T. Hisatomi, K. Maeda, Y. Moriya, K. Domen, *J. Am. Chem. Soc.,* 2012, **134**, 19993-19996.

[30] T. T. Zhuang, Y. Liu, Y. Li, Y. Zhao, L. Wu, J. Jiang, S. H. Yu, *Angew. Chem., Int. Ed. Engl.,* 2016, **55**, 6396-6400.

[31] G. Liu, T. Wang, H. Zhang, X. Meng, D. Hao, K. Chang, P. Li, T. Kako, J. Ye, *Angew. Chem., Int. Ed. Engl.,* 2015, **54**, 13561-13565.

[32] J. D. Xiao, H. L. Jiang, *Acc. Chem. Res.,* 2019, **52**, 356-366.

[33] C. Dai, B. Liu, *Energy Environ. Sci.,* 2020, **13**, 24-52.

[34] Y. Zheng, L. Lin, B. Wang, X. Wang, *Angew. Chem., Int. Ed. Engl.,* 2015, **54**, 12868-12884.

[35] Y. Cui, Z. Ding, P. Liu, M. Antonietti, X. Fu, X. Wang, *Phys. Chem. Chem. Phys.,* 2012, **14**, 1455-1462.

[36] X. Wang, K. Maeda, A. Thomas, K. Takanabe, G. Xin, J. M. Carlsson, K. Domen, M. Antonietti, *Nat. Mater.,* 2009, **8**, 76-80.

[37] K. Chang, X. Hai, J. Ye, *Adv. Energy Mater.,* 2016, **6**, 1502555.

[38] J. Ran, J. Zhang, J. Yu, M. Jaroniec, S. Z. Qiao, *Chem. Soc. Rev.,* 2014, **43**, 7787-7812.

[39] S. Bai, W. Yin, L. Wang, Z. Li, Y. Xiong, *RSC Adv.,* 2016, **6**, 57446-57463.

[40] J. Ran, G. Gao, F. T. Li, T. Y. Ma, A. Du, S. Z. Qiao, *Nat. Commun.,* 2017, **8**, 13907.

[41] X. Fang, Q. Shang, Y. Wang, L. Jiao, T. Yao, Y. Li, Q. Zhang, Y. Luo, H. L. Jiang, *Adv. Mater.,* 2018, **30**, 1705112.

[42] W. Liu, L. Cao, W. Cheng, Y. Cao, X. Liu, W. Zhang, X. Mou, L. Jin, X. Zheng, W. Che, Q. Liu, T. Yao, S. Wei, *Angew. Chem., Int. Ed. Engl.,* 2017, **56**, 9312-9317.

[43] J. Zhang, Y. Zhao, X. Guo, C. Chen, C.-L. Dong, R.-S. Liu, C.-P. Han, Y. Li, Y. Gogotsi, G. Wang, *Nat. Catal.,* 2018, **1**, 985-992.

[44] J. Sato, N. Saito, Y. Yamada, K. Maeda, T. Takata, J. N. Kondo, M. Hara, H. Kobayashi, K. Domen, Y. Inoue, *J. Am. Chem. Soc.,* 2005, **127**, 4150-4151.

[45] B. Ma, J. Yang, H. Han, J. Wang, X. Zhang, C. Li, *J. Phys. Chem. C,* 2010, **114**, 12818-12822.

[46] H. Fei, J. Dong, Y. Feng, C. S. Allen, C. Wan, B. Volosskiy, M. Li, Z. Zhao, Y. Wang, H. Sun, P. An, W. Chen, Z. Guo, C. Lee, D. Chen, I. Shakir, M. Liu, T. Hu, Y. Li, A. I. Kirkland, X. Duan, Y. Huang, *Nat. Catal.,* 2018, **1**, 63-72.

[47] X. Li, J. Yu, M. Jaroniec, X. Chen, *Chem. Rev.,* 2019, **119**, 3962-4179.

[48] S. Cao, Y. Li, B. Zhu, M. Jaroniec, J. Yu, *J. Catal.,* 2017, **349**, 208-217.

[49] L. Cao, S. Sahu, P. Anilkumar, C. E. Bunker, J. Xu, K. A. Fernando, P. Wang, E. A. Guliants, K. N. Tackett, II, Y. P. Sun, *J. Am. Chem. Soc.,* 2011, **133**, 4754-4757.

[50] Y. X. Pan, Y. You, S. Xin, Y. Li, G. Fu, Z. Cui, Y. L. Men, F. F. Cao, S. H. Yu, J. B. Goodenough, *J. Am. Chem. Soc.,* 2017, **139**, 4123-4129.

[51] J. Ran, M. Jaroniec, S. Z. Qiao, *Adv. Mater.,* 2018, **30**, 1704649.

[52] C. Gao, Q. Meng, K. Zhao, H. Yin, D. Wang, J. Guo, S. Zhao, L. Chang, M. He, Q. Li, H. Zhao, X. Huang, Y. Gao, Z. Tang, *Adv. Mater.,* 2016, **28**, 6485-6490.

[53] R. Kuriki, K. Sekizawa, O. Ishitani, K. Maeda, *Angew. Chem., Int. Ed. Engl.,* 2015, **54**, 2406-2409.

[54] C. Cometto, R. Kuriki, L. Chen, K. Maeda, T. C. Lau, O. Ishitani, M. Robert, *J. Am. Chem. Soc.,* 2018, **140**, 7437-7440.

[55] K. Maeda, *Adv. Mater.,* 2019, **31**, e1808205.

[56] G. Zhao, H. Pang, G. Liu, P. Li, H. Liu, H. Zhang, L. Shi, J. Ye, *Appl. Catal., B,* 2017, **200**, 141-149.

[57] H. Takeda, K. Ohashi, A. Sekine, O. Ishitani, *J. Am. Chem. Soc.,* 2016, **138**, 4354-4357.

[58] H. Rao, C. H. Lim, J. Bonin, G. M. Miyake, M. Robert, *J. Am. Chem. Soc.,* 2018, **140**, 17830-17834.

[59] H. Rao, L. C. Schmidt, J. Bonin, M. Robert, *Nature,* 2017, **548**, 74-77.

[60] J. Di, C. Chen, S. Z. Yang, S. Chen, M. Duan, J. Xiong, C. Zhu, R. Long, W. Hao, Z. Chi, H. Chen, Y. X. Weng, J. Xia, L. Song, S. Li, H. Li, Z. Liu, *Nat. Commun.,* 2019, **10**, 2840.

[61] X. Hai, K. Chang, H. Pang, M. Li, P. Li, H. Liu, L. Shi, J. Ye, *J. Am. Chem. Soc.,* 2016, **138**, 14962-14969.

[62] P. Wang, Y. Mao, L. Li, Z. Shen, X. Luo, K. Wu, P. An, H. Wang, L. Su, Y. Li, S. Zhan, *Angew. Chem., Int. Ed. Engl.,* 2019, **58**, 11329-11334.

[63] Y.-J. Yuan, Z.-K. Shen, S. Song, J. Guan, L. Bao, L. Pei, Y. Su, S. Wu, W. Bai, Z.-T. Yu, Z. Ji, Z. Zou, *ACS Catal.,* 2019, **9**, 7801-7807.

[64] S. Chen, S. Shen, G. Liu, Y. Qi, F. Zhang, C. Li, *Angew. Chem., Int. Ed. Engl.,* 2015, **54**, 3047-3051.

[65] N. Zhang, M. Q. Yang, Z. R. Tang, Y. J. Xu, *ACS Nano,* 2014, **8**, 623-633.

[66] X. Cui, J. Wang, B. Liu, S. Ling, R. Long, Y. Xiong, *J. Am. Chem. Soc.,* 2018, **140**, 16514-16520.

[67] S. Bai, J. Ge, L. Wang, M. Gong, M. Deng, Q. Kong, L. Song, J. Jiang, Q. Zhang, Y. Luo, Y. Xie, Y. Xiong, *Adv. Mater.,* 2014, **26**, 5689-5695.

[68] J. Wen, J. Xie, H. Zhang, A. Zhang, Y. Liu, X. Chen, X. Li, *ACS Appl. Mater. Interfaces,* 2017, **9**, 14031-14042.

[69] G. Bi, J. Wen, X. Li, W. Liu, J. Xie, Y. Fang, W. Zhang, *RSC Adv.,* 2016, **6**, 31497-31506.

[70] Y. Zhong, J. Yuan, J. Wen, X. Li, Y. Xu, W. Liu, S. Zhang, Y. Fang, *Dalton Trans.,* 2015, **44**, 18260-18269.

[71] J. Li, G. Zhan, Y. Yu, L. Zhang, *Nat. Commun.,* 2016, **7**, 11480.

[72] S. Yang, Y. Gong, J. Zhang, L. Zhan, L. Ma, Z. Fang, R. Vajtai, X. Wang, P. M. Ajayan, *Adv. Mater.,* 2013, **25**, 2452-2456.

[73] J. Ji, J. Wen, Y. Shen, Y. Lv, Y. Chen, S. Liu, H. Ma, Y. Zhang, *J. Am. Chem. Soc.,* 2017, **139**, 11698-11701.

[74] P. Yang, H. Ou, Y. Fang, X. Wang, *Angew. Chem., Int. Ed. Engl.,* 2017, **56**, 3992-3996.

[75] P. Niu, L. Zhang, G. Liu, H.-M. Cheng, *Adv. Funct. Mater.,* 2012, **22**, 4763-4770.

[76] J. Zhang, M. Zhang, C. Yang, X. Wang, *Adv. Mater.,* 2014, **26**, 4121-4126.

[77] X. Lu, K. Xu, P. Chen, K. Jia, S. Liu, C. Wu, *J. Mater. Chem. A,* 2014, **2**, 18924-18928.

[78] J. Xu, L. Zhang, R. Shi, Y. Zhu, *J. Mater. Chem. A,* 2013, **1**, 14766.

[79] M. Rahman, K. Davey, S. Z. Qiao, *Small,* 2017, **13**, 1700376.

[80] X. Wang, K. Maeda, X. Chen, K. Takanabe, K. Domen, Y. Hou, X. Fu, M. Antonietti, *J. Am. Chem. Soc.,* 2009, **131**, 1680-1681.

[81] Q. Han, B. Wang, Y. Zhao, C. Hu, L. Qu, *Angew. Chem., Int. Ed. Engl.,* 2015, **54**, 11433-11437.

[82] Q. Han, B. Wang, J. Gao, Z. Cheng, Y. Zhao, Z. Zhang, L. Qu, *ACS Nano,* 2016, **10**, 2745-2751.

[83] S. Guo, Z. Deng, M. Li, B. Jiang, C. Tian, Q. Pan, H. Fu, *Angew. Chem., Int. Ed. Engl.,* 2016, **55**, 1830-1834.

[84] J. Zheng, H. Zhang, S. Dong, Y. Liu, C. T. Nai, H. S. Shin, H. Y. Jeong, B. Liu, K. P. Loh, *Nat. Commun.,* 2014, **5**, 2995.

[85] H. Yang, Z. H. Wang, Y. Y. Zheng, L. Q. He, C. Zhan, X. Lu, Z. Q. Tian, P. P. Fang, Y. Tong, *J. Am. Chem. Soc.,* 2016, **138**, 16204-16207.

[86] J. Ran, T. Y. Ma, G. Gao, X.-W. Du, S. Z. Qiao, *Energy Environ. Sci.,* 2015, **8**, 3708-3717.

[87] H. Ou, X. Chen, L. Lin, Y. Fang, X. Wang, *Angew. Chem., Int. Ed. Engl.,* 2018, **57**, 8729-8733.

[88] X. Wang, X. Chen, A. Thomas, X. Fu, M. Antonietti, *Adv. Mater.,* 2009, **21**, 1609-1612.

[89] Y. Li, Z. Wang, T. Xia, H. Ju, K. Zhang, R. Long, Q. Xu, C. Wang, L. Song, J. Zhu, J. Jiang, Y. Xiong, *Adv. Mater.,* 2016, **28**, 6959-6965.

[90] Z. Chen, E. Vorobyeva, S. Mitchell, E. Fako, M. A. Ortuno, N. Lopez, S. M. Collins, P. A. Midgley, S. Richard, G. Vile, J. Perez-Ramirez, *Nat. Nanotechnol.,* 2018, **13**, 702-707.

[91] X. Li, W. Bi, L. Zhang, S. Tao, W. Chu, Q. Zhang, Y. Luo, C. Wu, Y. Xie, *Adv. Mater.,* 2016, **28**, 2427-2431.

[92] Y. Cao, S. Chen, Q. Luo, H. Yan, Y. Lin, W. Liu, L. Cao, J. Lu, J. Yang, T. Yao, S. Wei, *Angew. Chem., Int. Ed. Engl.,* 2017, **56**, 12191-12196.

[93] W. Che, W. Cheng, T. Yao, F. Tang, W. Liu, H. Su, Y. Huang, Q. Liu, J. Liu, F. Hu, Z. Pan, Z. Sun, S. Wei, *J. Am. Chem. Soc.,* 2017, **139**, 3021-3026.

[94] Y. Yu, W. Yan, X. Wang, P. Li, W. Gao, H. Zou, S. Wu, K. Ding, *Adv. Mater.,* 2018, **30**, 1705060.

[95] J. Zhang, X. Chen, K. Takanabe, K. Maeda, K. Domen, J. D. Epping, X. Fu, M. Antonietti, X. Wang, *Angew. Chem., Int. Ed. Engl.,* 2010, **49**, 441-444.

[96] P. Niu, L. C. Yin, Y. Q. Yang, G. Liu, H. M. Cheng, *Adv. Mater.,* 2014, **26**, 8046-8052.

[97] P. Yang, H. Zhuzhang, R. Wang, W. Lin, X. Wang, *Angew. Chem., Int. Ed. Engl.,* 2019, **58**, 1134-1137.

[98] J. Low, J. Yu, M. Jaroniec, S. Wageh, A. A. Al-Ghamdi, *Adv. Mater.,* 2017, **29**, 1601694.

[99] J. Zhang, M. Zhang, R. Q. Sun, X. Wang, *Angew. Chem., Int. Ed. Engl.,* 2012, **51**, 10145-10149.

[100] Y. Hou, A. B. Laursen, J. Zhang, G. Zhang, Y. Zhu, X. Wang, S. Dahl, I. Chorkendorff, *Angew. Chem., Int. Ed. Engl.,* 2013, **52**, 3621-3625.

[101] F. T. Wagner, G. A. Somorjai, *Nature,* 1980, **285**, 559-560.

[102] S. Ouyang, H. Tong, N. Umezawa, J. Cao, P. Li, Y. Bi, Y. Zhang, J. Ye, *J. Am. Chem. Soc.,* 2012, **134**, 1974-1977.

[103] X. Meng, S. Ouyang, T. Kako, P. Li, Q. Yu, T. Wang, J. Ye, *Chem. Commun.,* 2014, **50**, 11517-11519.

[104] T. Kako, X. Meng, J. Ye, *Appl. Catal., A,* 2014, **488**, 183-188.

[105] Q. Xiang, J. Yu, M. Jaroniec, *J. Am. Chem. Soc.,* 2012, **134**, 6575-6578.

[106] J. Zhang, J. Yu, M. Jaroniec, J. R. Gong, *Nano Lett,* 2012, **12**, 4584-4589.

[107] T. Peng, K. Li, P. Zeng, Q. Zhang, X. Zhang, *J. Phys. Chem. C,* 2012, **116**, 22720-22726.

[108] F. He, G. Chen, Y. Zhou, Y. Yu, L. Li, S. Hao, B. Liu, *J. Mater. Chem. A,* 2016, **4**, 3822-3827.

[109] Q. Xu, B. Zhu, B. Cheng, J. Yu, M. Zhou, W. Ho, *Appl. Catal., B,* 2019, **255**, 117770.

[110] K. Chang, Z. Mei, T. Wang, Q. Kang, S. Ouyang, J. Ye, *ACS Nano,* 2014, **8**, 7078-7087.

[111] Q. Han, B. Wang, J. Gao, L. Qu, *Angew. Chem., Int. Ed. Engl.,* 2016, **55**, 10849-10853.

[112] X. F. Yang, A. Wang, B. Qiao, J. Li, J. Liu, T. Zhang, *Acc. Chem. Res.,* 2013, **46**, 1740-1748.

[113] H. Fei, J. Dong, M. J. Arellano-Jimenez, G. Ye, N. Dong Kim, E. L. Samuel, Z. Peng, Z. Zhu, F. Qin, J. Bao, M. J. Yacaman, P. M. Ajayan, D. Chen, J. M. Tour, *Nat. Commun.,* 2015, **6**, 8668.

[114] L. Fan, P. F. Liu, X. Yan, L. Gu, Z. Z. Yang, H. G. Yang, S. Qiu, X. Yao, *Nat. Commun.,* 2016, **7**, 10667.

[115] W. Chen, J. Pei, C. T. He, J. Wan, H. Ren, Y. Zhu, Y. Wang, J. Dong, S. Tian, W. C. Cheong, S. Lu, L. Zheng, X. Zheng, W. Yan, Z. Zhuang, C. Chen, Q. Peng, D. Wang, Y. Li, *Angew. Chem., Int. Ed. Engl.,* 2017, **56**, 16086-16090.

[116] W. Chen, J. Pei, C. T. He, J. Wan, H. Ren, Y. Wang, J. Dong, K. Wu, W. C. Cheong, J. Mao, X. Zheng, W. Yan, Z. Zhuang, C. Chen, Q. Peng, D. Wang, Y. Li, *Adv. Mater.,* 2018, **30**, e1800396.

[117] Y. Xue, B. Huang, Y. Yi, Y. Guo, Z. Zuo, Y. Li, Z. Jia, H. Liu, Y. Li, *Nat. Commun.,* 2018, **9**, 1460.

[118] J. Yu, J. Jin, B. Cheng, M. Jaroniec, *J. Mater. Chem. A,* 2014, **2**, 3407.

[119] C. Bie, B. Zhu, F. Xu, L. Zhang, J. Yu, *Adv. Mater.,* 2019, **31**, e1902868.

[120] C. Gao, S. Chen, Y. Wang, J. Wang, X. Zheng, J. Zhu, L. Song, W. Zhang, Y. Xiong, *Adv. Mater.,* 2018, **30**, e1704624.

[121] C. Zhao, X. Dai, T. Yao, W. Chen, X. Wang, J. Wang, J. Yang, S. Wei, Y. Wu, Y. Li, *J. Am. Chem. Soc.,* 2017, **139**, 8078-8081.

[122] E. Zhang, T. Wang, K. Yu, J. Liu, W. Chen, A. Li, H. Rong, R. Lin, S. Ji, X. Zheng, Y. Wang, L. Zheng, C. Chen, D. Wang, J. Zhang, Y. Li, *J. Am. Chem. Soc.,* 2019, **141**, 16569-16573.

[123] Y. Pan, R. Lin, Y. Chen, S. Liu, W. Zhu, X. Cao, W. Chen, K. Wu, W. C. Cheong, Y. Wang, L. Zheng, J. Luo, Y. Lin, Y. Liu, C. Liu, J. Li, Q. Lu, X. Chen, D. Wang, Q. Peng, C. Chen, Y. Li, *J. Am. Chem. Soc.,* 2018, **140**, 4218-4221.

[124] F. Xu, K. Meng, B. Zhu, H. Liu, J. Xu, J. Yu, *Adv. Funct. Mater.,* 2019, **29**, 1904256.

[125] J. Ran, W. Guo, H. Wang, B. Zhu, J. Yu, S. Z. Qiao, *Adv. Mater.,* 2018, **30**, e1800128.

[126] M. Zhu, S. Kim, L. Mao, M. Fujitsuka, J. Zhang, X. Wang, T. Majima, *J. Am. Chem. Soc.,* 2017, **139**, 13234-13242.

[127] W.-J. Ong, L.-L. Tan, S.-P. Chai, S.-T. Yong, A. R. Mohamed, *Nano Energy,* 2015, **13**, 757-770.

[128] W. Yu, J. Chen, T. Shang, L. Chen, L. Gu, T. Peng, *Appl. Catal., B,* 2017, **219**, 693-704.

[129] J. Xue, M. Fujitsuka, T. Majima, *ACS Appl. Mater. Interfaces,* 2019, **11**, 40860-40867.

Chapter 2 Atomic carbon chains-mediated carriers transfer over polymeric carbon nitride for efficient photocatalysis

2.1 Introduction

The generation of clean and renewable chemicals from H_2O and CO_2 using photocatalysts is a highly promising solution to the conversion and storage of solar energy.[1] The development of efficient, durable, and sustainable photocatalysts is always at the heart of photocatalytic research. Layered polymeric carbon nitride (CN), a metal-free and chemically stable material, has attracted intense interest in all kinds of solar to chemical energy conversion processes including H_2/O_2 evolution from water splitting and CO_2 reduction.[2-11]

However, similar to other kinds of organic framework, e.g., metal-organic frameworks (MOFs), and covalent organic frameworks (COFs), efficient solar-to-energy conversion over polymeric CN still encounters great challenges of sluggish radiative carriers transfer within layers due to rich defects in layers. Notably, these defects in polymeric CN are mainly related to NH_2 and NH groups because of the incomplete polymerization of amide groups-rich precursors.[12] Abundant intralayered hydrogen bonds are thus (as illustrated by the dash line in Figure 2.1) formed in the defect regions.[12, 13] As a result, the transport of charge carriers across the layers of CN is signally different from that of other materials only containing covalent bonds within the layers, e.g., MoS_2 with Mo-S bonds and nitrogen doped graphene with C-N/C-C bonds.[12] These hydrogen bonds are not favorable relative to covalent bonds for the transport of photocarriers within the plane and thus cause the high localization of photocarriers within the tri-*s*-triazine units.[12, 14]

The direct atomic engineering of intralayered defects/motifs is the most fundamental and straightforward pathway to facilitate the transport of carriers in the layered CN and also can provide deeper insight into the behavior of the carriers in CN. Owing to the unique chemical composition and layered feature, polymeric CN possesses high adjustability and compatibility and thus offer us huge potential to targetedly tailor its structure and properties towards diverse applications.[15-24] Recently, several pioneering approaches have been sought in the perspective of this sight.[16, 25-27] First, Liu et al. selectively broke the hydrogen bond via reducing the residual NH_2/NH groups at high temperature, in part resulting in a remarkable suppression of radiative carriers

recombination in photocatalyst.[12] Another reported strategy is to implant the carbon ring including two similar types—"C_{ring}" and "gradually doped graphited carbon rings" into the planar layer of CN.[25, 26] In the case of C_{ring} modified CN, the in-plane inserted C_{ring} not only expedites the carriers separation but also promotes the photoelectron transport.[25] Similarly, carbon quantum dots, with relatively larger size compared to atomic carbon ring, were also implanted in the 2D plane of CN seamlessly to facilitate the photoelectron transport.[27] However, these strategies above-mentioned still suffer from several drawbacks, such as moderate photocatalytic performance or complicated and energy consumption procedures. Besides, precise and targeted basal plane engineering of CN with atomic carbon species smaller than aforementioned carbon-based dopants, i.e., short carbon chains, has not been intentionally attempted yet and still remains a significant challenge.

Herein, we propose a conceptual and facile strategy to construct carbon chains incorporated CN, in which various kinds of carbon chains connected the in-plane defects of CN via strong covalent C-N bonds. Notably, these mediated carbon chains serve as the electron transport channel to reinforce the separation and transfer of photogenerated carriers in the basal plane of CN. Therefore, the optimized sample delivers a remarkably enhanced photocatalytic performance by achieving a 13.2 and 29.2-fold improvement for water reduction and CO_2 reduction, respectively, as well as good stability without noticeable attenuation.

2.2 Experimental section

2.2.1 Materials preparation

All reagents were analytical grade and used without further purification. The deionized water (18.2 MΩ) that was used throughout all experiments was produced using a Millipore Direct-Q System. The pristine polymeric CN (denoted as CN) was fabricated by annealing 1.5 g melamine up to 550 °C at a rate of 2.3 °C min^{-1} and kept for 4 h in a covered Al_2O_3 crucible. After cooled down to room temperature, the product was grounded to obtain a powder sample. To fabricate the carbon chains linked CN, precursors (melamine/dicyandiamide/urea/thiourea) and linker molecules (glycine/β-Alanine/4-Aminobutyric acid/L-cysteine/Allyl thiourea/L-Arginine) were first mixed fully. Using the linker glycine as an example, 1.5 g melamine and certain amount of glycine (5, 10, 15, 20, 30 mg) were first dissolved in 20 mL deionized water with stirring

and heated at ~80 ^{o}C to evaporate the water. Then, the white mixture followed the identical calcination procedure of CN as mentioned above. The samples thus obtained were named as CN-xGly, where x (mg) represents the amount of glycine. As shown in Figure 2.15a and 2.15b, the optimized amount of glycine was 10 mg. Therefore, for other linkers, the amount was roughly fixed at 10 mg to evaluate the validity of different linkers on photocatalytic activity. Other carbon chains doped samples derived from various precursors, i.e., dicyandiamide/urea/thiourea, were fabricated following the similar procedures with that of CN-xGly but with different precursor and dosage. Specially, in the case of samples prepared from urea and thiourea, the amount of both of them is 10 g. The samples in Figure 2.15d were fabricated using precursor dicyandiamide and different linker molecules. The CN-10Gly-(two steps) was synthesis by heating the mixture of CN (~600 mg, derived from 1.5 g melamine) and 10 mg glycine at 550 ^{o}C.

2.2.2 Material characterization

XRD patterns of the as-prepared samples were collected with a powder X-ray diffractometer (Cu Kα radiation source, X'pert powder, PANalytical B.V., Netherlands). UV−visible (UV−vis) diffuse reflectance spectra of the samples were recorded on an UV−visible spectrophotometer (UV-2700, Shimadzu, Japan) equipped with an integrating sphere, then converted into absorption spectra by Kubelka−Munk transformation. Nitrogen adsorption–desorption isotherms, and surface area were recorded using a BEL SORP-mini II (BEL Japan INC., Japan), and were calculated via the Brunauer-Emmett-Teller (BET) method. Infrared transmission spectra were collected using a Fourier Transform infrared (FT-IR) spectrophotometer (Nicolet 4700, Thermo SCIENTIFIC, America). The in situ FT-IR measurements were conducted on a JASCO FTIR-6300 spectrometer under argon with a homemade chamber. The Photoluminescence (PL) properties were investigated using a fluorescence spectrophotometer (Fluorolog-3, HORIBA Scientific, America). X-ray photoelectron spectroscopy (XPS) measurements were carried out on XPS instrument (Escalab 250, Thermo SCIENTIFIC, America). All binding energies were referenced to the C *1s* peaks of the surface adventitious carbon at 284.8 eV. The morphologies of samples were characterized with Field Emission Scanning Electron Microscope (JSM-6701F, JEOL Co., Japan) and Transmission Electron Microscope (TEM) (JEM-2100F, JEOL Co., Japan). X-ray absorption spectroscopy measurements were carried on CN samples drop casted on conductive Si wafer. The data were collected at the U49/2 PGM1 undulator

beamline of the BESSY II synchrotron radiation source using the LiXEdrom endstation. The XAS were measured in the total electron yield mode by scanning the samples in the energy range of 276 ~ 310 eV (for C K-edge) or 395 ~ 420 eV (for N K-edge) in 0.1 eV steps. The XAS spectra in the figures have been normalized to the background before and after the main features.

2.2.3 Photoelectrochemical measurement

The photoelectrodes were prepared according to previously reported method. The indium doped tin oxide (ITO) substrates were cleaned by ultrasonication in distilled water, absolute ethanol, and isopropanol for 15 min sequentially, and then dried in vacuum. 5 mg of photocatalysts and 20 μL of Nafion solution (5 wt%) were dispersed in 1 mL ethanol by at least 30 min sonication to prepare a homogeneous catalyst colloid. Then, 100 μL of the catalyst colloid was deposited onto areas of ≈1 cm^2 of the ITO conductive glass and then was dried in air to form the working electrode. The photoelectrochemical properties were investigated in a three-electrode cell by using an electrochemical station (Model-660D, CH instruments). The catalyst coated ITO glass, a Pt foil, and an Ag/AgCl electrode and 0.5 M Na_2SO_4 aqueous solution were used as the working electrode, the counter-electrode, the reference electrode, and the electrolyte, respectively. A 300 W Xe arc lamp equipped with a 400 nm cutoff filter was utilized as a light source. EIS were recorded at an applied potential of 0.2 V versus Ag/AgCl over the frequency range of 1 MHz ~ 0.1 Hz. The photocurrent with on/off cycles was measured at an applied potential of 1.0 V versus Ag/AgCl. Mott–Schottky plots were obtained under direct current potential polarization at the frequency of 1000 Hz. The potential ranged from -0.6 to 1.0 V (vs Ag/AgCl).

2.2.4 Photocatalytic activity measurement

Photocatalytic H_2 evolution test

The photocatalytic H_2 evolution test was carried out in a glass reactor with a closed gas circulation system. The light source was a 300 W Xe lamp. 50 mg photocatalyst was firstly dispersed with a magnetic stirrer in triethanolamine aqueous solution (30 mL of triethanolamine and 220 mL of H_2O) and was loaded with 2 wt% Pt as the co-catalyst via a photodeposition process (under UV-visible light irradiation, $\lambda > 350$ nm). After Pt loading and vacuumizing, H_2 evolution over the photocatalyst was carried out under

visible light irradiation (with an L42 filter, λ > 400 nm). The evolved H_2 was analyzed by online gas chromatography (GC-8A; Shimadzu Corp., Japan) equipped with a thermal conductivity detector.

Photocatalytic CO_2 reduction test

The photocatalytic CO_2 evolution test was carried out in a glass reactor with a closed gas circulation system. 20 mg photocatalyst, 1 μmol $CoCl_2$, and 15 mg 2, 2-bipyridine (bpy) were dispersed with a magnetic stirrer in solution (50 mL acetonitrile, 10mL of H_2O and 2 mL of triethanolamine). Note: the Co ions and 2, 2-bipyridine can spontaneously form a complex $Co(bpy)_3^{2+}$, which is widely used as robust cocatalyst for photocatalytic CO_2 reduction with a high selectivity towards CO.[28, 29] After complete vacuumizing, the reaction system was injected with pure CO_2 (~ 80 kPa). The produced gases were analyzed by a gas chromatography. The light source was a 300 W Xe lamp (with a L42 cutoff filter and water filter, λ > 400 nm). The water filter used here is to remove the IR irradiation.

2.3 Results and discussion

2.3.1 Atomic carbon chains linked polymeric CN

Generally, the key step for the generation of CN is the deamination process between amino groups of the precursors and intermediates.[30] Thus, these amino groups also possess the potential to react with NH_2 group or COOH group by releasing NH_3 and H_2O at some specified conditions, resulting in the formation of C-N bonds. Inspired by this point, the glycine molecules, with terminated COOH and NH_2 groups and short length, are selected as the potential linker to bridge the in-plane defects of layered CN as illustrated in Figure 2.1. The carbon chains linked CN was prepared by a direct thermal polymerization of melamine and glycine precursor and the obtained samples were denoted as CN-xGly (x means the amount of glycine). We use the glycine as a representative molecule to explore the underlying structure and performance of the products derived from melamine and glycine.

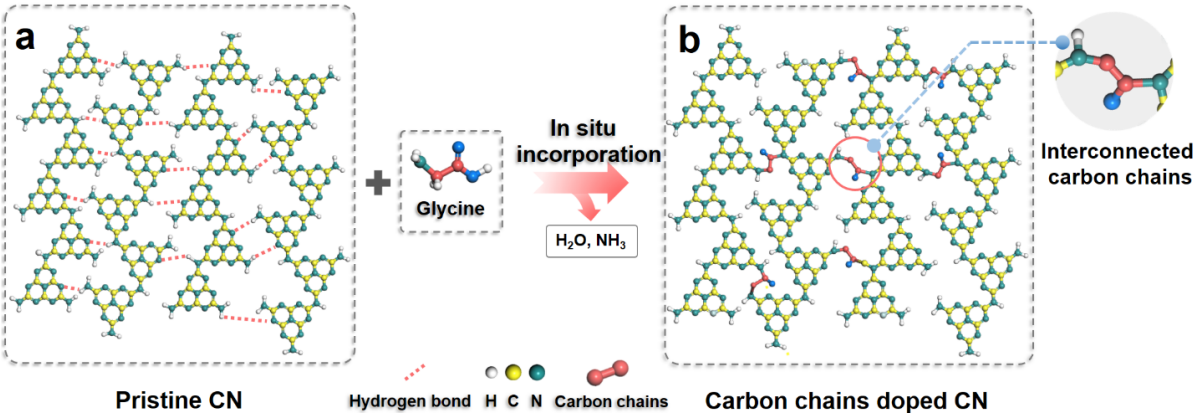


Figure 2.1 Structure of CN before (a) and after (b) doping with carbon chains. In the doping process, the glycine molecules reacted with terminal groups, i.e., NH_2 and NH, in CN, and thus the carbon chains were interconnected with the tri-s-triazine units via C-N bonds.

In situ FT-IR was conducted under Ar atmosphere to visualize the incorporating process of carbon chains, in which the detected signal at 100 °C was used as the background (Figure 2.2a). The direct polymerization of melamine and glycine is quite a complicated process, wherein abundant old bonds break and new bonds form. To avoid the appearance of various FT-IR signals caused by the transformation of rich bonds and study the potential inserting process of small molecules in the framework of CN clearly, we loaded glycine molecules on stable pristine CN and employed this composite as the model for in situ FT-IR observation. The calcination-time dependent infrared spectra (Figure 2.2a) present three distinct change regions. The signals in regions I and II increased gradually between 150 ~ 250 °C, whereas those in region III declined. When further increased the temperature up to 450 °C, all typical signals keep unchanged, indicating that glycine and CN could react entirely at approximately 250 °C and the established structure is steady even at high temperature. Here, we analyze the spectrum at 450 °C in detail to approach the established structure (Figure 2.2b). The decreased absorbance at 3450 cm^{-1} can be ascribed to the consumption of NH_2 group, along with the newly appeared NH (3180 cm^{-1}), C-N (1038 cm^{-1}) species,[31-33] suggesting that the suspended NH_2 groups adjacent to the tri-*s*-triazine units involved in the reaction with glycine and subsequently generated the C-NH motif by releasing NH_3 molecules (marked with gray circle in Figure 2.3a). The new bands at 1119 cm^{-1} (C-N) and 1656 cm^{-1} (C=O) imply the generation of N-C=O species (marked with cyan circle in Figure 2.3a),[4] which stemmed from the dehydration reaction between the (C2)-NH motif of CN and the

terminal COOH groups of glycine molecules. According to the newly formed C-N and N-C=O structural motifs, the structure schemed in Figure 2.3a is proposed. Meanwhile, another similar moiety NH-C=O (marked with red circle in Figure 2.3b), obtained from the dehydration reaction between the NH_2 over CN and the COOH group of glycine molecule, also formed as identified by the bands located at 1338 $cm^{-1}$and 1531 cm^{-1}. Note: NH–C=O species shows quite different bands positions from the similar N–C=O species. This is because, for the NH–C=O structure, also known as amide, there exists a strong coupling interaction between NH bending and the CN stretching vibration, which causes the splitting and results into two largely shifted bands towards large wavenumber compared to the C–N bonds in N–C=O.[34]

For comparison, the different signals (Figure 2.4) of pure CN and the glycine loaded Al_2O_3 from that of glycine loaded CN under same conditions further confirm that the glycine molecule chains indeed inserted into the framework of CN in the demonstrated way (Figure 2.3). For the pure CN (Figure 2.4a), in the regions between 1000 ~1750 cm^{-1}, only slight signals were observed until the temperature up to 450 ^oC, which presents distinct difference from the typical result of the hybrid of glycine and CN. In the case of glycine/Al_2O_3 (Figure 2.4b), typically, the signal of C=O species at 1719 cm^{-1} first increased and then decreased until faded away with the increased temperature, inferring that an interaction first formed between glycine molecules and then followed by decomposition (considering that the signal of glycine/Al_2O_3 at 100 ^oC was adopted as the background, i.e., a flat base line, the structure of glycine could slight change or new interaction formed between glycine molecules upon heating the sample, in this case, the position of C=O could present a shift relative to the original state of glycine molecules, thus the signal of C=O emerged when the temperature increased from 100 ^oC to 300 ^oC). In brief, the analyses above identify that the carbon chains are inserted into the defect of CN and exist as two forms as illustrated in Figure 2.3.

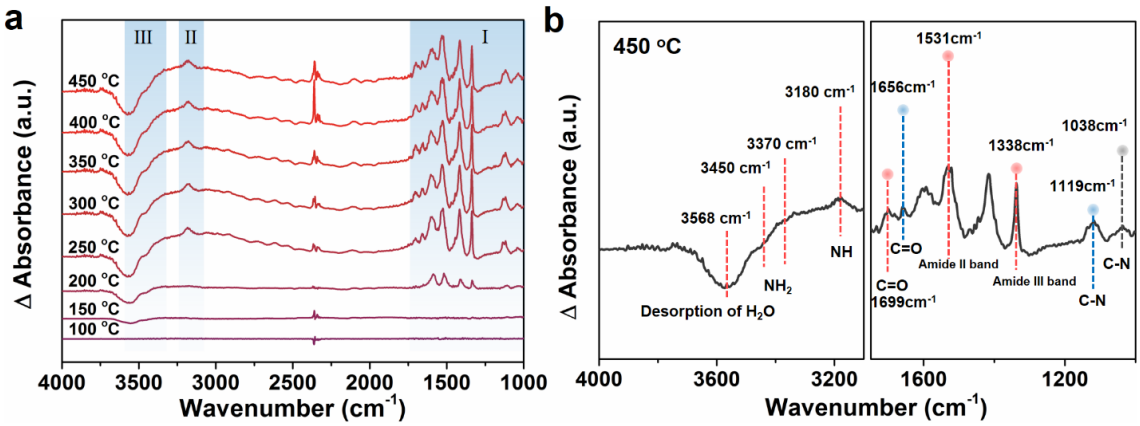


Figure 2.2 (a) In situ FT-IR spectra of glycine loaded CN measured at different temperature. (b) The in situ FT-IR spectrum at 450 °C.

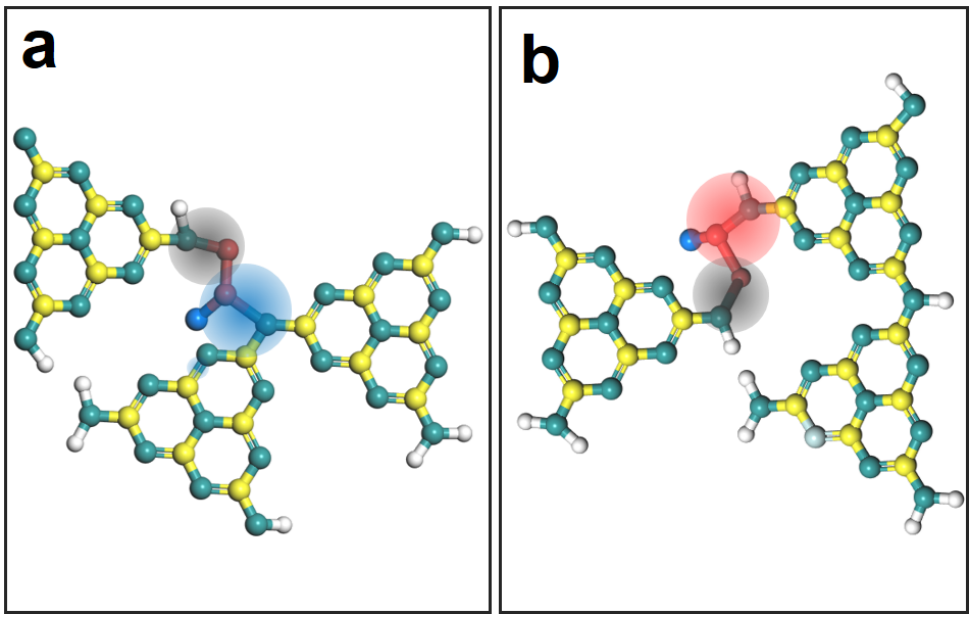


Figure 2.3 The illustration of two possible kinds of structure in the carbon chains doped CN.

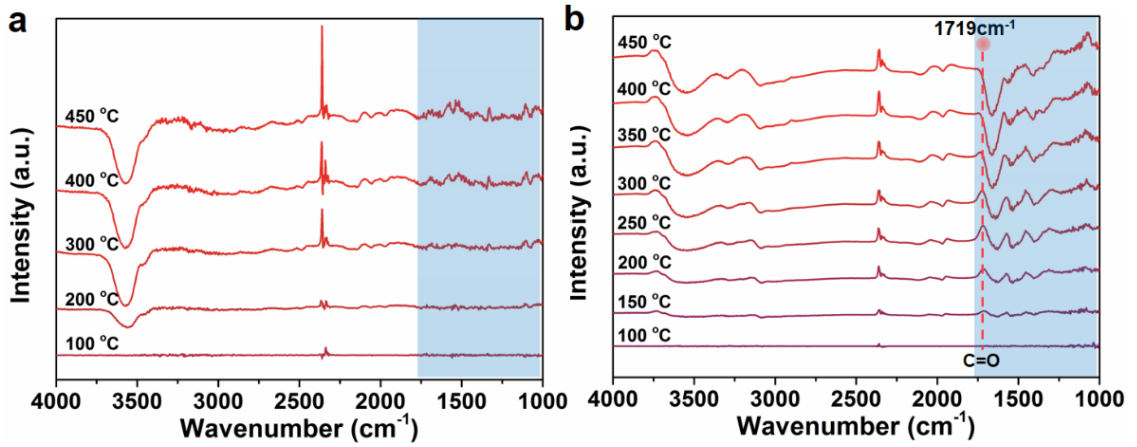


Figure 2.4 In situ FT-IR spectra of (a) pristine CN and (b) Al_2O_3 loaded with glycine measured at different temperature. Al_2O_3 was used as the inert support to avoid the possible reaction between support and glycine.

The chemical structure and local electronic configuration of the CN with and without carbon chains were further examined by the synchrotron-based X-ray absorption spectroscopy (XAS) and X-ray photoelectron spectroscopy (XPS). The carbon K-edge XA spectra (Figure 2.5a) present characteristic resonances of samples including π* transitions in C=C at 284.7 eV, C=N–C at 287.5 eV and σ* transitions in C-C between 290 and 298 eV.[35] The intensity ratio of σ* transition (in C-C) to π* transitions (in C=N–C) of CN-10Gly was higher than that of pristine CN, which could be ascribed to the additional C-C species from the doped carbon chains. (Note: C=N–C is the inherent motif in CN, thus it can be regarded as the reference for the qualitative study of the induced foreign units.) In the nitrogen K-edge region (Figure 2.5b), typical π* resonances at 399.6 and 402.3 eV are observed, corresponding to aromatic nitrogen atoms of heterocyclic rings ($\pi^*_{C=N-C}$) and sp^3 N-C bridging among tri-*s*-triazine moieties, respectively.[35, 36] The 1s → σ^*_{N-C} transition is located in the range of 404 to 412 eV.[36, 37] Taking the intensity of intrinsic $\pi^*_{C=N-C}$ as reference, the CN-10Gly sample delivered higher intensity of σ^*_{N-C} relative to that of CN, suggesting a slightly higher content of C-N bonds in the carbon chains doped CN. It reveals how the carbon chains link with the matrix of CN, i.e., via covalent bonds between C and N as illustrated in Figure 2.3a and 2.3b. The C and N K-edges XA spectra (Figure 2.6a and 2.6b) of CN-10Gly-(two steps) (synthesis details provided in experimental section) show similar results with those of CN-10Gly, identifying the rationality of the adopted model, i.e., glycine molecules loaded unmodified CN, used in situ FT-IR examination.

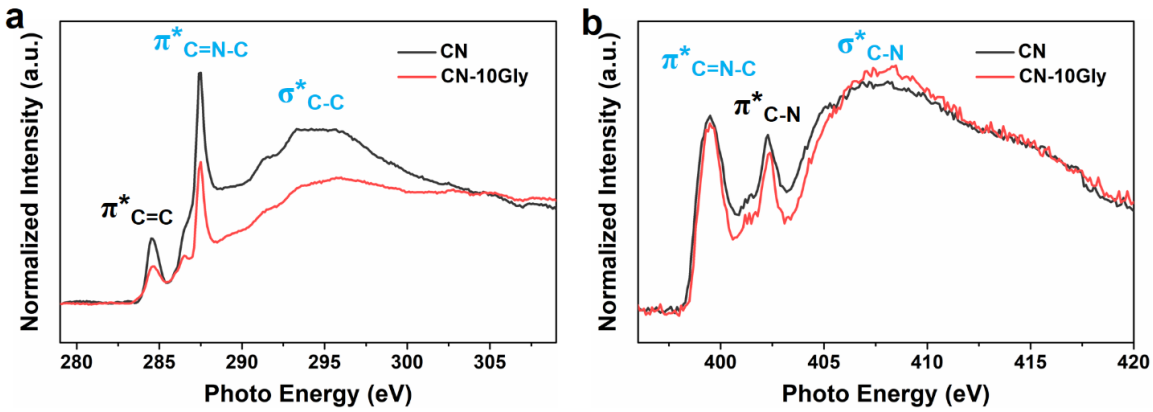


Figure 2.5 Carbon and nitrogen K-edge XA spectra of CN and CN-10Gly, respectively.

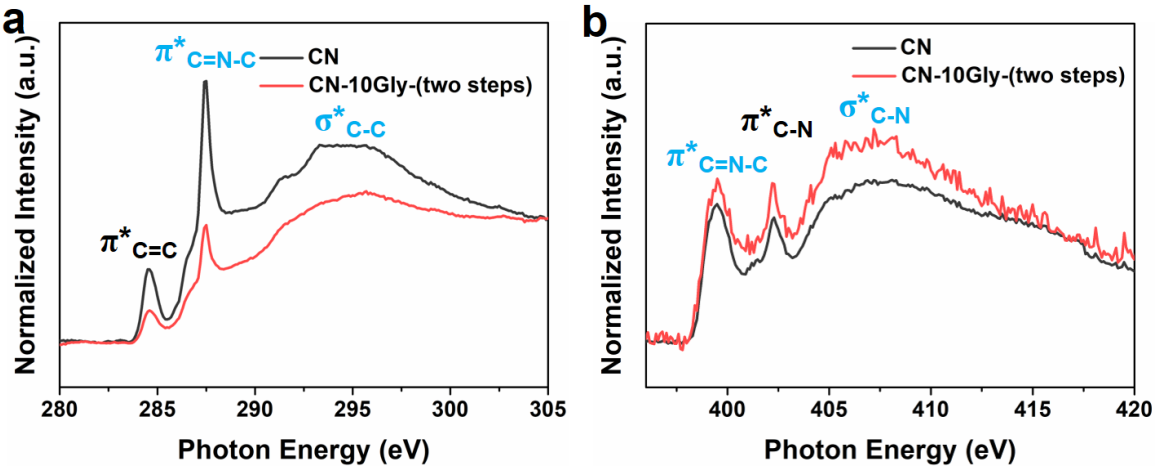


Figure 2.6 Carbon (a) and nitrogen (b) K-edge XA spectra of CN-10Gly-(two steps). Note: the CN-10Gly-(two steps) was prepared via heating the hybrid of pristine CN and glycine rather than melamine and glycine (CN-10Gly) to ascertain the reasonability of CN-/glycine system used in the in situ FT-IR. As proved by the parallel results of CN-10Gly and CN-10Gly-(two steps), the established carbon chains in these two samples should possess similar coordination environment.

The high-resolution C *1s* XPS spectra (Figure 2.7) for pristine CN can be deconvoluted into two components located at 288.25 eV and 284.78 eV, assigned to N-C=N motifs and adventitious hydrocarbons (in the form of C-C or C=C), respectively. It was reported that the glycine loaded on graphene oxide showed a close binding energy at 284.6 eV, corresponding to the C–C/C–H species in glycine.[38] Hence, the peak of designed carbon chains could overlap with the adventitious hydrocarbons due to the similar binding energy. Upon introducing the glycine into the feedstock (CN-10Gly), the percentage of C-C/C=C species to all detected carbon increased from 12.5% to 21.4% (Figure 2.7), clearly suggesting that additional C-C chains contained in the CN-10Gly sample. The slightly

increased atomic percentage of C (48.2%) and O (3.0%) (derived from XPS) in CN-10Gly relative to that of CN (C, 46.5%; O, 1.9%) also discloses the successful incorporation of carbon chains in the CN.

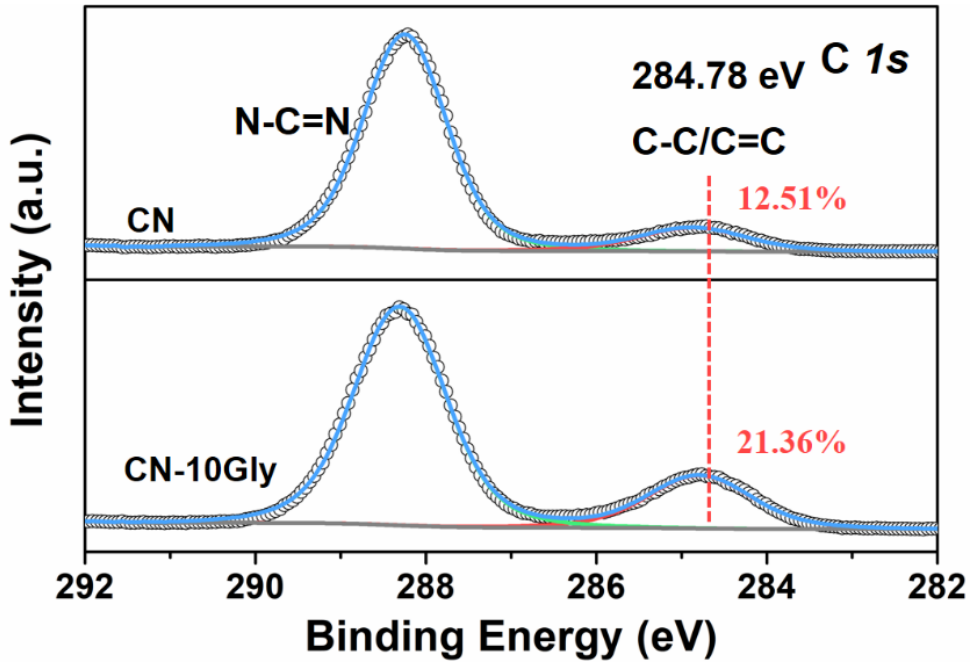


Figure 2.7 The C 1s spectra of CN and CN-10Gly.

The incorporation of carbon chains in CN was further verified by the UV-visible spectra and common-used FT-IR (Figure 2.8 and 2.9). Apart from the reactive groups, i.e., COOH and NH_2, on the molecule chains, the match of dimension between the inserting molecules and defects of CN could be another critical factor that determines the incorporation of carbon chains into layers of CN. It's preliminarily identified that the size of inserted carbon chains is comparable to that of defects of CN according to the XRD analysis (Figure 2.10). The two feature diffraction peaks (Figure 2.10a) located at 27.4° and 13.1° scarcely changed including the peak location, intensity and full width at half-maximum (FWHM), which means that the interlayer distance of the (002) plane and the in-planar repeat tri-*s*-triazine in the crystal kept unchanged before and after carbon chains modification. It can be rationally explained that the size of the doped carbon chains is comparable to that of the in-plane defects with negligible influence on the intrinsic structure of CN (as schemed in Figure 2.10b). Based on the above analyses, the carbon chains were successfully planted in the basal plane of CN and connected the tri-*s*-triazine units through strong C-N bonds.

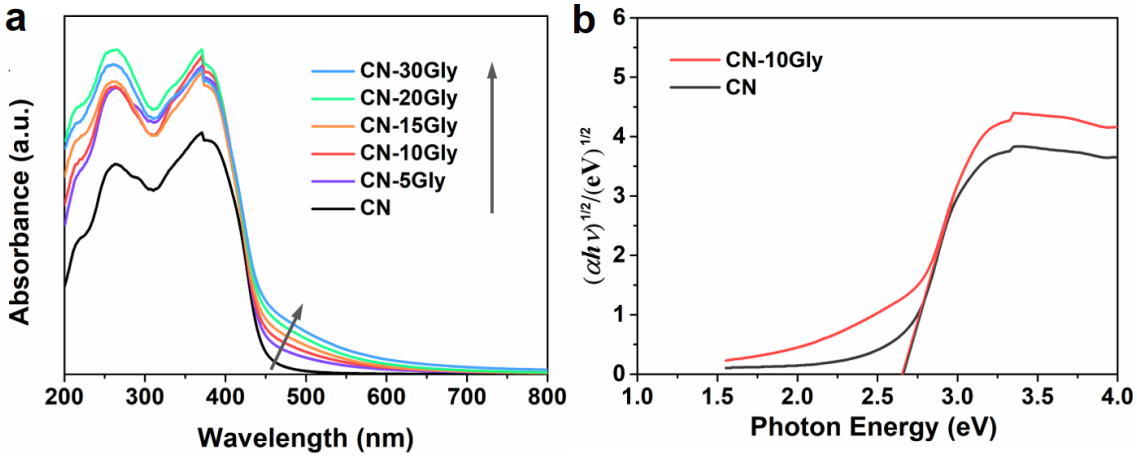


Figure 2.8 Optical properties of the as-synthesized samples. a) UV-visible absorption spectra of samples treated with different amount of glycine. b) the plots of the $(\alpha h\nu)^{1/2}$ versus photon energy ($h\nu$). Interestingly, there are slight absorption tails in the range of 450~700 nm for glycine treated samples, and the intensity of the absorption tail enhanced regularly with the increased addition of glycine, which can be well explained as a consequence of the gradually inserted carbon chains.

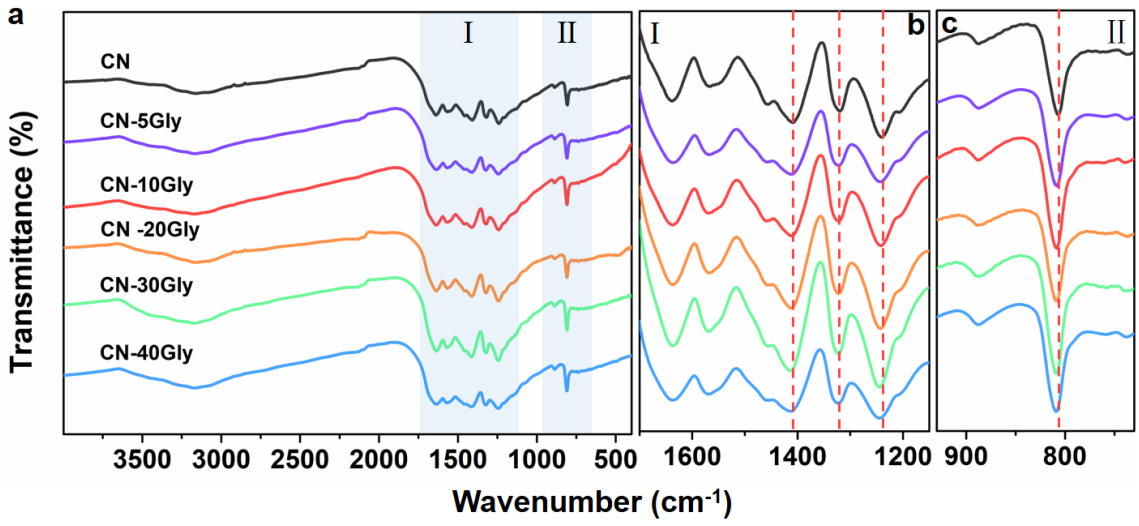


Figure 2.9 (a) FT-IR spectra of the as-prepared samples. (b, c) Two corresponding enlarged regions from (a). The FT-IR bands at 810 cm^{-1}, 1200 ~ 1700 cm^{-1} can be attributed to the triazine units and aromatic CN heterocycles of CN, respectively. Among these peaks, several typical bands marked with red dot line shift slightly but gradually towards the larger wavenumber with the increased addition of glycine. It could be caused by an interaction between the inserted carbon chains and the intrinsic structure of layered CN.

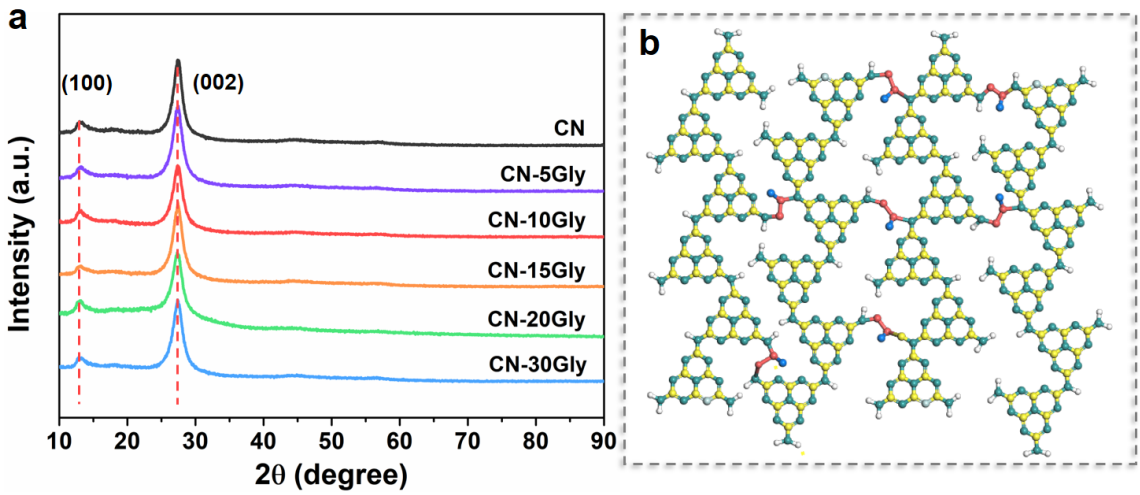


Figure 2.10 (a) XRD patterns of the as-prepared samples. (b) the schematic structure of the carbon chains doped CN.

2.3.2 Carbon chains-mediated photocarriers separation and transport

The modified CN with carbon chains remained comparable morphology and surface area to that of CN (Figure 2.11; CN-10Gly, 6.3 m^2/g, CN, 5.1 m^2/g), further illustrating that the carbon chains were embedded in the framework of CN in manner of molecular distribution as demonstrated above. Besides, the doped carbon chains barely affected the band structure (Figure 2.12), including the band gap (Figure 2.12a), flat-band potential (Figure 2.12b) and valence band (Figure 2.12c).

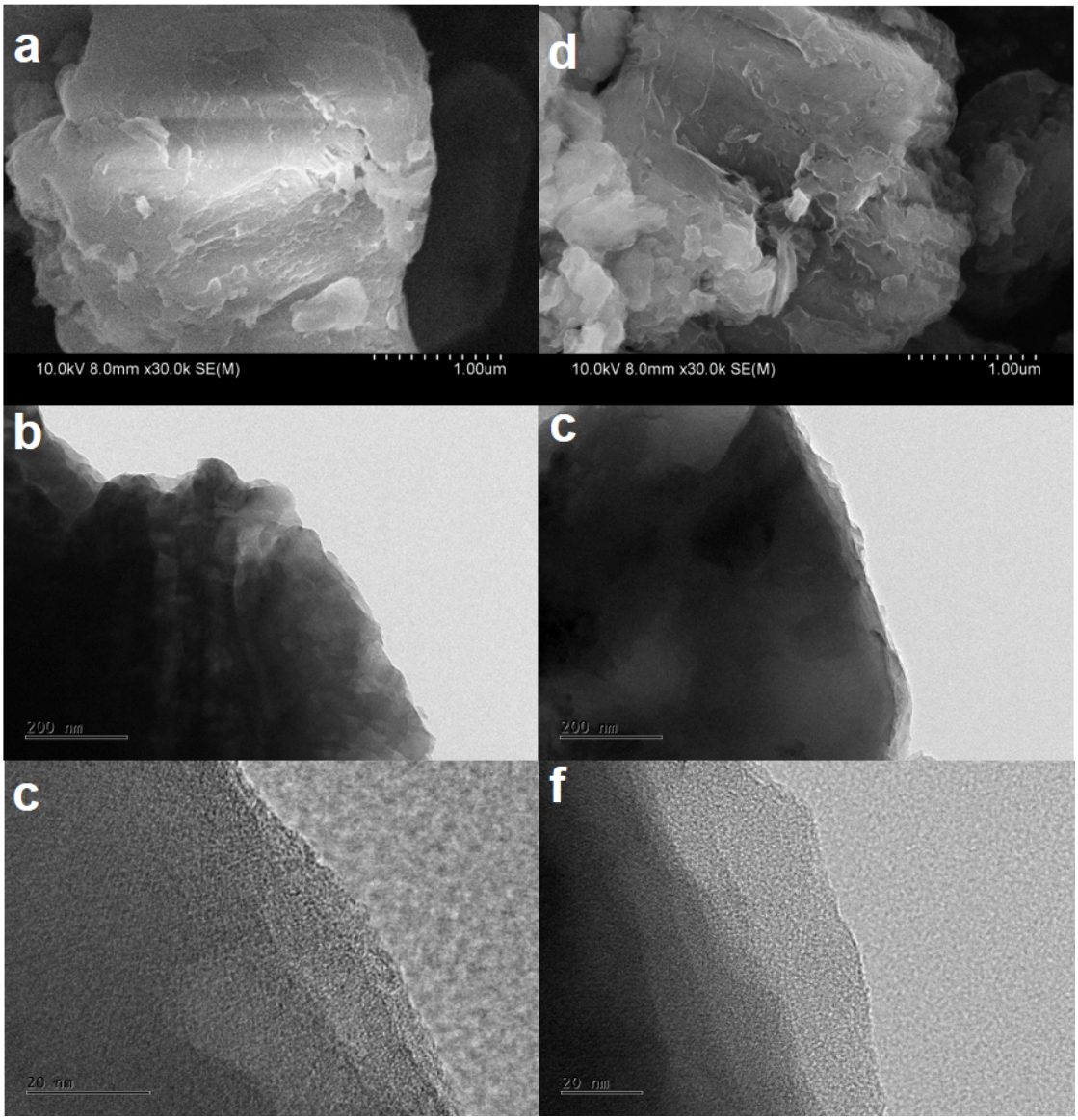


Figure 2.11 The SEM and TEM images of (a, b, c) the pristine CN and (d, e, f) the CN-10Gly.

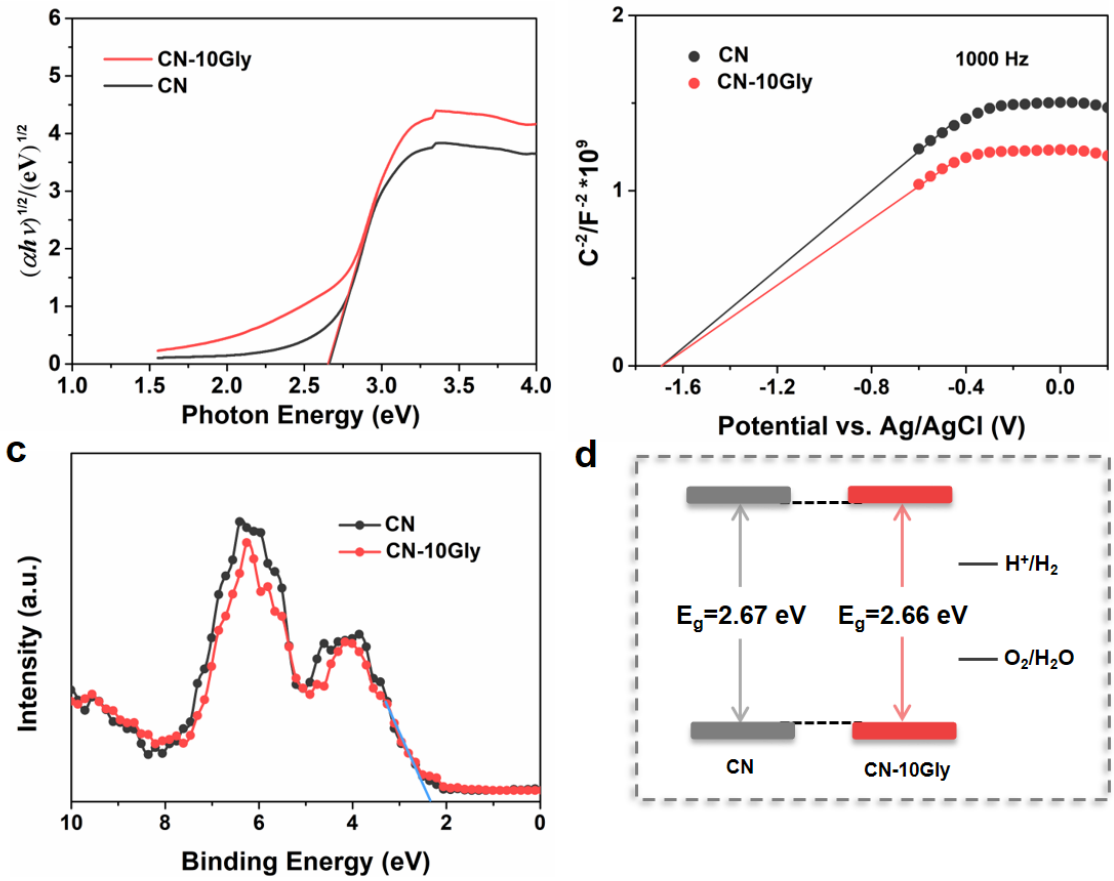


Figure 2.12 Band structure of CN and CN-10Gly. (a) The plots of the $(\alpha h\nu)^{1/2}$ versus photon energy ($h\nu$). (b) Mott-Schottky plots of CN and CN-10Gly. (c) The valence band spectra of X-ray photoelectron spectroscopy of CN and CN-10Gly. (d) Schematic illustration of the determined CB and VB edges of samples.

Usually, carbon materials, such as carbon nanotube, graphene, and even the doped carbon matrix in basal plane of CN, own excellent electrical conductivity. Therefore, we believe that the carbon chains with two C atoms interconnected with the intrinsic structure of CN covalently could enable the electron with faster mobility throughout the layers compared with the original layers full of hydrogen bonds. Hence, we focus on the study related to the kinetics of photocarriers in the CN with and without carbon chains modification. Steady-state/time-resolved photoluminescence (PL) spectroscopy characterizations, as powerful tools to monitor the excitonic processes, i.e., radiative recombination of photogenerated electron-hole pairs in photocatalyst, were carried out for a series of samples. PL intensity represents the combination possibility of light-induced electron-hole pairs.[39] As shown in Figure 2.13a, pristine CN gives a sharp emission peak at 470 nm, but the PL intensity is progressively and substantially

suppressed with the increased incorporation amount of carbon chains. This phenomenon means greatly enhanced separation and transfer of photocarriers, as profited from promotional effect of the carbon chains. In particular, time-resolved PL spectra of the doped samples (Figure 2.13b) detected at the emission wavelength, i.e., 470 nm, show the gradual and apparent decrease in fluorescence lifetime (fitted from the decay spectra, Table 2.1) in comparison with the unmodified CN. The fluorescence decay of the as-prepared samples is entirely in line with their decrease tendency of PL intensities, suggesting faster separation and transfer of electrons and holes in the framework of CN.[6] It signifies that the more photo-generated carriers captured by reactive substrates under reaction conditions, the more efficient photocatalysis reactions realized for carbon chains linked CN.

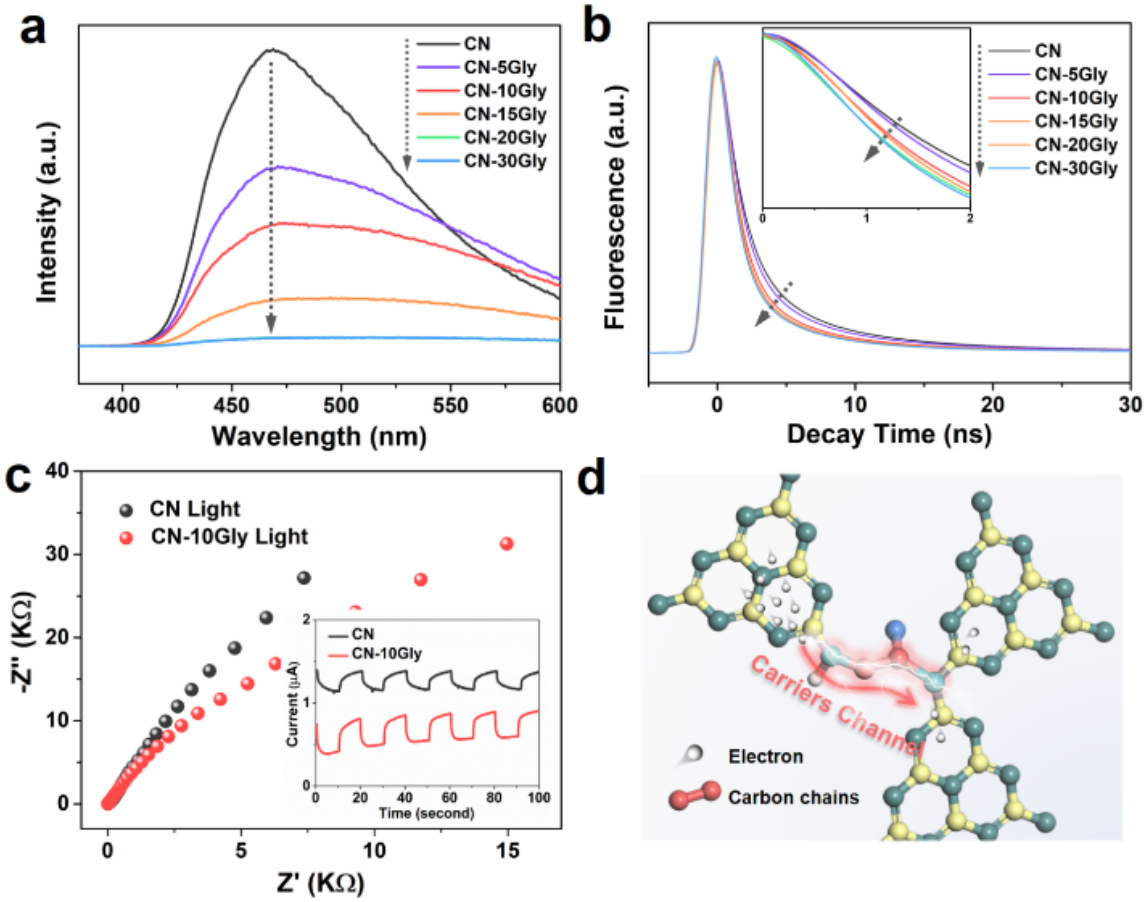


Figure 2.13 Characterization of the photocarriers kinetics of the as-prepared samples. (a, b) Steady-state and time-resolved photoluminescence spectroscopy of the samples, respectively. (c) Electrochemical impedance spectroscopy (EIS) Nyquist plots under irradiation condition. Inset: Periodic on/off photocurrent response under visible-light irradiation. (d) Schematic diagram of carriers channel role of bridged carbon chains.

Table 2.1 Best fitted parameters of time resolved PL spectra (Figure 2.13b).

Samples	τ_1 (ns)-Rel%	τ_2 (ns)-Rel%	τ_3 (ns)-Rel%	Goodness of fit parameter (χ^2)
CN	1.57-81%	6.30-18%	37.44-1%	1.26
CN-5Gly	1.41-82%	5.68-17%	30.14-1%	1.18
CN-10Gly	1.29-86%	5.54-14%	34.26-1%	1.43
CN-15Gly	1.16-85%	4.84-14%	27.55-1%	1.34
CN-20Gly	1.17-85%	4.71-14%	26.30-1%	1.30
CN-30Gly	1.20-88%	5.28-12%	34.51-1%	1.56

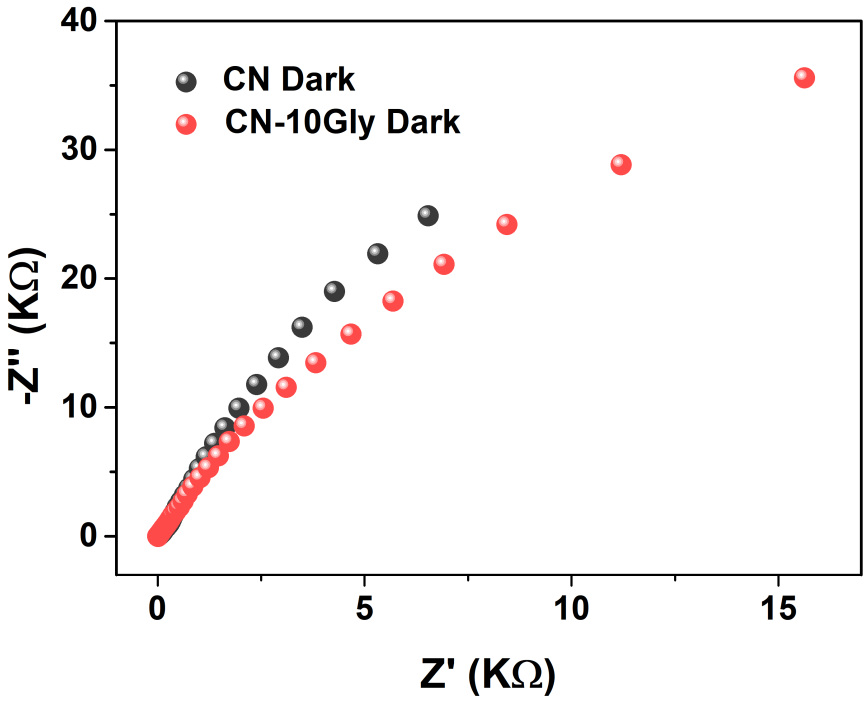


Figure 2.14 Electrochemical impedance spectroscopy (EIS) Nyquist plots under dark condition.

We also used photoelectrochemical characterizations to investigate the carriers separation and transfer behavior of as-prepared samples. Nyquist plot of CN-10Gly under the dark condition presents apparently declined semicircles in comparison with that of the pristine CN (Figure 2.14), indicative of the more favorable inherent electron transport ability. Upon irradiation with visible light, both of them show decreased semicircles and the carbon chains modified sample still exhibits smaller resistance value compared to the

pristine CN (Figure 2.13c). Above results suggest a significantly improved electronic conductivity in the non-photoexcited and photoexcited status. Meanwhile, a marked enhancement of photocurrent (inset of Figure 2.13c) is also observed for CN-10Gly relative to pristine CN, which further illustrates that the mobility of the photo-carriers is promoted remarkably. By combining the results as mentioned earlier, we can reasonably conclude that the embedded carbon chains in the plane of CN can dramatically promote the separation and transfer of photocarriers with framework of CN.

2.3.3 Superior light-driven H_2 evolution and CO_2 reduction

To assess the validity of carbon chains integration strategy over CN on improving photocatalytic efficiency, photocatalytic H_2 evolution was carried out over the as-synthesized samples. All the samples modified with various carbon chains (Figure 2.15a) exhibit substantial improvement in photocatalytic H_2 evolution in contrast to pristine CN. Particularly, CN-10Gly presents the highest H_2 evolution activity, increased by 13.2 times in comparison with that of pristine CN. Our strategy is not only quite simple but also achieves a high activity, i.e., among the top records for the in-plane engineered CN in H_2 evolution (Table 2.2). This modification strategy also dramatically boosts the photocatalytic CO_2 reduction performance because more photoelectrons are available for reactants at the interface between photocatalyst and reaction solution. The optimized sample (CN-10Gly) exhibits a 29.2 times enhancement relative to CN in CO generation (Figure 2.15b). Both the gaseous products for water splitting and CO_2 reduction over the optimized sample increased linearly with the irradiation time (Figure 2.16), suggesting good stability for CN-10Gly. It is further evidenced by the long-term H_2 evolution as shown in Figure 2.15c, only a slight decrease was observed during the 20 hours test. An adverse effect emerged for both H_2 evolution (Figure 2.15a) and CO evolution (Figure 2.15b) when excessive glycine was introduced. Actually, a similar phenomenon has also been revealed in the relevant studies.[40, 41] The negative effect could be ascribed to the fact that introducing too many foreign units may inevitably destruct the conjugated structures of CN.[40, 41] As a result, it could diminish the positive effect of efficient separation of photocarriers, leading to a decline in photocatalytic activity. Interestingly, when maintaining the terminal groups as COOH and NH_2 but increasing the carbon atom number in the doping molecule from two to four, the activity of samples presents a drastic change (Figure 2.17). When the carbon number is three, the H_2 evolution rate, reaching up to ~167 μmol/h, is almost twice that of glycine (carbon number is equal to two)

modified sample (90 μmol/h) and 24.6 folds higher than pristine CN. However, the activity (23 μmol/h) decreases drastically as the carbon number further increased to four. We preliminarily ascribe this phenomenon to the match degree of size between defects and molecules, that is, the dimension of molecules containing two or three carbon atoms is comparable to that of defects; however, the molecules with four carbon atoms are hard to be embedded into the defects of CN. Further studies are still needed to validate this assumption.

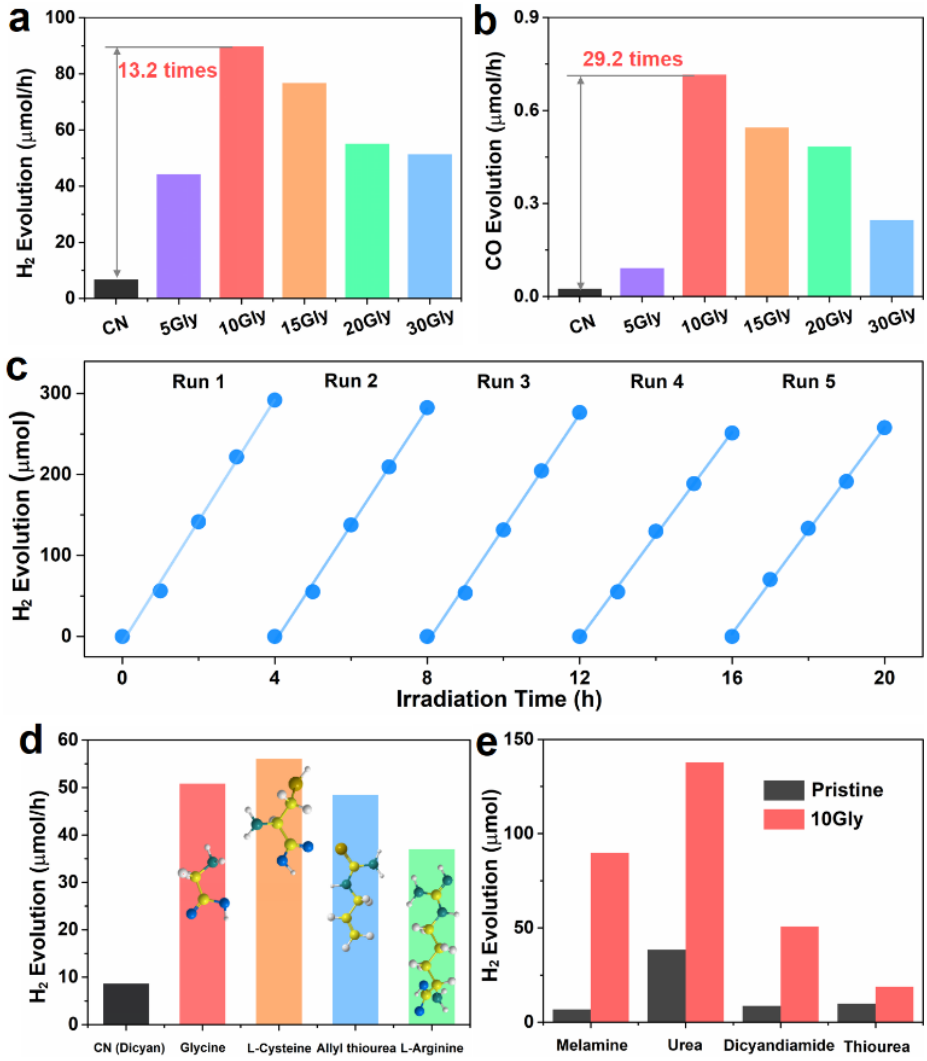


Figure 2.15 Photocatalytic activity evaluation of the as-prepared samples. (a, b) Comparison of the photocatalytic H_2 evolution and CO_2 reduction rate of the samples with different amount of glycine, respectively. (c) Cycle test of H_2 evolution over CN-10Gly. (d) Comparison of the photocatalytic H_2 evolution activity of samples obtained from dicyandiamide and different kinds of small molecules. (e) Comparison of the photocatalytic H_2 evolution activity of samples derived from glycine and different precursors.

Table 2.2 Comparison of H_2 evolution rates of samples using different strategies to modulate the in-plane structure of polymeric CN with or without carbon species.

Samples	H_2 evolution rates of the pristine CN (μmol/h)	H_2 evolution rates of the modified CN (μmol/h)	Enhancement factor	Approach	Notes
CN-10Gly (this study)	**6.8**	**89.8**	**13.2**	**In situ**	**50 mg 300 W Xe lamp (λ > 400 nm)**
CN-10Ala (this study)	**6.8**	**167.3**	**24.6**	**In situ**	**50 mg 300 W Xe lamp (λ > 400 nm)**
Carbon doped carbon nitride[16]	2.8	25.0	8.9	Microwave heating	10 mg 300 W Xe lamp (λ > 420 nm)
CCTs-CQDs implanted CN nanotubes[27]	71.9	176.9	2.5	Two steps 1. Preparing CQDs 2. 550 °C, 3 h	50 mg 300 W Xe lamp (λ > 400 nm)
GD-C_3N_4 -Gradual Doping with C_{gra} rings[26]	10.5	230.6	21.9	Two steps 1. 550 °C, 1 h 2. 500 °C, 1.5h	10 mg 300 W Xe lamp (λ > 420 nm)
CN (580 °C)[12]	0.9	29.9	33.2	Two steps 1. 550 °C, 1 h 2. 580 °C, 2 h	50 mg 300 W Xe lamp (λ > 440 nm)
ONLH-O and N linked g-C_3N_4[42]	0.4	10.2	25.5	Two steps 1. 600, 4h 2. Washing with water, acid and alkali	- 300 W Xe lamp (λ > 420 nm)
C_{ring}-C_3N_4-C_{ring} doped g-C_3N_4[25]	0.4	4.5	11.2	Two steps 1. multi-step heat treatment 2. Washing with acid at 80 °C	30 mg 300 W Xe lamp (λ > 420 nm) (Overall H_2O splitting)

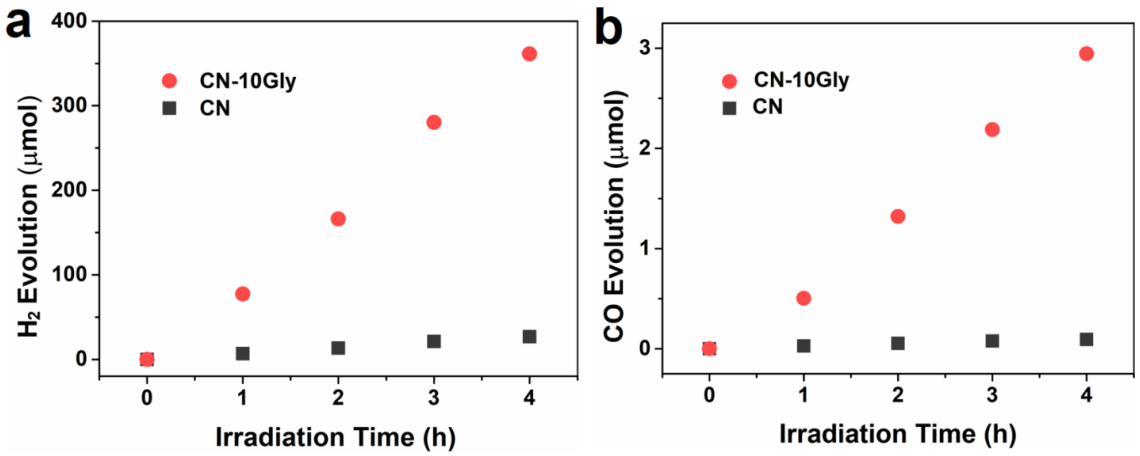


Figure 2.16 Photoactivity comparison of typical (a) H_2 generation and (b) CO evolution over CN and CN-10Gly.

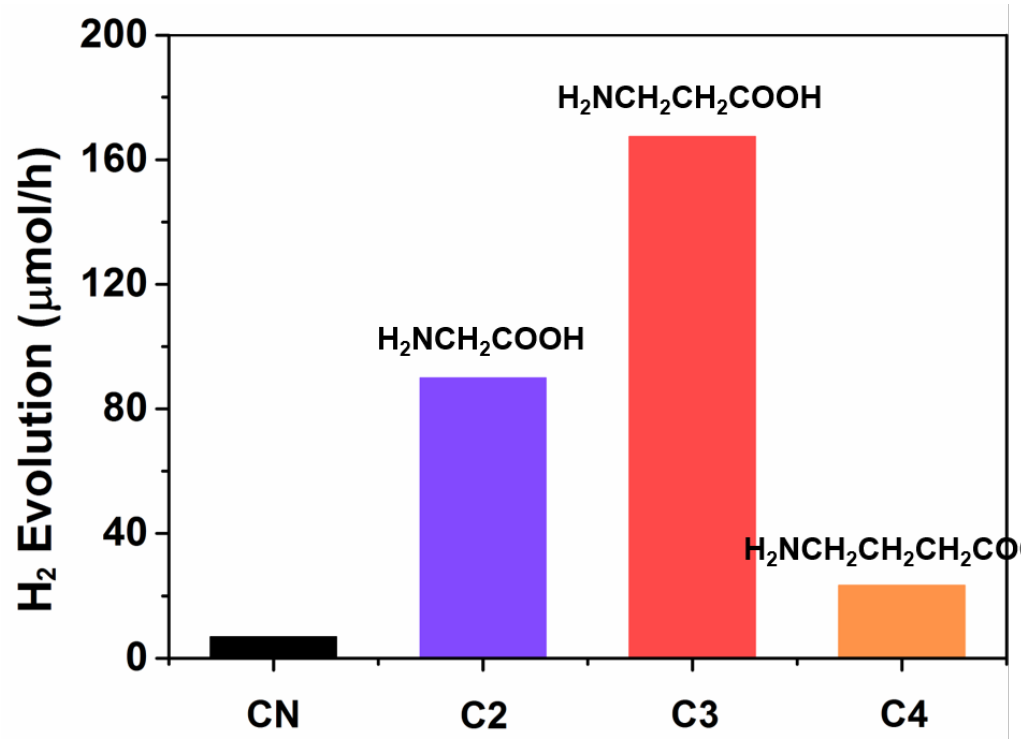


Figure 2.17 Comparison of H_2 evolution rates of CN doped with same mole amount of amino acid with different carbon numbers on the molecule chains.

To further demonstrate the universality of this strategy, various precursors and molecule linkers (Figure 2.18) have been adopted. All the as-prepared samples (Figure 2.15d and 2.15e) exhibited significant enhancement in H_2 evolution. (Note: these molecule chains linkers, i.e., L-cysteine, Allyl thiourea and L-Arginine, possess groups

on adjacent C atoms, including NH, NH_2 and COOH groups, which are apt to react with the residual NH_2 or NH groups in CN.)

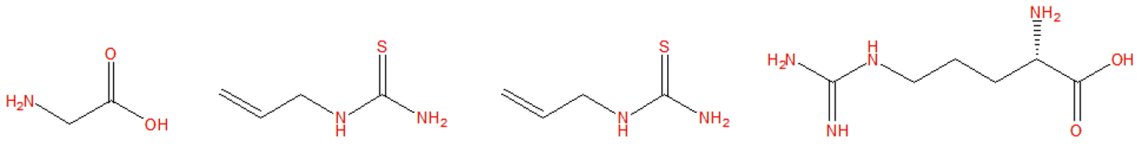


Figure 2.18 The schematic molecular structure of Glycine, L-cysteine, allyl thiourea and L-Arginine.

2.4 Conclusions

In conclusion, our study demonstrates a facile and efficient strategy to incorporate short carbon chains into the basal plane of CN while remaining the pristine tri-*s*-triazine structure. The carbon chains filled the defects in CN via covalent bonds, which mediates the electron transfer in a relatively smooth transport channel compared to the initial hydrogen bonds. By virtue of such a favorable transport channel of carriers, the carbon chains linked CN exhibits a dramatically improved photocatalytic water splitting and CO_2 reduction performance, achieving a 13.2- and 29.2-times enhancement, respectively, compared to pristine CN. This study highlights that the engineering of the defects in photocatalysts is one of the most effective approaches for improving solar energy conversion and also gives a research direction for the future rational design towards efficient photocatalysts, especially for organic-based ones.

References

[1] S. N. Habisreutinger, L. Schmidt-Mende, J. K. Stolarczyk, *Angew. Chem. Int. Ed. Engl.,* 2013, **52**, 7372-7408.

[2] X. Wang, K. Maeda, A. Thomas, K. Takanabe, G. Xin, J. M. Carlsson, K. Domen, M. Antonietti, *Nat. Mater.,* 2009, **8**, 76-80.

[3] G. Zhang, G. Li, T. Heil, S. Zafeiratos, A. Savateev, X. Wang, M. Antonietti, *Angew Chem Int Ed* 2019, **58**, 3433-3437.

[4] G. Zhao, H. Pang, G. Liu, P. Li, H. Liu, H. Zhang, L. Shi, J. Ye, *Appl. Catal., B,* 2017, **200**, 141-149.

[5] P. Yang, H. Zhuzhang, R. Wang, W. Lin, X. Wang, *Angew. Chem., Int. Ed. Engl.,* 2019, **58**, 1134-1137.

[6] Y. Li, S. Ouyang, H. Xu, X. Wang, Y. Bi, Y. Zhang, J. Ye, *J. Am. Chem. Soc.,* 2016, **138**, 13289-13297.

[7] N. Tian, K. Xiao, Y. Zhang, X. Lu, L. Ye, P. Gao, T. Ma, H. Huang, *Appl. Catal., B,* 2019, **253**, 196-205.

[8] J. Cai, J. Huang, S. Wang, J. Iocozzia, Z. Sun, J. Sun, Y. Yang, Y. Lai, Z. Lin, *Adv. Mater.,* 2019, **31**, e1806314.

[9] G. Liao, Y. Gong, L. Zhang, H. Gao, G.-J. Yang, B. Fang, *Energy Environ. Sci.,* 2019, **12**, 2080-2147.

[10] W. Cui, J. Li, Y. Sun, H. Wang, G. Jiang, S. C. Lee, F. Dong, *Appl. Catal., B,* 2018, **237**, 938-946.

[11] J. Cheng, Z. Hu, K. Lv, X. Wu, Q. Li, Y. Li, X. Li, J. Sun, *Appl. Catal., B,* 2018, **232**, 330-339.

[12] Y. Kang, Y. Yang, L. C. Yin, X. Kang, L. Wang, G. Liu, H. M. Cheng, *Adv. Mater.,* 2016, **28**, 6471-6477.

[13] B. V. Lotsch, M. Döblinger, J. Sehnert, L. Seyfarth, J. Senker, O. Oeckler, W. Schnick, *Chem. – Eur. J.,* 2007, **13**, 4969-4980.

[14] L. Lin, H. Ou, Y. Zhang, X. Wang, *ACS Catal.,* 2016, **6**, 3921-3931.

[15] J. Ji, J. Wen, Y. Shen, Y. Lv, Y. Chen, S. Liu, H. Ma, Y. Zhang, *J. Am. Chem. Soc.,* 2017, **139**, 11698-11701.

[16] J. Li, D. Wu, J. Iocozzia, H. Du, X. Liu, Y. Yuan, W. Zhou, Z. Li, Z. Xue, Z. Lin, *Angew. Chem.,* 2019, **58**, 1985–1989.

[17] Z. Teng, N. Yang, H. Lv, S. Wang, M. Hu, C. Wang, D. Wang, G. Wang, *Chem,* 2019, **5**, 664-680.

[18] H. Yu, L. Shang, T. Bian, R. Shi, G. I. Waterhouse, Y. Zhao, C. Zhou, L. Z. Wu, C. H. Tung, T. Zhang, *Adv. Mater.,* 2016, **28**, 5080-5086.

[19] Z. Chen, E. Vorobyeva, S. Mitchell, E. Fako, M. A. Ortuño, N. López, S. M. Collins, P. A. Midgley, S. Richard, G. Vilé, J. Pérez-Ramírez, *Nat. Nanotechnol.,* 2018, **13**, 702-707.

[20] P. Yang, L. Wang, H. Zhuzhang, R. Wang, M.-M. Titirici, X. Wang, *Appl. Catal., B,* 2019, **256**, 117794.

[21] Y. Li, H. Xu, S. Ouyang, D. Lu, X. Wang, D. Wang, J. Ye, *J. Mater. Chem. A,* 2016, **4**, 2943-2950.

[22] Y. Zheng, J. Liu, J. Liang, M. Jaroniec, S. Z. Qiao, *Energy Environ. Sci.,* 2012, **5**, 6717-6731.

[23] P. Qiu, C. Xu, N. Zhou, H. Chen, F. Jiang, *Appl. Catal., B,* 2018, **221**, 27-35.

[24] J. Cheng, Z. Hu, Q. Li, X. Li, S. Fang, X. Wu, M. Li, Y. Ding, B. Liu, C. Yang, L. Wen, Y. Liu, K. Lv, *Appl. Catal., B,* 2019, **245**, 197-206.

[25] W. Che, W. Cheng, T. Yao, F. Tang, W. Liu, H. Su, Y. Huang, Q. Liu, J. Liu, F. Hu, Z. Pan, Z. Sun, S. Wei, *J. Am. Chem. Soc.,* 2017, **139**, 3021-3026.

[26] Y. Yu, W. Yan, X. Wang, P. Li, W. Gao, H. Zou, S. Wu, K. Ding, *Adv. Mater.,* 2018, **30**, 1705060.

[27] Y. Wang, X. Liu, J. Liu, B. Han, X. Hu, F. Yang, Z. Xu, Y. Li, S. Jia, Z. Li, Y. Zhao, *Angew. Chem. Int. Ed.,* 2018, **57**, 5765-5771.

[28] Y. Zheng, L. Lin, X. Ye, F. Guo, X. Wang, *Angew. Chem. Int. Ed. Engl.,* 2014, **53**, 11926-11930.

[29] S. Wang, B. Y. Guan, X. W. D. Lou, *J. Am. Chem. Soc.,* 2018, **140**, 5037-5040.

[30] A. Thomas, A. Fischer, F. Goettmann, M. Antonietti, J.-O. Müller, R. Schlögl, J. M. Carlsson, *J. Mater. Chem.,* 2008, **18**, 4893-4908.

[31] G. Zhao, Y. Sun, W. Zhou, X. Wang, K. Chang, G. Liu, H. Liu, T. Kako, J. Ye, *Adv. Mater.,* 2017, **29**, 1703258.

[32] H. Yu, R. Shi, Y. Zhao, T. Bian, Y. Zhao, C. Zhou, G. I. N. Waterhouse, L. Z. Wu, C. H. Tung, T. Zhang, *Adv. Mater.,* 2017, **29**, 1605148-1605154.

[33] P. Niu, L. Zhang, G. Liu, H.-M. Cheng, *Adv. Funct. Mater.,* 2012, **22**, 4763-4770.

[34] J. Kong, S. Yu, *Acta Biochim Biophys Sin (Shanghai),* 2007, **39**, 549-559.

[35] Y. Zheng, Y. Jiao, Y. Zhu, L. H. Li, Y. Han, Y. Chen, A. Du, M. Jaroniec, S. Z. Qiao, *Nat. Commun.,* 2014, **5**, 3783.

[36] N. Meng, J. Ren, Y. Liu, Y. Huang, T. Petit, B. Zhang, *Energy Environ. Sci.,* 2018, **11**, 566-571.

[37] H. B. Yang, J. Miao, S. F. Hung, J. Chen, H. B. Tao, X. Wang, L. Zhang, R. Chen, J. Gao, H. M. Chen, L. Dai, B. Liu, *Sci. Adv.,* 2016, **2**, e1501122.

[38] K. Pytlakowska, V. Kozik, M. Matussek, M. Pilch, B. Hachuła, K. Kocot, *RSC Adv.,* 2016, **6**, 42836-42844.

[39] D. Zheng, X. N. Cao, X. Wang, *Angew. Chem. Int. Ed.,* 2016, **55**, 11512-11516.

[40] J. Zhang, G. Zhang, X. Chen, S. Lin, L. Mohlmann, G. Dolega, G. Lipner, M. Antonietti, S. Blechert, X. Wang, *Angew. Chem. Int. Ed.,* 2012, **51**, 3183-3187.

[41] J. Qin, S. Wang, H. Ren, Y. Hou, X. Wang, *Appl. Catal., B,* 2015, **179**, 1-8.

[42] Y. Wang, M. K. Bayazit, S. J. A. Moniz, Q. Ruan, C. C. Lau, N. Martsinovich, J. Tang, *Energy Environ. Sci.,* 2017, **10**, 1643-1651.

Chapter 3 Targeted exfoliation and reassembly of polymeric carbon nitride for efficient photocatalysis

3.1 Introduction

Rational design of efficient photocatalytic system is highly promising and attractive for realizing environment remediation and counteracting energy shortage via solar energy.[1, 2] The development of efficient, durable, and sustainable photocatalysts is always the core mission of photocatalysis research. Metal-free, layered polymeric carbon nitride (CN) and its modified samples have attracted intensive attention due to its high stability, unusual electronic structure properties, and wide application in various fields.[3-7] However, up to now, such a promising material can only exhibit considerable performance in a single photocatalytic reaction, either H_2 generation,[8-10] or pollutant degradation,[11] or CO_2 reduction.[12] Maximizing its potential in different photoredox reactions via alternating the properties facilely is highly desired for achieving superior reactivity but still presents an impassable challenge. The polymeric feature and tunable chemical composition of CN endow the material with high adjustability and compatibility.[13-16] For example, various groups such as hydroxyl (−OH) and cyano (−C≡N), and some carbon-rich species can be facilely embedded into the layered matrix of CN.[8, 11, 17, 18] These functional groups and species could provide us possibility to further delicately tailor the structure and properties of CN.

Generally, the optimal efficiency of different photocatalytic reactions requires a distinct balance among diverse parameters, such as light absorption, exposed active sites and kinetics of photocarriers. Targeted and reversible regulation of these parameters to achieve outstanding activity in different photocatalytic reactions will promote solar energy conversion and storage but has not yet been reported. For CN, featuring layered structure, reversible, efficient and controllable exfoliation-reassembly may enable the targeted switch of these properties over CN, and thus make full use of these features in different photoredox reactions. Such an exfoliation-reassembly process strongly depend on the separate establishment of a facile, green, efficient exfoliation and reassembly processes, both of which still encounter great difficulties, especially for exfoliation part.[19, 20]

Previous exfoliation strategies for fabricating ultrathin CN nanosheets are generally classified into two categories: 1) the universal methods available for various layered materials such as the liquid exfoliation in solvents;[21-23] 2) the exfoliation approaches intentionally established based on its unique properties of chemical composition and structure.[24-28] However, these methods still suffer from several drawbacks, such as high energy consumption, low exfoliation yield and moderate photocatalytic performance. Liquid exfoliation is a universal route used to prepare ultrathin 2D nanosheets of various layered materials including CN.[29-31] However, the mismatch of size between solvent molecules and layer distance of CN severely limit the exfoliation efficiency. Alternatively, we assume that if H_2O molecules can be in situ generated between layers, a highly efficient exfoliation can be achieved via effectively overcoming strong van der Waals attraction between adjacent CN layers. For reassembly process, the critical point is reconstructing the interaction force between exfoliated nanosheets to drive the stack behavior.

In this work, we develop a reversible exfoliation-reassembly functionalized polymeric CN. The OH groups are implanted between the layers of CN in advance, then the introduced small-sized protons enter into the layer spacing and neutralize the OH to produce H_2O; the expansion effect achieves a green, high yield and controllable exfoliation. Subsequently, these exfoliated nanosheets can approximately reassemble into their original state mainly by rebuilding surface OH. Moreover, the exfoliation-reassembly effect of CN, accompanied by switchable properties, can be applied to different photocatalytic reactions to achieve superior photocatalytic activity, giving a high AQY of 27% and 46 % for iso-propanol (IPA) degradation and H_2 evolution, respectively, at ~420 nm.

3.2 Experimental section

3.2.1 Material preparation

Preparation of CNK-OH: The pristine polymeric carbon nitride (CN) and K doped/shallow surface alkalized sample (CNK-OH) was fabricated using method as our previous report.[11] To synthesize CNK-OH, typically, melamine (1.5 g; ≥99.0%), KCl (7.5 g, ≥ 99.5%) and NaOH (0.125g; ≥ 98.0%) were mixed fully by grinding. Then the homogeneous mixture was placed in crucible and heated up to 550 °C for 4 h at a rate of 2.3 °C min^{-1}. After calcination treatment, the powders were washed fully with distilled

water until the supernatant was close to neutralization. Then, the resulting powders were dried at 80 °C overnight. The CN was obtained directly by heating the melamine with the same calcination procedure as mentioned above.

Reversible and robust process for few-layer polymeric carbon nitride

Bulk CNK-OH to few-layer polymeric CN procedure: Few-layer polymeric CN was obtained via a low concentration acid treatment over the bulk CNK-OH. Typically, 100 mg CNK-OH was dispersed into 20 mL distilled water with stirring, then different amount H_2SO_4 (the proton concentrations varied from 6.25 mM to 50 mM, the corresponding initial pH value varies from 2.1 to 1.3) was added into the above solution, followed by sonication for about 30 mins to ensure the complete reaction between shallow surface hydroxyl and proton. The sample treated with 0.05 M proton (H_2SO_4) solution was denoted as CNK-OH/Acid. Actually, the suspension turned into white color when sonication continued for about 10 mins and even can achieved via stirring for about 10 mins. The resulting suspensions were first washed several times by centrifugation at 20000 rpm for 5 mins until the supernatant was close to neutralization. To obtain the ultrathin sheet of polymeric CN, the obtained solid was re-dispersed in centrifuge tube containing around 40 mL distilled water, the ultrathin nanosheets of polymeric CN was collected by another centrifugation at the 4000 rpm for 10 mins. Note: the typical AFM images were acquired by taking the sample in the middle of dispersion after this round centrifugation (4000 rpm). Finally, the obtained supernatant was collected by another centrifugation at 20000 rpm for 10 mins, then dried at 80 ^{o}C. The dried nanosheets product was weighed to calculate the percentage yield using following equation:

Percentage yield = weight of nanosheets/the original weight of CNK-OH * 100% (1)

Few-layer polymeric CN return back to bulk CNK-OH process: Recovered bulk CNK-OH was prepared by directly adding alkali solution into the suspension of above obtained few-layer polymeric CN. In a typical synthesis, ~0.55 mL 2M NaOH solution was added into the fresh solution of few layer polymeric CN. The color of the suspension turned into bright yellow (close to the color of the suspension of CNK-OH, means that the few-layer polymeric CN may self-assembled into CNK-OH) from white quickly. The sample stirred for about 30 mins, washed via centrifugation for several times until the supernatant was close to neutralization and then the bright yellow solid was dried at 80 ^{o}C.

Reversible conversion between bulk CNK-OH (bright yellow) and few-layer polymeric CN (white): Reversible conversion was conducted by circular adding of acid

and alkali into the dispersion of CNK-OH. For the first round of exfoliation and assembling, 100 mg CNK-OH was first dispersed into 20 mL distilled H_2O, then acid solution was injected into it (pH ~1.3), the bulk CNK-OH was exfoliated into few-layer polymeric CN via in situ generated interlayered H_2O molecular. For the inverse process, ~0.55 mL alkaline solution (2M NaOH) was directly added into the fresh acid treated dispersion, the white solution turn into bright yellow, suggests that the few-layer polymeric CN reassembled into bulk morphology via the hydrogen bonding and K ions bridging effect between layers (please see the discussions in the text part).

For comparison, ultrathin polymeric CN nanosheets obtained via other reported methods are prepared as follows.

Liquid exfoliation approach[32]: 200 mg bulk polymeric CN was added into 100 mL distilled water, then the sealed beaker was sonicated for 10 h, and then the solution was centrifuged at 3000 rpm for 10 min to remove the aggregate, giving rise to a homogenous dispersion of ultrathin polymeric CN nanosheets. Then the supernatant was dried at 80 ^oC. Finally, the light yellow ultrathin polymeric CN nanosheets (denoted as nanosheets 1) was obtained.

Gas template approach[27]: Dicyandiamide (1.5 g) and 7.5 g ammonium chloride were first dissolved in distilled H_2O, and then evaporated at 80 ^oC, the obtained mixture was then fully grinded. Finally, the mixed solid was heated at 570 ^oC for 4 h. To remove the bulk polymeric CN, we further exfoliated it with sonication for 10 h. the ultrathin polymeric CN nanosheets (denoted as nanosheets 2) was collected as show in "**Liquid exfoliation approach**" part.

3.2.2 Material characterization

XRD patterns of the as-prepared samples were collected with a powder X-ray diffractometer (Cu Kα radiation source, D8 Advanced, Bruker, Germany). UV−visible (UV−vis) diffuse reflectance spectra of the samples were recorded on an UV−visible spectrophotometer (UV-2700, Shimadzu, Japan) equipped with an integrating sphere, then converted into absorption spectra by Kubelka−Munk transformation. The morphologies of samples were characterized with Field Emission Scanning Electron Microscope (S4800, HITACHI, Japan) and Transmission Electron Microscope (TEM) (Tecnai G2 F20, FEI, Holland). AFM images were taken on an Agilent AFM5500 in the tapping mode. Specific surface areas were measured by nitrogen physisorption

(Autosorb-iQ2, Quantachrome, America), and were calculated via the Brunauer−Emmett−Teller (BET) method. Infrared transmission spectra were used to detect hydroxyl group on the surface of samples; the spectra were collected using a Fourier Transform infrared (FTIR) spectrophotometer (Nicolet 6700, Thermo SCIENTIFIC, America). The Photoluminescence (PL) properties were investigated using a fluorescence spectrophotometer (Fluorolog-3, HORIBA Scientific, America). X-ray photoelectron spectroscopy (XPS) measurements were carried out on XPS instrument (Escalab 250, Thermo SCIENTIFIC, America). All binding energies were referenced to the C 1s peaks of the surface adventitious carbon at 284.8 eV. Solid-state NMR spectra of powder samples were collected under ambient conditions on a NMR spectrometer (Infinity plus 300, Varian, America).

3.2.3 Photocatalytic activity measurement

Photocatalytic H_2 evolution: The photocatalytic H_2 evolution test was carried out in a glass reactor with a closed gas circulation system. The light source was a 300 W Xe lamp. 50 mg photocatalyst was firstly dispersed with a magnetic stirrer in triethanolamine aqueous solution (30 mL of triethanolamine and 240 mL of H_2O) and was loaded with 2 wt% Pt as the co-catalyst via a photodeposition process (under UV-visible light irradiation). After Pt loading and vacuuming, H_2 evolution over the photocatalyst was carried out under a 300 W Xe lamp equipped with an AM 1.5 filter. The evolved H_2 was analyzed by online gas chromatography (GC-2014C; Shimadzu Corp., Japan) equipped with a thermal conductivity detector.

Photocatalytic degradation of isopropanol (IPA): IPA photooxidation includes two degradation routes, i.e., a single-photon pathway to yield acetone and multiphoton pathway to generate the complete oxidation product, CO_2; therefore, the IPA photooxidation is used as a model reaction for photodegradation of volatile organic compounds. A 300 W Xe arc lamp (21 A imported current; focus through a 45 × 45 mm shutter window) equipped with an AM 1.5 filter was employed as the light source. A 50 mg of as-prepared catalyst was spread evenly on a plate (area, 7.1 cm^2). Then the vessel was pretreated by artificial air [$V(O_2)$: $V(N_2)$ = 1:4] for 5 min to remove the gaseous impurities. The IPA (ca. 1000 μmol) was injected into the vessel. Then the vessel was kept in the dark until ensuring an adsorption−desorption equilibrium of IPA on the sample before irradiation. A gas chromatograph (GC-2014, Shimadzu Corp., Japan) equipped

with methanizer and FID detector was used to detect the concentrations of IPA, acetone and CO_2.

Apparent quantum yield (AQY) calculation: The apparent quantum efficiency (AQY) was measured under similar conditions as described above except for the light intensity and the wavelength regions of the irradiation light. A glass filters consisting of band-pass (λ = 420 nm) and cutoff filters (λ > 400 nm) were adopted to control the wavelength regions of incident light. The irradiation lasted for 60 min in degradation of IPA and 4 h for H_2 evolution. The average intensity of irradiation was determined by using a spectroradiometer (AvaSolar-1, Avantes, America). AQY was calculated using following equation.

AQY for IPA degradation = [N(CO_2) * 6 + N(acetone)] / N(photons) * 100% (2)

AQY for H_2 evolution = N(H_2) * 2 / N(photons) * 100% (3)

Note: The activity with error bar were constructed using the standard deviation to the average of two repeated experiments.

3.3 Results and discussion

The reversible exfoliation-reassembly transformation over modified CN is shown in Figure 3.1. The transformation consists of two separate parts: an exfoliation status caused by in situ-generated H_2O molecules confined in interlayer and a self-assembly state aroused by the hydrogen bond interactions and K (Na)-ion bridging function. The presence of plentiful OH groups in the shallow surface region is fundamental for the switch of exfoliation-reassembly status.

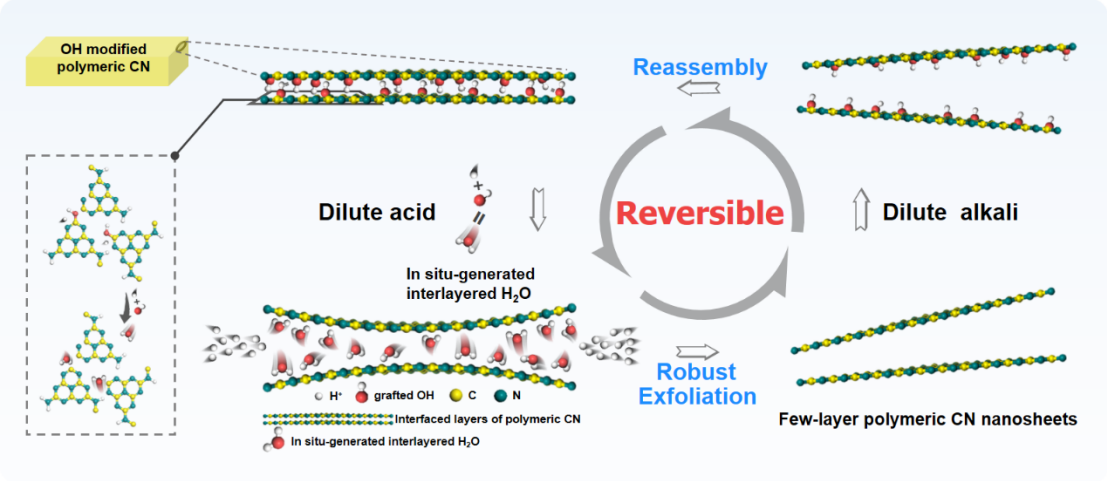


Figure 3.1. Schematic diagram of the reversible exfoliation-reassembly process of shallow surface-alkalized polymeric CN. To simplify the schematic model, the illustration of the K(Na)-N bond is omitted.

3.3.1 Formation of shallow surface-alkalized polymeric CN

The OH group-implanted polymeric CN (CNK-OH) was prepared following the method reported in our previous work.[11] Fourier transform-infrared (FT-IR) spectroscopy and X-ray photoelectron spectroscopy (XPS) were applied to identify the OH groups in the shallow surface over CNK-OH. Two new bands (983 and 1154 cm^{-1}) in FT-IR spectra (Figure 3.2a) and an extra peak centered at 530.80 eV in O *1s* spectra (Figure 3.2b) appear for CNK-OH compared with the spectra of pristine polymeric CN (denoted as "CN" in all Figures and Tables), which is consistent with our previous study and suggests the successful grafting of hydroxyl group.[11, 33] The O *1s* depth profile of CNK-OH shows that the content of hydroxyl groups is still 0.43 at % even after etching ~10 nm (Figure 3.3 and Table 3.1), indicating that OH groups don't only exist at outer surface of the sample.

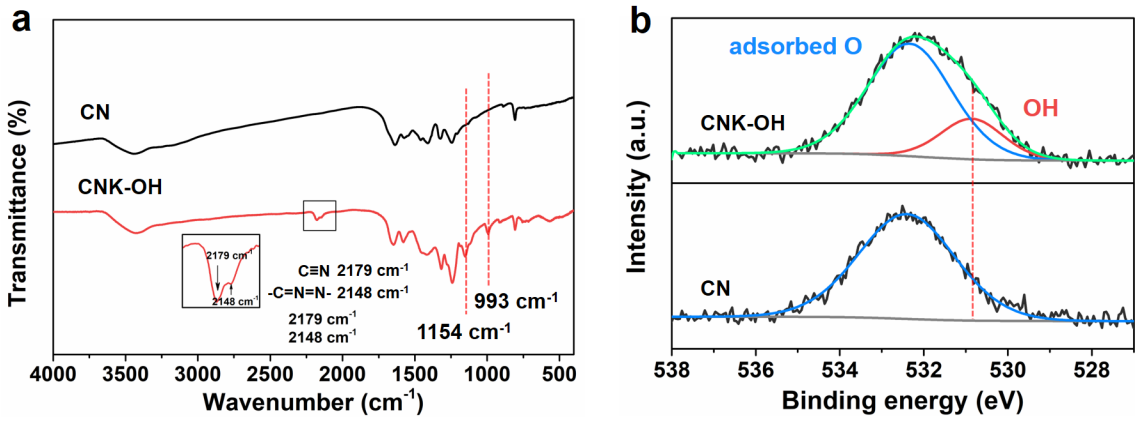


Figure 3.2 (a) FT-IR spectra of the pristine polymeric CN and CNK-OH. (b) XPS spectra of O *1s* for the obtained samples.

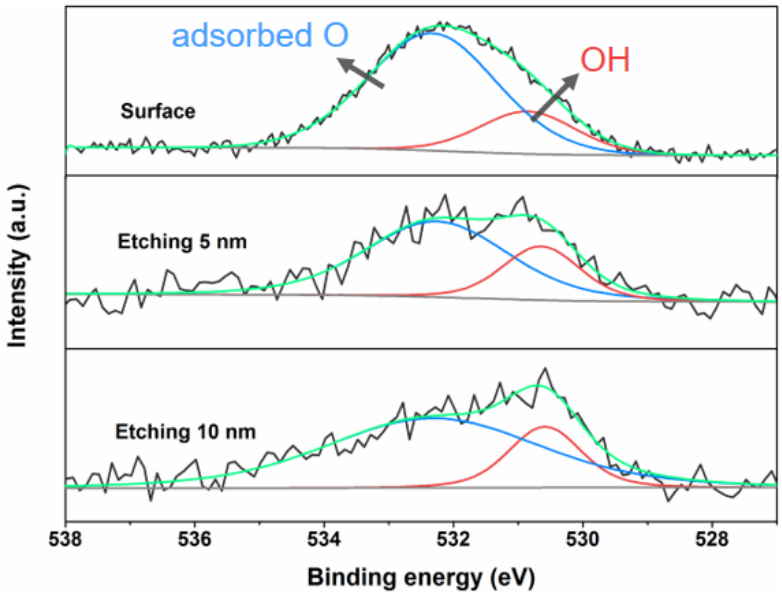


Figure 3.3 High-resolution XPS spectra of O *1s* for CNK-OH with different etching depth.

Table 3.1 Oxygen species and corresponding proportion of CNK-OH and etched samples.

	Peak Location (eV)	Species	Proportion (at%)
Surface	532.34	Adsorbed H_2O	5.38
	530.86	**OH**	**1.40**
Etching 5 nm	532.26	Adsorbed H_2O	1.72
	530.64	**OH**	**0.67**
Etching 10 nm	532.32	Adsorbed H_2O	1.45
	530.59	**OH**	**0.43**

3.3.2 Reversible exfoliation-reassembly of CNK-OH and related mechanism

Based on the fact that a proton easily neutralizes a hydroxy ion to produce H_2O, exfoliation of CNK-OH was realized via a facile dilute acid treatment. The morphology and thickness of CNK-OH before and after exfoliation were investigated by transmission electron microscopy (TEM) and atomic force microscopy (AFM) (Figure 3.4). CNK-OH presents a bulk microstructure with a thick lateral size of approximately 17.4 nm (Figure 3.4a, 3.4b, 3.4c, insert of Figure 3.4b, and Figure 3.5). After dilute acid (0.05 M H^+; H_2SO_4)-assisted exfoliation (termed as CNK-OH/Acid), the sample presents as ultrathin nanosheets with a thickness of approximately 1.9 nm (Figure 3.4d, 3.4e, 3.4f, insert of Figure 3.4e, and Figure 3.6; Figure 3.7 presents the photographs before and after exfoliation), which is in stark contrast to the bulk CNK-OH. A typical AFM image (Figure 3.4e) reveals the same ultrathin morphology observed in the TEM images. Moreover, the height statistics (Figure 3.4c and 3.4f) reveal that the thickness of the sample drastically decreased after acid-assisted exfoliation, i.e., from 10~20 nm to 1~2 nm. Generally, a reduction in thickness will broaden the band gap of semiconductors due to the quantum confinement effect.[34] The $(\alpha h\nu)^{1/2}$ versus photon-energy plots (Figure 3.8) reveal a wider band gap of approximately 2.84 eV for CNK-OH/Acid compared with that of untreated CNK-OH (2.69 eV), and the photoluminescence (PL) peak also blueshifts (Figure 3.9), both of which further verify an effective exfoliation. As expected, the freeze-dried exfoliated sample presented a loose, fluffy state with a light yellowish-white color and a large surface area of 136.8 m^2/g. Large accessible surface area can allow more reactants to be involved in the reactions. Meanwhile, such a thin feature can also shorten the diffusion distance of photocarriers and thus enable more efficient utilization of carriers (Figure 3.9, 3.10, Table 3.2).

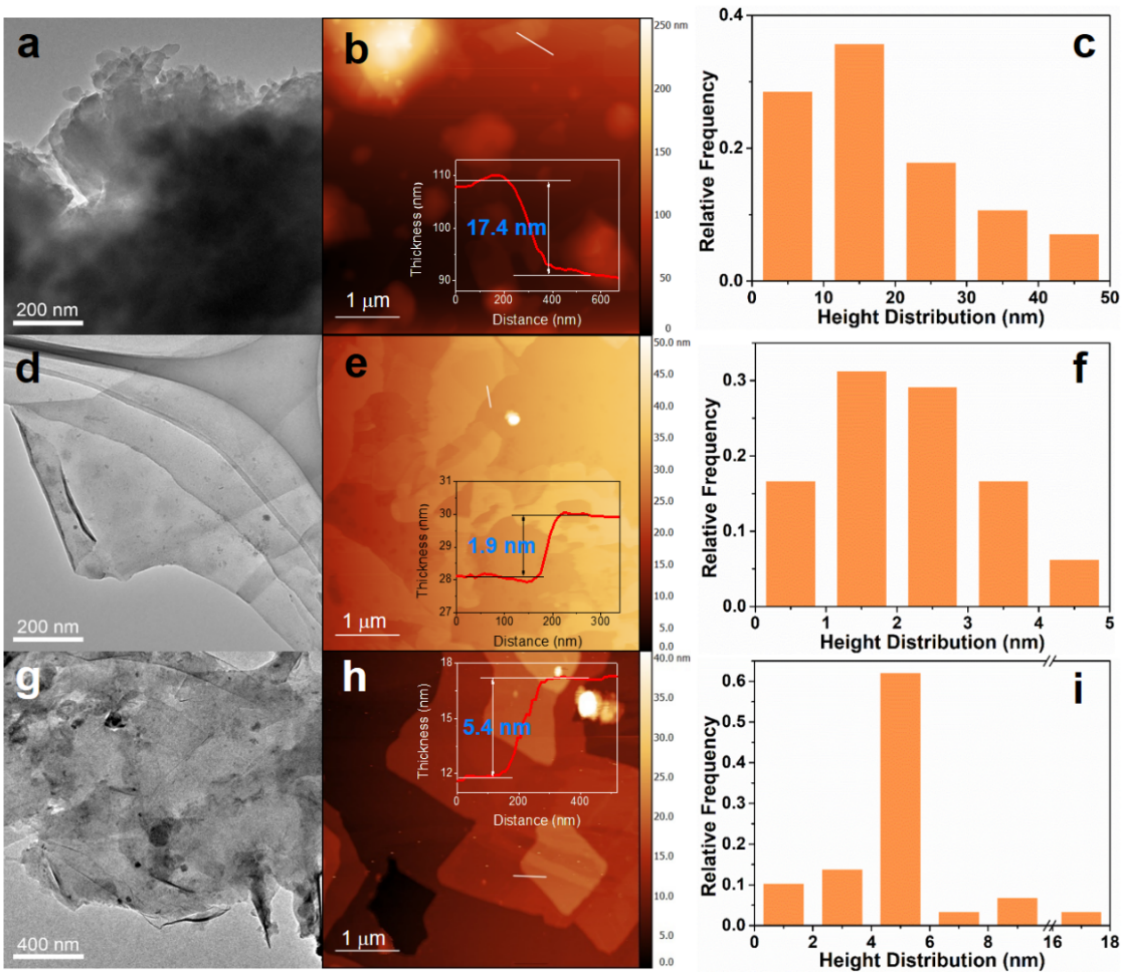


Figure 3.4 Characterization of the microstructure and thickness of the shallow surface-alkalized sample (CNK-OH), exfoliated nanosheets and reassembled samples. a) TEM micrograph, b) AFM image and c) the thickness histogram of bulk CNK-OH. d) TEM micrograph, e) AFM image and (f) thickness histogram of CNK-OH/Acid. g) TEM image, h) AFM image and i) thickness histogram of the assembled sample. Insert of AFM images shows a height profile along the white line.

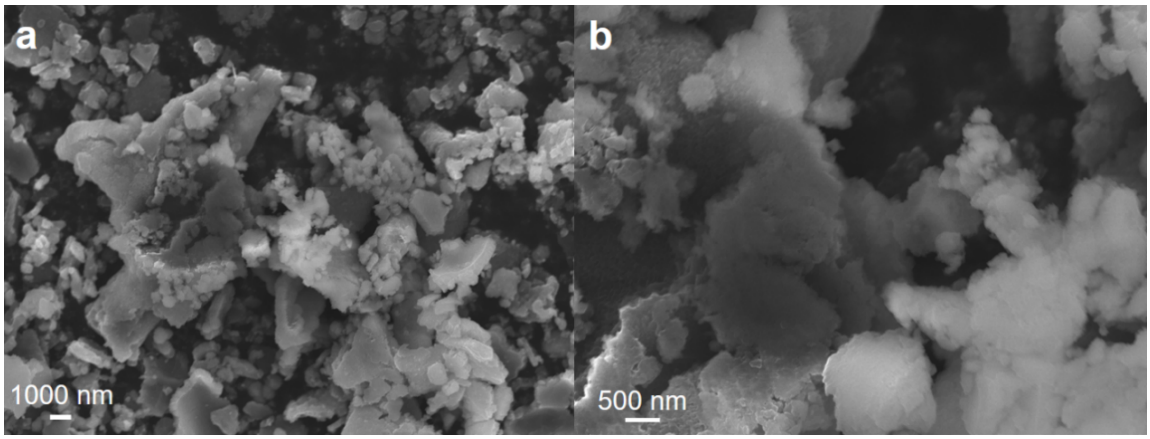


Figure 3.5 SEM images of bulk CNK-OH.

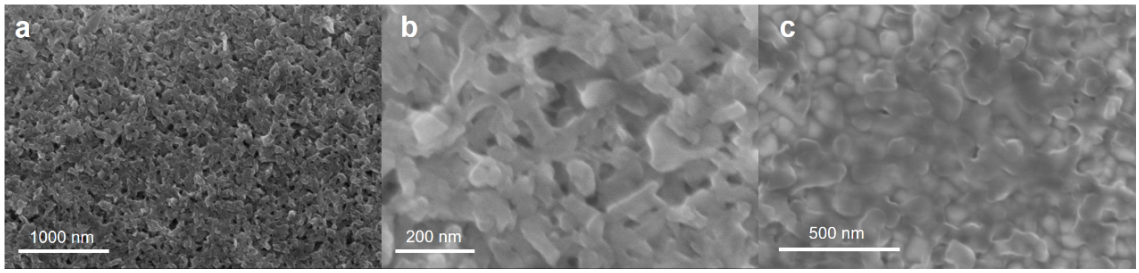


Figure 3.6 SEM images of exfoliated sample (CNK-OH/Acid) on FTO (Conductive glass). Note: the suspension of exfoliated sample was dropped upon FTO and then dried at room temperature for SEM test. (a) and (b) show the region of massive stacked ultrathin nanosheets and (c) exhibits the area with less exfoliated sample with typical ultrathin feature.

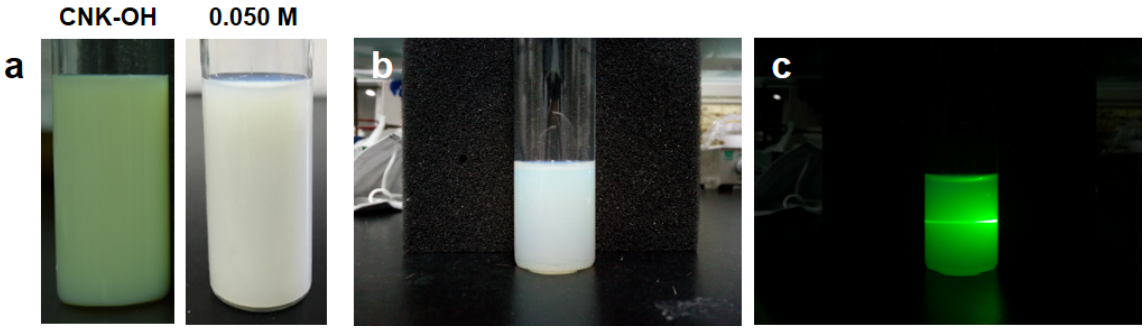


Figure 3.7 (a) The photographs of aqueous CNK-OH/Acid dispersion after standing for one week. (b) Diluted dispersion of CNK-OH/Acid. (c) Typical Tyndall effect of the diluted dispersion of CNK-OH/Acid. The nearly white color shown in (a) and (b) and well-defined Tyndall effect of the nanosheet solution shown in (c) signified that the ultrathin nanosheets were highly monodispersed in water.

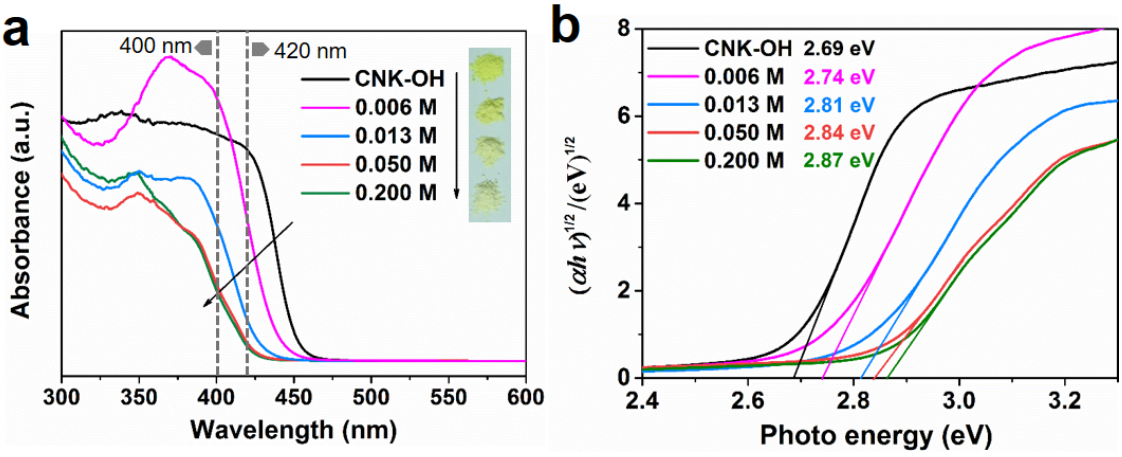


Figure 3.8 Optical properties of as-synthesized samples. (a) UV-visible absorption spectra of samples treated with different concentration acid. (b) the plots of the $(\alpha h\nu)^{1/2}$

versus photo energy ($h\nu$). Increasing the proton concentration to 0.20 M did not cause further obvious band gap narrowing, and a proton concentration of 0.05 M was enough to achieve complete exfoliation.

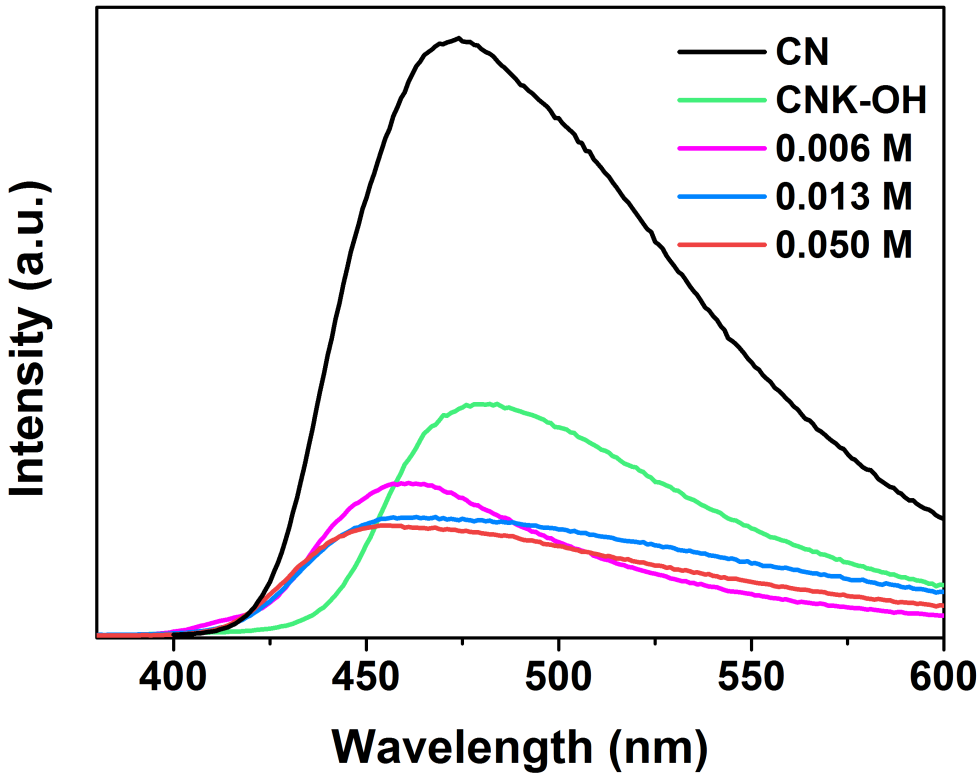


Figure 3.9 Steady-state photoluminescence spectroscopy of samples.

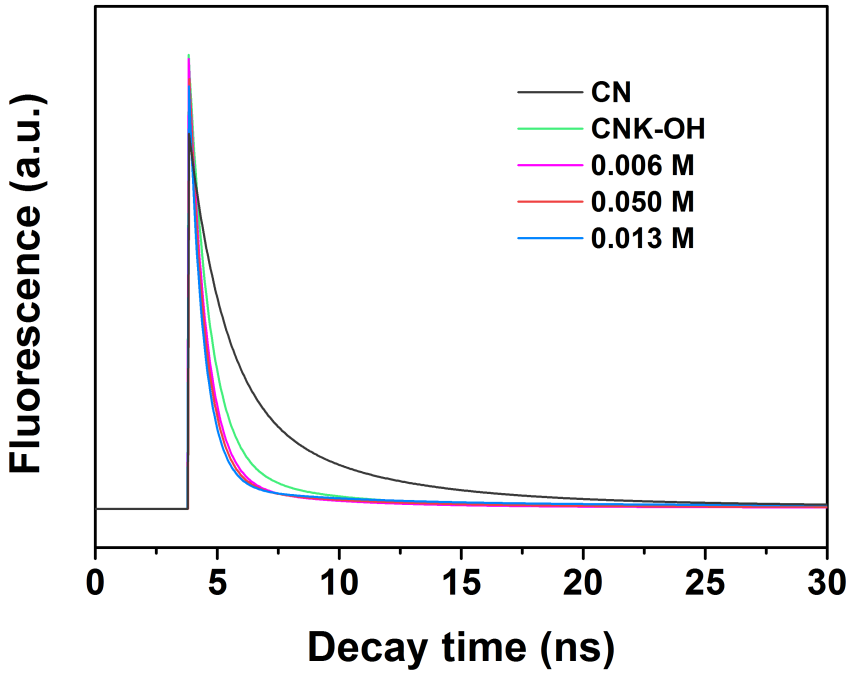


Figure 3.10 The fitting curves of time-resolved photoluminescence spectroscopy of samples.

Table 3.2 Best fitted parameters of time resolved PL spectra (Figure 3.10).

Samples	τ_1 (ns)-Rel%	τ_2 (ns)-Rel%	τ_3 (ns)-Rel%	Goodness of fit parameter (χ^2)
CNK-OH	0.85-90%	4.12-9%	26.30-0%	1.52
0.006 M	0.71-94%	4.12-6%	30.40-0%	1.62
0.013 M	0.61-95%	5.29-5%	40.70-1%	1.47
0.050 M	0.66-94%	4.80-5%	29.80-1%	1.43

To reveal the critical role of OH group for the exfoliation and the residual moieties over exfoliated sample, simple contrast experiments were carried out as follows. First, pristine CN without OH groups was treated with acid. The color of samples (Figure 3.11a) and their UV-visible absorption spectra (Figure 3.11b) are almost unchanged, which is totally different from the alkalized sample (Figure 3.7 and Figure 3.8a) and suggests that the OH groups in the shallow surface region are essential to acid-assisted exfoliation. Furthermore, the addition of CN to 0.05 M H_2SO_4 barely changed the pH value of the solution (Figure 3.12). However, when CNK-OH was introduced, the pH rapidly increased from 1.27 to 1.45, which indicates proton consumption, but the zeta potential analysis (Figure 3.13) shows that the protons do not operate in a protonation manner[35]. Besides, the two characteristic peaks in the FT-IR spectrum corresponding to the OH group (Figure 3.14a), the oxygen in the form of OH in high-resolution XPS spectra of O *1s* (Figure 3.14b) and C motif bonded with OH in the ^{13}C NMR spectra (Figure 3.15) disappear after the acid treatment. Therefore, it's rational to conclude that the protons enter into the inner space between layers and neutralize anchored OH groups to produce H_2O molecules in the confined interlayer space (Figure 3.1, Figure 3.16), which overcomes the interlayer van der Waals attraction and yields ultrathin polymeric CN nanosheets (Figure 3.1). As illustrated in our previous study,[33] a new kind of carbon species exists in the bulk alkalized sample with the form of C-OH and a binding energy of 286.55 eV (Figure 3.17 and Table 3.3). With increasing acid concentration, the carbon (C-OH) binding energy gradually decreases from 286.55 eV to 286.15 eV. (Note: Oxygen is more electronegative than carbon; thus, dehydroxylation will reduce the binding energy of carbon.) This decrease revealed that the OH groups are gradually consumed by protons,

resulting in unsaturated and active carbon species without OH grafting, which is further supported by the FT-IR and O *1s* results (Figure 3.14a and 3.14b).

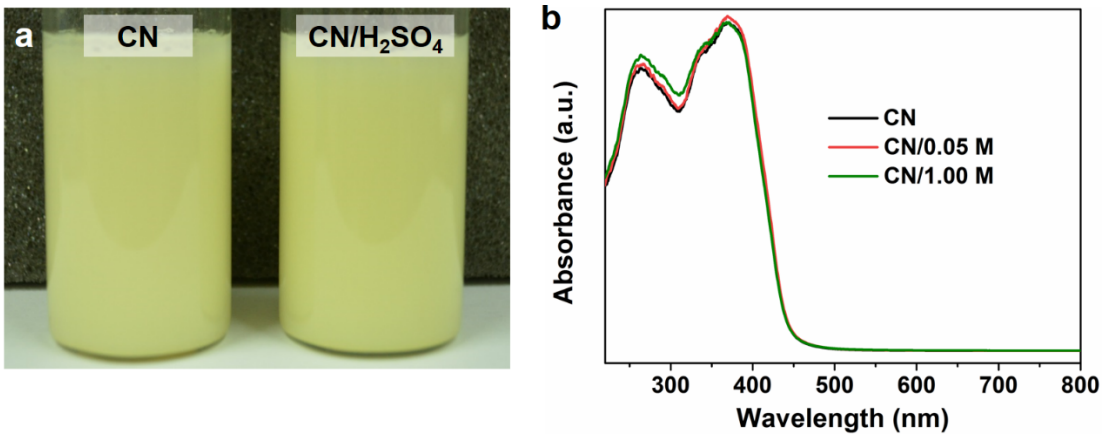


Figure 3.11 Characterization of CN before and after acid treatment. (a) The photograph of CN before and after treatment with 1.0 M (0.5 M H_2SO_4, sonicated for half hour) proton solution. (b) Corresponding UV-visible absorption spectra.

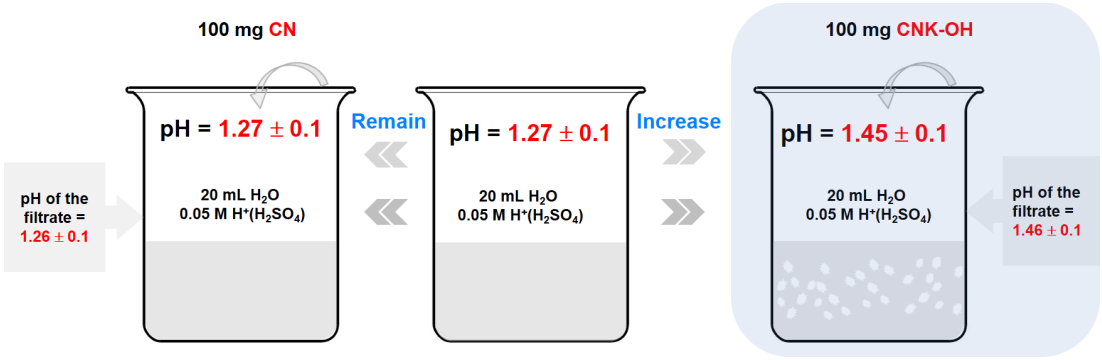


Figure 3.12 Schematic diagram of pH value change of acid solution after adding CN and CNK-OH.

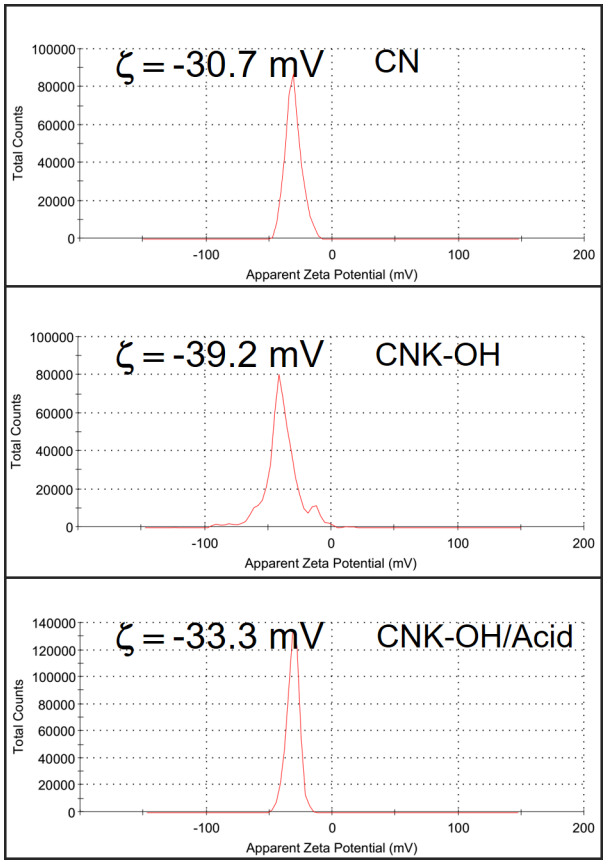


Figure 3.13 Zeta potential of a group of samples. The dilute acid-assisted exfoliation result is totally different from that reported for protonated polymeric CN according to the zeta potential results. Reportedly, the zeta potential of polymeric CN dispersions in water shifts from -47.4 to +30 mV after treatment with concentrated HCl, suggesting successful protonation.[35] However, in our case, the aqueous solution of fully washed CNK-OH/Acid exhibits a zeta potential of -33.3 mV, which is close to the value of CNK-OH (-39.2 mV) under the same test conditions and implies a neutralization mechanism other than protonation.

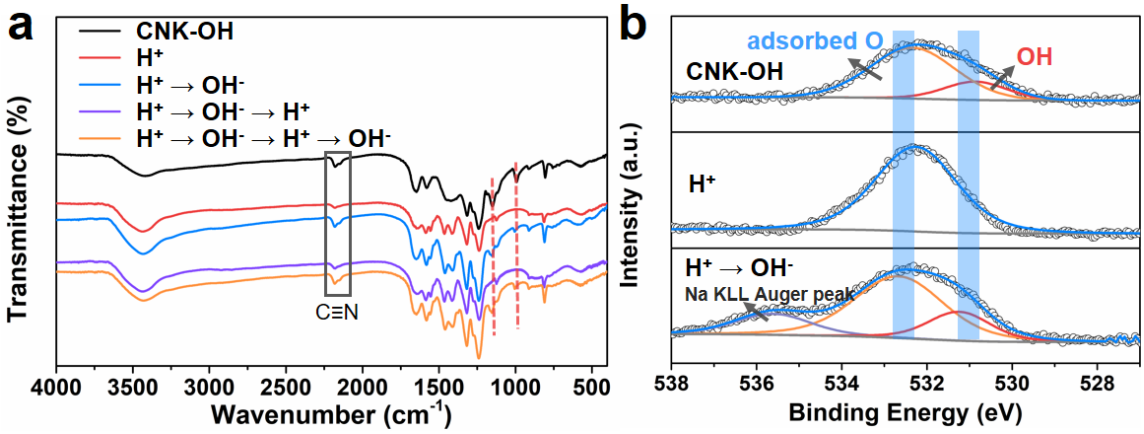


Figure 3.14 (a) FT-IR spectra and (b) the O *1s* spectra of the samples.

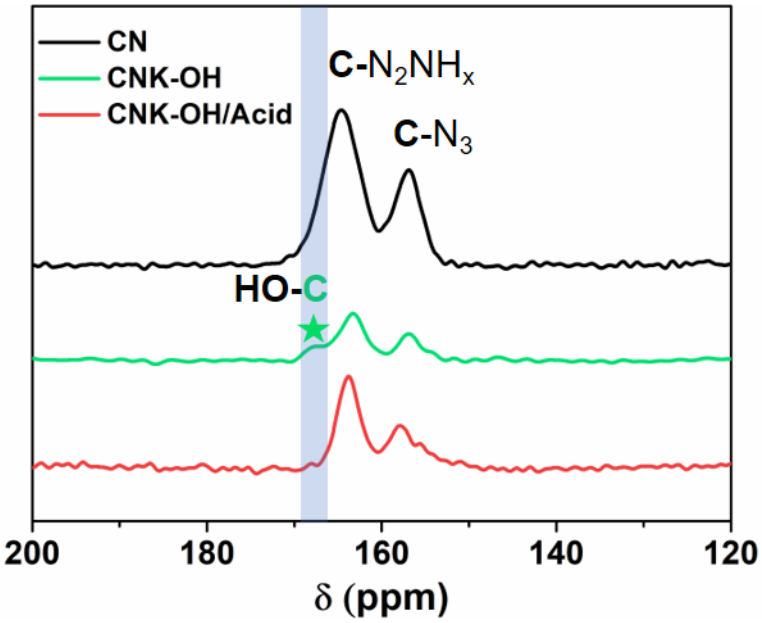


Figure 3.15 ^{13}C solid state NMR spectra over a group of samples.

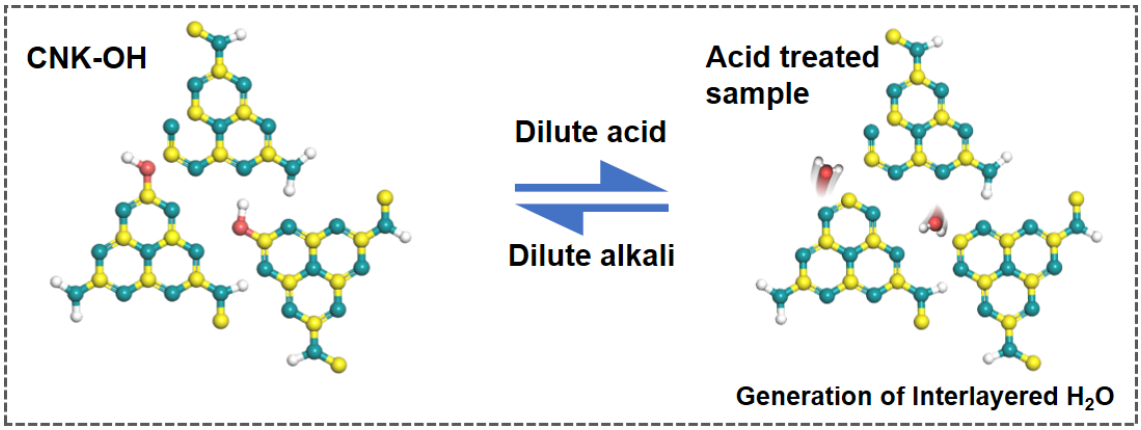


Figure 3.16 Illustration of the periodic changes in the structure with the cyclic addition of acid and alkali.

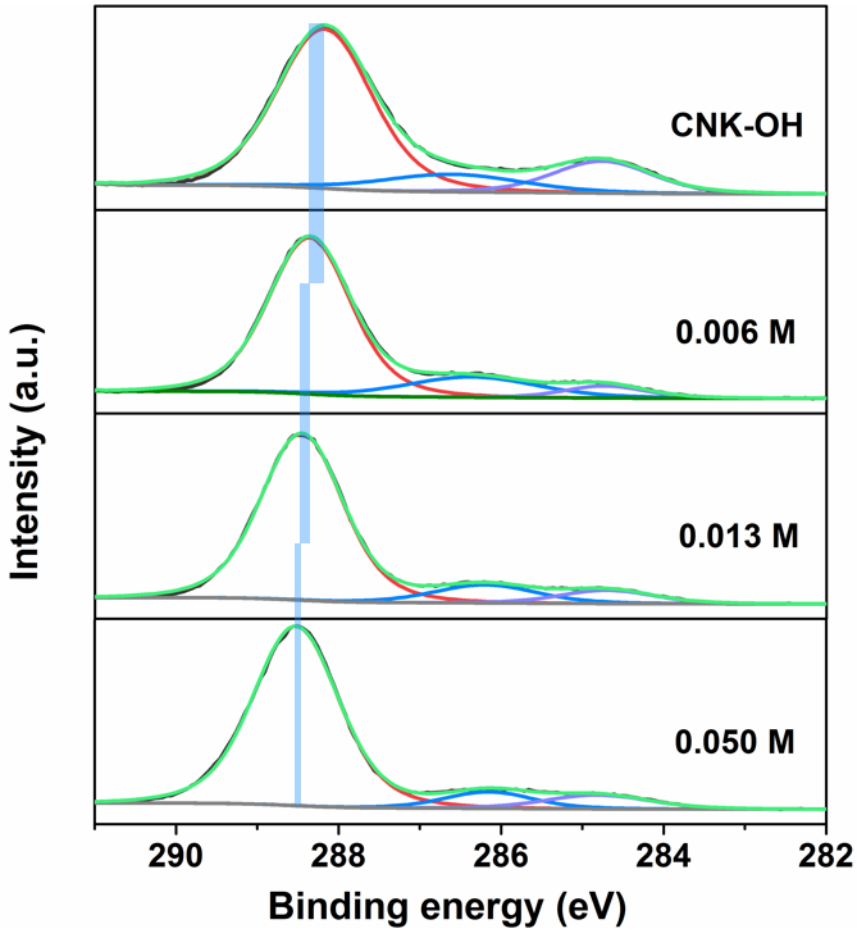


Figure 3.17 High-resolution C *1s* XPS spectra.

Table 3.3 Summaries of binding energy of carbon, corresponding species and proportion for CN, CNK-OH, exfoliated and reassembled samples.

	C-C-C/C=C	C-(OH)	N-C=N
CN	**284.88**	-	**288.31**
	11.22%		88.78%
CNK-OH	**284.72**	**286.55**	**288.07**
	12.19%	23.24%	64.57%
0.006 M	**284.72**	**286.36**	**288.36**
	5.96%	11.05%	77.98%
0.013 M	**284.70**	**286.20**	**288.46**
	7.44%	10.99%	81.56%
0.050 M	**284.81**	**286.15**	**288.53**
	7.94%	7.97%	84.08%

	C-C-C/C=C	C-(OH)	N-C=N
0.050M	**284.73**	**286.40**	**288.26**
→NaOH	17.97%	10.37%	71.66%

The aforementioned analyses show us that the C-OH in CNK-OH is readily removed by proton, but it's usually quite difficult to neutralize the OH groups bonded with C sites in organic chemistry by acid treatment. It's worth mentioning that the C-OH species in our case is intrinsically different from that in organic chemistry, such as the OH in alcohols. The OH groups in the CNK-OH are bonded with C sites in tri-s-triazine units, wherein abundant unpaired electrons. To verify the unique nature of OH connected with tri-s-triazine, we used electron spin resonance (ESR) examination over the pristine CN and CNK-OH (Figure 3.18). Pristine CN clearly presents an obvious signal associated with the unpaired electron in tri-s-triazine units.[14] Interestingly, the signal intensity decreased remarkably for CNK-OH when compared with CN, indicating the decline of unpaired electrons in the tri-s-triazine units after grafting OH groups. It's reported that alkali ions in CN will increase rather than decrease the signal intensity of unpaired electron in CN matrix.[36] We can preliminarily exclude the contribution of K ions to the reduced unpaired electron for CNK-OH. Thus, it's rational to conclude that the abundant unpaired electrons in tri-s-triazine units could transfer to the grafted OH groups, which confers the OH species with certain property of OH-. This point agrees well with our previous experimental result.[11] The concentrated dispersion of fully washed CNK-OH presents weak alkalinity, which reveals that the OH in the form of C-OH in CNK-OH has certain property of free OH. In brief, the OH groups in our case are negatively charged by attracting the electrons from conjugated tri-s-trizaine units and such feature could enable the reaction between OH groups and protons.

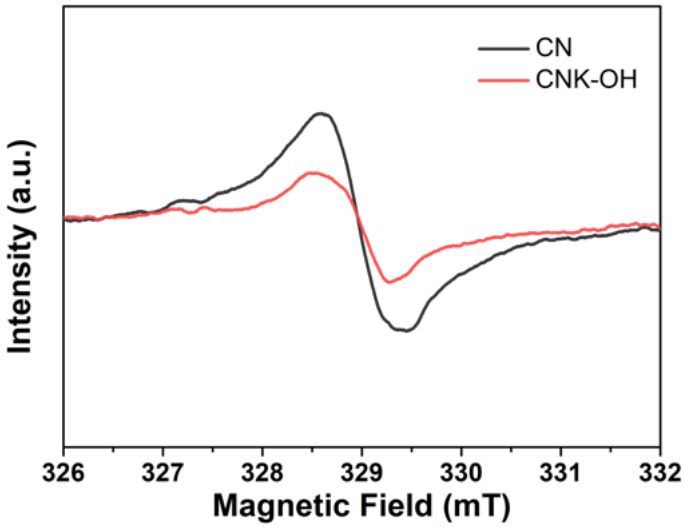


Figure 3.18 Solid-state ESR spectra of CN and CNK-OH under dark condition. The test conditions are identical for both samples.

Additionally, this facile top-down strategy achieves a high exfoliation yield to produce ultrathin nanosheets with various kinds of acids (Table 3.4) including strong acids (H_2SO_4 (Figure 3.4d, 3.4e and 3.4f), HCl, and H_3PO_4), weak acids (CH_3COOH) and salts donating protons (KH_2PO_4), which verifies the crucial role of protons for the acid-assisted exfoliation. Typically, with H_2SO_4 (0.025 M), the yield was measured to be as high as 48%, which is nearly 3 times greater than the yield from a traditional liquid exfoliation method with a long sonication time.[34]

Table 3.4 Ultrathin nanosheets yields with different kinds of acids.

Exfoliation reagents	**Yield of few layer sheets (%)**
H_2SO_4 (0.025M)	48.4 ± 4.2
HCl (0.05M)	39.8 ± 1.8
CH_3COOH (0.05M)	31.7 ± 13.4
H_3PO_4(0.05M)	32.7 ± 0.9
KH_2PO_4(6M)	40.3 ± 4.0

Based on the above analyses, the exfoliation mechanism and the advantages of the exfoliated sample can be summarized as follows (Figure 3.1): the protons in solution readily enter the interlayer of CNK-OH and further react with the OH groups bonded to carbon atoms to produce interlayered H_2O molecules, which cause the layer distance to

expand and result in effective exfoliation of polymeric CN. These exfoliated CN possesses three apparent advantages over bulk CNK-OH, including 1) large accessible surface area, 2) favorable kinetics of photocarriers, 3) abundant unsaturated and active C atoms.

Surprisingly, when adding a slight excess of alkali compared to the residual acid into a fresh solution of acid-treated CNK-OH, the color (Figure 3.19), light absorption (Figure 3.20a), band gap (Figure 3.20b), and thickness (Figure 3.4g, 3.4h and 3.4i) are largely recovered. The morphology (Figure 3.4g) presents a typical restacked feature driven by a force (clarified later) and the surface area of freeze-dried reassembled sample dramatically reduced to 77.0 m^2g^{-1}, strongly suggesting a partial self-assembly status. The height distribution indicates that the thickness of stacked sample lies between exfoliated sample and bulk sample.

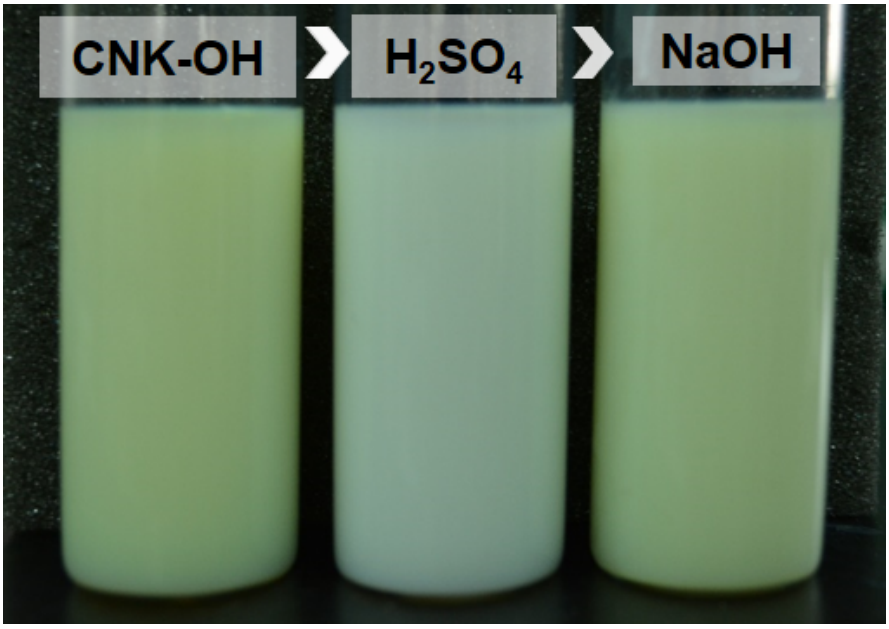


Figure 3.19 The photograph of aqueous solution of exfoliated sample and reassembled sample.

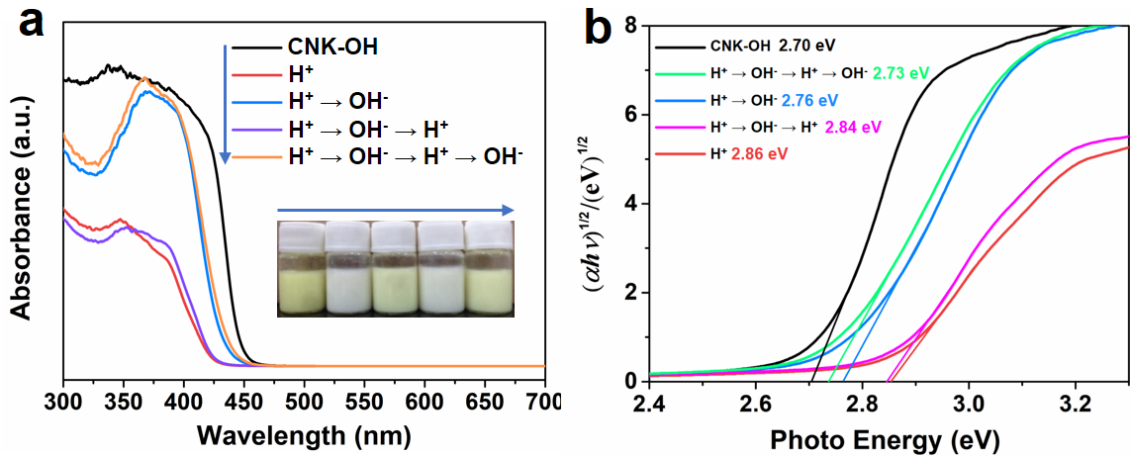


Figure 3.20 (a) Absorption spectra of acid- and alkali-treated samples. Inset: Photograph of the powder and suspension of samples. (b) The plots of the $(\alpha h\nu)^{1/2}$ versus photo energy ($h\nu$).

To elucidate the unique self-assembly mechanism and the structural characteristic of reassembled sample, FT-IR and XPS were conducted. First, as shown in Figure 3.14a, the two characteristic peaks of the OH group at 983 and 1154 cm^{-1} are observed after reassembly, which indicates that OH is rebonded with unsaturated C (as demonstrated above). This conclusion is further evidenced by the O *1s* (Figure 3.14b), C *1s* spectra (Figure 3.21a and Table 3.3) and the recovered O (in OH group) content (Table 3.5). Additionally, the CNK-OH/Acid sample shifted the pH of a 0.05 M NaOH solution from 12.45 to 12.22, demonstrating OH consumption, whereas the addition of pristine CN hardly altered the pH (Figure 3.22). These pH results support the FT-IR and XPS analyses. Therefore, hydrogen bond interactions between abundant OH groups on the surface of layers may drive the self-assembly of CN nanosheets into thick morphologies. We also find that the K ion concentration (bonded with N as demonstrated in our previous report, denoted as K-N, Figure 3.21b, Table 3.5) contained between layers increases to 3.0 at %.[11] In addition, 4.9 at % of Na ions (Na ions here were specifically chosen as probe ions to ascertain the key role of alkali ions in the assembly process) are present (also bonded with N; binding energy similar to that of the Na-N bond contained in polymeric CN,[37] Figure 3.23) when NaOH was used to trigger the reassembly behaviour. Thus, K-N and Na-N bonds may act as another potential self-assembly driving force.

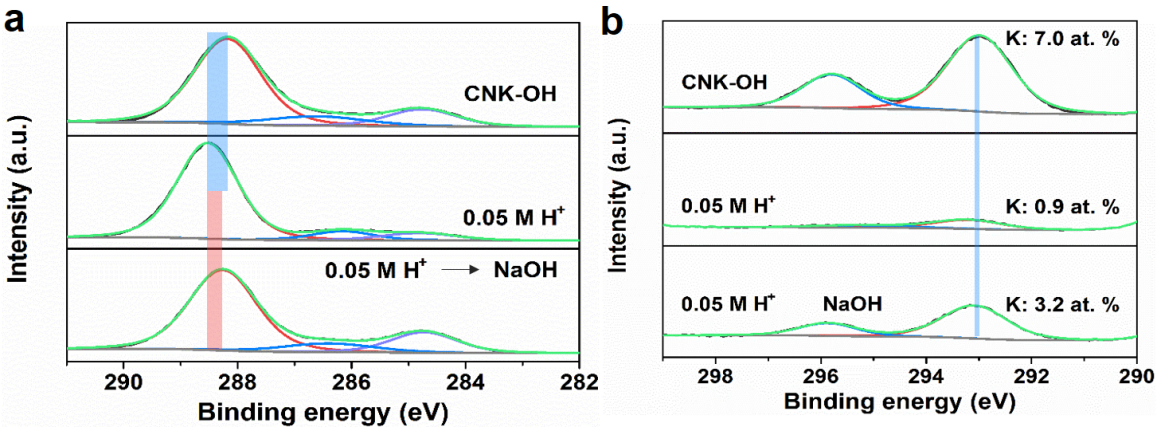


Figure 3.21 Detecting the reassemble course via high-resolution XPS spectra. (a) C *1s*. (b) K *2p*.

Table 3.5 Summaries of element content for CN, CNK-OH, exfoliated and reassembled samples.

	O (OH) (at. %)	O (adsorbed H_2O) (at. %)	K (at. %)	Na (at. %)	C (at. %)	N (at. %)
CN	-	1.8	-	-	45.8	52.4
CNK-OH	1.4	5.4	7.0	-	39.5	46.8
0.006 M	0.3	5.0	5.0	-	43.1	46.4
0.013 M	-	4.9	2.4	-	44.1	48.5
0.050 M	-	5.0	0.9	-	44.7	49.4
0.050 M→NaOH	1.4	3.1	3.0	4.9	42.8	44.8

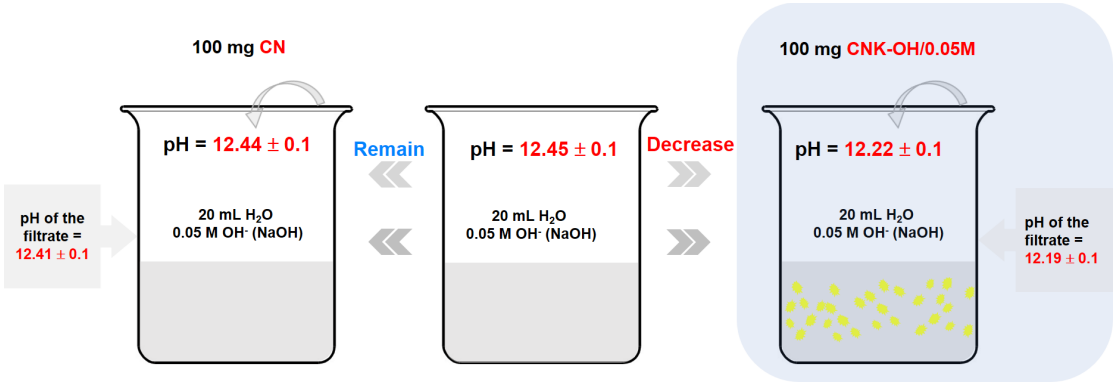


Figure 3.22 Schematic diagram of pH value change of basic solution after adding CN and CNK-OH/Acid.

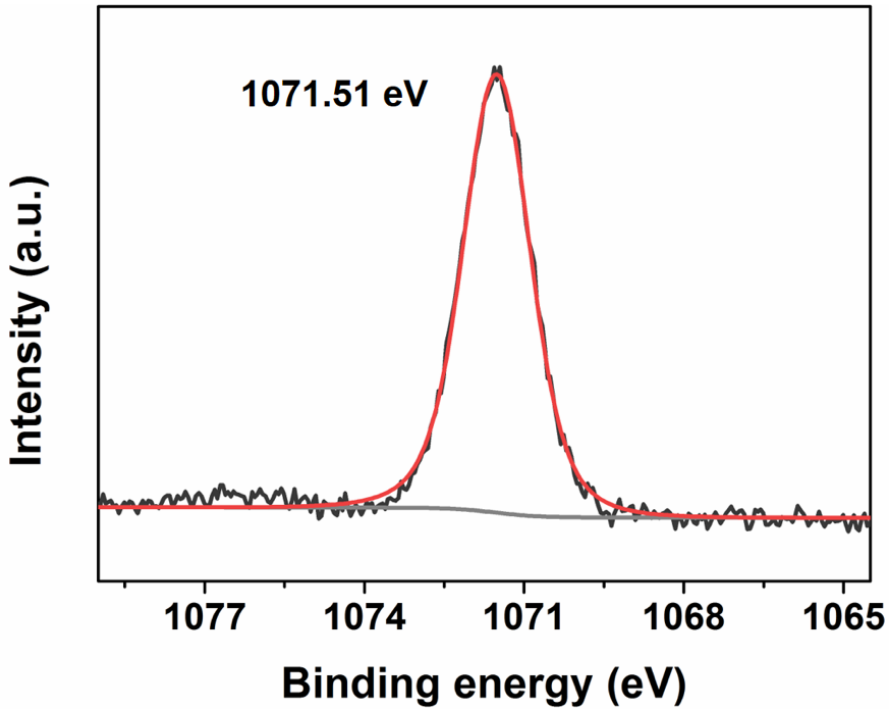


Figure 3.23 High-resolution XPS spectra of Na *1s* for reassembled sample.

In short, the partial reassembly behavior can readjust the properties of the stacked sample. Although partial reassembly behavior reduce the surface area, several merits are obtained for the stacked sample compared to the exfoliated samples including enhanced light absorption and increased hydrophilicity benefiting from regrafted OH groups[38]. Besides, thinner feature of partial reassembled sample relative to the bulk CNK-OH endow larger surface area and more favorable kinetics of carriers (Figure 3.9, Figure 3.10 and Table 3.2).

If a slight excess of acid was added, the exfoliation process occurred again, which was evidenced by the white color (insert of Figure 3.20a), broader band gap (Figure 3.20b) and disappearance of surface OH species (Figure 3.14a). Markedly, those parameters were reversible for at least 30 cycles (Figure 3.24). The critical point for this reversible exfoliation-reassembly transformation is that the OH groups can be cyclically consumed and regenerated between layers with an alternating acid and alkali treatment (Figure 3.1 and 3.16).

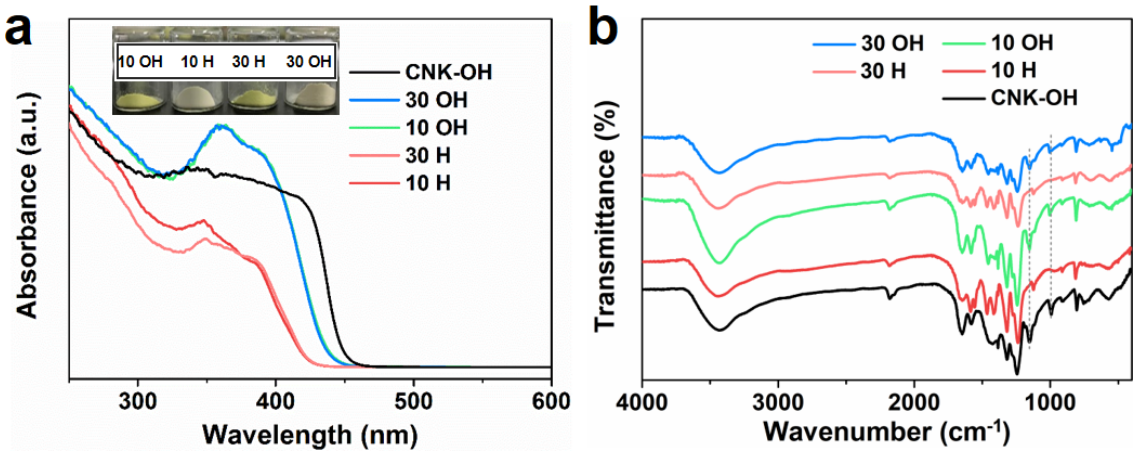


Figure 3.24 Characterization of multi-cycle reversible exfoliation-reassembly process over CNK-OH. (a) UV-visible absorption spectra of exfoliated and reassembled samples with 10 cycles and 30 cycles alternately dilute acid and alkali treatment. (b) Corresponding FTIR spectra.

3.3.3 Exfoliated-reassembled samples deliver high photoactivity

To assess the validity of this reversible exfoliation-reassembly effect of polymeric CN on improving photocatalytic efficiency, photocatalytic IPA oxidation and H_2 evolution were both carried out using the as-prepared samples. Surprisingly, CNK-OH/Acid achieves 69.5 times (acetone) and 104.8 times (CO_2) improvements relative to those obtained with pure CN and 2.7 times (acetone) and 24.6 times (CO_2) enhancements compared with the results obtained with CNK-OH (Figure 3.25a). In addition, as shown in Figure 3.25b, CNK-OH/Acid shows a much higher photooxidation activity than polymeric CN nanosheets fabricated by previously reported advanced methods (UV-vis absorption spectra are provided in Figure 3.26). Combining the structure features of exfoliated samples and some additional experiments (Figure 3.25c and Figure 3.27), we believe that the fully exposed active and unsaturated C atoms on large surface area mainly contribute to the outstanding degradation performance. In detail, nanosheets-1 and nanosheets-2 possess similar ultrathin 2D morphologies with ultrathin nanosheets obtained via acid treatment, as illustrated by their broadening band gaps (Figure 3.26) and a previously reported study.[22], [27] However, the nanosheets in our case exhibit superior generation of acetone and CO_2. Moreover, as identified above, with the increase in the acid concentration, OH will be consumed, and unsaturated carbon sites will be gradually generated. The photooxidation activity enhances with the increasing acid concentration (0.006 M ~ 0.2 M), as shown in Figure 3.27, and thus, the activity is also

positively correlated with the quantity of dehydroxylated C. In addition, the photooxidation activity is reversible when we alternate the exfoliation-reassembly process accompanied by the appearance and disappearance of dehydroxylated C atoms (Figure 3.25c). Therefore, we can reasonably infer that the active and unsaturated C atom, which easily adsorbs O from OH as demonstrated above, could be the main reason for the excellent performance. These carbon atoms may also readily participate in strong interactions with the O of IPA and acetone, which could weaken the bonds of the target molecules, accelerate reaction dynamics, and lead to fast production of acetone and CO_2.

For photocatalytic H_2 generation, the CNK-OH/Acid sample presents an enhancement for H_2 evolution from 134 μmol/h to 162 μmol/h compared with CNK-OH (Figure 3.25d). Notably, the alkalinity of TEOA (acting as a sacrificial agent for H_2 generation) can induce the self-adapting reassembly as identified above. Hence, the enhanced H_2 evolution can be ascribed to the rebalanced properties of partially reassembled CNK-OH/Acid including more favorable photocarriers kinetics and larger exposed surface relative to bulk CNK-OH. Remarkably, such rebalanced parameters can be further utilized and magnified by employing K_2HPO_4, which simultaneously improves proton reduction and hole oxidation as previously reported by Liu et al.[39] when K_2HPO_4 (0.2 mol) was added to the CNK-OH/Acid photocatalytic system, the acid-treated sample delivered an 8.5-fold enhancement relative to CNK-OH, reaching up to 1370 μmol/h (Figure 3.25d; ca. 27,400 μmol/h/g_{cat}). In short, the exfoliation and self-adapting reassembly effect can balance the key factors, including the light absorption, exposure of active sites and kinetics of carriers, favorable for photocatalytic IPA oxidation and H_2 generation, respectively, and thus results in excellent performance in these reactions. The optimal CNK-OH/Acid system can achieve superior photoactivity with a high AQYs of 46% (H_2 evolution, 0.2 mol K_2HPO_4) and 27% (IPA oxidation) at a wavelength of 420 ± 16 nm (Table 3.6), and these AQYs are among the highest values for polymeric CN-based photocatalysts for H_2 generation and pollutant degradation (Table 3.7). The specific results, stability tests of H_2 evolution and IPA photodegradation and characterizations before and after degradation are presented in Figure 3.28, 3.29, 3.30, 3.31, respectively.

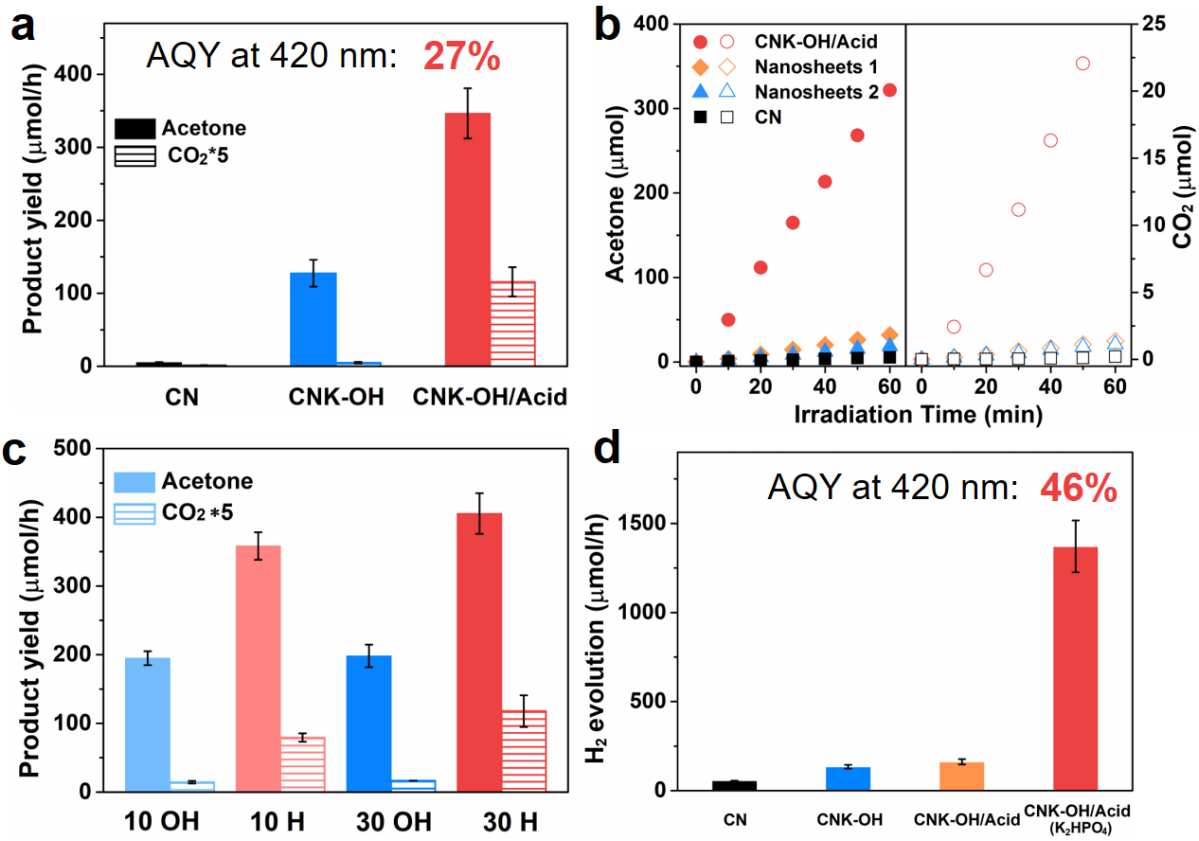


Figure 3.25 Photocatalytic activity of samples. (a) Photooxidation performance of samples. (b) Comparison of acetone and CO_2 evolution over pristine CN, CN nanosheets 1 (liquid exfoliation method), CN nanosheets 2 (gas template method) and CNK-OH/Acid. (c) Photooxidation performance of the samples with continuous cycles of acid and alkali treatment. (d) H_2 production rates.

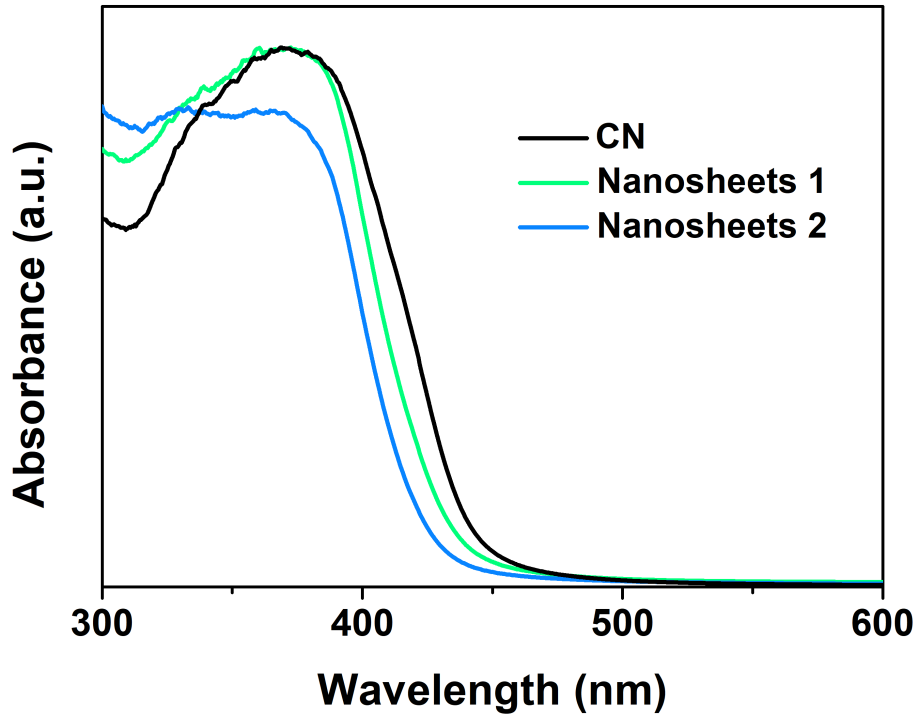


Figure 3.26 UV-visible absorption spectra of polymeric CN nanosheets obtained via other reported methods.

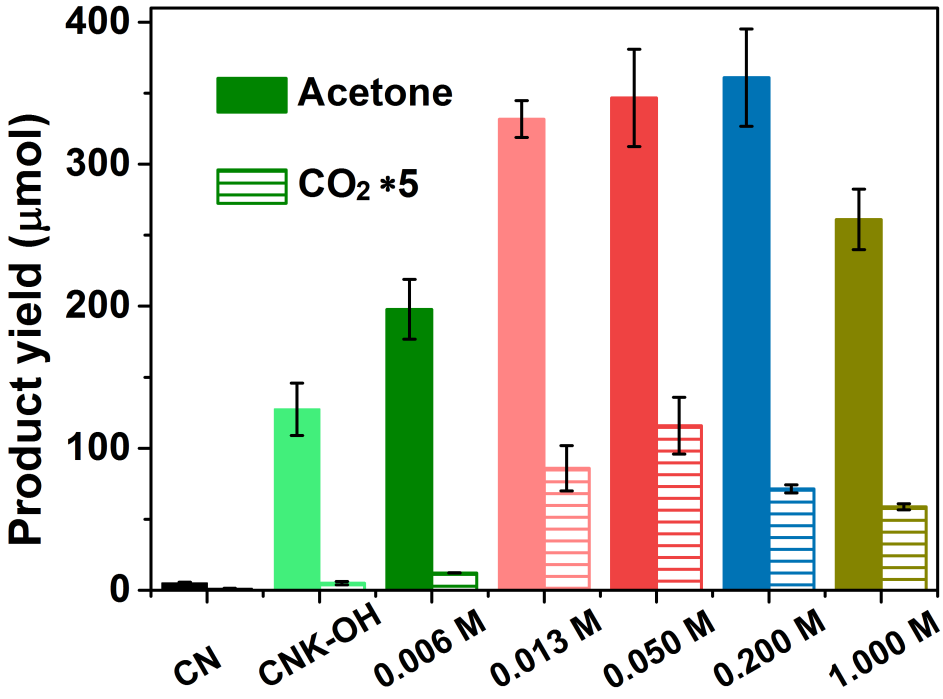


Figure 3.27 Photoactivity comparison of IPA degradation as a function of the concentration of acid (H_2SO_4).

Table 3.6 Polymeric CN-based photocatalysts for H_2 evolution.

Samples	H_2 Yield (μmol/h)	AQY	Reaction Conditions
Nanosheets[39]	947	26% (at 420 nm)	50 mg catalyst, 3 wt% Pt, 300 W Xe lamp, L40 filter 0.2 mol K_2HPO_4
3D mesoporous g-C_3N_4[40]	179	28% (at 420 nm)	50 mg catalyst, 1 wt% Pt, 300 W Xe lamp, λ > 420 nm
Atomically thin mesoporous g-C_3N_4[41]	85	5% (at 420 nm)	10 mg catalyst, 3 wt% Pt, 300 W Xe lamp, λ > 420 nm
P3HT (sensitizer)/ g-C_3N_4[42]	3045	77.4 (at 420 nm)	10 mg catalyst, 1 wt% Pt, 3 wt% P3HT, 300 W Xe lamp, λ > 500 nm
Nanosheets[27]	~60	-	50 mg catalyst, 3 wt% Pt, 300 W Xe lamp, λ > 420 nm
Nanosheets[25]	171	-	50 mg catalyst, 6 wt% Pt, 300 W Xe lamp, λ > 400 nm
Holey nanosheets[14]	83	-	10 mg catalyst, ~3 wt% Pt, 300 W Xe lamp, λ > 420 nm
Porous P-doped g-C_3N_4[43]	80	3.56% (at 420 nm)	50 mg catalyst, 1 wt% Pt, 300 W Xe lamp, λ > 400 nm
Link controlled g-C_3N_4[10]	10	10% (at 420 nm)	50 mg catalyst, 5 wt% Pt, 120 mW cm^{-2} Xe lamp, λ > 420 nm
Nanospherical g-C_3N_4[44]	574	10% (at 420 nm)	40 mg catalyst, 3 wt% Pt, 300 W Xe lamp, λ > 400 nm
Alkali metal modified g-C_3N_4[45]	502	21% (at 420 nm)	100 mg catalyst, 3 wt% Pt, 300 W Xe lamp, λ > 400 nm
Crystalline g-C_3N_4[46]	770	51% (at 405 nm)	50 mg catalyst, 3 wt% Pt, 300 W Xe lamp, λ > 420 nm, 0.01 mol K_2HPO_4
Crystalline g-C_3N_4[47]	509	57% (at 420 nm)	50 mg catalyst, 3 wt% Pt, White LED, 3 wt. % NaCl
Crystalline g-C_3N_4[21]	53	9% (at 420 nm)	50 mg catalyst, 3 wt% Pt, -, λ > 420 nm
Layered g-C_3N_4[24]	170	11.3% (at 405 nm)	50 mg catalyst, 3 wt% Pt, 300 W Xe lamp, λ > 400 nm
Nitrogen deficient g-C_3N_4[48]	69	-	10 mg catalyst, 1 wt% Pt, 300 W Xe lamp, λ > 420 nm
This work	**1370**	**46% (at 420 nm)**	**50 mg catalyst, 300 W Xe lamp, AM 1.5 filter 0.2 mol K_2HPO_4**

Table 3.7 Polymeric CN-based photocatalysts for gaseous pollutant degradation.

Samples	Pollutant	Product Yield (μmol/h)	UPN[a] (μmol/h)	Reaction Conditions
g-C_3N_4/WO_3[49]	CH_3CHO	CO_2, 0.9	4.5	100 mg catalyst, LED lamp, λ = 435 nm
g-C_3N_4/WO_3[50]	CH_3CHO	CO_2, 0.6	3	50 mg catalyst, λ > 420 nm
g-C_3N_4/Bi_2O_3[51]	$(CH_3)_2CHOH$	Acetone, 8.9	8.9	50 mg catalyst, 300 W Xe lamp, 420 nm ≤ λ ≤ 800 nm
g-C_3N_4/TiO_2[52]	HCHO	CO_2, 2.8	11.2	300 mg catalyst, UV lamp
HT-g-C_3N_4[53]	NO	NO_2, 0.3 NO_2^-, 0.2 $(NO_3)^-$, 0.5	1.3	200mg catalyst, W-type fluorescent lamps, λ > 380 nm
g-C_3N_4/P25 (M400)[54]	NO	NO_2, 0.4 NO_x, 0.6	1.0	50 mg catalyst, 500-W Hg lamp, 420 nm ≤ λ ≤ 700 nm
g-C_3N_4/GO[55]	NO	NO_2, 0.6 NO_x, 1.9	3.1	200 mg catalyst, A 150 W halide lamp, λ > 400 nm
CNK-OH/Fe[11]	$(CH_3)_2CHOH$	CO_2, 23.1 Acetone, 688.3	826.9 (AQY = 49% at 420 nm)	50 mg catalyst, 300 W Xe lamp, λ > 400 nm
This work	**$(CH_3)_2CHOH$**	**CO_2, 23.2 Acetone, 329.5**	**468.7 (AQY=27 % at 420 nm)**	**50 mg catalyst, 300 W Xe lamp, AM 1.5 filter**

[a] UPN: Utilized photon number, which was calculated via the transfer electrons in photooxidation reaction.

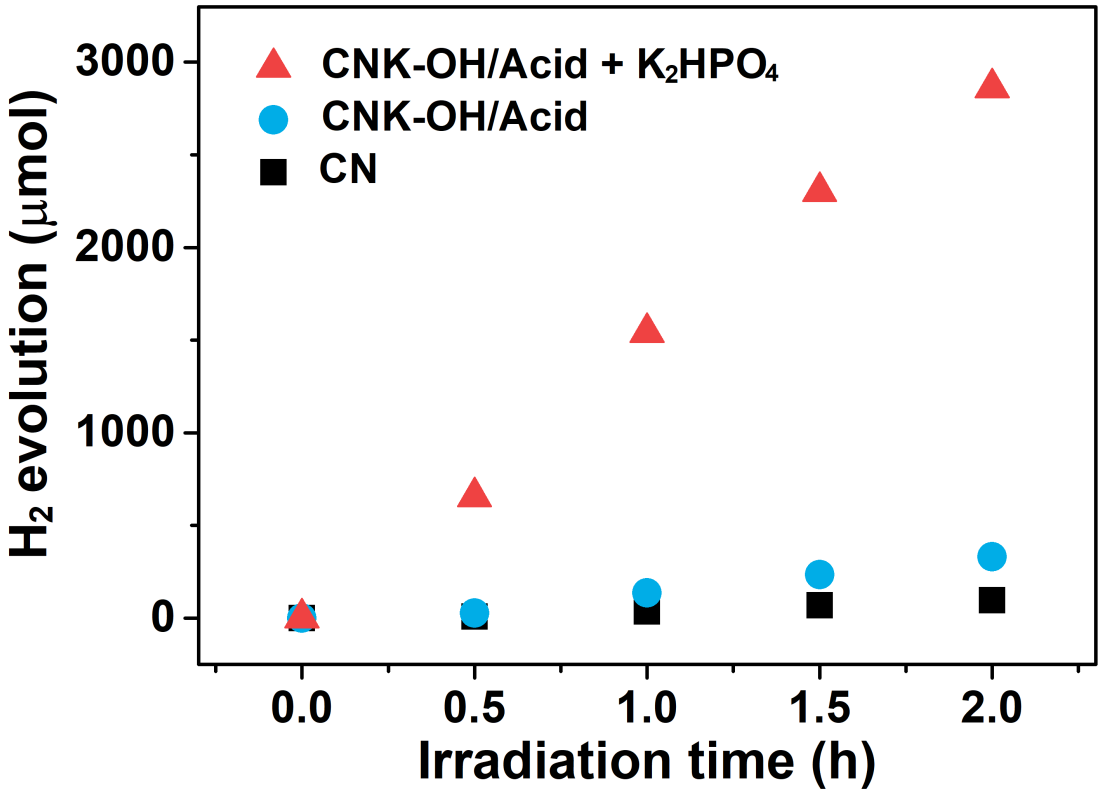


Figure 3.28 Photoactivity comparison of typical H_2 generation over the as-prepared samples. The generated H_2 gas is linearly increased with the irradiation time.

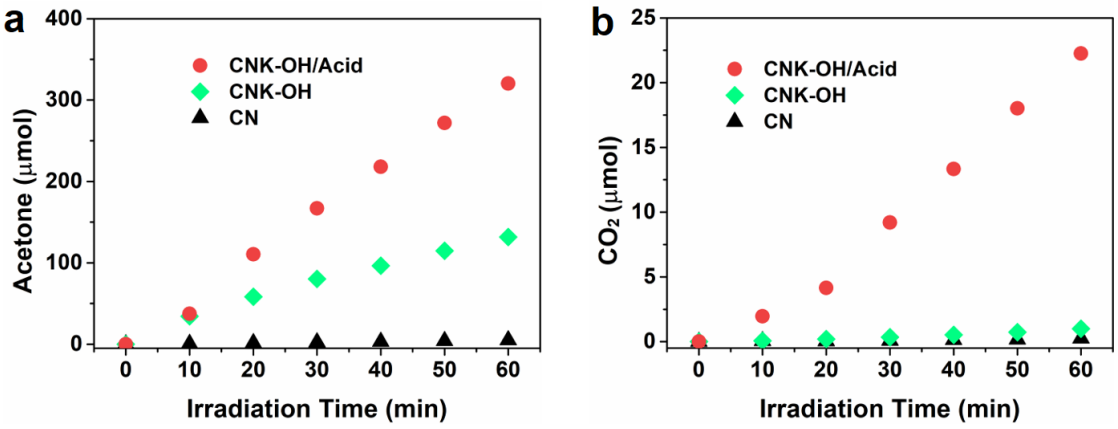


Figure 3.29 Photoactivity comparison of typical IPA oxidation over the as-prepared samples. (a) acetone evolution. (b) CO_2 evolution.

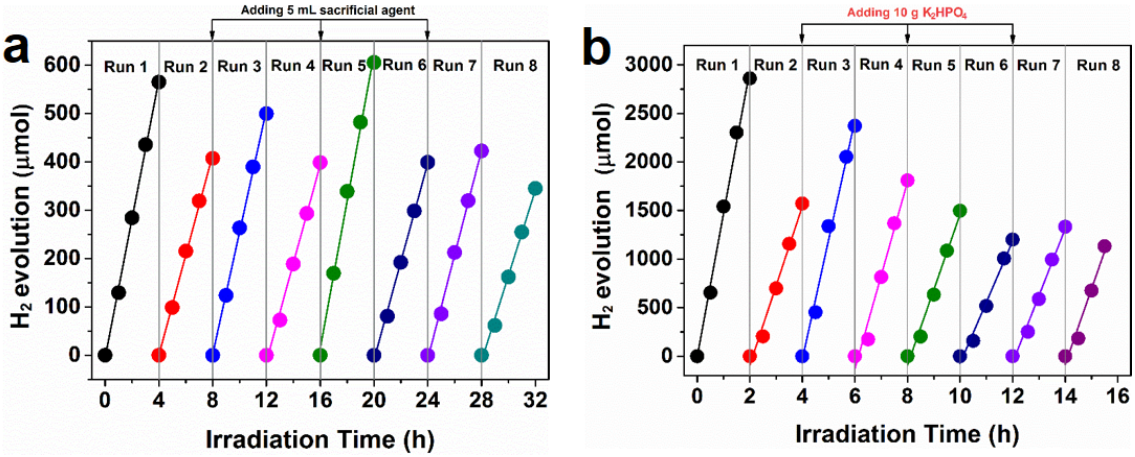


Figure 3.30 Cycle test of H_2 evolution over CNK-OH/Acid and CNK-OH/Acid with K_2HPO_4. (a) Cycle test of H_2 evolution over CNK-OH/Acid. (b) Cycle test of H_2 generation over CNK-OH/Acid with the adding of 0.2 mol K_2HPO_4. For the CNK-OH and corresponding exfoliated sample with the adding of K_2HPO_4, the photocatalytic H_2 evolution declines but the decay pace becomes slow during the eight cycles. It should be noted that the activity recovered partly when added the sacrificial agent and K_2HPO_4 during the long-term test.

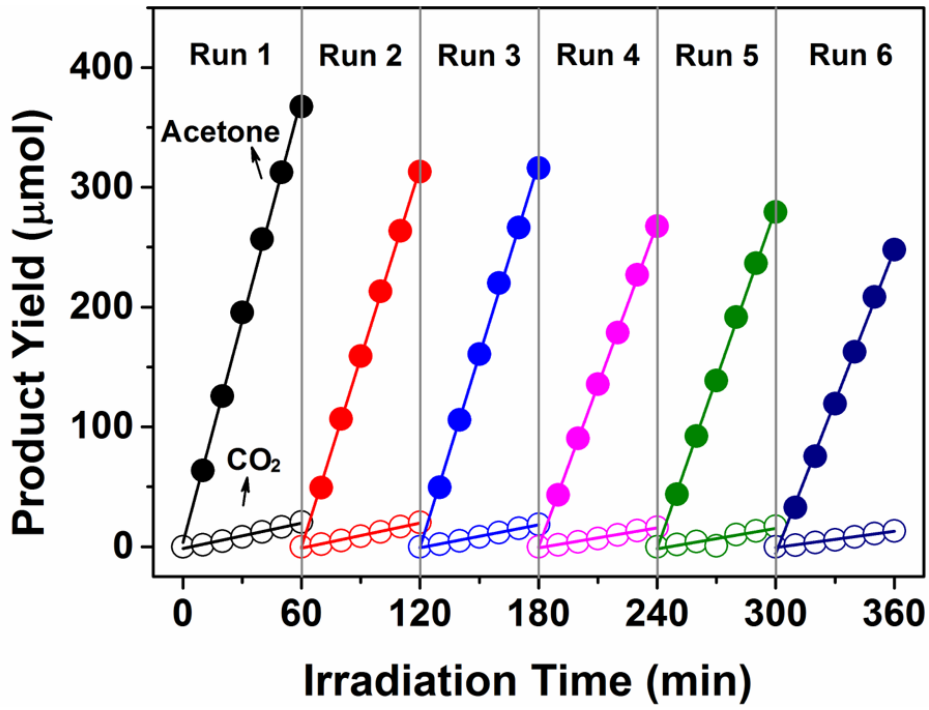


Figure 3.31 Cycle test of IPA photodegradation over CNK-OH/Acid. In general, the photodegradation declines but the decay pace becomes slow during the six cycles. The acetone and CO_2 evolution declines but the decay pace becomes slow during the six cycles.

3.4 Conclusions

In summary, we have developed a facile and controllable strategy to manipulate the exfoliation-reassembly status and the properties of polymeric CN via switching the interlayer species. Three remarkable advantages are created: 1) high exfoliation yield of ultrathin nanosheets reaches up to 48% in a mild solution; 2) the physical properties of the system are highly reversible by switching the exfoliation-reassembly state; 3) the exfoliated and reassembled CN with tunable properties can be applied to photocatalytic IPA degradation and H_2 evolution, giving a high AQY of 27% and 46 % for IPA degradation and H_2 evolution, respectively, at ~420 nm. This new proof-of-concept strategy will open up further opportunities for more effective delamination of extensive layered 2D materials towards advanced applications.

References

[1] X. Chen, S. Shen, L. Guo, S. S. Mao, *Chem. Rev.,* 2010, **110**, 6503-6570.

[2] H. Tong, S. Ouyang, Y. Bi, N. Umezawa, M. Oshikiri, J. Ye, *Adv. Mater.,* 2012, **24**, 229-251.

[3] X. Wang, K. Maeda, A. Thomas, K. Takanabe, G. Xin, J. M. Carlsson, K. Domen, M. Antonietti, *Nat. Mater.,* 2009, **8**, 76-80.

[4] W. J. Ong, L. L. Tan, Y. H. Ng, S. T. Yong, S. P. Chai, *Chem. Rev.,* 2016, **116**, 7159-7329.

[5] J. Liu, H. Wang, M. J. C. S. R. Antonietti, *Chem. Soc. Rev.,* 2016, **45**, 2308-2326.

[6] A. Savateev, M. Antonietti, *ACS Catal.,* 2018, **8**, 9790-9808.

[7] A. Savateev, I. Ghosh, B. Konig, M. Antonietti, *Angew. Chem. Int. Ed.,* 2018, **57**, 15936-15947.

[8] H. Yu, R. Shi, Y. Zhao, T. Bian, Y. Zhao, C. Zhou, G. I. N. Waterhouse, L. Z. Wu, C. H. Tung, T. Zhang, *Adv. Mater.,* 2017, **29**, 1605148-1605154.

[9] G. Zhang, G. Li, Z. A. Lan, L. Lin, A. Savateev, T. Heil, S. Zafeiratos, X. Wang, M. Antonietti, *Angew. Chem. Int. Ed.,* 2017, **56**, 13445-13449.

[10] Y. Wang, M. K. Bayazit, S. J. A. Moniz, Q. Ruan, C. C. Lau, N. Martsinovich, J. Tang, *Energy Environ. Sci.,* 2017, **10**, 1643-1651.

[11] Y. Li, S. Ouyang, H. Xu, X. Wang, Y. Bi, Y. Zhang, J. Ye, *J. Am. Chem. Soc.,* 2016, **138**, 13289-13297.

[12] P. Yang, H. Zhuzhang, R. Wang, W. Lin, X. Wang, *Angew. Chem., Int. Ed. Engl.,* 2019, **58**, 1134-1137.

[13] W. Liu, S. Xu, S. Guan, R. Liang, M. Wei, D. G. Evans, X. Duan, *Adv. Mater.,* 2018, **30**, 1704376-1704383.

[14] Q. Liang, Z. Li, Z. Huang, F. Kang, Q. Yang, *Adv. Funct. Mater.,* 2015, **25**, 6885-6892.

[15] Z. Zhou, Y. Zhang, Y. Shen, S. Liu, Y. Zhang, *Chem. Soc. Rev.,* 2018, **47**, 2298-2321.

[16] Y. Kang, Y. Yang, L. C. Yin, X. Kang, L. Wang, G. Liu, H. M. Cheng, *Adv. Mater.,* 2016, **28**, 6471-6477.

[17] Y. Yu, W. Yan, X. Wang, P. Li, W. Gao, H. Zou, S. Wu, K. Ding, *Adv. Mater.,* 2018, **30**, 1705060.

[18] G. Liu, G. Zhao, W. Zhou, Y. Liu, H. Pang, H. Zhang, D. Hao, X. Meng, P. Li, T. Kako, J. Ye, *Adv. Funct. Mater.,* 2016, **26**, 6822-6829.

[19] J. Zhang, Y. Chen, X. Wang, *Energy Environ. Sci.,* 2015, **8**, 3092-3108.

[20] X. Dong, F. Cheng, *J. Mater. Chem. A,* 2015, **3**, 23642-23652.

[21] H. Ou, L. Lin, Y. Zheng, P. Yang, Y. Fang, X. Wang, *Adv. Mater.,* 2017, **29**, 1700008-1700013.

[22] S. Yang, Y. Gong, J. Zhang, L. Zhan, L. Ma, Z. Fang, R. Vajtai, X. Wang, P. M. Ajayan, *Adv. Mater.,* 2013, **25**, 2452-2456.

[23] X. Zhang, H. Wang, H. Wang, Q. Zhang, J. Xie, Y. Tian, J. Wang, Y. Xie, *Adv. Mater.,* 2014, **26**, 4438-4443.

[24] P. Yang, H. Ou, Y. Fang, X. Wang, *Angew. Chem. Int. Ed.,* 2017, **56**, 3992-3996.

[25] P. Niu, L. Zhang, G. Liu, H.-M. Cheng, *Adv. Funct. Mater.,* 2012, **22**, 4763-4770.

[26] J. Ji, J. Wen, Y. Shen, Y. Lv, Y. Chen, S. Liu, H. Ma, Y. Zhang, *J. Am. Chem. Soc.,* 2017, **139**, 11698-11701.

[27] X. Lu, K. Xu, P. Chen, K. Jia, S. Liu, C. Wu, *J. Mater. Chem. A,* 2014, **2**, 18924-18928.

[28] J. Xu, L. Zhang, R. Shi, Y. Zhu, *J. Mater. Chem. A,* 2013, **1**, 14766.

[29] V. Nicolosi, M. Chhowalla, M. G. Kanatzidis, M. S. Strano, J. N. Coleman, *Science,* 2013, **340**, 1226419-1226419.

[30] P. Yasaei, B. Kumar, T. Foroozan, C. Wang, M. Asadi, D. Tuschel, J. E. Indacochea, R. F. Klie, A. Salehi-Khojin, *Adv. Mater.,* 2015, **27**, 1887-1892.

[31] S. Zhao, Y. Wang, J. Dong, C.-T. He, H. Yin, P. An, K. Zhao, X. Zhang, C. Gao, L. Zhang, J. Lv, J. Wang, J. Zhang, A. M. Khattak, N. A. Khan, Z. Wei, J. Zhang, S. Liu, H. Zhao, Z. Tang, *Nat. Energy,* 2016, **1**, 16184-16193.

[32] S. Yang, Y. Gong, J. Zhang, L. Zhan, L. Ma, Z. Fang, R. Vajtai, X. Wang, P. M. Ajayan, *Adv. Mater.,* 2013, **25**, 2452-2456.

[33] Y. Li, H. Xu, S. Ouyang, D. Lu, X. Wang, D. Wang, J. Ye, *J. Mater. Chem. A,* 2016, **4**, 2943-2950.

[34] X. Zhang, X. Xie, H. Wang, J. Zhang, B. Pan, Y. Xie, *J. Am. Chem. Soc.,* 2013, **135**, 18-21.

[35] Y. Zhang, A. Thomas, M. Antonietti, X. Wang, *J. Am. Chem. Soc.,* 2008, **131**, 50-51.

[36] G. Zhang, G. Li, T. Heil, S. Zafeiratos, A. Savateev, X. Wang, M. Antonietti, *Angew. Chem. Int. Ed.,* 2019, **58**, 3433-3437.

[37] J. Zhang, S. Hu, Y. Wang, *RSC Adv.,* 2014, **4**, 62912-62919.

[38] S. Ouyang, H. Tong, N. Umezawa, J. Cao, P. Li, Y. Bi, Y. Zhang, J. Ye, *J. Am. Chem. Soc.,* 2012, **134**, 1974-1977.

[39] G. Liu, T. Wang, H. Zhang, X. Meng, D. Hao, K. Chang, P. Li, T. Kako, J. Ye, *Angew. Chem. Int. Ed. Engl.,* 2015, **54**, 13561-13565.

[40] N. Tian, Y. Zhang, X. Li, K. Xiao, X. Du, F. Dong, G. I. Waterhouse, T. Zhang, H. Huang, *Nano Energy,* 2017, **38**, 72-81.

[41] Q. Han, B. Wang, J. Gao, Z. Cheng, Y. Zhao, Z. Zhang, L. Qu, *ACS Nano,* 2016, **10**, 2745-2751.

[42] X. Zhang, B. Peng, S. Zhang, T. Peng, *ACS Sustainable Chem. Eng.,* 2015, **3**, 1501-1509.

[43] J. Ran, T. Y. Ma, G. Gao, X.-W. Du, S. Z. Qiao, *Energy Environ. Sci.,* 2015, **8**, 3708-3717.

[44] J. Zhang, M. Zhang, C. Yang, X. Wang, *Adv. Mater.,* 2014, **26**, 4121-4126.

[45] H. Gao, S. Yan, J. Wang, Y. A. Huang, P. Wang, Z. Li, Z. Zou, *Phys. Chem. Chem. Phys.,* 2013, **15**, 18077-18084.

[46] L. Lin, H. Ou, Y. Zhang, X. Wang, *ACS Catal.,* 2016, **6**, 3921-3931.

[47] G. Zhang, G. Li, Z. A. Lan, L. Lin, A. Savateev, T. Heil, S. Zafeiratos, X. Wang, M. Antonietti, *Angew. Chem.,* 2017, **129**, 13630-13634.

[48] H. Yu, R. Shi, Y. Zhao, T. Bian, Y. Zhao, C. Zhou, G. I. Waterhouse, L. Z. Wu, C. H. Tung, T. Zhang, *Adv. Mater.,* 2017, **29**, 1605148.

[49] Z. Jin, N. Murakami, T. Tsubota, T. Ohno, *Appl. Catal., B,* 2014, **150-151**, 479-485.

[50] K.-i. Katsumata, R. Motoyoshi, N. Matsushita, K. Okada, *J. Hazard. Mater.,* 2013, **260**, 475-482.

[51] H.-Y. Jiang, G. Liu, T. Wang, P. Li, J. Lin, J. Ye, *RSC Adv.,* 2015, **5**, 92963-92969.

[52] J. Yu, S. Wang, J. Low, W. Xiao, *Phys. Chem. Chem. Phys.,* 2013, **15**, 16883-16890.

[53] T. Sano, S. Tsutsui, K. Koike, T. Hirakawa, Y. Teramoto, N. Negishi, K. Takeuchi, *J. Mater. Chem. A,* 2013, **1**, 6489-6496.

[54] J. Ma, C. Wang, H. He, *Appl. Catal., B,* 2016, **184**, 28-34.

[55] W. Wan, S. Yu, F. Dong, Q. Zhang, Y. Zhou, *J. Mater. Chem. A,* 2016, **4**, 7823-7829.

Chapter 4 Single-Co on N-rich carbon as co-catalyst for efficient photocatalytic H_2 production: the key roles of cleared interfaces and isolated metal sites

4.1 Introduction

Efficient conversion of renewable solar energy into clean H_2 via photocatalytic water splitting has been widely regarded as an attractive approach to solve the energy crisis and environment problem.[1-3] However, it still remains a great challenge to construct a low cost, robust system for highly efficient photocatalytic H_2 evolution despite enormous progress in this field during the past decades.[4] Most photocatalysts lack active sites on the surface for targeted reactions, leading to the fast recombination of excited carriers and poor performance.[5, 6] Loading co-catalysts with robust active sites can not only lower the activation energy of reactants but also accelerate the electron-hole separation at the semiconductor/co-catalyst interface.[7, 8] For the photocatalytic H_2 evolution test over polymeric carbon nitride in chapter 2 and chapter 3, noble metal Pt are used as efficient co-catalysts, however, its high-cost and extreme scarcity strongly restrain the potential commercialization of those photocatalytic system.

To date, great achievement has been made in exploring noble-metal-free co-catalysts to replace precious metal for constructing efficient photocatalytic system.[9-15] However, several major issues related to the intrinsic properties of current co-catalysts still exist for H_2 generation: (i) low atom utilization efficiency of the metal in co-catalysts because they usually exist as aggregated status; (ii) lack of surface functionalities to form robust connection with semiconductors towards fast transfer of carriers across junction; (iii) unfavorable Gibbs free energy for H_2 generation. Hence, it is highly imperative to design and construct favorable active sites with merits of cost-effective, high utilization efficiency and high turnover frequency for realizing efficient solar energy conversion.

Single-site catalysts, with isolated metal sites supported on solid substrates, especially on N-rich carbon (NC), are emerging as a highly attractive class of catalysts because of their unusual electronic structures, extraordinary catalytic properties, etc.[16-21] These materials feature diverse moieties such as rich N species[22] on surface, tunable metal sites with flexible coordination[23-25] and maximum utilization of metal-site[26] especially when

those single sites are anchored on ultrathin support. These attractive characteristics of single-atom embedded carbon-based family might be utilized for solving the issues mentioned above and render it to be highly promising as co-catalysts. However, such kind of materials have rarely been used as co-catalysts in photocatalytic system, especially for achieving outstanding performance in photocatalysis.

The co-catalysts with elaborate single-site can generate the targeted product upon capturing the energetic photoelectrons; however, it also inevitably brings a contaminated interface between photoharvester and co-catalyst caused by the adventitious carbon at the junction. The interfaces, where electrons shuttle, are extremely crucial for efficient photochemistry process. A contaminated interface will severely block the electron transfer to the co-catalytic single-site and such negative effect might also exist for various advanced heterostructures[27-31]. It is worth stressing that surface adventitious carbon widely exists on various materials, such as TiO_2, carbon nitride and black phosphorus;[32-35] upon forming heterostructure, these carbon species will locate at the interface and lead some substantial and underlying effects on the photocatalytic process. However, the detailed roles of those adventitious carbon at the surface or interface in photocatalysis are often neglected but should arise our attention. Recently, Diebold et al. disclosed that TiO_2 selectively adsorbs carboxylic acids on its surface from air/solution and further pointed out the potential effect of the surface carboxylate monolayers on photocatalysis;[32] Medford et al. revealed that the surface adventitious carbon could strongly interact with N_2 molecules and promote photocatalytic N_2 fixation.[33] Further clarifying the exact effect of these carbon species located interfaces in heterostructures are quite essential for constructing robust photocatalytic system but has not been explored at present.

Motivated by the aforementioned key issues, we seek to create a clean heterostructured interface aiming at speeding up the carriers flow to the robust single-site co-catalysts for constructing photocatalytic system with record activity and metal utilization efficiency. Herein, we report a rational design and novel synthesis of single Co implanted ultrathin N-rich carbon nanosheets (Co-NC) and create a cleared junction between photoharvester CdS and co-catalyst Co-NC through calcination-induced elimination of interfacial adventitious carbon. The cleared interfaces collaborate with the robust isolated $Co-N_4$ sites to achieve an outstanding visible-light-driven H_2 evolution activity with a rate of 4.34 mmol/h, an AQY of 63.9% at 400 nm. Remarkably, the optimal system achieves an ultrahigh TOF_{Co} of up to 16714.7 h^{-1}. This new strategy constructs an efficient system for

H_2 photogeneration via creating robust single-atom co-catalyst Co-NC and simultaneously clearing the interface between CdS and Co-NC. This built-in system not only clarifies the significant blocking effect of widely existed surface adventitious carbon on charge transport, but also highlights both the essential roles of cleared interface and single-atom based materials in photocatalysis.

4.2 Experimental section

4.2.1 Materials preparation

Chemicals: chemicals including melamine (99.0%), zinc acetate ($Zn(OAc)_2$), cobalt acetate tetrahydrate ($Co(CH_3COO)_2{\cdot}4H_2O$; 99%), iron(III) nitrate nonahydrate ($Fe(NO_3)_3{\cdot}9H_2O$; 99.9%), nickel chloride hexahydrate ($NiCl_2{\cdot}6H_2O$; 99.9%), methanol (99.5%), ethanol (99.5 %), lactic acid, sodium hydroxide (NaOH; 97%) and hydrochloric acid (HCl; 36%) were purchased from the Wako Co. and cadmium sulfide (CdS; 98%) was purchased form Strem Chemical, Inc. All of them were used without further purification.

Synthesis of (M)-NC: Co/Zn-supermolecular precursor was first prepared by a facile and scalable wet-chemical method. Typically, melamine (1.26g, 10 mmol), $Zn(OAc)_2$ (1.82g, 9.9 mmol) and $Co(OAc)_2{\cdot}4H_2O$ (24.91 mg, 0.1 mmol) was added to 100 mL methanol with vigorous stirring, then the dispersion was transferred to an oil bath and refluxed at 70 ^oC for 3 h. The obtained light pink solid was centrifuged and washed with ethanol for two times, then dried at 70 ^oC under vacuum. The yield wad estimated to be 85.8 % with 2.66 g light pink powder product.

Subsequently, the above powder precursor underwent a two-stage pyrolysis and carbonization process (retained at 650 ^oC for 1h, then increased to at 950 ^oC and held for 3 h with a ramping rate of 3 ^oC/min) in tube furnace under argon atmosphere. After cooling down to the room temperature, the obtained black product was leached with 0.5 M HCl to remove metal particles and unstable species and successively washed using distilled water. Afterwards, the obtained sample was further crushed into small-sized ultrathin nanosheets by ball milling treatment, the final resultant sample was denoted as Co-NC. A typical wet-milling was performed on a planetary ball mill (Fritsch, P-7) and conducted at 400 rpm for 15 h using distilled water as the solvents.

Other (M)-NC(NS) (M = Fe, Ni) were synthesized using similar procedure, except employing different metal precursors and different solvents for the preparation of

corresponding supermolecular precursors. In detail, 0.1 mmol $Fe(NO_3)_3 \cdot 9H_2O$ and 0.1 mmol $NiCl_2 \cdot 6H_2O$ severed as the metal source for precursor fabrication of Fe-NC and Ni-NC. In the case of Ni-NC, 10 mL ethanol and 90 mL methanol were employed as the solvent to prepare the precursor. For NC, only 10 mmol $Zn(OAc)_2$ was used to prepare the precursor.

Preparation of CdS/Co-NC composites: well-dispersed (M)-NC in aqueous solution was added into the dispersion of commercial CdS with stirring, after stirring for 5 mins, the mixture was filtered and dried at 30 ^oC under vacuum. A series of CdS/Co-NC samples with different Co-NC content (0.5, 1, 1.5, 2.0, 2.5 wt %) were prepared. To reinforce the interface interaction between CdS and (M)-NC, the dried sample was annealed at different temperature (400, 450, 500, 550 ^oC) for 1 h under Ar atmosphere. The CdS/Co-NC(RT) and CdS/Co-NC(500) refers to the hybrid CdS/Co-NC without and with annealing at 500 ^oC under Ar atmosphere, respectively. The composites with different loading amount or treated at different temperature will be specifically stated.

4.2.2 Material characterization

XRD patterns of the as-prepared samples were collected with a powder X-ray diffractometer (Cu Kα radiation source, X'pert powder, PANalytical B.V., Netherlands). UV−visible (UV−vis) diffuse reflectance spectra of the samples were recorded on an UV−visible spectrophotometer (UV-2700, Shimadzu, Japan) equipped with an integrating sphere, then converted into absorption spectra by Kubelka−Munk transformation. Nitrogen adsorption–desorption isotherms, and surface area were recorded using a BEL SORP-mini II (BEL Japan INC., Japan), and were calculated via the Brunauer-Emmett-Teller (BET) method. The Photoluminescence (PL) properties were investigated using a fluorescence spectrophotometer (Fluorolog-3, HORIBA Scientific, America). X-ray photoelectron spectroscopy (XPS) measurements were carried out on XPS instrument (Escalab 250, Thermo SCIENTIFIC, America). All binding energies were referenced to the C *1s* peaks of the surface adventitious carbon at 284.8 eV. The morphologies of samples were characterized with Field Emission Scanning Electron Microscope (JSM-6701F, JEOL Co., Japan) and Transmission Electron Microscope (TEM) (JEM-2100F, JEOL Co., Japan). Energy-dispersive X-ray spectroscopy (EDS) mapping was also recorded with same TEM instrument. The STEM characterizations were performed on a JEOL ARM-200F field-emission transmission electron microscope. Raman spectra were collected using a Horiba Jobin Yvon LabRAM

system with a 532 nm excitation laser. The electron spin resonance (ESR) measurements were performed on an ESR spectrometer (JES-FA200, JEOL Co., Japan) at liquid nitrogen temperature (77 K). The X-ray absorption fine structure spectra were performed at 1W1B station in Beijing Synchrotron Radiation Facility (BSRF). The XAFS data were recorded in fluorescence excitation mode using a Lytle detector. Co foil, CoO and Co_3O_4 were used as the reference. The acquired XAFS data were analyzed by Athena and Artemis interfaces to the IFFEFIT software, according to the standard procedures.

4.2.3 Photoelectrochemical measurement

The photoelectrochemical properties were investigated in a three-electrode cell by using an electrochemical station (Model-660D, CH instruments). The catalyst coated ITO glass, a Pt foil, and an Ag/AgCl electrode and lactic acid solution (20 vol % lactic acid, pH: 5.1) were used as the working electrode, the counter-electrode, the reference electrode, and the electrolyte, respectively. A 300 W Xe arc lamp equipped with a L42 cutoff filter was utilized as a light source ($\lambda > 400$ nm). EIS were recorded at an applied potential of -0.6 V versus Ag/AgCl over the frequency range of 0.1 MHz-0.1 Hz. The photocurrent with on/off cycles was measured at an applied potential of -0.6 V versus Ag/AgCl.

4.2.4 Computational details

Spin-polarized calculations were conducted with the Vienna Ab-initio Simulation Package (VASP 5.4.4).[36, 37] The electron exchange and correlation were described with the generalized gradient approximation (GGA) using Perdew–Burke–Ernzerhof (PBE) functional.[38] The electron-ion interaction was described by the projector augmented-wave formalism (PAW).[39, 40] Since GGA was not able to correctly describe the d electronic structure of the metal, the GGA+U approximation was adopted with the Dudarev ‘‘+U’’ term with a U-J value of 3 eV for the d electrons of Fe, Ni and Co atoms,[41, 42] since the U-J value chosen from 3.00 eV to 3.42 eV has merely influence for the H binding energy from our test results. The plane wave cut-off energy is set to 400 eV and electronic self-consistent convergence is 10^{-6} eV. Geometries were converged to a residual force smaller than 0.02 eV/Å. The Brillouin zone was integrated by a 3 × 3 × 1 Monkhorst–Pack grid. In the case of H_2 molecular, which was set in a 15×15×15 Å cubic box, the Gamma point only calculation was performed.

The CC model was built from 5×5 graphene (001) surface monolayer, which contains 50 atoms in total, and the vacuum thickness was set to 12 Å. To create the NC model, one of C atom was replaced by an N atom from the CC model. While the Fe-NC model was built by embedding a FeN_4 atomic structure in the CC model. During geometry optimization of CC model, NC model, and Fe-NC model, all atomic positions were fully relaxed and the lattice constant was relaxed in 2 dimensions. The Fe was replaced by Co, Ni, and vacancy, resulting in the Co-NC, Ni-NC and NC_{vac} model, respectively. In order to compare the influence of metal, the lattice constant was consistent with the Fe-NC model.

The binding free energies of the H atom on surface were calculated via $\Delta G = G_{H/surf} - G_{surf} - 1/2G_{H2}$, where $G_{H/surf}$ denoted the free energy of H adsorbent model, G_{H2} represented the free energy of H_2 molecular and G_{surf} stood for the free energy of surface, including CC, NC, NC_{vac}, Fe-NC, Ni-NC, and Co-NC model. The free energy was obtained from the equation $G = E_{ele} + E_{vib} + E_t + E_r - TS$ as in previous work,[43] where E_{ele}, E_t, E_r, and E_{vib} are the electronic, translational, rotational and vibrational energies, respectively. And S is the entropy, T was set to room temperature (298.15 K).

4.2.5 Photocatalytic activity measurement

The photocatalytic H_2 evolution test was carried out in a glass reactor with a closed gas circulation system. In a typical test, 150 mg photocatalyst was firstly dispersed with a magnetic stirrer in 280 mL 20 vol % lactic acid solution (the pH of the solution was adjusted by NaOH in advance). After vacuumizing, H_2 evolution over the photocatalyst was carried out under visible light irradiation (light source, 300 W Xe lamp equipped with an L42 cutoff filter, $\lambda > 400$ nm). The evolved H_2 was analyzed by online gas chromatography (GC-8A; Shimadzu Corp., Japan) equipped with a thermal conductivity detector. The photocatalytic H_2 generation rates over as-prepared samples were fitted with the four points ranging from 0.5 h to 2h.

The apparent quantum efficiency (AQY) was measured under similar conditions as described above except for the light intensity and the wavelength regions of the irradiation light. A series of band-pass filters were adopted to control the wavelength regions of incident light. A water filer was also used together with the band-pass filter to avoid the possible damage caused by heating effect of Xe lamp. The average intensity of irradiation

was determined by using a spectroradiometer (Ushio, USR-40, Japan). The AQY at each monochromatic wavelength was calculated by following the equation below:

AQY for H_2 evolution = N(H_2) * 2 / N(photons) * 100%

Note: N(H_2) represents the molecular number of evolved H_2 and N(photons) means the number of incident photons.

4.3 Results and discussion

4.3.1 Synthesis and characterization of co-catalyst Co-NC

The ultrathin single atom co-catalysts ((M)-NC; M = Co, Fe, Ni) were synthesized mainly via two steps as illustrated in Figure 4.1: (i) pyrolysis of a supramolecular precursor; (ii) downsizing the obtained hierarchical sheets into small-sized ultrathin nanosheets by ball milling treatment. X-ray powder diffraction (XRD) pattern of Co-NC (Figure 4.2a) exhibits a broad peak centered at ~26.0º, assigned to the (002) plane of graphitic carbon. Raman spectra (Figure 4.2b) show two typical signals belonging to defect-rich carbon, i.e., D band (1355.9 cm^{-1}) and G band at (1591.6 cm^{-1}). The Co-NC possesses a specific surface area of 222.7 m^2/g and presents as uniform 2D sheets with a planar size of ~200 nm (Figure 4.3a and 4.3b) and an ultrathin thickness of ~1.5 nm (Figure 4.3c and 4.3d). The high-resolution transmission electron microscopy (HRTEM) image (Figure 4.3b) reveals some typical fringes, corresponding to few-layer carbon sheet. In particular, no signal of Co clusters or nanoparticles are detected on the ultrathin nanosheets by scanning electron microscopy (SEM), TEM and XRD. The TEM-EDS (energy disperse X-ray) mapping results (Figure 4.4a) reveal that Co, N and C distribute homogeneously across the entire architecture. Moreover, atomic-resolution aberration-corrected high-angle dark-field scanning TEM (HAADF-STEM) was used to directly distinguish the Co species with atomic scale. As clearly revealed in Figure 4.4b, isolated Co sites, appeared as individual bright spots with an average size ~0.2 nm, are well dispersed on the N-rich carbon nanosheets.

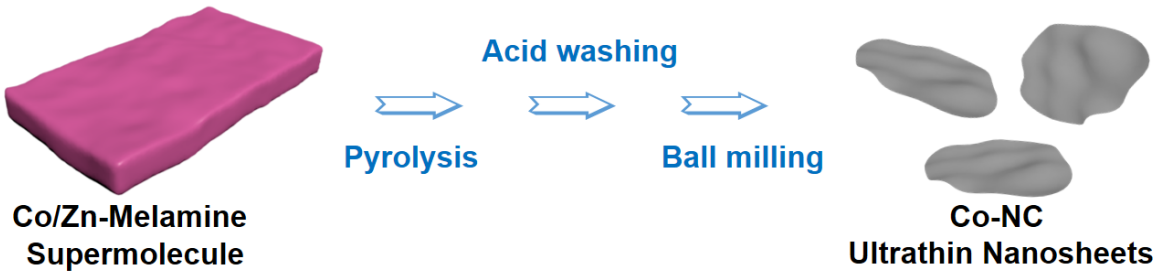


Figure 4.1 Scheme of the formation process Co-NC co-catalyst.

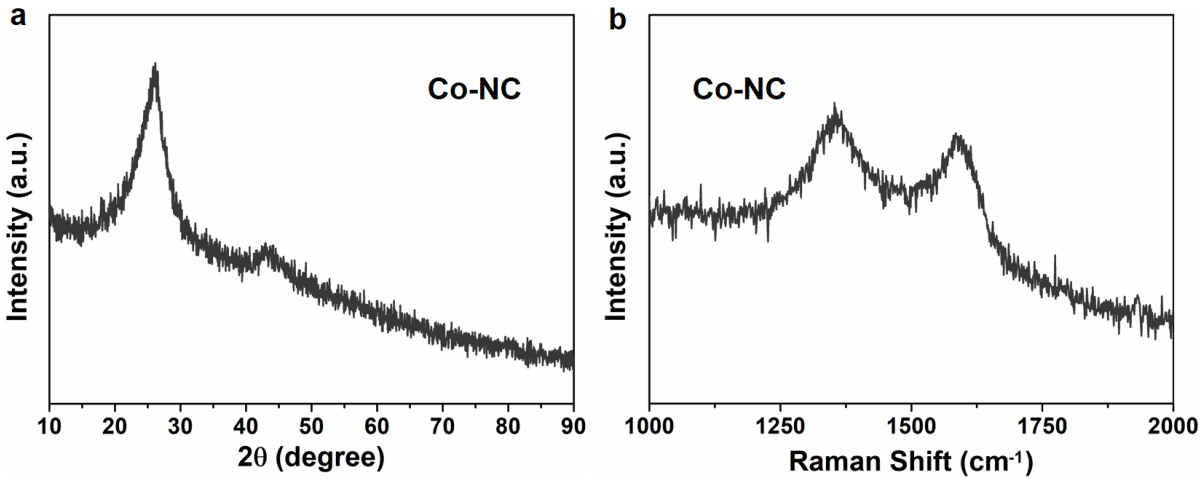


Figure 4.2 XRD pattern (a) and Raman spectrum (b) of Co-NC.

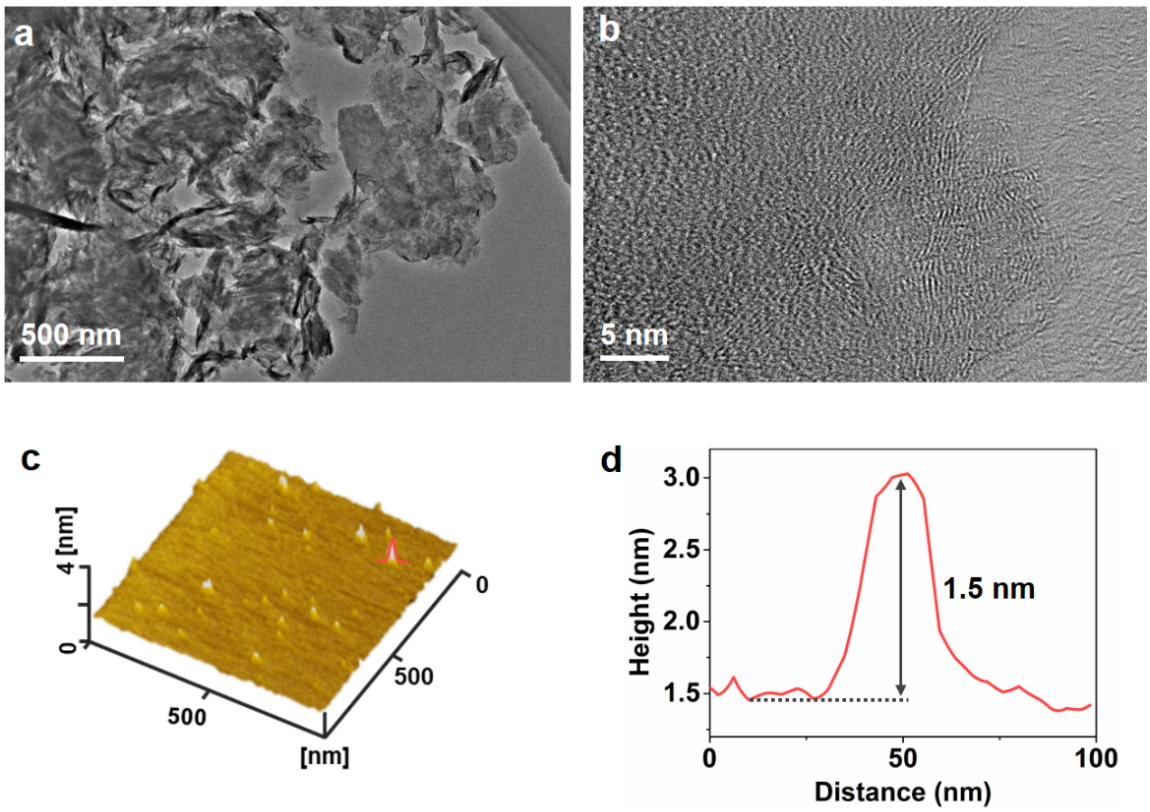


Figure 4.3 (a, b) TEM images of Co-NC. Atomic force microscopy (AFM) image of Co-NC (c) and its typical height profile (d).

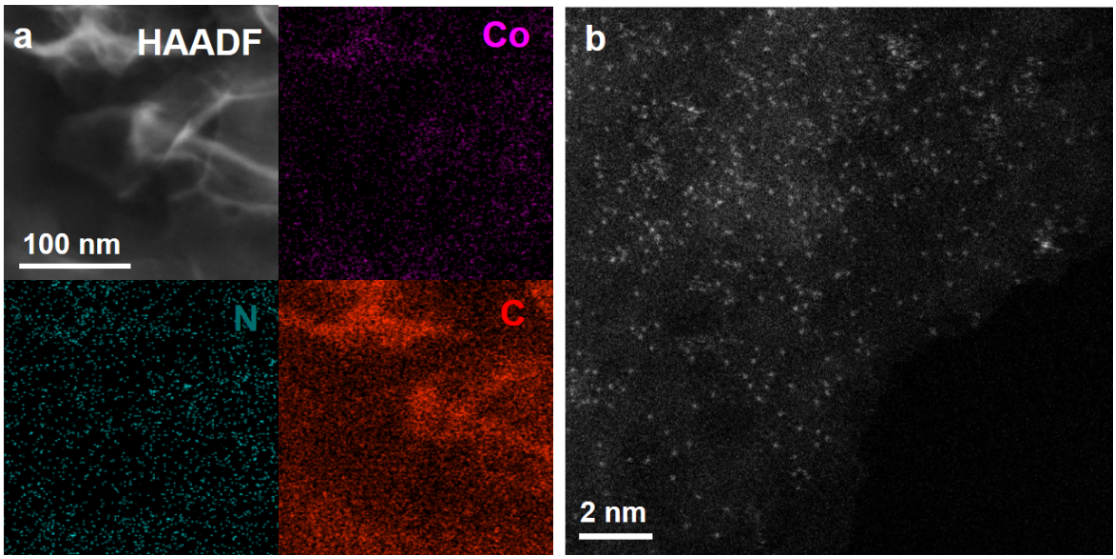


Figure 4.4 (a) EDS elemental mapping of Co-NC. (b) Aberration-corrected HAADF-STEM image of Co-NC.

The chemical composition and valence states of Co-NC were examined using X-ray photoelectron spectroscopy (XPS) (Figure 4.5) measurement. The isolated Co sites

exhibit a peak at 780.6 eV, corresponding to the Co-N species (Figure 4.5a).[44] The atomic content of Co in Co-NC determined by XPS is 0.77 at % (3.5 wt %, close to 3.38 wt % examined by inductively coupled plasma atomic emission spectroscopy). Four types of N species (Figure 4.5b) including pyridinic-N (398.8 eV), pyrrolic-N (400.0 ev), graphitic-N (401.3 eV), oxidized-N (402.8 eV) can be clearly distinguished, among which the pyridinic N serves as the anchor sites for stabilizing the single Co. This assumption was supported by the shift of pyridinic N peak towards higher binding energy after introducing Co species while other kinds of N species remain almost unchanged, revealing the binding formation between Co and pyridinic N.

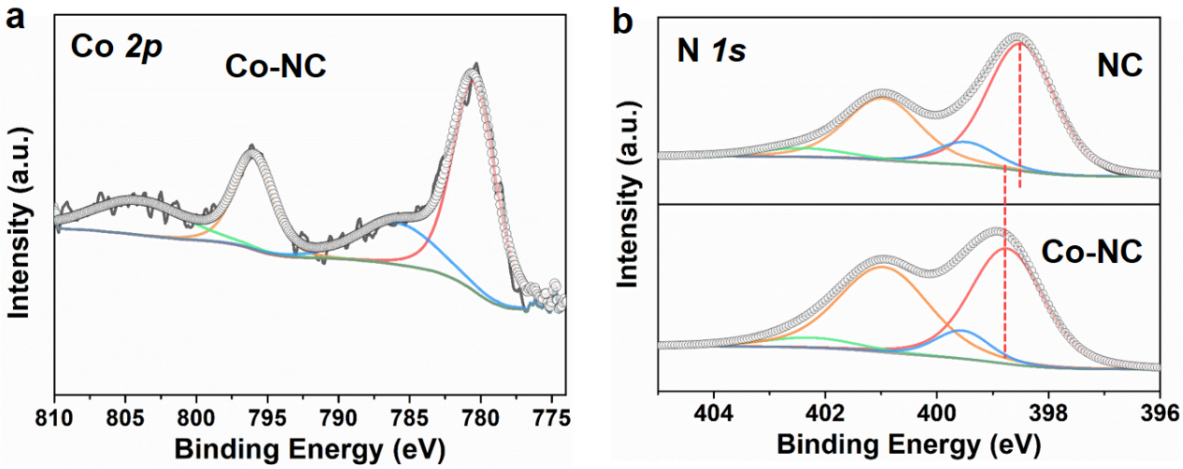


Figure 4.5 Chemical composition of Co-NC co-catalyst. High-resolution Co *2p* (a) and N *1s* (b).

To further examine the coordination configuration and chemical state of the single Co sites, X-ray absorption fine structure (XAFS) measurements were performed. The results reveal that the Co species exist in an isolated state and stabilized by nitrogen in the form of Co-N_4. Figure 4.6a presents the X-ray absorption near-edge structure (XANES) spectra of Co-NC in comparison to standard spectra of Co foil, CoO and Co_3O_4. The absorption edge of Co-NC locates between those for CoO and Co_3O_4, and close to that of CoO, clearly suggesting the Co sites deliver a slightly higher oxidation state than Co^{2+}.

More detailed structural information of Co sites can be obtained based on extended X-ray absorption fine structure (EXAFS) analysis (Figure 4.6b). The Co-NC shows a dominant Co-N peak at 1.42 Å, which is shorter than Co-O signal at 1.71 Å in CoO and 1.49 Å in Co_3O_4. Additionally, no Co-Co peak can be observed at 2.12 Å for Co-NC, corroborating the atomic dispersion of single Co sites in Co-NC. We further investigate the coordination of Co sites by EXAFS curve fitting analysis. The surrounded N number

of Co center is estimated to be four according to the fitting results (Figure 4.6c, Table 4.1). In further electron spin resonance (ESR) analysis (Figure 4.6d), the similar spectra with close g value for Co-NC and commercial cobalt (II) phthalocyanine (CoPc) at 77 K reveal that the Co sites in Co-NC exhibits similar coordination with four N sites and valence state (Co^{2+}) with those in CoPc, which coincides well with the XAFS analyses. Note that the signal pointed by an arrow with the g value of 2.2097 is attributed to the low spin Co (II) in CoPc.[45]

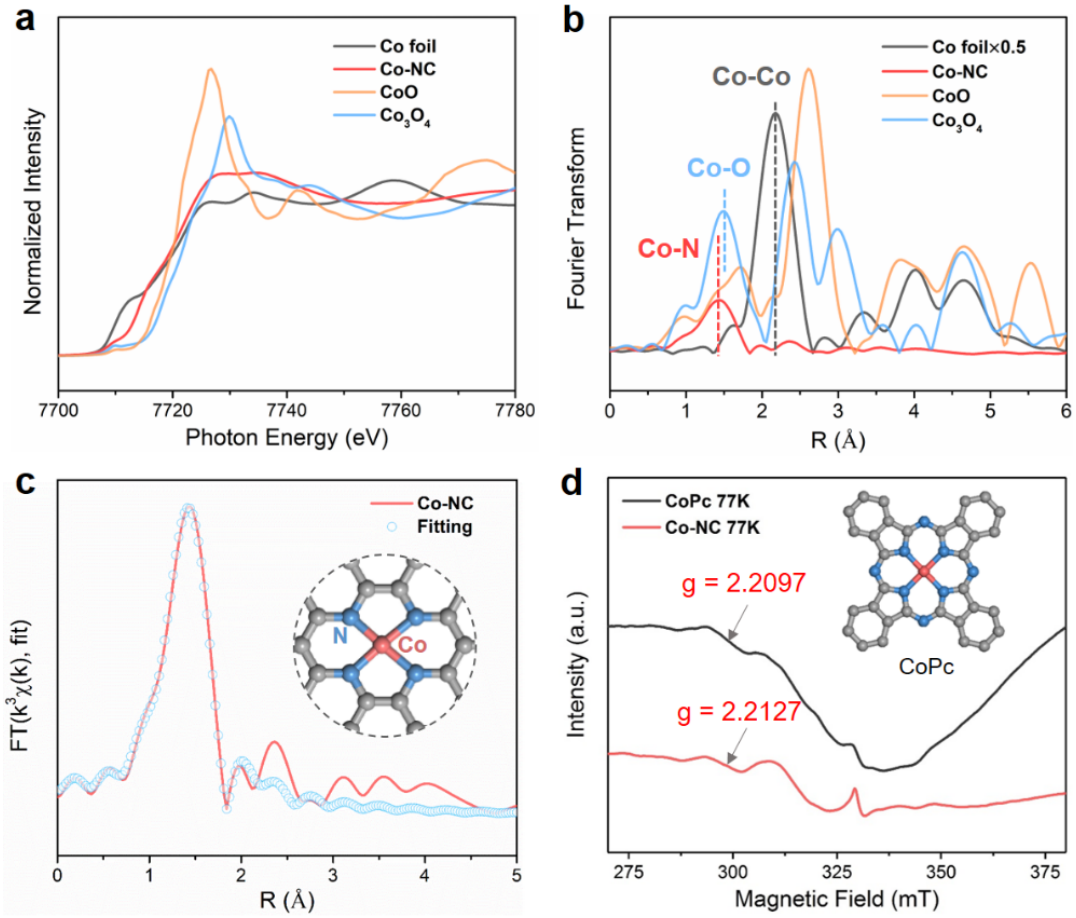


Figure 4.6 Site coordination analyses of Co-NC co-catalyst. (a) Co K-edge XANES spectra of Co-NC and reference samples. (b) Fourier transformed k^3-weighted χ(k)-function of the EXAFS spectra for Co K-edge. (c) Corresponding EXAFS fitting curve for Co-NC. Inset: the proposed Co-N_4 configuration. (d) ESR spectra of Co-NC and reference CoPc.

Table 4.1 Structural parameters of Co-NC extracted from the EXAFS fitting.

Sample	Path	CN	*R* (Å)	σ^2 (Å^2)	ΔE_0 (eV)	R factor
Co-NC	**Co-N**	**4**	**1.915**	**0.00804**	**0.585**	**0.01300**

*Reduction factor S_0^2 is 0.706; CN is the coordination number; *R* is interatomic distance (the interatomic length between cobalt site and surrounding N sites); σ^2 is Debye-Waller factor (a measure of thermal and static disorder in absorber-scatter distances); ΔE_0 is edge-energy shift (the difference between the zero kinetic energy value of the sample and that of the theoretical model). R factor is used to value the goodness of the fitting. Definition of *R* factor is a measure of mean square sum of the misfit at each data point.

4.3.2 Photocatalytic H_2 evolution activity

As single Co sites based catalysts have been reported as promising electrocatalysts for hydrogen evolution,[46] enlightened by this, here we constructed a system composed of CdS/(M)-NC for visible-light-driven hydrogen generation, wherein the CdS serves as the photo-harvester and (M)-NC acts as the co-catalysts for water reduction. The CdS/(M)-NC(RT) and CdS/(M)-NC(500) represent the composites without and with annealing treatments, respectively; the loading amount of co-catalysts for these hybrids is 1 wt% unless otherwise stated. These ultrathin (M)-NC co-catalysts can be uniformly and facilely grafted on the surface of CdS via simple mixing process as identified by the SEM analyses, UV-vis spectra, and TEM elemental mapping analyses (Figure 4.7 and 4.8).

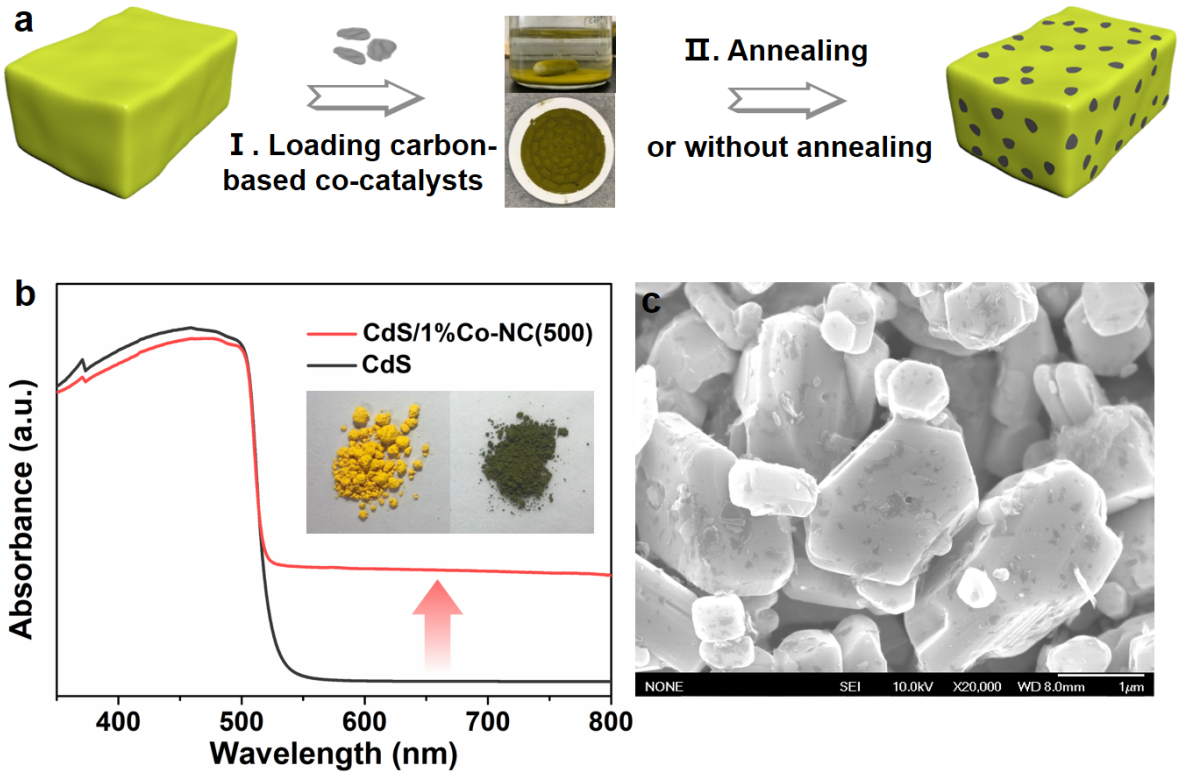


Figure 4.7 Synthesis and characterizations of CdS/Co-NC. (a) Schematic synthesis process of CdS/co-catalysts. (b) UV−vis spectra of CdS and CdS/Co-NC(500). Inset

shows their photographs (left: CdS; right: CdS/Co-NC(500)). (c) SEM images of CdS/Co-NC(500).

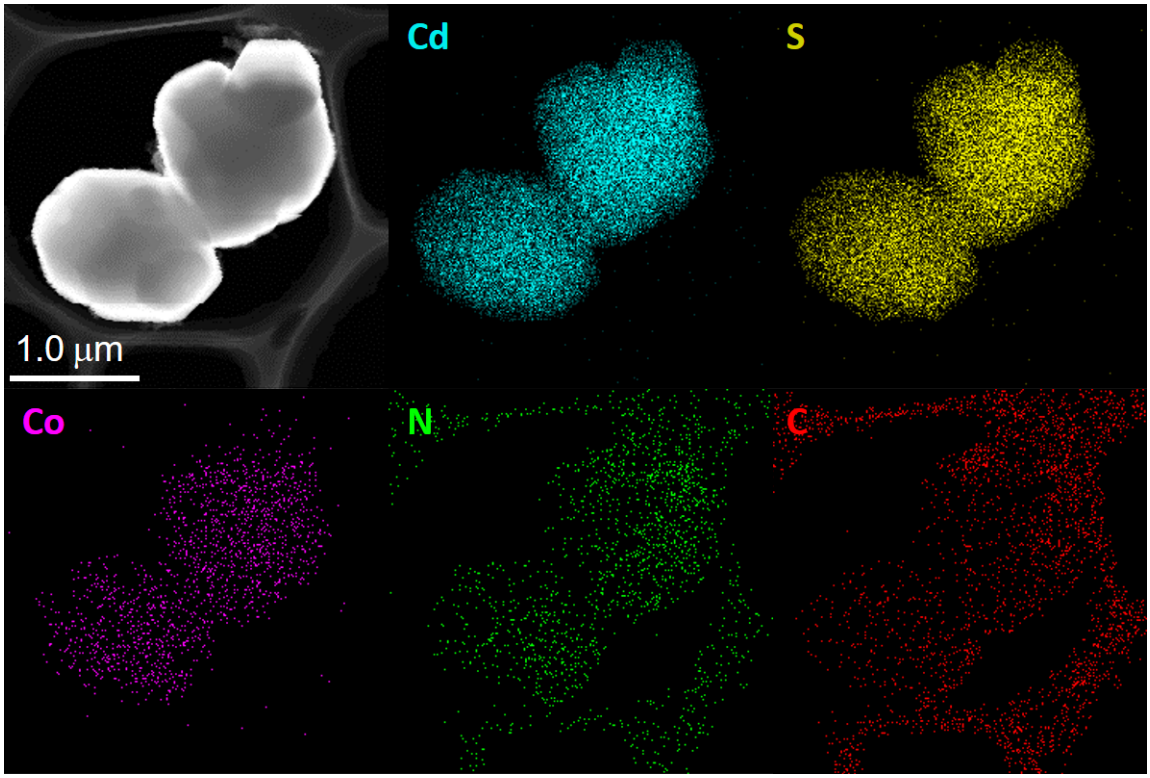


Figure 4.8 EDS elemental mapping of CdS/1%Co-NC(500).

As shown in Figure 4.9a, bare CdS shows a poor photocatalytic hydrogen evolution activity of ~15 μmol/h and sole Co-NC is inactive for hydrogen evolution. Remarkably, the coupling of Co-NC with CdS drastically boost the activity of CdS, reaching up to 4.34 mmol/h under optimized conditions (Figure 4.10) and achieve an apparent quantum yield (AQY) of 63.9% at 400 nm (Figure 4.9b), representing the currently achieved state-of-the-art H_2 generation activity among all the CdS-based H_2 generation system (Table 4.2). Such an activity of CdS/Co-NC(500) even far exceeds that of CdS/1wt%Pt under appropriate conditions (Figure 4.9a). Besides that, the isolated Co sites in this system can afford an ultrahigh turnover frequency (TOF) reaching up to 16714.7 h^{-1} (the number of moles of generated H_2 divided by the number of moles of Co (derived from XPS) in Co-NC) when we altered amount of catalysts (Figure 4.11a). Such a high TOF value far surpasses that of advanced Co-based species on CdS (600 h^{-1}) by a factor of 27.9 times.[12] In addition, the CdS/Co-NC(500) exhibits considerable stability as identified by the relatively stable H_2 generation in the four-cycle test (Figure 4.12a,b; at pH = 6 and 7). Figure 4.11b shows that the optimal sample CdS/Co-NC(500) can even exhibit an activity

of 814 μmol/h with excellent stability under the irradiation of simulated sunlight with a light intensity of 100 mW cm^{-2}. To further judge the advantage of ultrathin morphology of support in H_2 evolution activity, another single-Co (Co-N_4) co-catalysts with rhombic dodecahedron morphology (Co-NC_{rd}) was fabricated according to the previous report[24] (Figure 4.13, inset of Figure 4.13c,d shows the atomic structure of Co site) and further anchored on CdS followed by heat treatment at 500 °C. Under the same conditions, the CdS with ultrathin Co-NC (Figure 4.14; 4.34 mmol/h; 4801.7 h^{-1}) achieves a ~3 times H_2 evolution rate and a ~2 times TOF those of CdS/Co-NC_{rd}(500) (1.51 mmol/h; 2249.6 h^{-1}), respectively.

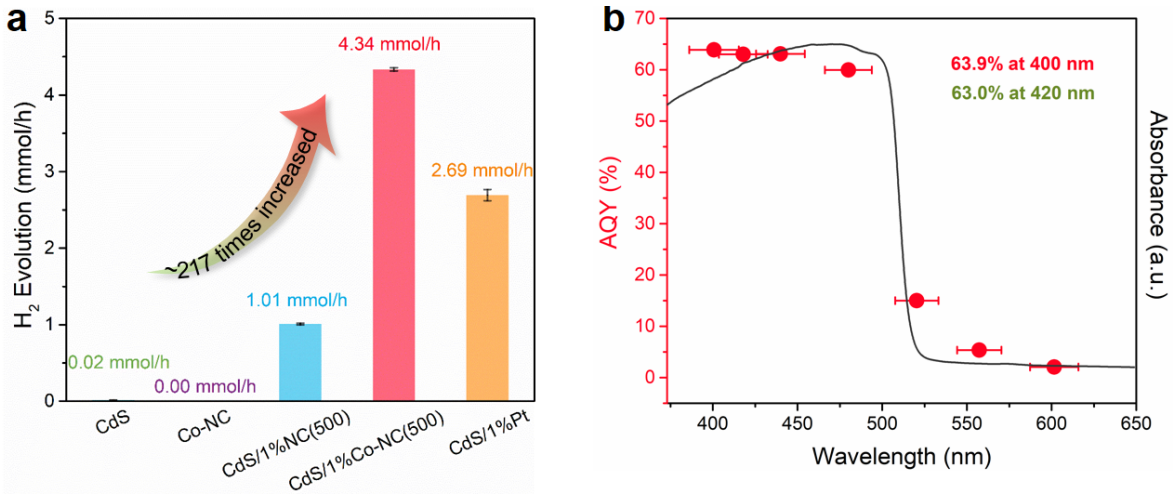


Figure 4.9 (a) A comparison of H_2 evolution activity of as-prepared samples. (b) Wavelength-dependent apparent quantum yield (AQY) of H_2 generation from CdS/1%Co-NC(500).

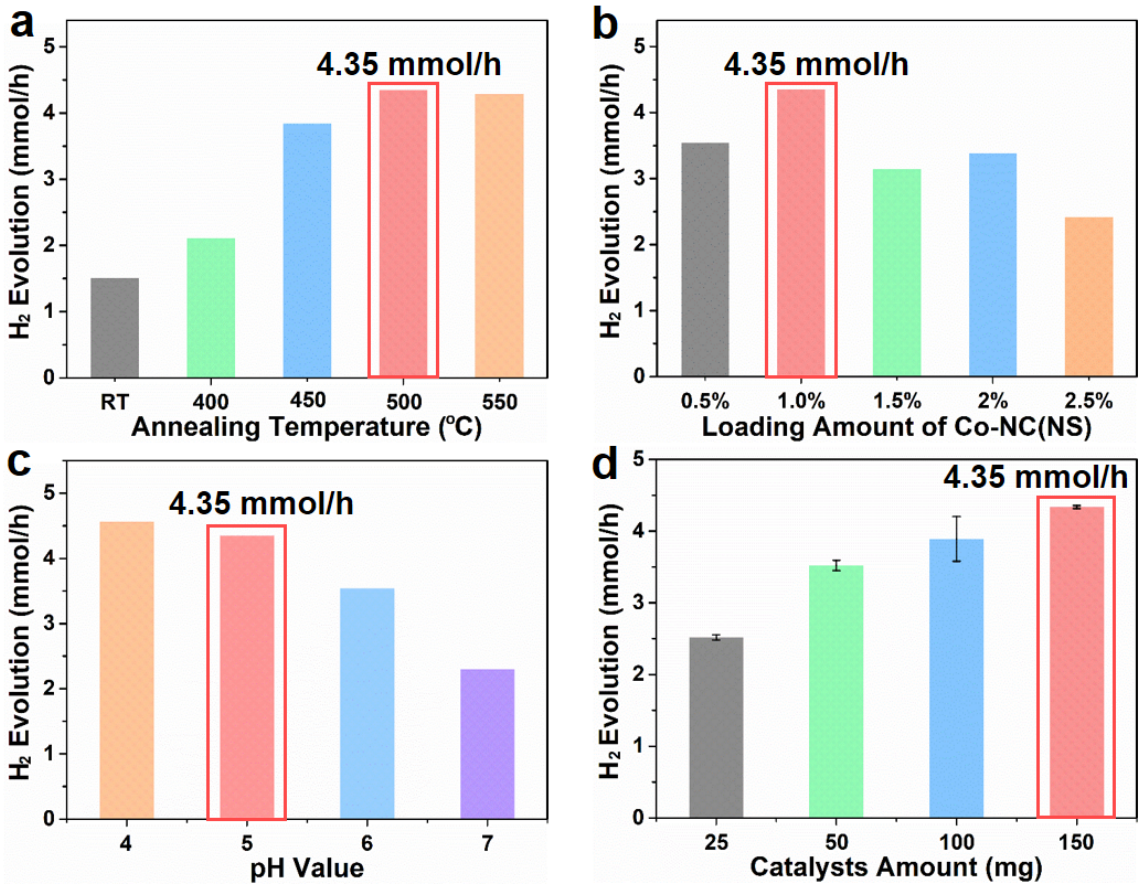


Figure 4.10 Optimized conditions for CdS/Co-NC. (a) Effect of annealing temperature on H_2 generation activity. (b) Effect of Co-NC loading amount on H_2 generation activity. (c) Effect of pH values of reaction solution on H_2 generation activity. (d) Effect of weight of catalyst CdS/Co-NC(500) on H_2 generation activity.

Table 4.2 Comparison of various advanced co-catalyst with CdS-based semiconductor for photocatalytic H_2 production.

Co-catalysts	H_2 evolution rate (mmol/h)	Apparent quantum yield	Turnover frequency	Reaction conditions
Co-NC (this work)	**4.34**	**63.9% at 400 nm; 63.0% at 420 nm**	**16714.7 h^{-1}**	150 mg catalyst; 20 vol % lactic acid adjusted by NaOH to pH ≈ 5.0
Pd nanoparticles[47]	1.45	11.65 at 420 nm	3148.5 h^{-1}	10 mg catalysts; 0.5 M Na_2S and 0.5 M Na_2SO_3
Pd nanoparticles[47]	0.89	N.A.	1932 h^{-1}	10 mg catalysts; 0.1 M Na_2S and 0.1 M Na_2SO_3

Co-catalysts	H_2 evolution rate (mmol/h)	Apparent quantum yield	Turnover frequency	Reaction conditions
Pt nanoparticles[48]	1.68	33.0% at 420 nm	81.9 h^{-1}	100 mg catalysts; 0.25 M Na_2SO_3 and 0.35 M Na_2S
Single Pt atom[49]	0.99	N.A.	1428.6 h^{-1}	50 mg catalyst; 20 vol % lactic acid (pH = 2.1)
Single Pt atom[49]	2.37	N.A.	943.85 h^{-1}	50 mg catalyst; 20 vol % lactic acid (pH = 2.1)
2D-CoS_2[50]	0.55	10.2% at 420 nm	16.9 h^{-1}	100 mg catalyst; 20 vol % 0.75 M ascorbic acid
Co_9S_8[51]	0.02	N. A.	-	20 mg catalyst; Na_2S and Na_2SO_3
CoP[52]	0.001	N.A.	0.4 h^{-1}	5 mg catalyst; pure water
CoE-300[12]	3.65	N.A.	600 h^{-1}	100 mg; 30 vol % lactic acid adjusted by NaOH to pH ≈ 5.0
NiE-350[12]	5.0	78.4% at 420 nm	864 h^{-1}	100 mg; 30 vol % lactic acid adjusted by NaOH to pH ≈ 4.5
Ti_3C_2[9]	0.29	40.1 % at 420 nm	-	20 mg catalyst; 22 vol % lactic acid
MoO_x clusters[13]	0.57	13.4% at 420 nm	32.0 h^{-1}	200 mg catalyst; 20 vol % lactic acid (pH = 2.1)
Single-layer WS_2[53]	0.02	N. A.	-	10 mg catalyst; 10 vol% lactic aqueous solution
Monolayer 2H-MoS_2[54]	4.84	62.1% at 420 nm	-	100 mg catalyst; 20 vol % lactic acid adjusted by NaOH to pH ≈ 5.0
MoS_2[55]	0.18	54% at 420 nm	-	20 mg catalyst; 10 vol % lactic acid
MoS_2/graphene[56]	1.8	28.1% at 420 nm	-	20 mg catalyst; 20 vol % lactic acid
Single-layer MoS_2[57]	2.59	38.4% at 420 nm	-	200 mg catalyst; 20 vol % lactic acid
Poorly crystalline MoS_2 monolayer[58]	5.5	71.6% at 420 nm	-	200 mg catalyst; 20 vol % lactic acid adjusted by NaOH to pH ≈ 5.0
Cobalt substituted MoS_2 monolayer with poor crystallinity[15]	6.2	80.2 at 420 nm	-	200 mg catalyst; 20 vol % lactic acid adjusted by NaOH to pH ≈ 5.0

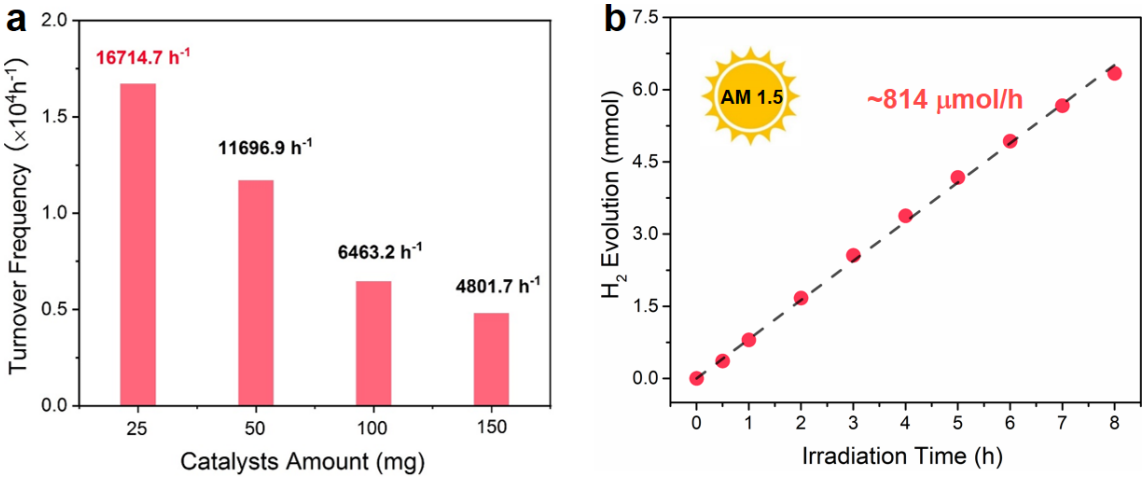


Figure 4.11 (a) Turnover frequency (TOF) calculated based on the single Co sites in CdS/Co-NC(500). (b) H_2 evolution activity of CdS/1%Co-NC(500) under the irradiation of AM 1.5 with a light intensity of 100 mW cm^{-2}.

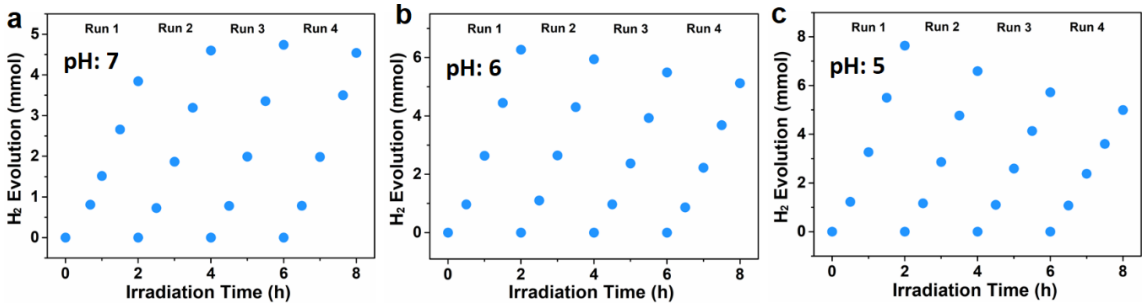


Figure 4.12 Stability of H_2 generation for CdS/Co-NC(500) over several runs at different pH values.

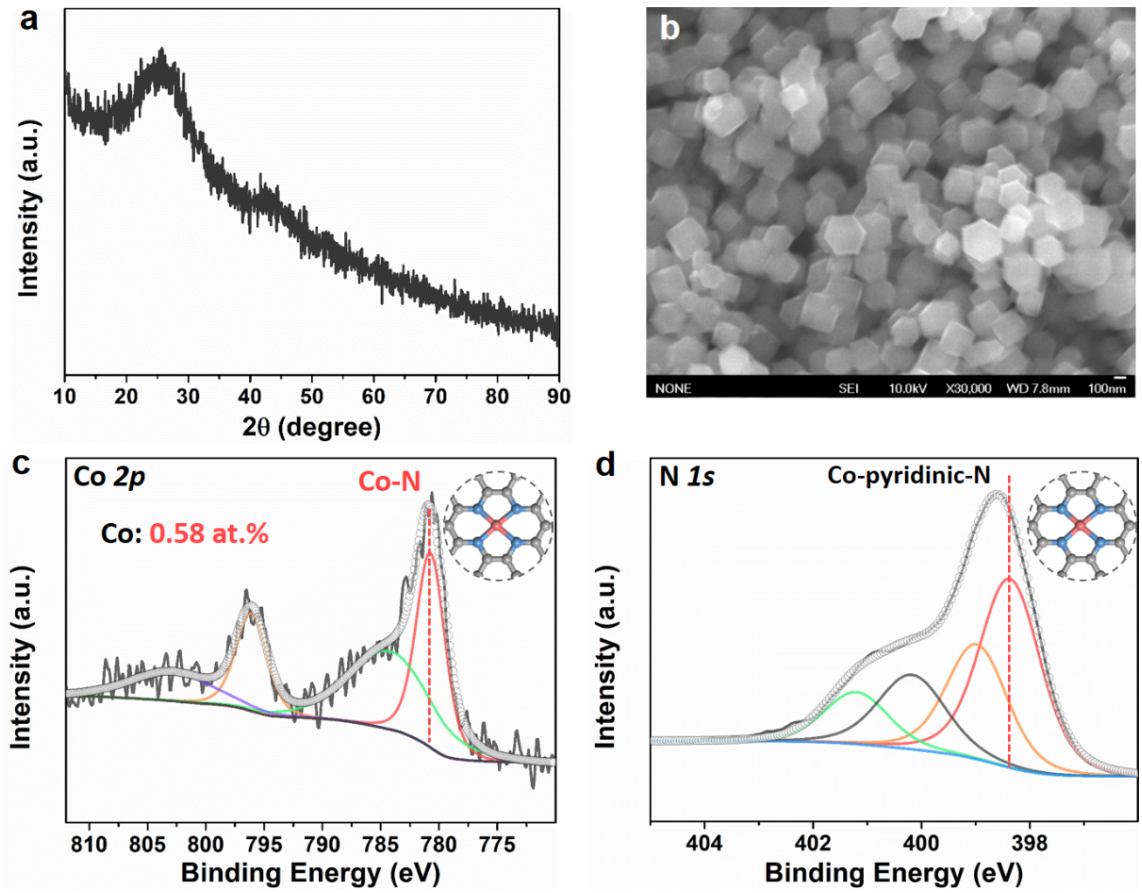


Figure 4.13 (a) XRD pattern of Co-NC$_{rd}$. (b) SEM images of Co-NC$_{rd}$. High-resolution Co 2p (c) and N 1s (d) XPS spectra of Co-NC$_{rd}$.

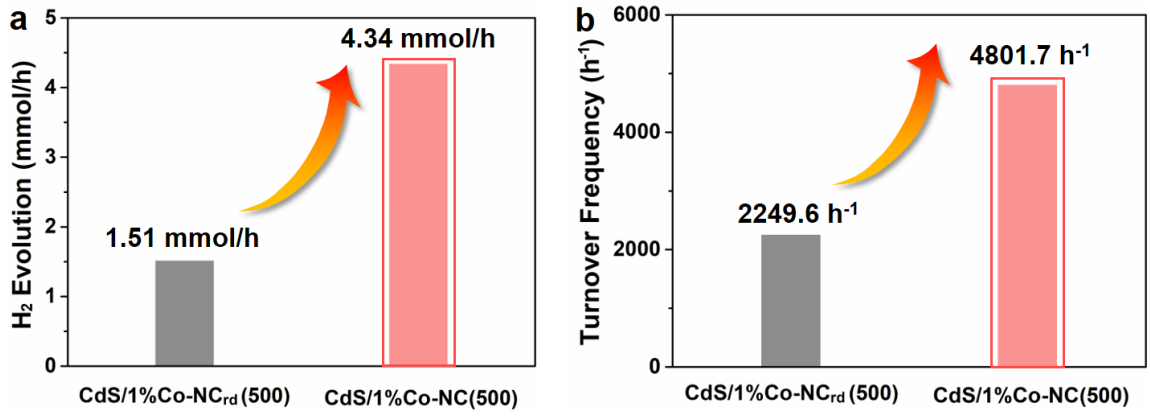


Figure 4.14 Comparison of H_2 generation and TOF of CdS/Co-NC(500) and CdS/Co-NC$_{rd}$(500).

4.3.3 The roles of cleared interfaces and robust Co-N_4 moieties in high performance

We further explored the reason that the CdS/Co-NC(500) delivers superior photocatalytic hydrogen evolution efficiency. Generally, to fully exploit the activity of a photocatalytic system, three requirements should be met: (i) excellent photohavester with suitable band level and band gap; (ii) high mobility of light-induced carriers from the photoabsorber to active centers; (iii) outstanding active sites to collect the photoelectrons and subsequently transform the reactants into the products. To clarify the exact role of Co-NC in the highly efficient H_2 generation system CdS/Co-NC(500), a contrast experiment was conducted. Besides co-catalyst NC, we also prepared co-catalysts Fe-NC and Ni-NC with isolated Fe and Ni centers (Figure 4.15) respectively, in a similar way to fabrication of Co-NC. As illustrated in Figure 4.16a, the co-catalysts NC, Fe-NC and Ni-NC loaded CdS exhibit poor and similar activity of ~1.0 mmol/h, which are much lower than that of Co-NC modified one. Apparently, the isolated Co center in Co-NC with unique properties mainly acts as the active site for superior H_2 evolution. The slight deactivation of CdS/Co-NC(500) at pH = 5 compared with the excellent stability at pH = 7 (Figure 4.12) lends further support to the essential role of isolated Co sites in H_2 generation. The acid solution (pH = 5) might slightly etch CdS and generate some free S^{2-} species, which could poison the single Co sites and account for the slight decrease in activity. The stable performance of CdS/NC(500) without discrete Co sites (Figure 4.17) at pH = 5 further verifies above assumption. Moreover, the annealing process are also quite significant for boosting the performance of CdS/NC and CdS/Co-NC. For both co-catalysts NC and Co-NC, a dramatic enhancement can be observed (Figure 4.16b) when heat treatment was adopted. The annealing treatment may strengthen the interface interaction between CdS and the attached co-catalysts and thus accelerate the charge transfer from CdS to co-catalysts. In brief, the efficient H_2 evolution activity attributes to both the distinct single Co sites and the potential interface structure evolution caused by annealing considering above contrast experiments. Therefore, we try to gain deeper insight into the underlying mechanism from these two aspects.

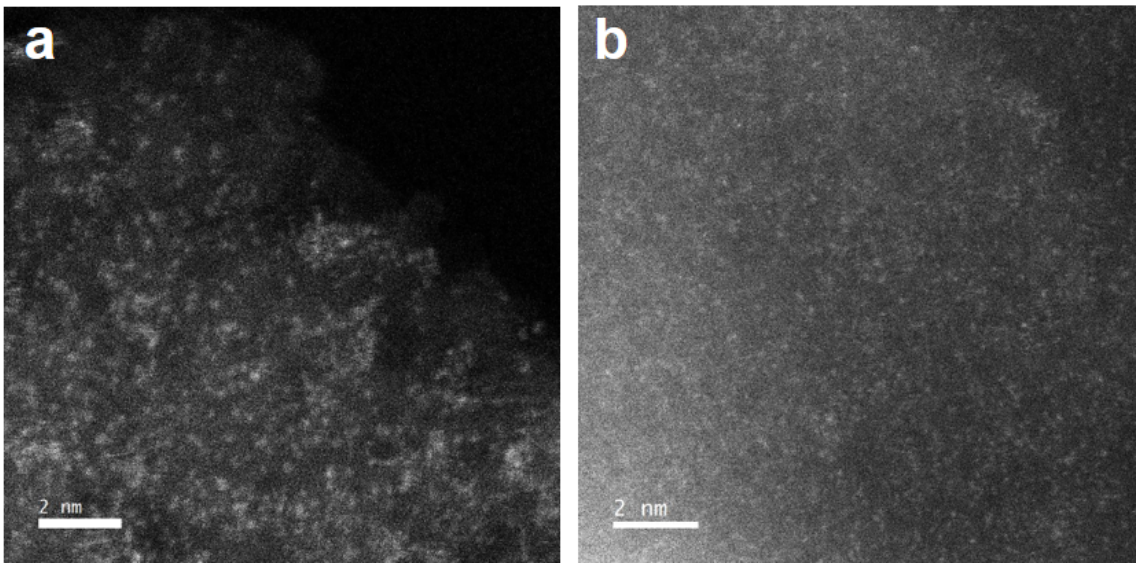


Figure 4.15 Aberration-corrected HAADF-STEM images of (a) Fe-NC and (b) Ni-NC.

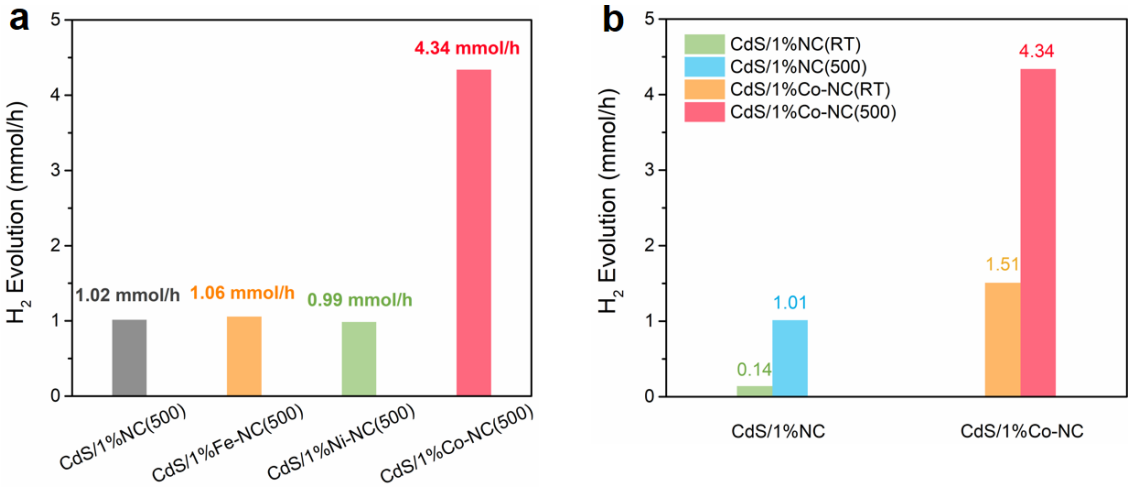


Figure 4.16 (a) Comparison of H_2 evolution activity over CdS coupled with different co-catalysts (M)-NC (M = Fe, Ni and Co). (b) Comparison of H_2 generation activity of as-prepared samples with and without annealing.

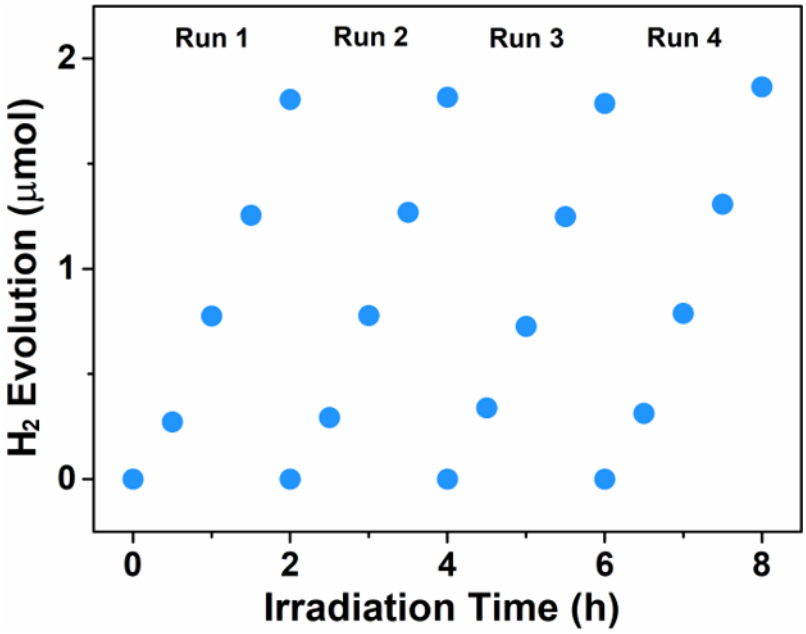


Figure 4.17 Stability of H_2 generation for CdS/1%NC(500) over several runs with a pH of 5.

First, to unravel the root of the excellent co-catalytic H_2 production performance of Co-N_4 sites embedded in co-catalyst Co-NC, the hydrogen adsorption free energy change ΔG_H on various sites including graphitic-C, graphitic-N, pyridinic-N and metal sites coordinated with four pyridinic-N (the models for calculation are provided in Figure 4.18), were employed as a descriptor to reflect hydrogen evolution activity. Usually, the ideal value of ΔG_H is 0 eV, which means hydrogen is bound neither too strongly nor too weakly and thus favors both the hydrogen adsorption and consequent desorption. The diagram in Figure 4.19 demonstrates the isolated Co sites bonded with four N atoms exhibit the nearest value to 0 eV compared with Fe, Co sites with identical coordination environment and other possible sites. This result indicates that the isolated Co sites are the most favorable sites for H_2 evolution among all the studied sites and mainly account for the H_2 generation for CdS/Co-NC(500).

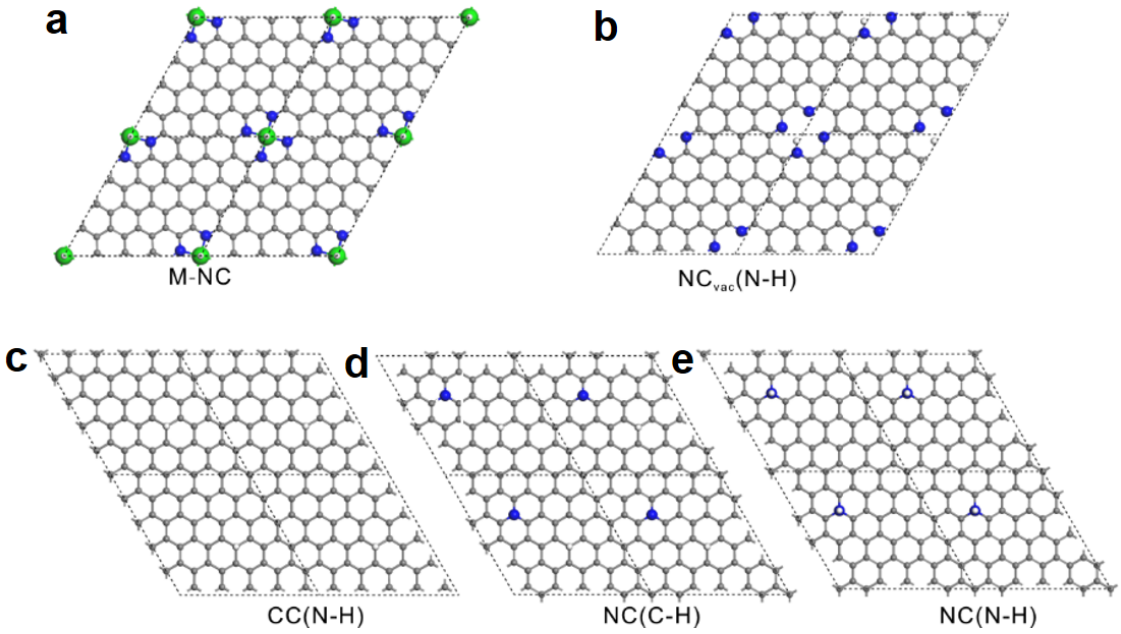


Figure 4.18 The calculated sites for hydrogen adsorption.

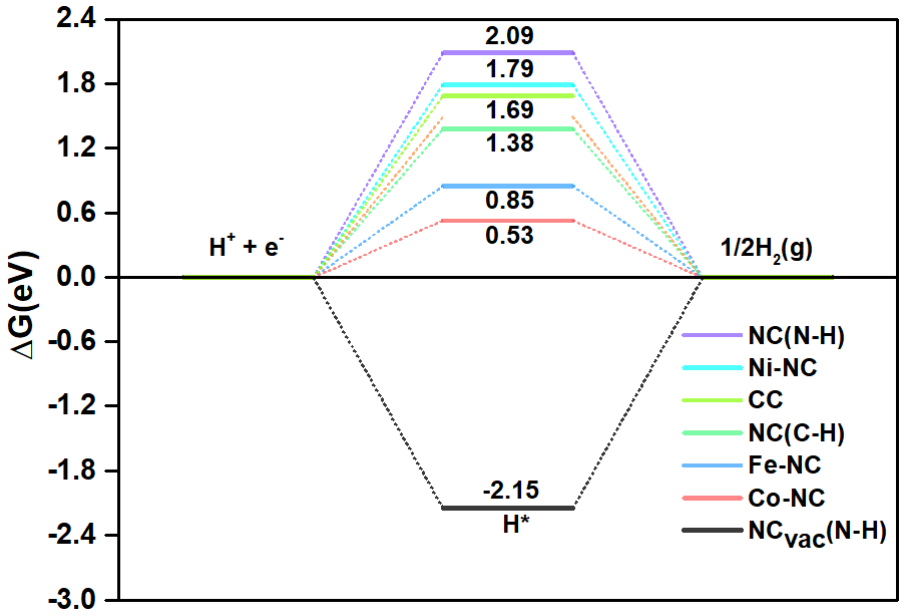


Figure 4.19 Calculated Gibbs free energy diagram for hydrogen adsorption on various sites.

Furthermore, the giant H_2 evolution activity enhancement by the annealing process ignited our interest in disclosing how the interfacial structure evolve upon annealing and how it affects the charge flow across the junction between CdS and Co-NC. A series of characterizations including HRTEM, XPS, photoelectrochemical method, in situ FT-IR (Fourier transform infrared spectroscopy) and photoluminescence (PL) spectroscopy were adopted to approach the detailed charge flow process and interfacial structure

evolution. High-resolution TEM image (Figure 4.20) of CdS/Co-NC reveals an intimate interfacial heterostructure composed of ultrathin Co-NC tightly wrapping on a bulk CdS. Such a compact contact between CdS and ultrathin Co-NC could enable the fast electron transfer through the interface. The analyses of chemical valence of Cd, S, C and N contained in the composites allow us to understand the flow direction of electrons. High-resolution Cd *3d* (Figure 4.21a) and S *2p* XPS spectra (Figure 4.21b) show that both the binding energy of Cd and S increases after loading Co-NC, clearly suggesting the electron donating feature of CdS and thus the electron accepting nature of the Co-NC in CdS/Co-NC obtained without annealing. More interestingly, heat treatment at 500 °C under Ar can further promote charge flow from CdS to Co-NC as evidenced by the larger binding energy of Cd and S in CdS/Co-NC after annealing and cause dramatically enhanced H_2 generation activity from ~1.0 to 4.3 mmol/h (Figure 4.16b). In relative to the NC, the Co-NC possesses stronger ability for collecting the electron from photohavester CdS as identified by the higher binding energy of Cd and S for CdS/Co-NC compared to CdS/NC (Figure 4.21a and Figure 4.21b).

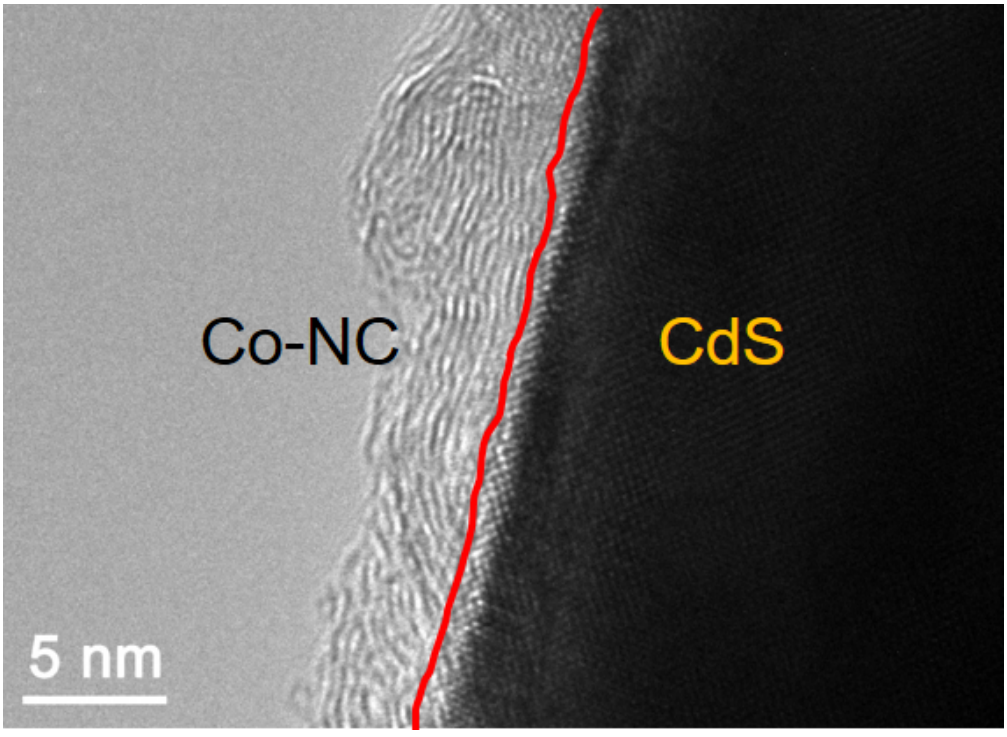


Figure 4.20 High resolution TEM image of the interface between CdS and ultrathin Co-NC.

Additionally, the anchored co-catalysts Co-NC, as the electrons acceptor, should present as an electron rich state. The high-resolution N *1s* spectra reveal (Figure 4.21c)

that all N species including pyridinic N coordinated with Co sites, pyrrolic N and graphitic N in Co-NC could accept the donated electron from CdS as verified by the shifted binding energy towards low energy side. Beyond that, the further increased binding energy of pyridinic N sites bonded with Co centers caused by annealing process clearly indicates that the heat treatment can further enrich the electrons on these N sites and then transfer to the active Co sites for H_2 generation. Unfortunately, the content of Co in the composite CdS/Co-NC(500) is too low to detect using XPS method, thus it's difficult to directly observe the electron-rich state of Co sites currently. However, according to the remarkably enhanced activity induced by Co-NC (Figure 4.16a) in relative to NC, Fe-NC and Ni-NC, it's rational to conclude that the Co sites can accept the electrons for robust H_2 evolution.

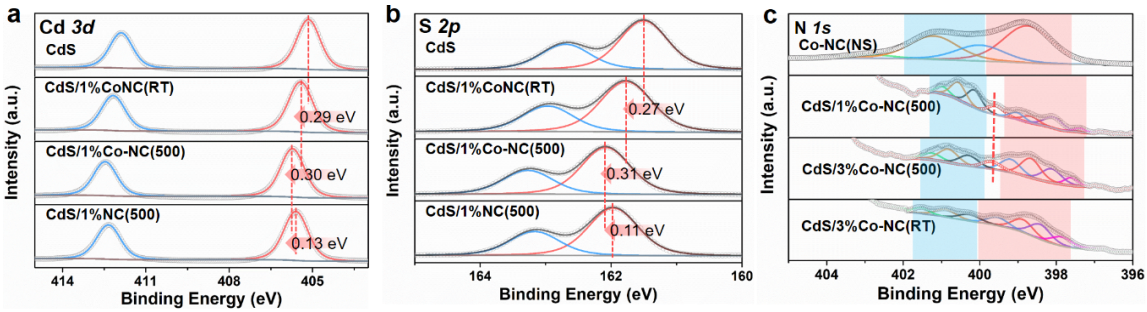


Figure 4.21 Cd *3d* (a), N *1s* (b) and N *1s* (c) XPS spectra of samples.

To explore the origin of aforementioned annealing-promoted electrons transfer from CdS to Co-NC and visualize the interfacial structure evolution in the system CdS/Co-NC with annealing, in-situ FT-IR was conducted under elevated temperature and Ar atmosphere, in which CdS/Co-NC(RT) was examined and the detected signal at 100 °C was used as the background. It's worth noting that surfaces of commercial CdS in our case are covered with abundant adventitious carbon species (Figure 4.22), similar to the widely studied TiO_2[32] and carbon nitride[35]; upon forming heterostructures, the interfaces will be enriched with these carbon species. The calcination-time dependent infrared spectra (Figure 4.23) of CdS/Co-NC(RT) present gradually decreased absorbance at ~1000 (O-H, out-of-plane bend), ~1177-1232 (C-O, stretch), ~1405 (C-H, bend), and ~1626 cm^{-1} (C=O, stretch) with increasing temperature, clearly indicating the decomposition of the adventitious carbon. The distinct signals of contrast samples CdS and Co-NC compared with hybrid CdS/Co-NC(RT) indicates that, in CdS/Co-NC(RT), most of those reduced C=O, C-O and OH groups originate from the decomposition of adventitious hydrocarbon confined at the interfaces between CdS and Co-NC rather than

on the naked surfaces of CdS and Co-NC (Figure 4.24 and relevant discussion). Therefore, the fully calcined sample CdS/Co-NC(500) should contain no or very limited interfacial adventitious carbon, which is evidenced by the in-situ FT-IR spectra of fully annealed CdS/Co-NC(500) (Figure 4.25 and relevant discussion). In brief, annealing process can effectively remove the interfacial adventitious carbon for CdS/Co-NC(RT). As a result, a much cleaner interface is created, which could enable the smoother electron transport from CdS to Co-NC. Interestingly, an extra peak appears in high resolution N *1s* spectrum for annealed CdS/Co-NC(500) (Figure 4.21c) in contrast to CdS/Co-NC obtained at room temperature. This additional signal may come from the N-S bonds at the interfaces between CdS and Co-NC because of the elimination of interfacial adventitious hydrocarbon after heat treatment. Such an extra bond might act as a new interfacial electron shuttle channel to mediate the electron transfer from CdS to Co-NC. Benefitting from the cleaner junction and the possible newly formed bonds between CdS and Co-NC induced by the increased annealing temperature, the activity of CdS/Co-NC was improved progressively (Figure 4.10a), which further corroborates the effective annealing-induced clearing of the junction between CdS and Co-NC.

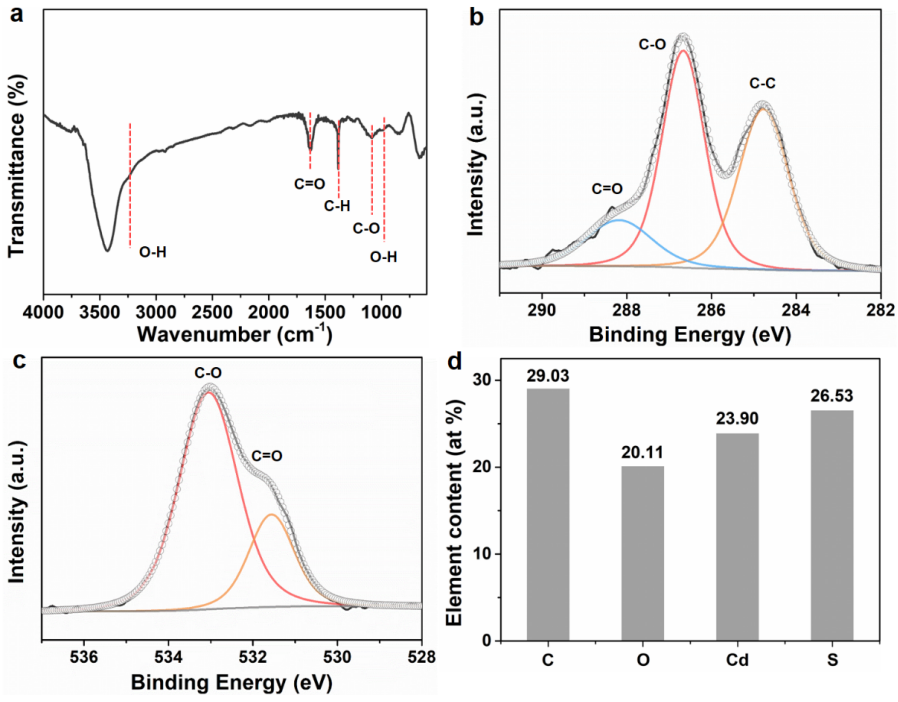


Figure 4.22 Identification of abundant surface adventitious carbon on commercial CdS. (a) FT-IR spectrum. Note: the signals marked with red dash lines refer to the species in adventitious carbon on the surfaces of bare CdS. (b) High-resolution C *1s* and (c) O *1s* spectra. (d) Element content.

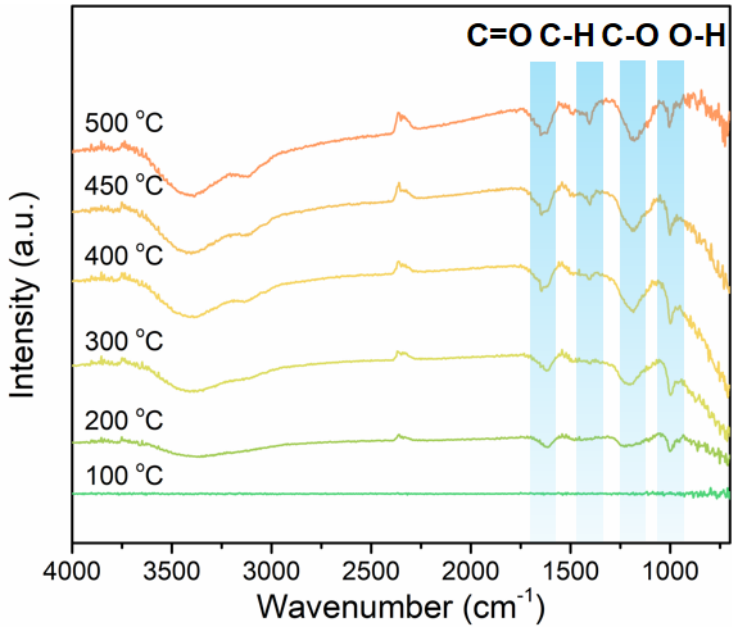


Figure 4.23 In situ FT-IR spectra of CdS/Co-NC measured at increased temperature.

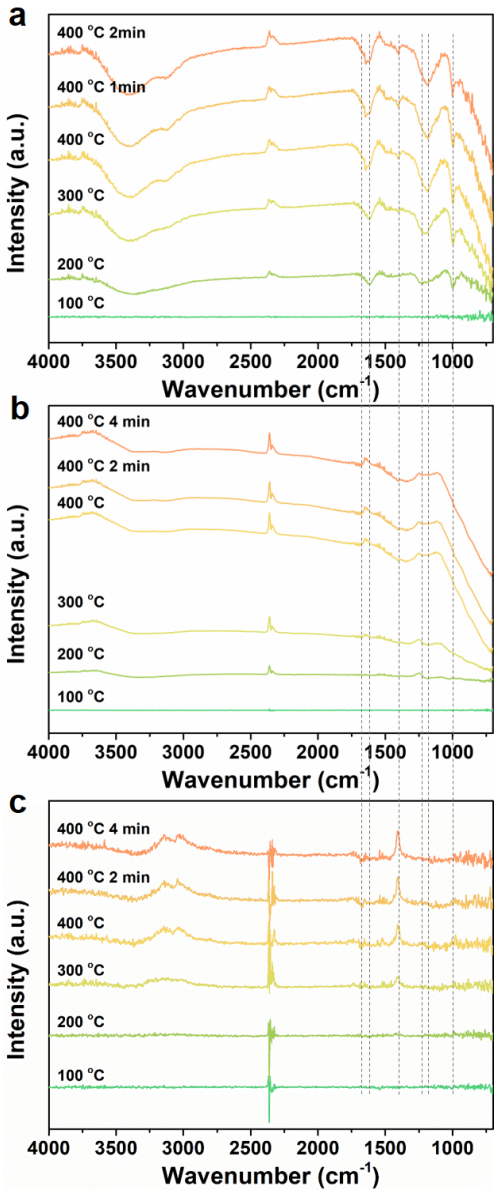


Figure 4.24 In situ FT-IR spectra of CdS/Co-NC(RT) (a), pure CdS (b) and Co-NC (c) measured at increased temperature. Noting that most of surface region of CdS in CdS/Co-NC(RT) hybrid is uncovered with Co-NC (refer to the SEM image of annealed hybrid provided in Figure 4.7c) and such areas are comparable to those of pristine CdS; similarly, the outward-facing surfaces of Co-NC in CdS/Co-NC should be same as those of pure Co-NC. Considering these two points, it's supposed to observe similar FT-IR signals for CdS, Co-NC and CdS/Co-NC(RT). Unexpectedly, the CdS/Co-NC(RT) exhibits different signals, especially those at ~1000 and 1626 cm^{-1}, relative to pure CdS and Co-NC under identical conditions (Figure 4.24). This distinction indicates that, in CdS/Co-NC(RT), most of those reduced C=O, C-O and OH groups originate from the decomposition of adventitious hydrocarbon confined at the interfaces between CdS and Co-NC rather than on the naked surfaces of CdS and Co-NC.

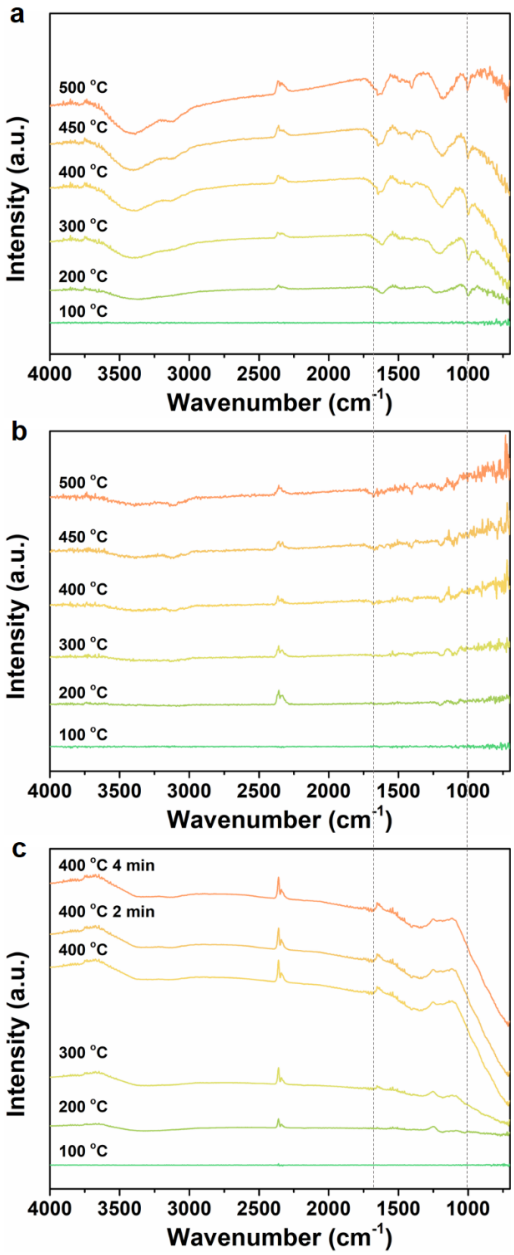


Figure 4.25 In situ FT-IR spectra of CdS/Co-NC(RT) (a), CdS/Co-NC(500) (b) and pure CdS (c) measured at increased temperature. A weak declined signal at ~1676 cm^{-1} (C=O) appears for CdS/Co-NC(500), which is same as that of bare CdS but different from that of CdS/Co-NC(RT) locating at ~1626 cm^{-1}. Besides that, the CdS/Co-NC(500) and bare CdS show negligible signal at ~1000 cm^{-1} while CdS/Co-NC(RT) delivers obvious declined signal this location. This contrast experiment confirms that CdS/Co-NC(500) possesses negligible interfacial carbon species because of the pre-annealing process but some readsorbed carbon species on its' surface.

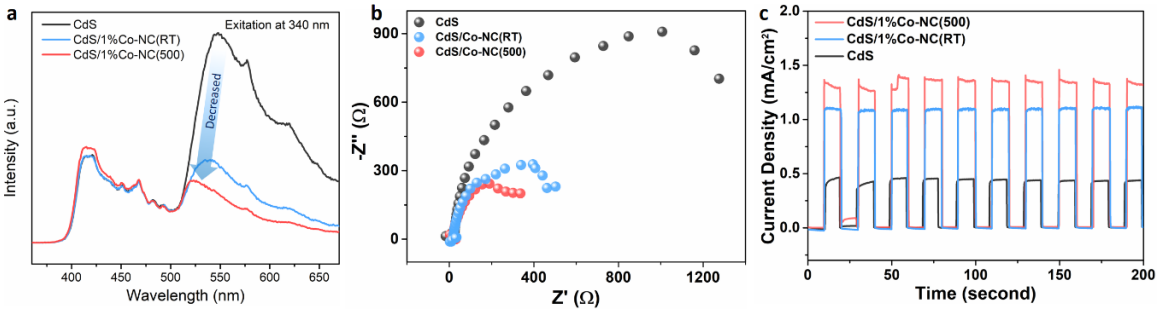


Figure 4.26 (a) Steady-state photoluminescence spectroscopy of the samples. (b) Electrochemical impedance spectroscopy (EIS) Nyquist plots under irradiation condition. (c) Periodic on/off photocurrent response under visible-light irradiation.

The cleared interfaces enable the fast charge transfer from CdS to Co-NC as identified by in situ FT-IR and XPS analyses. We further focus on the promoted kinetics of photocarriers benefitted from this point by comparing a group of CdS-based composites. Steady-state photoluminescence (PL) spectroscopy characterization, as a powerful tool to monitor the excitonic processes, i.e., radiative recombination of photogenerated electron-hole pairs in photocatalyst, was carried out for a series of samples. As shown in Figure 4.26a, pristine CdS presents two distinct emission peaks in the range of 385-503 nm and 503-670 nm, assigned to the excitonic emission of CdS and surface states related carriers recombination, respectively.[59] Upon loading Co-NC on CdS without further annealing, the PL peak centered at ~547 nm is substantially suppressed meanwhile the one centered at ~417 nm remains almost unchanged. It signifies that the Co-NC can collect the energetic electrons trapped by surface defect level of CdS although adventitious carbon layer exists between CdS and Co-NC (Figure 4.27a). After removing the organic layer by annealing the composite at 500 °C, Co-NC captures most photogenerated electrons from CdS side as evidenced by the further quenched emission peak in the range of 503-670 nm (Figure 4.26a and Figure 4.27b). Consequently, those massively collected electrons will power the robust isolated Co sites for highly efficient hydrogen evolution. Additionally, compared with pristine CdS and CdS/Co-NC(RT) without heating, the obvious blue shift

of emission peak related to surface states for annealed CdS/Co-NC(500) could be ascribed to the strong interfacial interaction after eliminating the adventitious carbon at the junctions.

Photoelectrochemical characterizations lend further support to the essential role of smooth carrier transport channel created by removing the interfacial adventitious carbon. Nyquist plot of CdS/Co-NC(500) under irradiation presents smallest semicircle in comparison with that of the pristine CdS and CdS/Co-NC(RT) (Figure 4.26b), indicating the smallest resistance across the interface between CdS and Co-NC for annealed CdS/Co-NC(500). Meanwhile, a marked boosted photocurrent (Figure 4.26c), benefitting from the smoother junction, is also observed for CdS/Co-NC(500) compared to that of CdS and CdS/Co-NC(RT).

According to the analyses above, the outstanding photocatalytic performance of CdS/Co-NC system originates from two reasons: (i) the distinctive single Co sites with moderate attraction for robust H_2 generation; (ii) the smooth carrier channel created by eliminating the interfacial adventitious carbon species between CdS and Co-NC as illustrated in Figure 4.27.

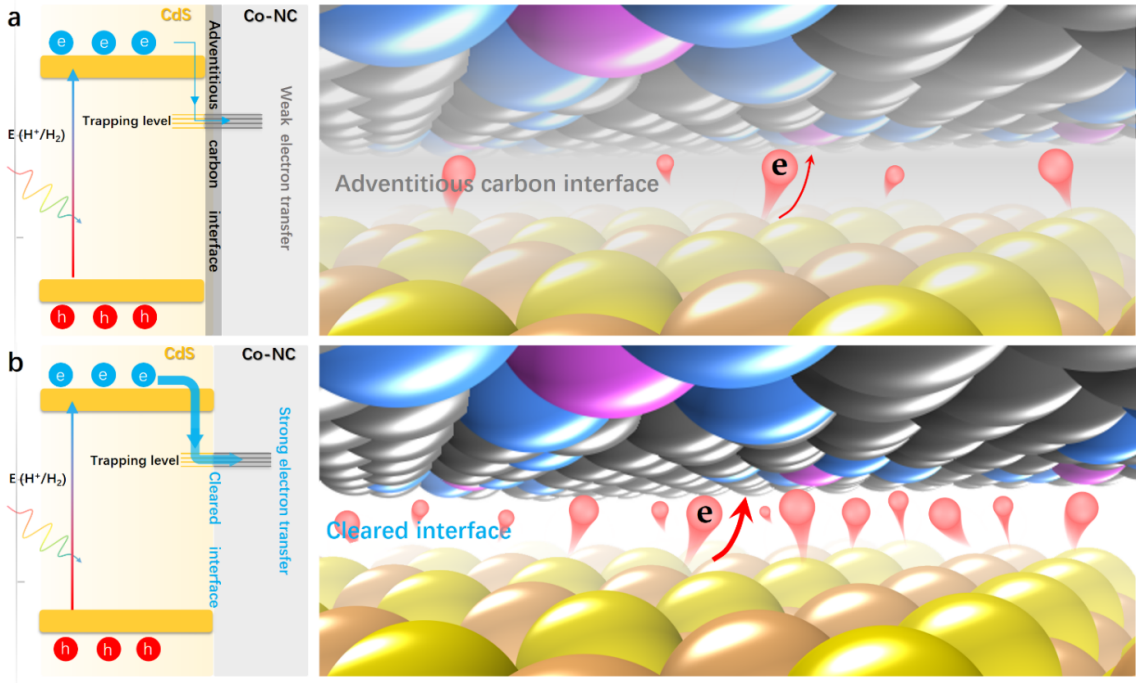


Figure 4.27 Origin and mechanism of the efficient photocatalytic system CdS/Co-NC. (a) Illustration of carriers separation and transfer in CdS/Co-NC(RT) system with interfacial adventitious carbon. (b) Scheme of fast electron separation and transfer across cleared interface created by facile calcination treatment for CdS/Co-NC(500).

4.4 Conclusions

In summary, our study demonstrates an outstanding visible-light-driven H_2 evolution system CdS/Co-NC(500), which achieves a superb performance with an activity of 4.34 mmol/h, an AQY 63.9% at 400 nm and an remarkably high TOF_{Co} of up to 16714.7 h^{-1}. The excellent performance mainly attributes to two reasons as disclosed by experiment analyses and theoretical investigation. First, eliminating the interfacial adventitious hydrocarbon layer by annealing process enables directional and fast delivery of electron from CdS to Co-NC; second, the isolated Co site coordinated with four N owns favorable hydrogen adsorption ability and thus can fully utilize the collected electrons from photosensitizer for H_2 evolution. This study clarifies the significant negative role of widely existed surface adventitious carbon on materials in photocatalytic process and highlights both the great potential of cleared interface and single-atom based materials in photocatalysis. Thus, our results offer new opportunities for the exploration and design of high-performance system for efficient solar energy-driven conversion.

References

[1] T. A. Kandiel, I. Ivanova, D. W. Bahnemann, *Energy Environ. Sci.,* 2014, **7**, 1420-1425.

[2] H. Tong, S. Ouyang, Y. Bi, N. Umezawa, M. Oshikiri, J. Ye, *Adv. Mater.,* 2012, **24**, 229-251.

[3] X. Chen, S. Shen, L. Guo, S. S. Mao, *Chem. Rev.,* 2010, **110**, 6503-6570.

[4] A. Kudo, Y. Miseki, *Chem. Soc. Rev.,* 2009, **38**, 253-278.

[5] K. Chang, X. Hai, J. Ye, *Adv. Energy Mater.,* 2016, **6**, 1502555.

[6] X. Li, J. Yu, M. Jaroniec, X. Chen, *Chem. Rev.,* 2019, **119**, 3962-4179.

[7] J. Ran, J. Zhang, J. Yu, M. Jaroniec, S. Z. Qiao, *Chem. Soc. Rev.,* 2014, **43**, 7787-7812.

[8] S. Wang, Y. Wang, S. L. Zhang, S. Q. Zang, X. W. D. Lou, *Adv. Mater.,* 2019, **31**, e1903404.

[9] J. Ran, G. Gao, F. T. Li, T. Y. Ma, A. Du, S. Z. Qiao, *Nat. Commun.,* 2017, **8**, 13907.

[10] J. Li, G. Zhan, Y. Yu, L. Zhang, *Nat. Commun.,* 2016, **7**, 11480.

[11] C. Peng, P. Wei, X. Li, Y. Liu, Y. Cao, H. Wang, H. Yu, F. Peng, L. Zhang, B. Zhang, K. Lv, *Nano Energy,* 2018, **53**, 97-107.

[12] G. Zhao, Y. Sun, W. Zhou, X. Wang, K. Chang, G. Liu, H. Liu, T. Kako, J. Ye, *Adv. Mater.,* 2017, **29**, 1703258.

[13] H. Zhang, P. Zhang, M. Qiu, J. Dong, Y. Zhang, X. W. D. Lou, *Adv. Mater.,* 2019, **31**, e1804883.

[14] Q. Li, B. Guo, J. Yu, J. Ran, B. Zhang, H. Yan, J. R. Gong, *J. Am. Chem. Soc.,* 2011, **133**, 10878-10884.

[15] X. Hai, W. Zhou, S. Wang, H. Pang, K. Chang, F. Ichihara, J. Ye, *Nano Energy,* 2017, **39**, 409-417.

[16] Y. Chen, S. Ji, C. Chen, Q. Peng, D. Wang, Y. Li, *Joule,* 2018, **2**, 1242-1264.

[17] C. Gao, S. Chen, Y. Wang, J. Wang, X. Zheng, J. Zhu, L. Song, W. Zhang, Y. Xiong, *Adv. Mater.,* 2018, **30**, e1704624.

[18] P. Yin, T. Yao, Y. Wu, L. Zheng, Y. Lin, W. Liu, H. Ju, J. Zhu, X. Hong, Z. Deng, G. Zhou, S. Wei, Y. Li, *Angew. Chem. Int. Ed. Engl.,* 2016, **55**, 10800-10805.

[19] J. Wang, Z. Li, Y. Wu, Y. Li, *Adv. Mater.,* 2018, **30**, e1801649.

[20] X. Li, X. Yang, Y. Huang, T. Zhang, B. Liu, *Adv. Mater.,* 2019, e1902031.

[21] X. Cui, H. Li, Y. Wang, Y. Hu, L. Hua, H. Li, X. Han, Q. Liu, F. Yang, L. He, X. Chen, Q. Li, J. Xiao, D. Deng, X. Bao, *Chem,* 2018, **4**, 1902-1910.

[22] W. Liu, L. Zhang, X. Liu, X. Liu, X. Yang, S. Miao, W. Wang, A. Wang, T. Zhang, *J. Am. Chem. Soc.,* 2017, **139**, 10790-10798.

[23] S. Tian, Q. Fu, W. Chen, Q. Feng, Z. Chen, J. Zhang, W. C. Cheong, R. Yu, L. Gu, J. Dong, J. Luo, C. Chen, Q. Peng, C. Draxl, D. Wang, Y. Li, *Nat. Commun.,* 2018, **9**, 2353.

[24] X. Wang, Z. Chen, X. Zhao, T. Yao, W. Chen, R. You, C. Zhao, G. Wu, J. Wang, W. Huang, J. Yang, X. Hong, S. Wei, Y. Wu, Y. Li, *Angew. Chem. Int. Ed. Engl.,* 2018, **57**, 1944-1948.

[25] Z. Liang, W. Guo, R. Zhao, T. Qiu, H. Tabassum, R. Zou, *Nano Energy,* 2019, **64**, 103917.

[26] Y. Zhu, W. Sun, J. Luo, W. Chen, T. Cao, L. Zheng, J. Dong, J. Zhang, M. Zhang, Y. Han, C. Chen, Q. Peng, D. Wang, Y. Li, *Nat. Commun.,* 2018, **9**, 3861.

[27] J. Low, B. Dai, T. Tong, C. Jiang, J. Yu, *Adv. Mater.,* 2019, **31**, 1802981.

[28] J. Ran, W. Guo, H. Wang, B. Zhu, J. Yu, S. Z. Qiao, *Adv. Mater.,* 2018, **30**, e1800128.

[29] J. Low, J. Yu, M. Jaroniec, S. Wageh, A. A. Al-Ghamdi, *Adv. Mater.,* 2017, **29**, 1601694.

[30] S. Wang, B. Y. Guan, X. Wang, X. W. D. Lou, *J. Am. Chem. Soc.,* 2018, **140**, 15145-15148.

[31] S. Wang, B. Y. Guan, X. W. D. Lou, *J. Am. Chem. Soc.,* 2018, **140**, 5037-5040.

[32] J. Balajka, M. A. Hines, W. J. I. DeBenedetti, M. Komora, J. Pavelec, M. Schmid, U. Diebold, *Science,* 2018, **361**, 786-789.

[33] B. M. Comer, Y. H. Liu, M. B. Dixit, K. B. Hatzell, Y. Ye, E. J. Crumlin, M. C. Hatzell, A. J. Medford, *J. Am. Chem. Soc.,* 2018, **140**, 15157-15160.

[34] S. K. Muduli, E. Varrla, Y. Xu, S. A. Kulkarni, A. Katre, S. Chakraborty, S. Chen, T. C. Sum, R. Xu, N. Mathews, *J. Mater. Chem. A,* 2017, **5**, 24874-24879.

[35] P. Niu, L. Zhang, G. Liu, H.-M. Cheng, *Adv. Funct. Mater.,* 2012, **22**, 4763-4770.

[36] G. Kresse, J. Hafner, *Phys. Rev. B,* 1993, **47**, 558-561.

[37] G. Kresse, J. Furthmüller, *Phys. Rev. B,* 1996, **54**, 11169-11186.

[38] J. P. Perdew, K. Burke, M. Ernzerhof, *Phys. Rev. Lett.,* 1996, **77**, 3865-3868.

[39] P. E. Blöchl, *Phys. Rev. B,* 1994, **50**, 17953-17979.

[40] G. Kresse, D. Joubert, *Phys. Rev. B,* 1999, **59**, 1758-1775.

[41] Q.-K. Li, X.-F. Li, G. Zhang, J. Jiang, *J. Am. Chem. Soc.,* 2018, **140**, 15149-15152.

[42] H. Xu, D. Cheng, D. Cao, X. C. Zeng, *Nat. Catal.,* 2018, **1**, 339-348.

[43] K. Niu, Y. Xu, H. Wang, R. Ye, H. L. Xin, F. Lin, C. Tian, Y. Lum, K. C. Bustillo, M. M. Doeff, M. T. M. Koper, J. Ager, R. Xu, H. Zheng, *Sci. Adv.,* 2017, **3**, e1700921.

[44] Y. Pan, R. Lin, Y. Chen, S. Liu, W. Zhu, X. Cao, W. Chen, K. Wu, W. C. Cheong, Y. Wang, L. Zheng, J. Luo, Y. Lin, Y. Liu, C. Liu, J. Li, Q. Lu, X. Chen, D. Wang, Q. Peng, C. Chen, Y. Li, *J. Am. Chem. Soc.,* 2018, **140**, 4218-4221.

[45] A. Singh, S. Roy, C. Das, D. Samanta, T. K. Maji, *Chem. Commun. (Camb.),* 2018, **54**, 4465-4468.

[46] H. Fei, J. Dong, M. J. Arellano-Jimenez, G. Ye, N. Dong Kim, E. L. Samuel, Z. Peng, Z. Zhu, F. Qin, J. Bao, M. J. Yacaman, P. M. Ajayan, D. Chen, J. M. Tour, *Nat. Commun.,* 2015, **6**, 8668.

[47] Q. Sun, N. Wang, J. Yu, J. C. Yu, *Adv. Mater.,* 2018, **30**, e1804368.

[48] L. Shang, B. Tong, H. Yu, G. I. N. Waterhouse, C. Zhou, Y. Zhao, M. Tahir, L.-Z. Wu, C.-H. Tung, T. Zhang, *Adv. Energy Mater.,* 2016, **6**, 1501241.

[49] X. Wu, H. Zhang, J. Dong, M. Qiu, J. Kong, Y. Zhang, Y. Li, G. Xu, J. Zhang, J. Ye, *Nano Energy,* 2018, **45**, 109-117.

[50] P. Wang, Y. Mao, L. Li, Z. Shen, X. Luo, K. Wu, P. An, H. Wang, L. Su, Y. Li, S. Zhan, *Angew. Chem., Int. Ed. Engl.,* 2019, **58**, 11329-11334.

[51] B. Qiu, Q. Zhu, M. Du, L. Fan, M. Xing, J. Zhang, *Angew. Chem. Int. Ed. Engl.,* 2017, **56**, 2684-2688.

[52] R. Shi, H. F. Ye, F. Liang, Z. Wang, K. Li, Y. Weng, Z. Lin, W. F. Fu, C. M. Che, Y. Chen, *Adv. Mater.,* 2018, **30**, 1705941.

[53] J. Chen, X. J. Wu, L. Yin, B. Li, X. Hong, Z. Fan, B. Chen, C. Xue, H. Zhang, *Angew. Chem. Int. Ed. Engl.,* 2015, **54**, 1210-1214.

[54] K. Chang, X. Hai, H. Pang, H. Zhang, L. Shi, G. Liu, H. Liu, G. Zhao, M. Li, J. Ye, *Adv. Mater.,* 2016, **28**, 10033-10041.

[55] B. Sun, W. Zhou, H. Li, L. Ren, P. Qiao, W. Li, H. Fu, *Adv. Mater.,* 2018, **30**, e1804282.

[56] K. Chang, Z. Mei, T. Wang, Q. Kang, S. Ouyang, J. Ye, *ACS Nano,* 2014, **8**, 7078-7087.

[57] K. Chang, M. Li, T. Wang, S. Ouyang, P. Li, L. Liu, J. Ye, *Adv. Energy Mater.,* 2015, **5**, 1402279.

[58] X. Hai, W. Zhou, K. Chang, H. Pang, H. Liu, L. Shi, F. Ichihara, J. Ye, *J. Mater. Chem. A,* 2017, **5**, 8591-8598.

[59] J. Su, T. Zhang, Y. Li, Y. Chen, M. Liu, *Molecules,* 2016, **21**, 735.

Chapter 5 Conclusions and future prospects

5.1 General conclusions

In this thesis, the main objective is to design and develop efficient carbon-based materials via modulating the intrinsic properties of photocatalyst CN, creating novel carbon-based co-catalyst, and removing the relevant interfacial adventitious carbon for efficient photochemical processes. Also, the findings in this study develop new understandings of carbon-based materials as well as the corresponding mechanism of photocatalysis.

The detailed study could be concluded in the following parts.

1. Atomic carbon chains-mediated carriers transfer over polymeric carbon nitride for efficient photocatalysis

In this part, we demonstrate a facile and efficient strategy to incorporate short carbon chains into the basal plane of CN while remaining the pristine tri-*s*-triazine structure. The carbon chains filled the defects in CN via covalent bonds, which mediates the electron transfer in a relatively smooth transport channel compared to the initial hydrogen bonds. By virtue of such a favorable transport channel of carriers, the carbon chains linked CN exhibits a dramatically improved photocatalytic water splitting and CO_2 reduction performance, achieving a 13.2- and 29.2-times enhancement, respectively, compared to pristine CN. This study highlights that the engineering of the defects in photocatalysts is one of the most effective approaches for improving solar energy conversion and also gives a research direction for the future rational design towards efficient photocatalysts, especially for organic-based ones.

2. Targeted exfoliation and reassembly of polymeric carbon nitride for efficient photocatalysis

In this part, a facile and controllable strategy was developed to manipulate the exfoliation-reassembly status and the properties of polymeric CN via switching the interlayer species. Three remarkable advantages are created: 1) high exfoliation yield of ultrathin nanosheets reaches up to 48% in a mild solution. 2) the physical properties of the system are highly reversible by switching the exfoliation-reassembly state. 3) the exfoliated and reassembled CN with tunable properties can be applied to photocatalytic IPA degradation and H_2 evolution, giving a high AQY of 27% and 46 % for IPA

degradation and H_2 evolution, respectively, at ~420 nm. This new proof-of-concept strategy will open up further opportunities for more effective delamination of extensive layered 2D materials towards advanced applications.

3. Single-Co on N-rich carbon as co-catalyst for efficient photocatalytic H_2 production: the key roles of cleared interfaces and isolated metal sites

In this part, we report a rational design and novel synthesis of single Co implanted ultrathin N-rich carbon nanosheets (Co-NC) and create a cleared junction between photoharvester CdS and co-catalyst Co-NC through calcination-induced elimination of interfacial adventitious carbon. By combining the cleaned interface with fast electron delivery ability and robust single Co sites for HER, we were able to create a high-performance photocatalytic system of CdS/Co-NC, achieving a HER rate of 4.34 mmol/h, an apparent quantum yield (AQY) of 63.9% at 400 nm and a record turnover frequency of up to 16714.7 h^{-1}. This study clarifies the significant negative role of widely existed surface adventitious carbon on materials in the photocatalytic process and highlights both the great potential of cleared interface and single-atom based materials in photocatalysis.

5.2 Future prospects

Although some achievements have been made in developing carbon-based materials for efficient photocatalytic reactions, there are many challenges towards the significant enhancement in photocatalytic activity, especially for the single-atom doped carbon-based co-catalysts. Some issues listed below are worthy of special attention:

(1) Understanding the interfacial structure of carbon-based photocatalytic composites

Ex-situ method is an important way to fabricate carbon-based photocatalytic composites, while the interfacial coupling is usually weak and restricts the electron transfer across the junction. Although some studies attempt to improve the quality of interfaces in those heterostructures, there still lacks an insightful understanding of the exact interface structure, its evolution with the treatment process, and how it promotes the charge transfer across the junctions. In addition, it is highly desirable to explore more facile, effective, and controllable methods to precisely engineer the interfacial structure for fast interfacial charge transfer. For example, the attractive polymeric carbon nitride can form diverse heterostructures with different materials with improved photocatalytic activity. However, the interfaces between polymeric carbon nitride and other components still lack insightful investigation.

(2) Creation of robust single active sites on carbon substrate

The core mission of single-atom catalysis study is to construct single active sites with superior intrinsic activity and 100% atom utilization efficiency. Several issues of single atom doped carbon-based co-catalysts are worth to be noted. First, in many carbon-based single-atom catalysts, a large portion of single sites is embedded inside the substrate and is inaccessible to reactants, which largely restricts the atom utilization efficiency and apparent performance. Hence, how to enrich the single site on the surfaces of carbon-based materials and realize high loading amount at the same time is important to guarantee both high atom utilization efficiency and high apparent activity. Second, unlike the organic basis metal complex, not all of the isolated metal sites on carbon-based materials are equally accessible or equally active. It is highly desirable to realize the uniform single active sites on the carbon support, by virtue of which we can precisely correlate the atomic coordination and activity and gain a deep insight into the co-catalytic mechanism. Third, although the current single atom on carbon-based materials exhibits considerable activity, there is still a great opportunity to construct a more efficient active site. The intrinsic activity of isolated metal sites on carbon materials strongly relies on the atomic coordination and the interaction with the carbon-based substrates; therefore, it's highly promising to engineer those two aspects to modulate the final co-catalytic activity. Forth, realizing the large-scale, simple and controllable synthesis of single-atom embedded carbon-based co-catalysts is crucial to meet the demand for fundamental research and practical applications.

(3) Expanding the scope of single-atom embedded carbon-based co-catalysts to other applications

The research of single-atom embedded carbon-based co-catalysts is still at the early stage, further explorations and investigations of those materials and expansion of their applications to other photocatalytic reactions, including N_2 fixation, O_2 evolution, CO_2 reduction, organic transformation and pollutant degradation. Rational design and synthesis of targeted single active centers on carbon substrates and the subsequent selection of suitable photoharvester are crucial for constructing efficient photocatalytic systems with remarkable activity/selectivity.

Acknowledgement

At first, I would like to express great gratitude to my supervisor Prof. Jinhua Ye for her valuable guidance, kind help and patience throughout my Ph.D. studies. Her proficiency, intelligence, and unparalleled instruction ensure the progress of my Ph.D. research project, and these impacts will benefit me through my whole life. I would also like to extend my sincere appreciation of the freedom that Prof. Ye offered. There is nowhere for me to find a better supervisor than Prof. Ye.

I am also grateful to my supervisors, Dr. Shin-ichiro Fujita and Dr. Naoto Shirahata. Thank you for all your suggestions and kind help during my PhD study.

I am also grateful to Prof. Shuxin Ouyang, who gave me great support and help as always. Then, I would like to thank all the members in the Photocatalytic Materials Group in NIMS and the persons who have helped me. I would like to express my thanks to Dr. Shengyao Wang, Dr. Xusheng Wang, Dr. Mengli Li, Mr. Gaoliang Yang, Mr. Qi Wang, Dr. Dekang Huang, Dr. Kun Chang, Dr. Huiwen Lin, Dr. Ningdong Feng, Mr. Shunqin Luo, Dr. Hui Song, Mr. Yao Xie, Mr. Davin Philo, Ms. Shuang Song, Ms. Hong Pang, Mr. Fumihiko Ichihara, Dr. Li Shi, Dr. Tetsuya Kako and Ms. Haruna Kurokawa for their kind helps in both experiments and daily life.

At last, I would like to thank my parents, sister and girlfriend Miss Yu He for their support and belief in me.